# A role for detailed assessment of hippocampal function in studies of Alzheimer's Disease

Ruth Wood

Thesis submitted to University College London for the Degree of Doctor of Philosophy in Neuroscience

The Sainsbury Wellcome Centre

I, Ruth Wood, confirm that the work presented in this thesis is my own. Where information has been derived from other sources, I confirm that this has been indicated in the thesis.

# Acknowledgements

## Contributions from Others

I am grateful for the contributions of others to the work presented in this thesis. Dr Stephen Burton performed the surgical procedures for the hippocampal and entorhinal lesion studies presented in Chapter 3. Dr Burton also implanted microdrives, which I had built, into mice, to enable me to collect the data presented in Chapter 4. Dr Borgel Greenaway performed the histology as presented in Chapter 4. Paige Mumford assisted with scanning slides using the ZEISS Axio Scan. I collected the majority of Honeycomb Maze behavioural data myself (Chapter 3) but am grateful to Richard Wu, Michele Bertelli and David Howett for their assistance with this. Finally, I am grateful to members of the Barry and O'Keefe laboratories for sharing MatLab code with me which provided a helpful starting point for my analyses.

**Publications**

Sections of *Chapter 1* (*page 24*) have been published previously as:
Wood and Chan 2015, The hippocampus, spatial memory and Alzheimer's disease ACNR 2015;15(2):5-7.


Sections of *Chapter 3 (page 133)* have been published previously as:
Wood, RA., Bauza, M., Krupic, J., Burton, S., Delekate, A., Chan, D., and O'Keefe J. The Honeycomb Maze provides a novel test to study hippocampal-dependent spatial navigation. Nature. 2018 Feb 1;554(7690): 102-105.

## Abstract

The hippocampus is one of the first cortical regions to exhibit Alzheimer's Disease (AD) pathology. The spatially-related firing of hippocampal *place cells* provides the cellular basis for spatial memory, and this is impaired relatively early in AD, yet few studies examine place cell activity in AD mouse models. Furthermore, current spatial navigation paradigms for rodents are not suited to tracking the progressive impairment seen in AD. This project aimed to address these gaps; the results provide initial support for the hypothesis that AD pathology disrupts hippocampal function which manifests as altered place cell activity and spatial behaviour.

Chapter 3 outlines experiments validating a novel behavioural test of hippocampal function, the 'Honeycomb Maze', specifically designed to overcome the limitations of other tasks. Wild-type rats and mice rapidly learnt to navigate to a hidden goal, and a lesion study demonstrated the key contribution made by the hippocampus. Task difficulty was scalable through altering maze parameters, with difficult choices exhibiting a greater reliance on hippocampal processing. The findings suggest the Honeycomb Maze provides a reliable means of assessing hippocampal function in rodents and is well suited for application to studies of AD.

Chapter 4 provides an in-depth characterisation of hippocampal pyramidal cell activity in an APP knock-in model of AD. Electrophysiological recordings were performed in the left CA1 subregion of four 15-month-old, freely moving, $APP^{NL-G-F}$ mice and four age-matched wild-type controls. Significantly fewer $APP^{NL-G-F}$ pyramidal cells exhibited spatial firing, and

deficits were present in rate and temporal coding of spatial information. APP$^{NL-G-F}$ spatial cells had lower spatial information content, larger place fields, reduced phase-locking to the theta rhythm of the local field potential, and a reduction in theta phase precession. Despite the small sample size, a positive correlation was identified between amyloid β plaque burden and pyramidal cell spatial information in APP$^{NL-G-F}$ mice.

## Impact Statement

The determination of disease effect on hippocampal function is critical to understanding how the earliest stages of Alzheimer's Disease (AD) affect the brain, and the work presented here has the potential to impact future academic and clinical research and patient care.

### *Academic research*

Historically, studies of disease mechanism have been conducted *in vitro*. The experiments undertaken in Chapter 4 demonstrate that *in vivo* paradigms can be used to study disease mechanism, particularly when investigating the neurotoxic properties of candidate pathogenic species such as amyloid beta oligomers. *In vivo* techniques studying treatment effect on the function of vulnerable neurons, at single cell and population levels, could greatly benefit future mechanistic studies and preclinical evaluation of novel therapies with potential disease-modifying capabilities.

The novel behavioural task in Chapter 3 has been shown to provide a reliable means of testing hippocampal function in both rats and mice. This task has the potential to be applied in both AD and non-AD studies. The maze design allows precise task manipulation and has been applied in further studies to gain insights into the mechanisms underlying the spatial information processing in the hippocampal formation. Concurrent electrophysiological recordings can be performed as animals complete the task, providing a means of correlating place cell activity and spatial memory; studies using this approach could also be applied in the context of AD pathology.

*Clinical research and care*

An estimated 820,000 people in the UK have a diagnosis of dementia, of which the most common cause is AD, and it is estimated that three times as many people have mild cognitive impairment. Such figures illustrate the importance of detecting AD in its earliest, pre-dementia, stages to facilitate early treatment and interventions designed to maintain functional independence. Novel behavioural tests to detect early alterations in hippocampal or entorhinal function, such as that presented in Chapter 3, will inform the design of clinical tests with a higher sensitivity and specificity for pre-dementia AD.

In the first instance such tests will be applied to patients presenting with symptoms of mild cognitive impairment, but in the longer term they may be used to identify AD in pre-symptomatic individuals which will benefit both patients and clinicians. Those in the earliest stages of AD are more likely to benefit from future disease-modifying preventative therapies and identifying these individuals will provide more appropriate cohorts for Phase III clinical trials. Early detection of AD also has significant impact for public health studies involving the longitudinal clinical, cognitive, and imaging evaluation of the ageing population.

A major limitation of many AD drug trials is a lack of outcome measures that are comparable across preclinical and clinical phases. The development of tasks sensitive to hippocampal dysfunction in rodents, as presented in Chapter 3, has informed the design of analogous tasks for humans using virtual reality platforms. This approach aims to generate equivalent outcome

measures across studies of transgenic AD models and patients, thus addressing a major factor limiting trial design and impeding progress in the delivery of effective AD therapies.

# Table of Contents

13

# Index of Figures

18

# Index of Tables

# Abbreviations

| | |
|---|---|
| Aβ | amyloid β |
| ACh | acetylcholine |
| AD | Alzheimer's disease |
| ApoE | apolipoprotein E |
| APP | amyloid precursor protein |
| CA | cornu ammonis subfield of the hippocampus |
| ChAT | choline acetyltransferase |
| CSF | cerebrospinal fluid |
| DG | dentate gyrus |
| EC | entorhinal cortex |
| FFT | fast Fourier transform |
| GWAS | Genome Wide Association Studies |
| hGH | human growth hormone |
| iCJD | iatrogenic Creutzfeldt-Jakob disease |
| LEC | lateral entorhinal cortex |
| LFP | local field potential |
| LIA | large irregular amplitude activity |
| LTD | Long Term Potentiation |
| LTP | Long Term Depression |
| MAPT | Microtubule Associated Protein Tau |
| MCI | Mild Cognitive Impairment |
| MEC | medial entorhinal cortex |
| mEPSC | miniature excitatory postsynaptic current |
| mIPSC | miniature inhibitory postsynaptic current |
| MRI | Magnetic Resonance Imaging |
| NFTs | Neurofibrillary tangles |

| | |
|---|---|
| NICE | National Institute of Health and Care Excellence |
| NLGF | APP$^{NL-G-F}$ mouse model |
| NTs | Neuropil threads |
| PDGF-B | Platelet derived growth factor B |
| PHF | Paired helical filaments |
| PrP$^c$ | Prion protein |
| PSEN1 | Presenilin 1 |
| PSEN2 | Presenilin 2 |
| ROS | Reactive Oxygen Species |
| SIA | small irregular amplitude activity |
| SWRs | sharp wave ripples |
| Thy-1 | Thymocyte differentiation antigen 1 |
| TMI | Theta modulation index |
| WT | wild-type |

## Nomenclature

In this thesis the term *hippocampal formation* is used to refer collectively to the dentate gyrus, cornu ammonis (CA) subfields of the hippocampus, subiculum, presubiculum, parasubiculum and entorhinal cortex. The term *hippocampus* or *hippocampus proper* is used to refer to the CA subfields alone.

The term *place cells* refers to pyramidal cells within the CA1 or CA3 hippocampal subfields which exhibit spatial firing activity and have a *place field*. The term *spatial cell* is used in Chapter 4 to refer to CA1 pyramidal cells which have significantly spatial firing patterns. These cells can broadly be considered as equivalent to place cells but may not have all the properties associated with a traditional place cell, for example a clearly circumscribed place field.

# 1. Introduction

## 1.1. General introduction

More than half a million people in the United Kingdom have a diagnosis of dementia, and Alzheimer's disease (AD) is the underlying cause in more than 50% of cases (1). In addition to the associated morbidity and mortality the disease constitutes a huge economic burden; the current annual cost of dementia in the UK is £26 billion (1). It is therefore critical to develop effective ways of identifying at-risk individuals in order to permit future application of interventions with the potential to modify disease and delay or prevent progression to dementia. Understanding the effect of AD on the brain is central to early diagnosis and the study of disease mechanisms, but despite this, information is scarce regarding the effects of AD pathology on the *function* of individual brain cells. This PhD project aims to address the core issue of disease effect on neuronal function in two ways. First, by developing behavioural tasks for use in mouse models of AD which probe hippocampal function to a deeper level than tasks currently in use (*Chapter 3, page 3.* Honeycomb Maze and second, by undertaking an in-depth characterisation of the electrophysiology of hippocampal neurons *in vivo* in a mouse model of AD (*Chapter 4, page 178*).

### 1.1.1. Project rationale

The entorhinal cortex (EC) and hippocampus are the first cortical regions to exhibit AD pathology (2, 3) and therefore determining disease effect on the function of these brain regions is critical to understanding how the earliest stages of AD affect the brain. The importance of work translating

hippocampal neuroscience to AD research is illustrated both in the use of the Morris water maze, a task designed to test hippocampal function in rodents, as an outcome measure in preclinical phases of AD treatment trials (4), and in the demonstration that hippocampus-dependent tests of spatial memory are highly sensitive for the diagnosis of prodromal AD (5).

The aim of this project is to expand on prior work in two crucial ways. First, it will introduce a novel test of spatial memory capable of differentiating between entorhinal cortex (EC) and hippocampal function and delivering a parametric, scaled-difficulty behavioural output. These capabilities allow superior tracking of disease progression than current tasks. Second, it will address the relative paucity of knowledge on the cellular basis of spatial memory deficits in AD by recording from hippocampal place cells in an AD mouse model.

### 1.1.2. Project overview

The experimental work outlined in this thesis is divided into two main components:

- First, the validation of a novel behavioural task, the 'Honeycomb maze', which has been specifically designed to assess hippocampal and entorhinal function in rodents and to overcome the limitations associated with other, commonly used tests of spatial behaviour (*Chapter 3, page 133*)
- Second, hippocampal single cell and local field potential recordings in a novel mouse model of AD, alongside histological analysis, to

study the relationship between neural activity and amyloid β pathology (*Chapter 4, page 178*)

In the final chapter (*Chapter 5, page 301*) I will discuss the contribution of these two studies to our understanding of hippocampal function in AD and the potential to apply these two methods in future research studies.

This introductory chapter outlines the relevant background to this thesis and puts my work into context. First, I will provide an overview of AD, followed by a review of spatial cognition, with a focus on the neural basis of spatial behaviour and spatial memory in AD. Finally, I will discuss the hippocampal formation, specifically the relevant neuroanatomy and the electrophysiology of the hippocampus proper.

## 1.2. Alzheimer's Disease

This section aims to provide an overview of Alzheimer's disease (AD), focusing mainly on aspects which are relevant to this PhD project. Spatial navigation in AD is discussed in a later section (*page 71*).

### 1.2.1. Background and disease significance

The features of AD were first described over a century ago by Alois Alzheimer, a German histopathologist (6). Dr Alzheimer was intrigued by the clinical presentation of a 51-year-old patient in a Frankfurt asylum, Auguste Deter, who had short-term memory impairment and behavioural disturbance (*Figure 1.1*). Upon her death he received her medical records and brain, and using Bielschowsky silver staining identified the extracellular amyloid β (Aβ) plaques and intracellular neurofibrillary tangles (NFTs) which are now considered pathological hallmarks of AD. Today, Alzheimer's

disease (AD) is recognised as the most common underlying cause of dementia, affecting more than 36 million people worldwide (7). The personal, societal and economic costs of AD are significant and far-reaching; advanced disease results in severe cognitive deficits with the total cost of care reaching over £34.7 billion per year in the United Kingdom (8). Despite this, no disease modifying treatments are currently available.


Image redacted for copyright reasons
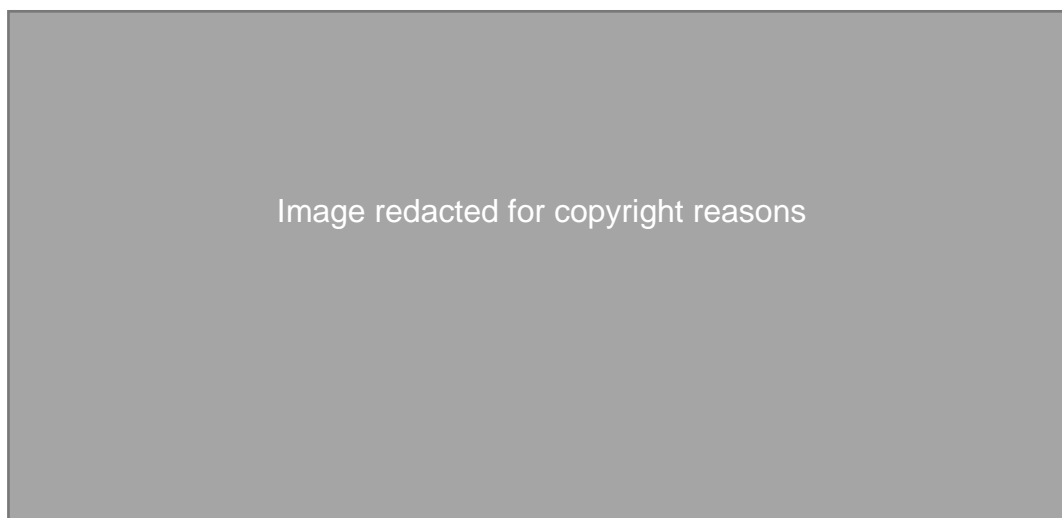
**Figure 1.1 Alois Alzheimer and Auguste Deter.** The first description of Alzheimer's disease was made by Alois Alzheimer (left) in 1901 when he described the clinical features, and later the associated pathology, of 51-year-old asylum patient Auguste Deter (right).

### 1.2.2. Clinical features

Risk factors for AD include advancing age, female sex, and vascular risk factors. The most common, sporadic, form of AD manifests as a progressive neurodegenerative disease usually presenting in the eighth decade of life with memory impairment and disorientation (9). In addition to progressive memory impairment, which is the hallmark clinical feature, other higher cortical functions can be affected leading to impairments in language, visuo-spatial processing, executive function, and personality change. There is a growing body of evidence that spatial navigation and memory are disproportionately affected early in the course AD, including at prodromal

and even preclinical stages. This is discussed further in a later section (*page 71*).

A definitive diagnosis of AD is made at post-mortem through the identification of amyloid β (Aβ) plaques and tau tangles in the brain, however a number of biomarkers exist which can assist pre-mortem diagnosis in conjunction with clinical features. These include elevated concentrations of phosphorylated tau, or decreased concentrations of Aβ, in the cerebrospinal fluid (CSF), hypometabolism in specific brain regions such as the medial temporal lobes on FDG-PET (Fluorodeoxyglucose Positron Emission Tomography), and atrophy of the medial temporal lobe, particularly the hippocampus, on Magnetic Resonance Imaging (MRI) (10). Amyloid-PET and tau-PET allow *in vivo* visualisation of AD pathology and are widely used in research studies to identify patients with pre-clinical disease who may respond best to novel disease-modifying therapies (11). However, a confounding factor is the appearance of AD pathology in the healthy aging brain; the incidence of both tau tangles and Aβ plaques increase with age, even among individuals who do not develop clinical features of AD.

### 1.2.3. Pharmacological therapies

There are few pharmacological treatment options available to patients with AD. Currently the UK National Institute of Health and Clinical Excellence (NICE) recommend the use of two classes of drug: cholinesterase inhibitors, such as donepezil, which increase the concentrations of acetylcholine within the brain and slow the rate of cognitive decline in mild to moderate disease, and an NMDA receptor antagonist, memantine, which acts by reducing glutamate-mediated neurotoxicity and has efficacy in more severe disease

(12). Both agents have only limited benefits and neither modifies or halts the progression of AD.

More recent pharmacological strategies target tau and Aβ themselves, aiming to reduce the concentrations of these pathological proteins in the brain. However, until recently, all trials of such agents in the symptomatic phases of disease have proved ineffective, potentially because the disease pathology was already fully established by the time the novel drugs were administered in clinical trials. In June 2021 Biogen's aducanumab, a monoclonal antibody targeting aggregated forms of Aβ, was granted a licence by the US Food and Drug Administration (FDA) and has since been hailed as "the first ever disease modifying drug for AD" (13). In a phase Ib trial, and a subsequent phase III trial, aducanumab was shown to reduce Aβ plaque accumulation and slow cognitive decline in patients with prodromal or mild AD, however, its approval has been controversial with another identically designed phase III trial failing to demonstrate any clinical benefit (14).

### 1.2.4. Disease course

AD develops over many years with evidence that neuropathology begins decades prior to the onset of symptoms (10, 15). This prolonged preclinical phase poses a challenge to clinicians who may only diagnose AD many years later once symptoms are manifest, by which time the neurodegenerative process is well underway, and the therapeutic window for any preventative treatments will have closed. Studies of CSF biomarkers and PET imaging suggest that the accumulation of amyloid β pathology in

the brain begins at the very earliest stages of disease, and this is followed by synaptic dysfunction, tau-mediated neuronal injury and even structural brain changes on volumetric MRI before overt symptoms develop (*Figure 1.2*) (16).
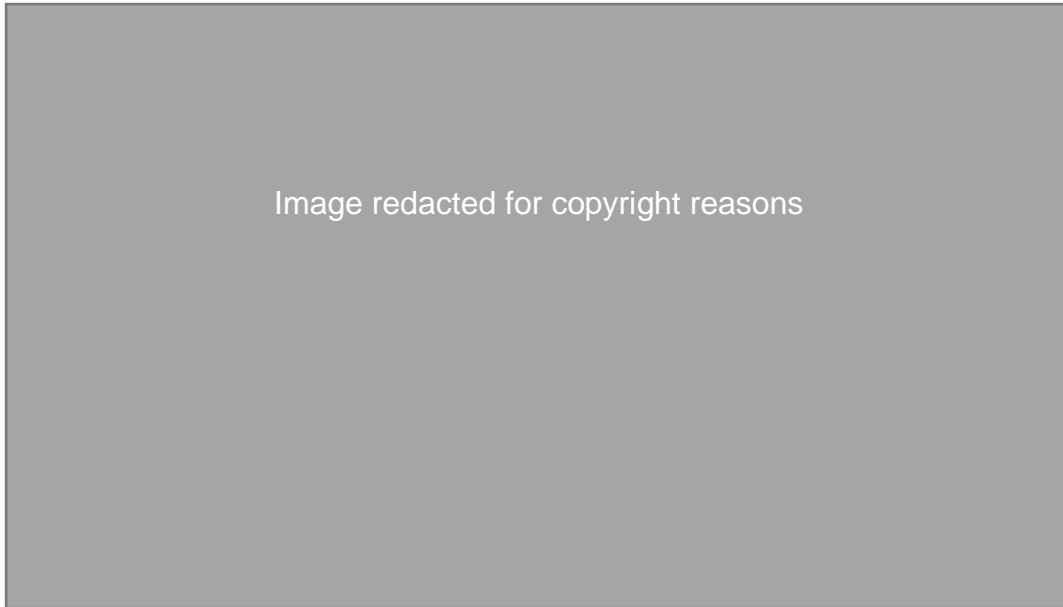


**Figure 1.2 A model of Alzheimer's disease biomarkers in the preclinical stages of disease.** Figure taken from (16).

Pre-symptomatic AD progresses to Mild Cognitive Impairment (MCI), a pre-dementia phase of AD in which individuals display subtle cognitive deficits beyond that expected for their age or level of education, but whose impairment is not sufficiently severe to constitute dementia (9, 10). MCI with predominant memory impairment (amnestic MCI) may represent a prodromal stage of AD with individuals being diagnosed with AD at a rate of 10-15% per year (17). Although 25% of MCI patients progress to a diagnosis of dementia within three years (18), MCI as a clinical state may be caused by other disorders, including non-AD neurodegenerative disorders (for e.g. Lewy Body pathology), anxiety, cerebrovascular disease and head injury (7). As such, identification of MCI on clinical grounds alone cannot

discriminate between these underlying aetiologies (19, 20) and so an active avenue of research is the development of tests, including potentially disease-specific spatial memory tasks, and biomarkers to differentiate between MCI secondary to AD pathology and MCI due to other underlying causes (21).

### 1.2.5. The genetics of Alzheimer's Disease

#### *1.2.5.1. Sporadic Alzheimer's Disease*

Sporadic AD occurs secondary to a combination of environmental and non-dominant genetic risk factors. Genome wide association studies (GWAS) have implicated several non-Mendelian polymorphisms in sporadic AD. The identification of genetic risk factors may provide a clue as to the underlying pathophysiology and putative susceptibility genes include those involved in lipid metabolism (ApoE, CLU, PICALM), immune activation (TREM2, CR1, CD33) and cell membrane homeostasis (SORL1, BIN1) (22). Of these, the apolipoprotein E (ApoE) ε4 allele is the most prevalent and largest known genetic risk factor for sporadic AD (23). ApoE is polymorphic with three major alleles, of which the ε4 allele is associated with sporadic AD and the ε2 allele is thought to be protective (24, 25). The ε4 allele is not a determinant of disease, however, as only 40 – 65% of patients with AD have at least one copy and some homozygous individuals do not develop AD (24, 25). There is strong evidence that the major mechanism through which ApoE genotype influences AD is through the effects of ApoE on Aβ metabolism (23).

### 1.2.5.2. Familial Alzheimer's Disease

Familial AD follows a Mendelian inheritance pattern and tends to have a more aggressive course, with an earlier age of onset and a more rapid progression of symptoms (26). Fewer than 1% of AD cases are familial, and cases are caused by fully penetrant autosomal dominant mutations in three genes: presenilin 1 (PSEN1) on chromosome 14, presenilin 2 (PSEN2) on chromosome 1 and amyloid precursor protein (APP) on chromosome 21. In 1982 a mutation in the APP gene, the 'Dutch mutation', was linked to a form of Cerebral Amyloid Angiopathy, a distinct clinical condition in which there is extensive Aβ deposition in the cerebral vasculature (27) . This discovery indicated that APP mutations could cause amyloid β deposition, albeit in blood vessels rather than the brain parenchyma. A decade later a missense mutation in the same exon of the APP gene was identified in a kindred with autosomal dominantly inherited early-onset AD (28). Since then a further 48 APP mutations have been linked to familial AD, along with more than 300 PSEN1 mutations and 50 PSEN2 mutations (29). Of note, all three of these genes are closely linked to APP processing and the production of amyloid β, a discovery which provided strong support for a leading model of AD pathophysiology, the amyloid hypothesis (*see page 42*). Familial APP mutations are traditionally named after the geographical region in which they were first located such as the Swedish (APP KM670/671**NL**), Arctic (APP E693**G**) and Iberian (APP I716**F**) mutations, which are the mutations present in the APP$^{NL-G-F}$ mouse model used in the experiments in Chapter 4 *(page 178).*

### 1.2.6. Alzheimer's Disease pathology

Post-mortem and MRI studies consistently demonstrate marked atrophy in the AD brain which is most pronounced in the medial temporal lobes, specifically the entorhinal cortices and hippocampi (30) (*Figure 1.3*). These volumetric changes are accompanied by two major neuropathological hallmarks: extracellular senile plaques which contain a core of amyloid β protein surrounded by dystrophic neurites, and intracellular neurofibrillary tangles (NFTs) composed of hyperphosphorylated tau (2, 3, 31) (*Figure 1.3*).
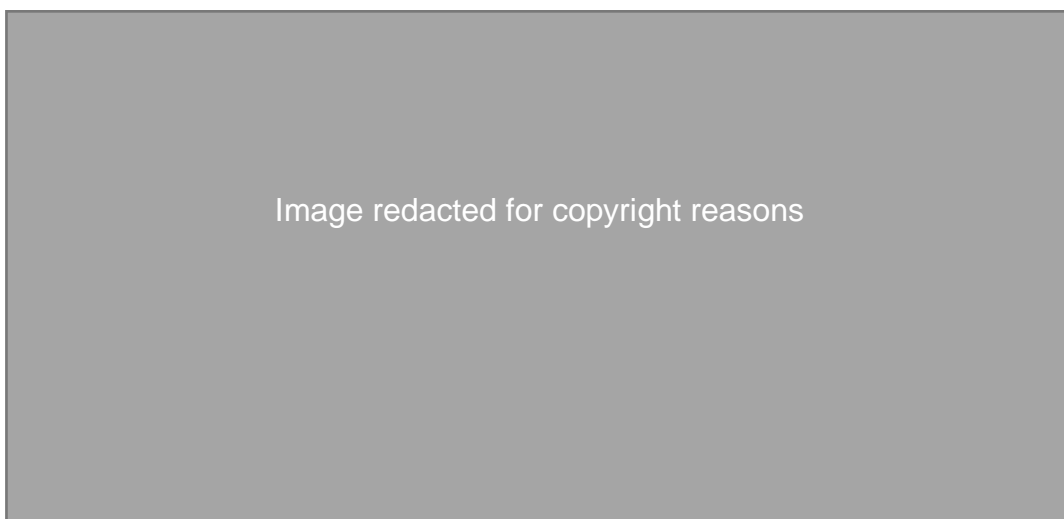


**Figure 1.3. The pathology of Alzheimer's disease.** The major pathological hallmarks of AD are amyloid β plaques and neurofibrillary tangles (B) which are absent in healthy brain tissue (A). At later stages of disease neuronal death results in profound atrophy (human brain slices, C). Figure taken from (32).

### *1.2.6.1. Microtubule Associated Protein Tau (MAPT)*

NFTs were first identified by Alois Alzheimer in 1907, but it wasn't until 1985 that their primary component was identified as tau (6, 33). Tau is abundant in the axons of neurons where it binds to microtubules which themselves are involved in axoplasmic transport, nucleic and cell division, and

organisation of intracellular structure (34, 35). Tau plays a key role in microtubule assembly, dynamic behaviour and spatial organisation, and is tightly regulated by a number of factors, in particular post-translational modifications such as site-specific phosphorylation (36). Alternative splicing of the MAPT gene in humans results in six tau isoforms (37, 38) (*Figure 1.4*). These differ by the presence of one or two additional inserts in the N-terminal domain (N1 and N2), and the presence of three-repeat (3R) or four-repeat (4R) sequences in the microtubule binding region. Disruption of the ratio of 3R and 4R tau isoforms has been implicated in the pathogenesis of AD (see (39) for a review) and, of note, the 3R tau isoform is not present in adult mice (40).



**Figure 1.4 Tau isoforms in the human brain.** Six tau isoforms are present in the human brain through alternative splicing of exons 2,3, and/or 10. Exons 2 (green) and 3 (blue) produce aspects N1 (green) and N2 (blue) of the N-terminal projection domain respectively. The microtubule binding domain can contain three or four repeats depending on the presence of the R2 domain (red) encoded by exon 10. Figure taken from (41).

In the AD brain tau is abnormally hyperphosphorylated, leading to a conformational change and an accumulation within neurons as NFTs and neuropil threads. NFTs are fibrillar intracytoplasmic inclusions present in the proximal dendrites and the soma of affected neurons and are rich in paired helical filaments (PHFs) composed of insoluble hyperphosphorylated tau

(42, 43) (*Figure 1.5*). Unlike Aβ plaques, NFTs are not unique to AD, and are present in over 20 different neurodegenerative diseases, collectively termed tauopathies. Neuropil threads (NTs) are also composed of PHFs and are present in swollen dendrites and dystrophic neurites in distorted axon terminals (44). Disturbances in the integrity of the cytoskeleton, thought to occur secondary to the abnormal accumulation of tau, can lead to impairment in axonal transport and synaptic recycling, compromising neuronal function. The death of affected neurons, possibly via apoptosis, leaves behind extracellular 'tombstone' tangles (44).



Image redacted for copyright reasons

**Figure 1.5 Tau pathology in Alzheimer's disease.** Tau accumulates in the neuronal cell bodies (arrow) as NFTs, often described as globose, or flame-shaped, and in neuronal extensions (arrowhead). Scale bar = 25µm. Section from the neocortex of a patient who died with AD Braak stage VI. Tau protein is stained brown with AT8, and the counterstain is hematoxylin (light blue). Image from (45).

The progression of tau pathology in AD follows a predictable course and post-mortem studies have differentiated six distinct neuropathological stages (31). NFTs and NTs first develop in the medial temporal lobe, specifically the lateral then the medial entorhinal cortex (Braak stages I and II), before progressing to involve the limbic regions (stages III and IV) where the pyramidal cell layer of the CA1 hippocampal subfield and subiculum are particularly affected. Finally, pathology spreads to the midbrain and isocortex (Braak stages V and VI) (31, 46). The progression of tau pathology throughout the brain correlates with the pattern of neuronal loss and is

mirrored by the clinical progression of AD, supporting the view that tau aggregates cause neurodegeneration (46). The earliest symptoms of AD are deficits in episodic and spatial memory, in which the hippocampus and entorhinal cortex play a key role (47-50). In the later stages of disease when NFTs have spread throughout the neocortex, clinical features of disease include impairments in language, visuospatial processing and executive function (31, 51).

### 1.2.6.2. Amyloid β and amyloid precursor protein (APP)

Amyloid β (Aβ) is a peptide 38 to 43 amino acids in length, which is prone to aggregation and was first sequenced 40 years ago from the meningeal blood vessels of patients with AD and Down's syndrome. Shortly after this it was identified as the primary constituent of the extracellular amyloid plaques observed in AD (52, 53).

#### 1.2.6.2.1. Amyloid β histopathology

Extracellular senile plaques are one of the major pathological hallmarks of AD. Senile plaques are spherical, polymorphous protein deposits containing filamentous Aβ with a characteristic β-pleated sheet conformation (*Figure 1.6*). There are two types of senile plaques: neuritic plaques and diffuse plaques. Neuritic plaques contain a dense core of Aβ fibrils, surrounded by a halo, or corona, of dystrophic neurites containing paired helical filaments of hyperphosphorylated tau and ubiquitin, alongside reactive astrocytes, and microglia. Neuritic plaques positively stain with Congo Red showing an apple green birefringence. Smaller diffuse Aβ plaques which do not disrupt the neuropil are also seen in AD but are not diagnostic since they can feature in large numbers in older, non-demented individuals.

The CERAD neuritic plaque scoring system, developed by the Consortium to Establish a Registry for Alzheimer's Disease, is a semi-quantitative measure of plaque density in the neocortex, as identified by the Bielchowski silver stain, and is used alongside other measures to make a neuropathological diagnosis of AD (54). The deposition of Aβ in the brain follows a characteristic pattern as AD progresses. Deposits appear first in the neocortex (Thal phase 1) and later spread to the allocortex including the hippocampus (Thal phase 2), the deep nuclei (Thal phase 3), and in advanced cases the brainstem (Thal phase 4) and cerebellum (Thal phase 5) (55).

Image redacted for copyright reasons

**Figure 1.6 Alzheimer's disease neuritic plaques.** Diffuse plaques (*A*) and neuritic plaques (*B*) stained using immunohistochemistry. Bielchowsky silver staining (*C*) and Thioflavin S (*D*) stain neuritic plaques and neurofibrillary tangles composed of hyperphosphorylated tau (arrow heads). Scale bars are 40µm. Image taken from (56).

### 1.2.6.2.2. APP processing

APP is a transmembrane glycoprotein associated with axonal growth and guidance, and synaptogenesis (57). APP processing by canonical

secretases occurs via two distinct and competing pathways, only one of which produces the Aβ peptides found in AD plaques (*Figure 1.7*) (58-63).

Image redacted for copyright reasons
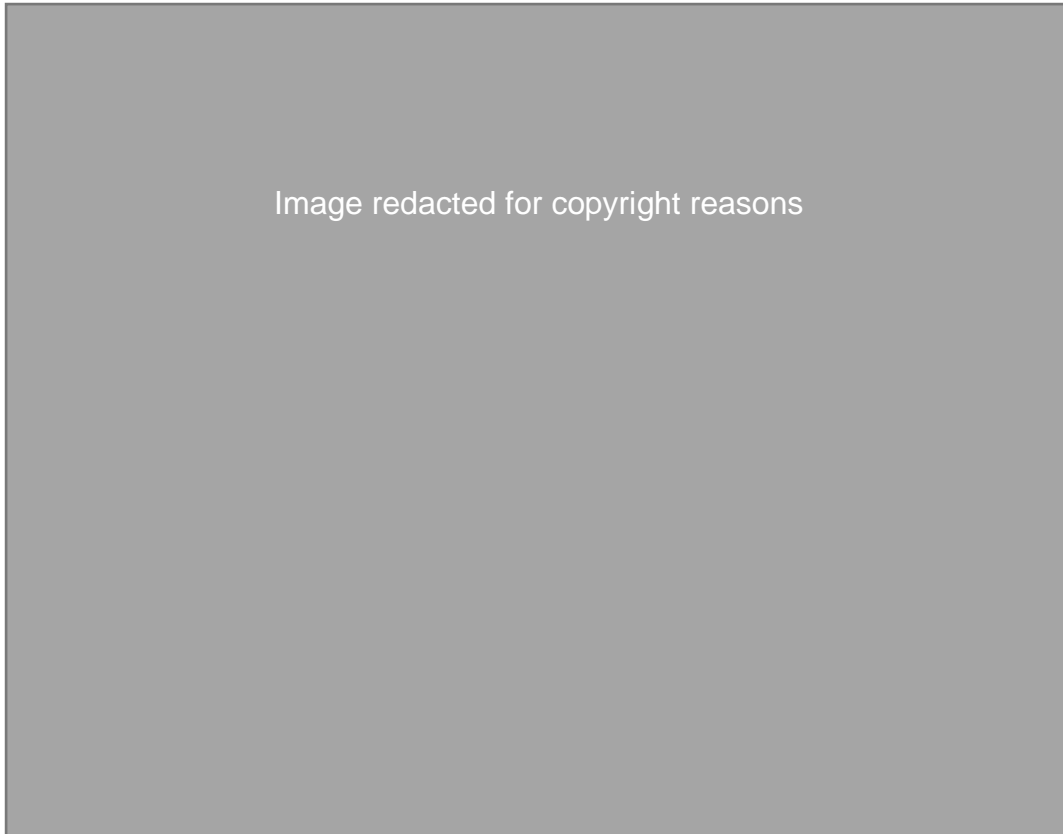
**Figure 1.7 APP processing.** APP can be processed via a non-amyloidogenic α secretase pathway, and an amyloidogenic β and γ secretase pathway. APP, amyloid precursor protein; AICD, APP intracellular domain; CTF, C terminal fragment. Figure modified from (67).

In the *non-amyloidogenic* pathway, APP expressed on the cell surface membrane is subject to proteolytic cleavage by α secretase (64, 65). The α secretase cleavage site lies within the Aβ domain, and cleavage at this location produces a large, soluble N-terminal fragment, sAPPα, and a truncated APP C-terminal fragment (αCTF) (*Figure 1.7*). The αCTF is subsequently cleaved by γ secretase to produce the APP intracellular domain (AICD), which may play a role in nuclear signalling, and a fragment p3 (60, 66). sAPPα reduces Aβ production by competing with uncleaved APP for β secretase binding, the first step in *amyloidogenic* pathway.

In the *amyloidogenic* pathway APP is internalised into an endocytic compartment and cleaved by a β secretase (BACE, β-site APP cleaving enzyme), and subsequently a γ secretase, to produce Aβ, in addition to two other fragments, sAPP$_\beta$ and AICD. Aβ fragments released into the extracellular space later polymerise to form the extracellular plaques characteristic of AD (67, 68). APP can also be processed via non-canonical pathways such as the η secretase pathway (69) and the meprin β cleavage pathway (70), both of which may play a role in the pathophysiology of AD.

### 1.2.6.2.3. Amyloid β isoforms

AAP cleavage produces two main Aβ isoforms, Aβ$_{1-40}$ and Aβ$_{1-42,}$ which are 40 and 42 amino acids in length respectively. Despite their similarity in length these isoforms differ in their toxicity and clearance and aggregation mechanisms; Aβ$_{1-42}$ is more prevalent in Aβ plaques, has a greater propensity to aggregate and is less readily cleared across the blood brain barrier than Aβ$_{1-40}$ which is the more abundantly generated peptide (71-73).

### 1.2.6.2.4. Amyloid β aggregation

Aβ monomers aggregate into various assemblies including oligomers, protofibrils and fibrils. Soluble monomers and oligomers move readily throughout the brain between intra- and extracellular compartments, in contrast to larger, insoluble Aβ fibrils which are more inert (74, 75). Relatively little is known about the structure of Aβ oligomers due to their transient states and heterogeneity (76). Aβ oligomers differ in their toxicity and propensity to aggregate, with an inverse relationship identified between oligomer size and toxicity (77, 78). Low molecular weight Aβ$_{1-40}$ oligomers exist primarily as a combination of monomers, dimers, trimers and

tetramers, whereas Aβ$_{1-42}$ preferentially exists as pentameric or hexameric units called paranuclei which more rapidly self-aggregate (79). Higher molecular weight oligomers exist as spherical aggregates which coalesce to form elongated protofibrils, and subsequently mature fibrils (*Figure. 1.8*).



Image redacted for copyright reasons

**Figure 1.8 Formation of amyloid β fibrils from monomers.** Aβ aggregates to form mature fibrils via a number of intermediate steps. Figure taken from (74).

### 1.2.6.2.5. Amyloid β clearance

In the healthy adult brain the rate of Aβ clearance is approximately equal to its rate of synthesis (80), however a disruption of this dynamic equilibrium can affect the brain's ability to maintain healthy Aβ levels and may play an important role in the pathophysiology of AD (81). Aβ clearance occurs via enzymatic and non-enzymatic mechanisms (73). Multiple Aβ degrading enzymes have been identified including neprilysin, matrix metalloproteinase-9 and insulin-degrading enzyme, and increasing the activity of these enzymes may be a potential AD treatment strategy (for a review see (82)). Non-enzymatic clearance pathways include the glymphatic pathway, via which interstitial fluid in the parenchyma is

exchanged with CSF (83), uptake of soluble and fibrillar Aβ by microglia (84), and clearance across the blood brain barrier by astrocytes (85). All these processes have been shown to be altered in AD (72, 86-88).

### 1.2.6.2.6. Familial AD and the APP processing pathway

As previously discussed, APP mutations are associated with familial AD (*page 32*). Many of these mutations cluster around the β and γ cleavage sites and are thought to promote Aβ generation by enhancing β and γ secretase activity. APP mutations also occur within the Aβ sequence itself and may affect the toxicity of Aβ oligomers or their propensity to aggregate. Some pathogenic APP mutations have also been shown to alter the ratio of $A\beta_{1-40}$ and $A\beta_{1-42}$ isoforms produced (89).

Mutations in PSEN1 and PSEN2 are also linked to APP processing; the presenilins are catalytic components of the γ secretase complex and AD-related mutations in PSEN1 and PSEN2 have been shown to increase the $A\beta_{1-42}$:$A\beta_{1-40}$ ratio in patient-derived fibroblasts, cell lines and mouse overexpression and knock-in models of AD (90).

### 1.2.7. Alzheimer's Disease pathogenesis

### 1.2.7.1. The cholinergic hypothesis

The observation of a presynaptic cholinergic deficit in the brain tissue of patients with AD led to the formation of the *cholinergic hypothesis*. Post-mortem studies demonstrated a deficit in choline acetyltransferase (ChAT) (91-93), the enzyme responsible for the synthesis of acetylcholine (ACh), in the neocortex of AD patients, and a reduction in choline uptake and ACh release (94, 95). These findings supported the idea that dysfunction of cholinergic neurons significantly contributes to the cognitive decline

observed in AD patients. The involvement of the cholinergic system in the generation of theta oscillations and sharp wave ripples in the local field potential (LFP), and hippocampal reactivation (*see later, page 91*), and the role of cholinergic tone in the modulation of synaptic plasticity in CA1, all suggest that cholinergic neurotransmission plays an important role in memory consolidation and learning (96, 97). Further support for the cholinergic hypothesis comes from the use of cholinesterase inhibitors as a treatment for mild to moderate AD, with these agents shown to slow the rate of cognitive decline (98). However, these drugs do not halt disease progression, and while the cholinergic hypothesis may partially explain some aspects of the memory impairment seen in AD, it leaves many unanswered questions.

### 1.2.7.2. The amyloid hypothesis

The amyloid hypothesis, also called the *amyloid cascade hypothesis*, is the dominant model of AD pathogenesis (99). In its earliest form it postulated that Aβ released into the extracellular space accumulated in plaques, leading to the formation of NFTs and causing neuronal death and dementia (100). As more data accumulate this hypothesis has been further refined and a shift has occurred from viewing aggregated Aβ sequestered in plaques as the pathogenic agent, to oligomeric Aβ (101). Despite this, the central tenet remains that Aβ dyshomeostasis is the primary driving force underlying the development of AD.

### 1.2.7.2.1. Evidence in support of the amyloid hypothesis

A very large body of literature on Aβ exists and has been extensively reviewed elsewhere (for examples see (99, 102, 103)). Broadly speaking

the three main strands of supporting evidence for the amyloid hypothesis are as follows:

(i)     observations that a progressive accumulation of Aβ occurs in AD and predates other pathological changes,

(ii)    strong links between mutations which cause or increase the risk of AD and the production, clearance, and pathogenicity Aβ, and

(iii)   evidence that Aβ oligomers cause neuronal death and dysfunction.

Each of these will be examined briefly.

(i) Aβ pathology predates other changes in AD

First, AD patients display progressive Aβ pathology in brain regions important for memory and cognition (55). In addition, human biomarker studies using CSF measurements of  $Aβ_{1-42}$ and amyloid PET, along with post-mortem studies, consistently demonstrate that Aβ pathology precedes other changes seen in AD such as the accumulation of tau pathology, atrophy and cognitive decline (99).

(ii) Genetic studies suggest an important role for Aβ in AD pathogenesis

As previous discussed (*page 32*), mutations in key components of the APP processing pathway cause aggressive forms of familial AD and, in addition, individuals with Down's syndrome (trisomy 21) who have an extra copy of the APP gene are at an increased risk of developing AD (104). Evidence also arises from the genetics of sporadic AD with the ApoE4 allele being associated with reduced Aβ clearance (105). Finally, a missense mutation in APP which decreases the production and aggregation of Aβ has been found to be protective against AD (106).

(iii) Aβ oligomers cause neuronal dysfunction and death

Soluble Aβ oligomers, as opposed to larger insoluble aggregates, are now widely believed to be the main toxic Aβ species. In mouse models of AD the concentration of oligomeric Aβ correlates with memory impairment; in the Tg2576 mouse model of AD Aβ plaques were not associated with memory impairment in the absence of Aβ oligomers and a reduction in the concentration of Aβ oligomers correlated with an improvement in memory (107). Intraventricular injection of Aβ oligomers into healthy rats has also been shown to result in learning and memory deficits in the Morris Water Maze (107, 108).

*In vitro* neurotoxicity studies have demonstrated that Aβ oligomers inhibit neuronal viability and are more toxic to neurons than Aβ fibrils and protofibrils (109, 110). Aβ oligomers can induce tau hyperphosphorylation (111) and neurite degeneration (112), and have been shown to form pore-like structures which disrupt membrane permeability and permit calcium influx into cells (113, 114). Aβ oligomers may also cause a reduction in synaptic plasticity. In brain slice preparations, synthetic oligomeric Aβ, and oligomeric Aβ isolated from the brains of AD patients, inhibit hippocampal long-term potentiation (LTP), a well-known electrophysiological correlate of learning and memory. The concentrations of oligomers required to disrupt LTP are similar to those found in the CSF of AD patients (115-118). In addition, oligomeric Aβ enhances long term depression (LTD) in mouse hippocampal slices (117), and reduces synaptic density (99). The toxic effects of Aβ oligomers may be mediated through certain ligand receptors; via interactions with the NMDA receptor Aβ oligomers were found to induce

rapid and protracted depolarisation of neurons, leading to glutamate release, excitotoxicity and neuronal death (119), and binding of Aβ oligomers to prion protein (PrP$^c$) receptors has also been implicated in their toxicity (120). Oligomeric Aβ may also exert toxic effects by inducing the production of reactive oxygen species (ROS) (121) and through the initiation of an inflammatory cascade (122), including a role in promoting microglial maturation (123).

*1.2.7.2.2. Criticisms of the amyloid hypothesis*

A key criticism is that Aβ plaque burden correlates less well with the degree of cognitive impairment than tau NFTs (46). Proponents of the amyloid hypothesis argue that Aβ deposition is an early widespread event leading to cognitive deficits via numerous distant downstream effects, including the formation of NFTs. It therefore follows that the downstream effects, which may themselves mediate neuronal dysfunction, are more closely correlated with neuronal death and symptoms of dementia (99). This argument can be used to counter another criticism: the observation that some individuals with Aβ deposits at post-mortem did not display clinical features of AD. It may be that rigorous cognitive testing was not conducted in such cases, and it has been noted that the deposits identified tended to be diffuse rather than neuritic plaques. One interesting study showed that the levels of Aβ oligomers per plaque were much lower in the brains of such asymptomatic individuals compared to those with a clinical diagnosis of AD (124).

The suggestion from human neuropathological studies that tau pathology in limbic regions precedes the formation of Aβ plaques is another challenge to the amyloid hypothesis (125). However, neuropathological studies have not

routinely included assays for oligomeric Aβ, looking mainly for neuritic plaques, and the existence of subtle tau pathology in the limbic regions of individuals dying from other causes does not necessarily imply that these individuals would have developed AD had they lived longer.

Perhaps the biggest criticism is the failure of numerous clinical trials of agents which act to lower the concentration of Aβ species within the brain, such as monoclonal antibodies directed against amyloid β species, gamma secretase inhibitors, and Aβ immunisation. Until recently none of the phase III clinical trials of therapies targeting Aβ has shown significant positive outcomes (126, 127), although many argue that a common failure of such trials is the use of cohorts with established AD, and that in order for anti- Aβ treatments to be effective they should be given at the very earliest stages of the disease process, before neurodegeneration occurs and clinical symptoms develop (128). Studies in pre-symptomatic individuals from familial AD kindreds, and the use of novel clinical biomarkers to identify individuals at increased risk of AD, are underway and may prove useful in addressing this issue.

### 1.2.7.3. Prion-like propagation of pathological proteins

Both Aβ and tau pathology have been shown to propagate through the brain in a stereotypical pattern (31, 55). An increasing body of evidence suggests this reflects a prion-like spread of pathological proteins through anatomically connected networks.  In prion diseases a misfolded, abnormal form of an endogenous protein forms a seed or template which then converts further monomers into the pathogenic isoform (129).

*1.2.7.3.1. Evidence for the prion-like spread of amyloid β*

It has long been known that Aβ can self-propagate a misfolded conformation *in vitro* (130) and this has subsequently been demonstrated *in vivo*. Injection of human brain extracts containing Aβ species has been shown to induce Aβ pathology in AD transgenic mice, and when extracts were immunodepleted of Aβ this effect was greatly diminished (131). Subsequent studies have shown that synthetic Aβ preparations accelerate Aβ pathology *in vivo* (132). Prion-like propagation of Aβ seeds has also been observed with intraperitoneal and intravenous administration (133, 134). In a 2008 post-mortem study, eight individuals who contracted iatrogenic Creutzfeldt-Jakob disease (iCJD) from the administration of contaminated human growth hormone (hGH) also displayed Aβ pathology to a greater extent than controls with other forms of prion disease (135). Aβ pathology has since been observed in other hGH recipients who did not have CJD (136), and an association found between iCJD caused by dural grafting and Aβ pathology (137). Taken together these findings support the hypothesis that Aβ pathology may be transmissible between humans (129).

*1.2.7.3.2. Evidence for the prion-like spread of tau*

Accumulating evidence also indicates that tau pathology spreads in a prion-like fashion. Brain extracts from a mouse line expressing mutant tau (P301S tau) induced aggregation of wild-type human tau into filaments when injected into the brain of a mouse model expressing a human tau isoform. Tau pathology propagated systematically from the original injection site to anatomically connected brain regions providing evidence for the neuronal uptake, transport and release of tau seeds (138). Tau oligomers from human brain extracts of patients with AD and tauopathies have been shown

to seed tau pathology in wild-type mice (139, 140), and in one study intracerebral injection of brain extracts from patients with different tauopathies induced tau lesions in mice which resembled those present in the corresponding human disease (140). *In vitro* studies also support a prion-like spread; extracellular tau aggregates can be taken up by naïve cells where they promote intracellular tau fibrillization, with seeds spreading between cells in a trans-synaptic fashion (141-144).

## 1.2.8. Mouse models of Alzheimer's disease

### *1.2.8.1. Transgenic mouse models of Alzheimer's Disease*

Nearly 200 transgenic rodent models of AD exist with the majority containing mutations in genes linked to the APP processing pathway found in familial AD (145). Such models can be powerful resources for elucidating human disease mechanisms although are not without their limitations. Broadly speaking, the main transgenic mouse models of AD fall into three categories: mice which overexpress mutant APP and/or PSEN, mice which overexpress human tau, and models which overexpress a combination of mutations. Many APP models exist, with some overexpressing mutant APP from a single AD kindred, such as the Tg2576 and APP23 models which overexpress APP with the Swedish mutation (K670N/ M671L), and others containing mutant APP from two or more kindreds, such as the J20 model which contains APP with the Swedish and Indiana mutations (V717F) (29). The expression pattern and concentrations of APP are driven largely by the choice of promoter, with common examples being the thymocyte differentiation antigen 1 (Thy-1), prion protein (PrP) and platelet-derived

growth factor B-chain (PDGF-B) genes (146). These animals exhibit Aβ pathology, synaptic loss, cognitive deficits, and behavioural impairment. Criticisms of these models include the lack of tau pathology, and the absence of neuronal loss.

Tau transgenic mice express either wild-type or mutant human tau using various promoters (147). Models aiming to reproduce the sequential tau propagation observed in AD, beginning with NFTs in the entorhinal cortex, have been developed in transgenic lines which overexpress P301L tau (148). Tau models show that MAPT mutations accelerate the aggregation of tau and can lead to neuronal death and dysfunction, although it has been argued they may be better understood as models of non-AD tauopathies (149).

Models with a combination of mutations can exhibit both Aβ and tau pathology and have been used to create mice with an accelerated pathological profile. Examples include the triple transgenic model (3xTg) which overexpresses mutant APP, PSEN1 and MAPT, and the 5xFAD model which overexpress APP with the Swedish, Florida, and London mutations, in addition to doubly mutated PSEN1. While these models can be useful in answering specific questions, a criticism is that the genetic conditions do not resemble those seen in human disease.

### 1.2.8.2. Limitations of APP overexpression models

The development of second-generation AD mouse models which use a 'knock-in' technique to express mutant APP has highlighted the limitations of the more traditional APP overexpression models which they were designed to replace. Overexpression of APP generates elevated Aβ

concentrations and mimics the Aβ deposition seen in AD, however it also increases the concentration of APP itself, and of APP fragments (*see page 37*). These fragments have neurobiological functions; sAPPα and sAPPβ have a neurotrophic effect (150), and high concentrations of βCTF have been linked with memory impairment (151). In addition, unphysiologically high levels of APP itself have been linked to disruption of intracellular transport (152). Sudden death, possibly secondary to seizures, is a problem associated with APP overexpression models and may reflect an underlying physiological disruption (152).

In APP overexpression models the mutant APP gene is inserted into the host mouse genome using a process of random integration. Consequently, insertion of the mutant APP gene can disrupt or alter the expression of a random subset of endogenous genes thus influencing the phenotype in an unpredictable manner. As discussed above, the expression of mutant APP is driven by artificial promoters which leads to an artificial expression pattern; APP may be expressed at unphysiologically high levels within cell populations where it is not normally expressed. Another consequence is that artificial promoters may compete with endogenous promoters for transcription factors, providing another mechanism by which endogenous gene expression could be disrupted. Finally, under the influence of artificial promoters, cell-type specific splicing may be disrupted. Taken together these limitations make it difficult to distinguish between genuine disease-related effects and artefacts. This becomes even more challenging when APP mice are bred with other transgenic mice models inducing potentially more artefacts.

### 1.2.8.3. APP knock-in models of Alzheimer's Disease

These next-generation mouse models use a knock-in approach to substitute the murine APP gene with an engineered APP construct. APP is therefore expressed under the influence of its natural murine promoter at wild-type concentrations within the appropriate cell populations at the appropriate times, removing the artefacts associated with APP overexpression models (153). The features of the APP[NL-G-F] model are outlined here since it is the model used for the experiments presented in Chapter 4 (*see page 178*).

In the APP[NL-G-F] mouse the combined effects of APP mutations found in three familial AD kindreds result in elevated concentrations of pathogenic Aβ. The APP construct contains a humanised Aβ region along with the Swedish (NL), Arctic (G) and Iberian (F) mutations and is expressed in mice with a C57BL/6J background. The Swedish mutation (KM670/671NL) occurs close to the β-secretase cleavage site where it increases cleavage and therefore total Aβ concentrations. The Iberian mutation (I716F) occurs near the γ-secretase cleavage site and results in an increased $A\beta_{1-42}$:$A\beta_{1-40}$ ratio. Finally, the Arctic (E693G) mutation occurs within the Aβ sequence itself and facilitates the oligomerisation of $A\beta_{1-40}$ and reduces its proteolytic degradation (29).

#### 1.2.8.3.1. Pathology in the APP[NL-G-F] mouse

Homozygous APP[NL-G-F] mice display early and aggressive Aβ plaque deposition which is detectable by two months of age and plateaus at around seven months (153-155). One study has shown that female APP[NL-G-F] mice have a significantly greater degree of cortical amyloidosis (156). It has been noted the Aβ plaques in the brains of APP[NL-G-F] mice are heterogenous in

terms of their Aβ composition compared to the Aβ plaques in an overexpression model (the APP PSEN1 mouse) (157). Aβ deposition in the APP$^{NL-G-F}$ mouse is accompanied by an inflammatory response with astrogliosis and microgliosis being particularly prominent in the vicinity of plaques (153). Synaptic loss is concentrated around Aβ plaques, as measured by synaptophysin and PSD95 immunoreactivity (153). The presence of the Arctic mutation accelerates the accumulation of pathology and leads to Aβ deposition in subcortical, as well as cortical and hippocampal, regions, as is seen in humans with this mutation. NFTs are absent but phosphorylated tau concentrations are increased in dystrophic neurites surrounding Aβ plaques. As with other APP models, no neurodegeneration is seen (153).

Hippocampal Aβ deposition occurs later than cortical deposition with hippocampal plaques visible on immunostaining at 6 months of age (158). Regional differences are observed within the hippocampal formation with a greater degree of amyloidosis seen in the CA1 and CA3 subregions, and relative sparing of the DG (158).  The CA1 and CA3 subregions show APP$^{NL-G-F}$ mice show a reduction in hippocampal dendritic spine density, particularly in CA1,  and studies of APP$^{NL-G-F}$ neurons in culture suggest this occurs in direct response to extracellular Aβ$_{1-42}$ in the culture media (159). There are conflicting accounts as to precisely which population of dendritic spines are affected, with one study suggesting a loss of postsynaptic mushroom spines (158), and another a selective loss of thin spines (160). A greater density of microglia are observed in the CA1 hippocampal subregion of APP$^{NL-G-F}$ mice compared to age-matched wild-type controls, and microglial density increases with rising Aβ plaque load (161). Finally,

changes in neuronal cilia length have been observed within CA1 and CA3, but not the DG, of APP$^{NL-G-F}$ mice (158).

*1.2.8.3.2. Behavioural changes in the APP$^{NL-G-F}$ mouse*

Behavioural changes in APP$^{NL-G-F}$ mice vary according to the age and sex of the mice tested, and even the laboratory undertaking the study, however some general themes emerge. In accordance with the anxiolytic phenotype observed in APP overexpression models, a reduction in anxiety, as demonstrated using the elevated plus maze, is seen in male and female APP$^{NL-G-F}$ mice from the age of six months compared to wild-type (WT) controls (155, 162, 163). Findings in the open field were contradictory with locomotion reported to be increased (155), decreased (154, 162, 164) and unaltered (165, 166) in APP$^{NL-G-F}$ mice. APP$^{NL-G-F}$ mice exhibit subtle memory deficits on traditional memory tasks; female and male mice show impairments in the Novel Object Recognition task from nine months (164, 166) and a reduction in spontaneous alternation in the Y maze from ten months (153, 164). Other behavioural tests yield mixed findings. Reductions have been reported in contextual fear conditioning from six months (166) (but see (163)), and spatial memory impairments have also been reported although the results have not been consistently reproduced. Two studies have shown impaired performance on the Morris Water Maze from the age of six months in male and female mice (164, 166), although other studies failed to find differences in similarly aged female mice (155) and male mice (154, 167), and one study found no deficits in 18-month-old APP$^{NL-G-F}$ mice (153). Deficits have been reported on the Barnes maze in both male and female APP$^{NL-G-F}$ mice (163, 164). The use of touchscreen tasks and

'intelligent cage' systems provides additional evidence to support a deficit in learning and memory (156, 167). Taken together these results suggest that there is a subtle cognitive impairment in APP[NL-G-F] mice but that these deficits may not be sufficiently robust, particularly at younger ages, to be reliably reproduced across multiple different testing environments.

### 1.2.8.3.3. Electrophysiology in the APP[NL-G-F] mouse

Extracellular recordings in acute slices of APP[NL-G-F] prefrontal cortex revealed synaptic impairment was present by three to four months of age (168). Recordings from the CA1 subfield of the hippocampus indicated that there was no evidence of synaptic impairment in four-month-old slices, but by six to eight months there was an impairment in LTP. Whole-cell patch-clamp recordings of CA1 pyramidal cells at six to eight months found an increased frequency of miniature excitatory postsynaptic currents (mEPSCs) and miniature inhibitory postsynaptic currents (mIPSCs), suggestive of enhanced presynaptic activity, and an increase in mIPSC amplitude indicating an increase in postsynaptic inhibitory function (168). In a separate study, recordings in acute brain slices indicated alterations in glutamatergic-dependent gamma oscillations in the prefrontal cortex, but not the amygdala, of APP[NL-G-F] mice compared to WT controls (162). To date, only one published study has conducted *in vivo* electrode recordings in the APP[NL-G-F] mouse, and this is discussed in Chapter 4 (*see page 178*). A recent study by *Takamura et al.* used calcium imaging in head-fixed APP[NL-G-F] and wild-type mice during awake behaviour in a virtual reality environment (159a). They evaluated the responses of pyramidal cells in dorsal CA1 and found that in APP[NL-G-F] CA1 pyramidal cells the temporal

representation was preserved (i.e. time cell activity was unimpaired), but that spatial representations were degraded due to a reduction in the number of active place cells (*see page 95 for an introduction to place cells*). Interestingly, remaining place cells located in close proximity to Aβ aggregates exhibited hyperactivity.

### 1.2.8.3.4. Limitations of the APP$^{NL-G-F}$ mouse model

Although the APP$^{NL-G-F}$ model overcomes artefacts associated with the traditional APP overexpression models, it has features which differ from sporadic human AD which make it an imperfect model. In humans a single copy of a single pathogenic APP mutation is sufficient to induce familial AD. The APP$^{NL-G-F}$ model contains three such APP mutations, and the majority of experiments are conducted in homozygotes, rather than heterozygotes, since these exhibit more Aβ pathology. In addition, the pathology in the APP$^{NL-G-F}$ model differs from that of human AD; there is an absence of tau NFTs, although hyperphosphorylated forms of tau are present, and the inclusion of the APP Arctic mutation (E693G) results in changes in Aβ pathology. The APP$^{NL-G-F}$ model has a higher expression of the Aβ$_{1-38}$ isoform, displays an atypical distribution of Aβ plaques, with prominent subcortical deposition, and Aβ plaque morphology and fibrillization differ, with an increased prevalence of less dense, pre-fibrillar Aβ aggregates as opposed to the fibrillar, dense Aβ plaques seen in human AD and some other mouse models (169).

## 1.3. Spatial cognition

Navigation is one of the most fundamental behaviours and is conserved across species. From an ethological perspective, an animal's ability to navigate successfully between, and to remember, specific locations such as sources of food and shelter provides a clear survival advantage. In humans spatial behaviours are known to be affected in AD with topographical disorientation being a common feature (170). In this introductory section the cognitive processes underlying navigation are summarised with a focus on the role of the hippocampal formation. Studies of spatial navigation and memory in the context of AD are discussed.

### 1.3.1. Spatial cognition: a taxonomy

*Spatial cognition* describes the processes through which organisms acquire, represent, and use knowledge about the external world. It encompasses a complex set of cognitive abilities which together underpin *spatial navigation*, the determination and maintenance of a trajectory between two or more locations (171-173). Spatial cognition can be described as comprising three hierarchically linked components mediated by different neural structures: *object orientation*, which is the mental manipulation and representation of single objects, *spatial memory*, and *spatial orientation*, i.e. orienting oneself in large-scale space (*Figure 1.9*) (173). *Spatial memory* is a broad term referring to the ability to encode, store and retrieve spatial information, including both metric properties such as distance, size, orientation and direction, and non-metric properties such as relative positions and configuration or geometry. Spatial information can be encoded in the brain using a 'person-centred' *egocentric* framework, or a

'map-like' *allocentric* framework (*page 59*). Spatial memory, as with other types of memory, can be classified as short-term or long-term memory. For example, spatial working memory could be used to avoid bumping into an object in a room if the lights were suddenly extinguished, whereas long-term spatial memory might be used to navigate through a familiar large-scale environment.

Successful *spatial navigation* depends on a functioning spatial navigation network; an individual with a spatial memory deficit may have great difficulty in navigating a previously familiar route, or present with *topographical disorientation*, an inability to orient themselves within their environment. Impairment along any stage of the encoding – storage – retrieval axis in relation to the metric or non-metric properties of an environment could result in topographical disorientation and wayfinding or navigational difficulties (172). For example, both an inability to recognise salient environmental landmarks and an inability to create new representations of the environment can impair spatial memory and behaviour.
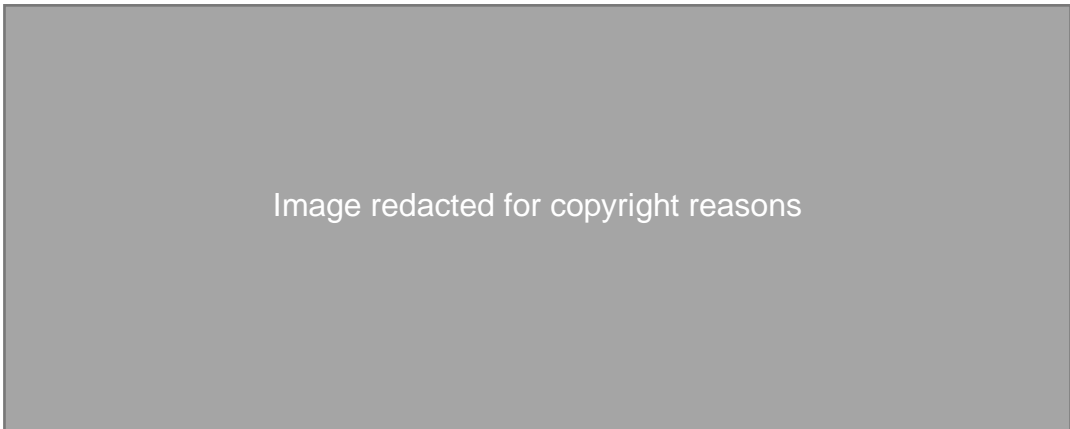


Image redacted for copyright reasons

**Figure 1.9 Spatial cognition schema.** Spatial cognition is proposed to comprise three hierarchically linked components. Object orientation refers to cognitive abilities such as the egocentric representation of an object within the environment, and the ability to perform mental manipulations such as object rotation. Spatial memory is a broad term and includes a memory for object locations and spatial scenes, and spatial orientation refers to an ability to orient oneself within a large-scale environment. Figure taken from (173).

Spatial memory can be evaluated in humans and animals using a range of tasks, for example, object-location tasks test the ability to make associations between specific objects and locations, maze-based tasks can test route-based spatial memory including procedural memory, and place memory tasks might require an animal or individual to navigate to a previously learned location via a novel route. In practice, there is no universal spatial memory test and tasks which test spatial orientation abilities may be solvable via different strategies meaning it is not always possible to discern which underlying aspect of spatial processing is being tested.

## 1.3.2. The neural basis of spatial behaviour

### 1.3.1.2. Processing of idiothetic and exteroceptive cues

Spatial navigation can rely on dynamic *self-motion* cues or static *environmental* cues (174). Self-motion cues, also known as *idiothetic* cues, include vestibular input, proprioception, motor efference copy and optic flow and provide the animal or individual with information regarding their own position and orientation in space. Inputs from vestibular afferents undergo early integration with other self-motion cues in the vestibular nuclei of the brainstem to produce estimates of linear and angular velocity (175). In primates further processing of self-motion cues occurs in multimodal association areas such as the medial superior temporal area (MST) and the ventral intraparietal area (VIP) to produce an integrated percept of self-motion (174). Environmental, or *exteroceptive*, cues refer to stable objects within the environment, such as landmarks or boundaries, which can have visual, auditory, tactile, and olfactory components. Sensory input relating to such cues is processed by single-modality primary and secondary cortices,

and subsequently by multimodal association areas in the posterior parietal cortex, to generate spatial representations.

The widely cited model of *Ungerleider* and *Mishkin* (176) posits that further information processing occurs along anatomically divergent pathways; information regarding objects is conveyed via an occipitotemporal pathway (the ventral 'what' pathway) whereas information regarding space is mediated by an occipitoparietal pathway (the dorsal 'where' pathway). At this stage spatial representation is *egocentric*, or 'self-centred' in nature. A further stage of processing is required, possibly occurring within the retrosplenial cortex of the parietal lobe, to transform the representation of space from an *egocentric* to an *allocentric* ('map-like') representation.

### 1.3.2.2. Spatial reference frames: egocentric and allocentric navigation

As alluded to above, there is evidence that two distinct reference frames are used to represent space within the mammalian brain. An e*gocentric* reference frame defines space relative to the body using a polar coordinate system, i.e., it is a first-person or self-centred perspective. In contrast, an *allocentric* reference frame uses a map-like representation of space and can be thought of as a third-person or world-centred perspective. Wayfinding using an egocentric strategy can be deconstructed into a series of directional choices relative to the animal's location. These choices can be guided by proximal cues, or *signposts*, within the environment and it is the relationship between the animal's location and these cues which is used to guide navigation rather than the relationship between the cues themselves. Memorising a route based on a sequence of left/right turns, for example, is an egocentric navigation strategy. Egocentric reference frames can also be

used when environmental cues are minimal, absent, or unreliable since idiothetic cues such as self-motion and optic flow can guide navigation using a path-integration strategy. In contrast, allocentric navigation uses the relationships between distal cues, or *landmarks*, to guide navigation. Navigation using a map and compass is an example of an allocentric navigation strategy since the compass directions are independent of an individual's location in space. An advantage of an allocentric navigational strategy is its flexibility, allowing animals to compute novel routes. Egocentric navigation strategies, particularly navigation with respect to a single landmark, have been linked to a navigational system in the dorsal striatum (177-181), whereas the hippocampal formation has been shown to be critical for allocentric spatial memory.

### 1.3.2.3. The cognitive map theory of hippocampal function

As discussed further in *section 1.4.2.2.* (*page 95*), the discovery of hippocampal place cells in the freely moving rat provided the first evidence of an allocentric spatial representation within the brain (182). The activity of a place cell is tuned to a specific location within the environment and thus encodes an animal's location in space. This discovery led to the formation of the *cognitive map theory of hippocampal function* (183).

The concept of a cognitive map derives from the work of 18$^{th}$ century German philosopher, *Immanuel Kant*, who proposed that humans have innate perceptual schemes for the processing of sensory information including a framework for spatial information (184). *Edward Tolman* developed this further suggesting that animals had cognitive maps which permitted flexible navigation (185). *Tolman* showed that rats were able to

navigate to a learned goal location via paths not previously taken and concluded they were able to calculate the vector separating them and the goal (186, 187). Since the rats travelled to the goal via a novel route, *Tolman* concluded that they could not be using a stimulus-response technique and suggested they used an internal representation of the environment, a *cognitive map*, to navigate (185). In their landmark book, *The Hippocampus as a Cognitive Map*, *O'Keefe* and *Nadel* proposed that place cells in the hippocampus formed part of the neural substrate underlying this cognitive map (183). Distinct sets of place cells are active with different place fields in different environments implying that the place cell system forms a unique spatial map for every environment an animal experiences (188). The discovery of other spatially tuned cells, such as head direction cells, grid cells and boundary vector cells (*page 117*) provided further support for this hypothesis (50, 189, 190) and together these spatial cells can provide the information required for successful spatial navigation. Grid cells have been hypothesized to provide a basis for calculating Euclidean distance, head direction cells encode orientation, and place cells bind together this information to encode specific locations, constructing a map. Once formed, such a cognitive map could be retrieved by the animal when required, for example on re-entering a familiar environment, updated in accordance with subsequent experience, and enable navigation via novel, alternate routes (179, 185).

The theory that the construction and maintenance of spatial maps is a fundamental function of the hippocampus has been challenged. In the relational theory of hippocampal function *Cohen* and *Eichenbaum* suggested a broader role for the hippocampus in processing and forming

associations between perceptually and conceptually distinct items by linking them in relational frameworks (191). *Eichenbaum* used the example of a family tree as something which could have its own relational framework within the hippocampus. In the same way that a relational framework pertaining to a specific spatial environment could be used to make novel detours and compute short-cuts, he argued that this 'family tree' framework could be used to make inferences about the relationships between different family members (192). A criticism of the relational model is that there is no consensus on which items require hippocampal processing before they can be represented and recognised by extrahippocampal brain regions, and this makes testing this theory in relation to specific stimuli challenging (193). Evidence from human fMRI studies also point to a bias in the human hippocampus for processing spatial relationships in support of the cognitive map theory (194). For a review on theories of hippocampal function please see (193).

### 1.3.2.4. The hippocampal formation as part of a wider navigational network

Functional neuroimaging studies in humans implicate several brain regions in spatial processing (*Figure 1.10*). This widely distributed navigational network includes parietal regions which receive spatial information in an egocentric reference frame, such as the precuneus which plays a role in visuospatial processing. Other important nodes include the posterior cingulate gyrus, which plays a role in object recognition, and the retrosplenial cortex, which has been proposed to transform egocentric information into an allocentric reference frame and additionally may encode

landmark information (195-197). The hippocampal formation is the primary brain structure involved in allocentric representations. Different subdivisions within the hippocampal formation appear to underlie separate components of spatial behaviour. Within the hippocampus proper animal and human studies support the notion of functional differentiation along an anteroposterior axis, with anterior regions encoding contextual information and spatial novelty, and posterior regions implicated in the storage of spatial representations. The entorhinal cortex is the primary source of afferents to the hippocampus, with medial and lateral subdivisions conveying spatial and object-related information respectively (198). The differing information content of these entorhinal inputs reflects the afferents to the medial and lateral entorhinal cortex from the parahippocampal cortex and perirhinal cortex, involved respectively in scene and object recognition. The frontal lobe, particularly the prefrontal cortex, is extensively involved in spatial working memory, and therefore contributes to aspects of navigation which require the maintenance of salient environmental features, such as a sequence of landmarks, in working memory (199). It also plays a role in planning which is important to allow flexible navigation. Finally, there is evidence for a striatal system for landmark-related representations of space, with some brain regions such as the caudate being specifically activated during egocentric learning  (177, 200).

**Figure 1.10 The navigational network within the human brain.** Neocortical brain regions are shown in solid boxes and subcortical regions in dotted boxes. Figure adapted from (202).

### 1.3.2.5. Evidence that the hippocampal formation plays a role in spatial cognition

There is extensive evidence that the hippocampal formation plays a role in navigation and spatial memory. First, allocentric learning is impaired following damage to the hippocampus in rodents, monkeys, and humans. Perhaps the most famous demonstration of this was by *Morris et al.* in 1982 who showed that rats with bilateral hippocampal lesions had impaired navigation in the Morris Water Maze, a task in which rodents swim in a pool of opaque water to locate a hidden escape platform (4). This finding was subsequently replicated in rats and mice, with additional studies demonstrating that lesions in the hippocampal formation increased the time taken and distance travelled to reach the hidden platform, and decreased

the time the animal spent searching for the platform in the correct quadrant of the maze (202-204). Human-derived data also highlight the important role of the hippocampus in spatial memory; a meta-analysis of 27 studies of patients with pre-existing cerebral damage showed that those with hippocampal involvement were impaired on maze learning tasks, object location memory, positional memory (recalling a specific location) and working memory. A lateralization of function was found with spatial memory impaired to a greater extent in those with lesions of the right hippocampus (205).

Second, the spatially-related firing activity of cells within the hippocampal formation, such as hippocampal place cells and entorhinal grid cells (*page 95*) provides strong support for the role of the hippocampus in spatial memory. Hippocampal place cell activity has also been shown to correlate robustly with spatial memory in rodents (182), and evidence of hippocampal place cells and entorhinal grid cells has been found in humans (206, 207).

Third, optogenetic studies in mice have demonstrated the important role of the hippocampal formation in spatial memory. For example, optogenetic inhibition of GABAergic interneurons in the dentate gyrus impaired spatial learning on the Morris Water Maze (208), and inhibition of layer III medial entorhinal cortex inputs to CA1 impaired performance on a forced choice T maze alternation task (209).

Finally, structural and functional changes in the human hippocampus have been linked to spatial navigation and memory. A study of London taxi drivers with extensive navigation experience found that they had a significantly larger posterior hippocampus relative to controls and that right posterior

hippocampal volume correlated with the length of time spent as a taxi driver (210). Right posterior hippocampal volume in study participants has also been shown to correlate with learning the allocentric topography of an artificial landscape (211) and the allocentric relationship between different buildings on an unfamiliar college campus (212). fMRI studies show hippocampal activation during virtual navigation tasks, particularly when the tasks require an allocentric navigational strategy such as the computation and use of shortcuts (181, 213, 214).

### 1.3.3. Tests of spatial behaviour in rodents

Even when the hippocampus is lesioned or removed rodents are still capable of performing above chance on many cognitive tasks unless those tasks involve a spatial component (215). In theory spatial tasks fall into two categories: those which can be solved using an allocentric place learning strategy, and those which use an egocentric strategy or a stimulus-response strategy. Allocentric tests require the animal to use distal cues to identify a location and have a paucity of proximal or intra-maze cues, whereas the converse is true for egocentric tests. In practice, however, many tasks do not force the animal to use a single identifiable spatial strategy. Several tasks which probe spatial behaviours are in routine use including the T-maze (216), Y-maze, Olton Radial Arm Maze (217), Barnes maze (218) and Morris Water Maze (4, 219). Each will be reviewed, briefly, to provide context for the experiments conducted using a novel spatial memory task in *Chapter 3* (*page 133*).

### 1.3.3.1. The T-maze

The T-maze exploits the natural tendency of rodents to preferentially explore a novel environment over a familiar one to locate resources such as food and shelter. It consists of a central stem and two goal arms (*Figure 1.11A*). A normal rodent repeatedly placed in the central stem will tend to alternate between the left and right goal arms from one trial to the next; this so-called *spontaneous alternation* is a natural behaviour and relies on spatial working memory. In addition to observing the spontaneous alternation rate, alternation can be reinforced using a reward in a *forced-choice alternation* protocol (*Figure 1.11B*). Both rewarded and spontaneous T-maze alternation are sensitive tests of hippocampal function (220). The T-maze has several limitations. Alternation rates are not always reliable, and rodents may develop a turning bias which can influence results. The task can be solved using either an egocentric strategy (recalling whether a left or right turn was previously taken) or an allocentric strategy (recalling the spatial location of the previous reward).

### 1.3.3.2. The Y-maze

The Y-maze also relies upon the principle of spontaneous alternation but employs a continuous trials procedure (*Figure 1.11C*). In this task the rodent freely explores the apparatus and the sequence in which arms are entered are recorded and the number of alternations counted. Advantages include reduced handling of the animal and suitability for task automation, however, alternation rates are not as high as on the T-maze and the task is not as sensitive to hippocampal damage since animals with a turning bias (which is more prevalent in hippocampal-lesioned animals) obtain misleadingly

high scores (221). As with the T-maze animals can use an egocentric or allocentric strategy to avoid revisiting arms.
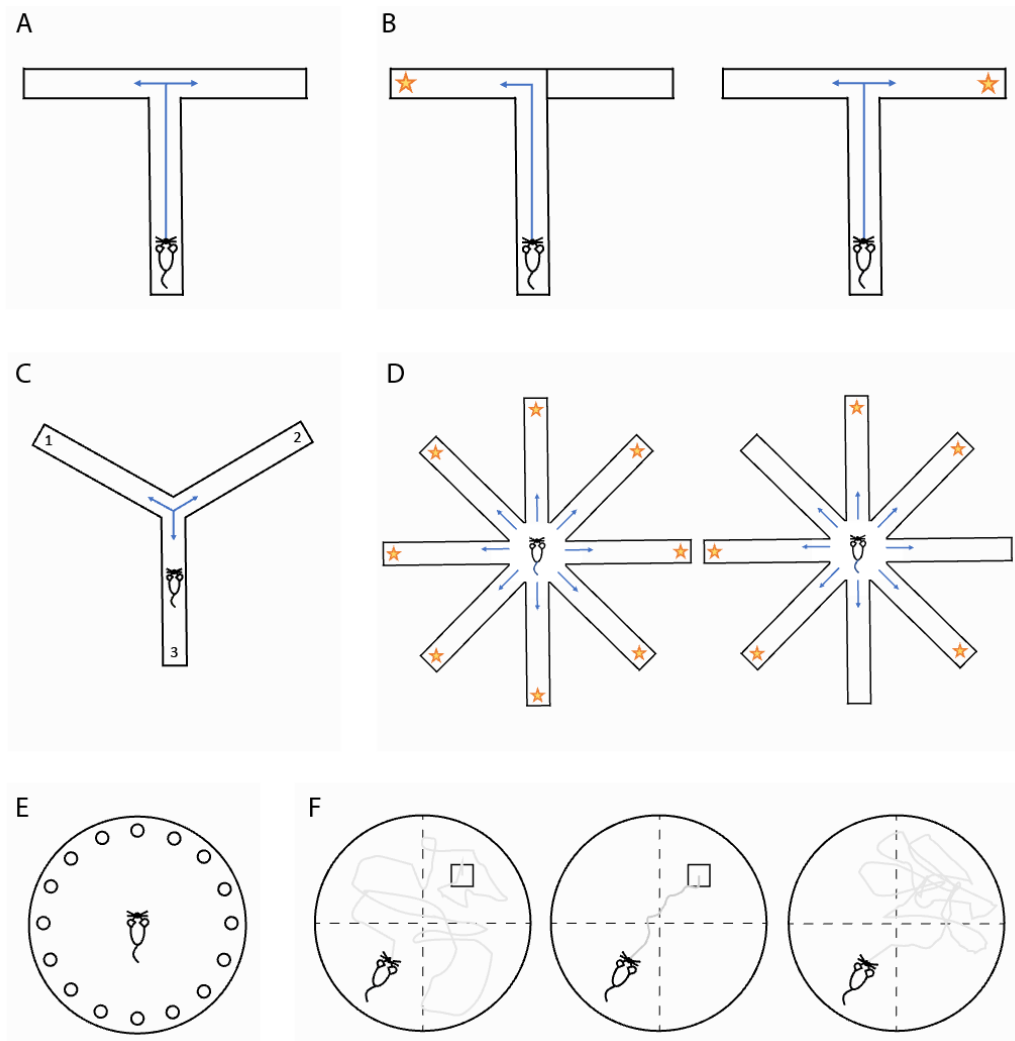


**Figure 1.11 Spatial memory tasks for rodents. *A*:** Spontaneous T maze alternation exploits the natural tendency of an animal to alternate. ***B*:** Forced choice T maze alternation reinforces the natural tendency of rodents to alternate. In the first trial (left) one arm is closed off and the other arm is rewarded (star). In the second trial (right) the rodent is required to choose the previously unvisited arm to receive a second food reward. ***C*:** The Y maze also measures spontaneous alternation. Animals freely explore and the sequence of arm entries is recorded. Entry into an arm which was not previously visited is scored as an alternation. ***D*:** The Olton radial arm maze can be used to test working memory (left) or working/reference memory (right). Stars indicate the location of food rewards. ***E*:** In the Barnes maze the rodent is placed at the centre of a circular environment and must locate an escape tunnel on the periphery. ***F*:** In the Morris Water Maze the animal is trained to swim to a hidden platform (square) from a number of different start locations. The path taken by an animal is shown in grey. Initially it takes the animal time to locate the hidden platform (left), but the animal soon learns the platform location and takes a more direct route (central image). On a probe trial (right) the platform is removed, and the animal spends the majority of its time exploring the quadrant where the platform was removed.

### 1.3.3.3. The Olton radial arm maze

The Olton Radial Arm Maze has eight identical arms radiating out from a central location and is surrounded by extra-maze cues (*Figure 1.11D*). There are two tasks. In the *working memory* task the animal explores the maze to locate food rewards at the end of each arm. Visiting a previously-visited an arm during the same trial is scored as an error. A drawback is that animals can use an alternative strategy to solve the task, for example visiting arms in a systematic order. This can be partially mitigated by using doors to confine the animal in central portion of maze thus introducing a delay. This task produces a limited range of scores so there can be a floor and ceiling effect.

In the *working/reference memory* version of the task not all arms of the maze are baited on all trials. If an animal revisits a baited arm during a trial it is counted as a working memory error, whereas visits to arms which were never baited are considered reference memory errors. This task has the advantage of producing a more protracted learning curve than tasks such as the Morris water maze, however training is more time-consuming. In addition, since two types of memory are being assessed fewer arms are available to test each type of memory which may reduce the sensitivity. Another disadvantage is that animals can use a non-spatial strategy to solve the task; instead of remembering the location of the rewards they may simply learn the relationships between the different arms. The Olton radial arm maze has been adapted to create other tasks including mazes with additional arms (to increase task sensitivity), and water-based versions.

### 1.3.3.4. The Barnes Maze

The Barnes maze consists of an elevated circular platform with a number of evenly spaced holes around the perimeter, one of which allows the animal to pass into an escape tunnel (*Figure 1.11E*) (218). This task exploits the preference of rodents for dark, enclosed spaces over bright, open environments. A rodent placed in the centre of the platform is highly motivated to escape and can use three strategies to locate the escape tunnel: a random, serial, or spatial search strategy. Rodents can be trained to learn the position of the escape tunnel in relation to external cues placed around the maze and spatial reference memory can be tested using a probe trial in which the escape tunnel is closed, and the time spent exploring near each perimeter hole is recorded. This task has the advantage of being able to identify which strategy the animal is using during training, however animals can solve the task using an object-heading strategy rather than a true allocentric place learning strategy.

### 1.3.3.5. The Morris Water Maze

The Morris water maze is the dominant method of assessing allocentric spatial memory in rodents and has played an important role in validating rodent models of AD through the demonstration of spatial memory deficits (4, 219, 222). In this task animals are placed in a large circular pool of opaque water in which there is a hidden platform. To escape from the water (an aversive stimulus) the animals are required to locate and swim to the hidden platform. Once training is complete a probe trial can be conducted in which the hidden platform is removed, and the time spent by the animal exploring each quadrant of the maze is recorded.

70

The Morris water maze has several advantages. The presence of external, but not local, cues and the varying start positions of the animal ensures an allocentric place learning strategy is used to identify the location of the hidden platform. In addition, it requires minimal training, learning is rapid and reliable, the animal does not need to be food or water deprived, and performance is not affected by differences in body weight or appetite. The Morris water maze has been demonstrated to be a reliable test of hippocampal function with hippocampal lesions and pharmacological disruption of the hippocampus impairing place learning (4). For a discussion of the limitations of the Morris Water Maze see *Chapter 3 (page 133).*

### *1.3.3.6. Testing spatial memory in AD mouse models*

A systematic review of 49 studies, which used a range of spatial memory tasks including those outlined above, found that performance on the forced-choice T maze alternation task provided the most sensitive means of detecting spatial memory impairments in an APP overexpression model of AD (the Tg2576 mouse) (223). Performance on the Morris water maze and continuous Y maze alternation were less sensitive but were better indicators than performance on the Barnes maze. The degree to which these findings can be extrapolated to other APP models is unclear, and relatively few studies of spatial memory have been conducted in the newer APP knock-in models (*see page 53*).

### 1.3.4. Spatial memory in Alzheimer's disease

### *1.3.4.1. Spatial memory tests in humans*

Several tests of spatial behaviour are available for use in humans and have

been applied in research studies, although are not yet in routine clinical use. These include tests of route learning (224), heading orientation (224), detecting differences between scenes (225), drawing floorplans, learning the location of a hidden goal, recognising landmarks or landscapes, and remembering a sequence of locations. Examples of spatial memory tests include the Hidden Goal Task, which is modelled on the Morris Water Maze for rodents, and the Four Mountains Test, which has been specifically designed to test allocentric spatial memory in humans and is sensitive to focal hippocampal damage (226). Virtual reality (VR) paradigms appear to provide comparable results to real world navigation tasks; in one study subjects completed analogous real world and VR tasks in which they were guided through an environment and then assessed on route learning, self-orientation, route drawing and landmark recall. The order in which the two tasks were completed was randomised and the authors found close correlations between real-world and VR navigational deficits (227).

### 1.3.4.2. Spatial memory impairment in Alzheimer's disease and Mild Cognitive Impairment

Several studies demonstrate an impairment in spatial memory in patients with AD and MCI (227-230), and deficits in short-term spatial memory in AD have been shown to precede deficits in other cognitive domains (231) likely reflecting the early involvement of the entorhinal cortex and hippocampus in the disease process (2, 3). In one study patients with MCI who were ApoE4 carriers performed worse on the Hidden Goal Task than healthy controls, with deficits as profound as those who had already been diagnosed with AD (232). Patients with AD are severely impaired when

72

memorising new routes as demonstrated in both real world and VR route finding tasks (227, 228, 233) and are impaired in memory for scenes and hidden locations (229, 233, 234). There is also a suggestion that patients with AD display impaired landmark recognition (landmark agnosia) (233) (*but see (229)*). Spatial memory performance correlates with hippocampal volumes in patients with MCI and AD (229, 235, 236) with one study finding an association between poor navigational performance and right hippocampal volume, and poor accuracy locating landmarks and posterior parietal volumes (229).

### 1.3.4.3. Allocentric and egocentric spatial memory in Alzheimer's disease and Mild Cognitive Impairment

Both allocentric and egocentric spatial memory are impaired in AD, but allocentric spatial memory appears to be affected to a greater extent (233, 237). One study, in which subjects with AD navigated to a hidden goal location, found that the degree of spatial memory impairment was greater when subjects were using an allocentric, as opposed to an egocentric, navigational strategy (238). Those with AD also appear less able to translate between allocentric and egocentric representations of space (239), an observation which is consistent with the degeneration of the retrosplenial cortex given its postulated role in egocentric-allocentric transformations (195-197). This finding may be more prominent in patients with familial AD (240).

Patients with Mild Cognitive Impairment (MCI) do not perform as well as age-matched controls on allocentric and egocentric navigational tasks (229, 237, 241, 242) but are less impaired than those with AD dementia (229).

The type and severity of the navigational impairment appears to be related to the cognitive profile of the MCI. In single-domain amnestic MCI, where patients have only memory impairments, there is a specific impairment of allocentric spatial memory (229, 237, 241-243) whereas those with multi-domain amnestic MCI, where there is impairment of additional cognitive domains, show deficits in egocentric and allocentric spatial memory (237, 241). Studies using the Four Mountains Test have shown that this test of allocentric spatial memory can distinguish between patients with AD and those with non-AD dementia (224, 234), and between MCI subjects with and without CSF AD biomarkers in their CSF (5). In a small proof-of-concept study the Four Mountains Test predicted conversion from MCI to AD over a 24-month period with 93% accuracy, equivalent to that of CSF biomarkers (21). The above findings suggest an inability to construct a cognitive map of novel environments likely contributes to the topographical disorientation observed in AD.

### 1.3.4.4. Synopsis

A decline in spatial memory and navigational skills is detectable from the earliest preclinical stages of AD, before the development of MCI. These impairments are associated with both structural and functional alterations in the neural network responsible for navigation which consists of brain regions, including the entorhinal cortex and hippocampus, that are particularly vulnerable to AD pathology. Allocentric spatial memory appears to be particularly affected in the early stages of AD and there is evidence that its impairment is a more specific clinical marker of AD than other forms of cognitive impairment.

## 1.4. The Hippocampal Formation

### 1.4.1. Overview

The hippocampal formation is one of the most studied brain regions in neuroscience and its important role in episodic memory is well documented following studies of famous patient H.M. who suffered profound anterograde amnesia after a bilateral medial temporal lobectomy for intractable epilepsy (47). The hippocampal formation is also the site where long term potentiation (LTP) was first identified (244); this form of synaptic plasticity is widely considered to be one of the major cellular mechanisms underlying learning and memory (245). While the role of the hippocampus in episodic memory has been extensively studied in the context of AD, fewer studies have focused on spatial memory in AD. An extensive body of evidence has demonstrated the critical role of the hippocampus and entorhinal cortex in navigation and spatial memory *(page 64)*, with the hippocampus proposed to encode spatial information, supporting the formation of a cognitive map (47, 179). After reviewing the relevant hippocampal neuroanatomy this introductory section will focus on the electrophysiology of the hippocampal formation and how the firing of hippocampal neurons encodes spatial information.

### 1.4.1. Neuroanatomy of the hippocampal formation

For clarity, the term hippocampus will henceforth refer to a single brain region, the hippocampus proper (consisting of subfields CA1, CA2 and CA3), which, along with interconnected, related brain regions, namely the

dentate gyrus, entorhinal cortex, parasubiculum, presubiculum, and subiculum, comprises the hippocampal formation.

### 1.4.1.1. Historical perspectives

The term hippocampus also refers to a genus of small fish, better known as seahorses. The resemblance of this brain region in its dissected form to the seahorse led 16th century Italian anatomist and surgeon *Giulio Cesare Aranzi* (1530 – 1589) to name it the hippocampus (246, 247). In the 18th century the hippocampus was also referred to as 'cornu ammonis', a reference to the ram-shaped horns atop the head of the ancient Egyptian God Amun (248-250); this terminology was not adopted but survives in the naming of the hippocampal subfields: CA1, CA2 and CA3.

### 1.4.1.2. Evolution and species differences

The hippocampus is a phylogentically conserved and ancient structure with a homologous brain region present in the vertebrate brain for at least the past 350 million years (251). It is universally present in the brains of mammals and although there are morphologic variations between species the basic underlying architecture is fairly uniform (252). When comparing rodent and primate hippocampi an obvious inter-species difference is the size, with the volume of the human hippocampus being more than two orders of magnitude greater than that of the rat but occupying a much smaller proportion of the total brain volume (253). While the position of the hippocampal formation within the brain is similar, the precise shape and orientation differ. In both rodents and primates the hippocampus is an 'elongated, curved, rod like structure' whose anatomical boundaries are

defined by the rhinal sulcus and the hippocampal fissure (252). However, in rodents the hippocampus is more 'C-shaped' with the long axis aligned in a dorsoventral plane and the open part of the 'C' oriented rostrally (*Figure 1.12*). In primates the hippocampus is more compact, less curved, and rotated 90° with respect to the rodent hippocampus, with the long axis running in a posterior-to-anterior direction and the open portion of the 'C' oriented superiorly (252, 254). The dorsal portion of the rodent hippocampus is more medial, close to the septal nuclei, and so is referred to as the septal pole, whereas the ventral portion is more lateral and is named the temporal pole.

The basic architecture of the rodent and primate hippocampus is very similar, however important differences exist; for example, in primates the CA1 pyramidal layer is thicker and more heterogenous, and the structure of the entorhinal cortex has a greater complexity with more cytoarchitectonically distinct subdivisions (253). The circuitry of the rodent and primate hippocampi follow similar underlying principles, but again there are a few key inter-species differences, including a lack of commissural connections in the dentate gyrus in the primate, and more developed interconnections between the entorhinal cortex and neocortical association areas (255, 256). Further differences exist in neurochemical anatomy and the anatomy of the perirhinal and parahippocampal cortices which are more developed in primates (253). Even within-species there may be slight anatomical variations with differences observed between some mouse strains (253).

**Figure 1.12 Orientation of the hippocampal long axis.** The location of the hippocampus (red) and entorhinal cortex (blue) are shown in the rat (**A**) versus the human (**B**) (left-hand images) oriented as indicated by the axes (V, ventral; D, dorsal; L, lateral; M, medial, R, rostral; C, caudal; A, anterior; P, posterior). The difference in shape and orientation of the hippocampi can be seen in the right-hand images. Note that the rodent hippocampus (**A**) which lies along the dorsoventral axis is rotated 90 degrees anticlockwise in comparison to the human hippocampus (**B**). The dorsal (septal) hippocampus in the rodent is equivalent to the posterior hippocampus in humans. Image adapted from (255).

This introductory section will primarily focus on the anatomy of the rat hippocampal formation since it is the primary model used in studies of the hippocampal function. The neuroanatomy of the mouse hippocampal formation is generally considered to be very similar to that of the rat (253).

### 1.4.1.3. Fibre systems of the Hippocampal Formation

Information is relayed to, from and within the hippocampal formation via three major fibre systems. The *angular bundle* is a composite fibre tract which originates in the ventral part of the entorhinal cortex, travelling along the septotemporal axis of the hippocampus to terminate in the hippocampal

subfields. It contains the fibres of the perforant path and commissural fibres interconnecting the entorhinal cortex with the hippocampus proper.

The *fimbria-fornix* connects the hippocampus and subiculum to various subcortical brain regions including the basal forebrain, hypothalamus and brain stem (257, 258). The white myelinated fibres originating from the temporal portions of the hippocampus are collectively referred to as the *alveus*, and these fibres coalesce to form a fibre bundle, the *fimbria*. As the fimbria extends along the length of the hippocampus, from the temporal to the septal pole, it receives progressively more hippocampal and subicular efferents and becomes thicker. In the midline the continuation of the fimbria forms the *fornix*. The fornix projects to structures such as the anterior thalamic nuclei, nucleus accumbens, mamillary bodies, septal nuclei, amygdala and regions of the hypothalamus (259, 260). The fimbria-fornix pathway also carries the fibres of the temporoammonic pathway, and contains inputs to the hippocampus, for example, from the septal nuclei (253).

Finally, the *dorsal and ventral commissures* connect the hippocampi of the two hemispheres. The fibres of the ventral commissure decussate the midline immediately caudal to the septal nuclei. Many of these fibres directly connect subregions of the hippocampal formation, while a minority contribute to the contralateral descending column of the fornix. The fibres of the dorsal commissure cross the midline rostral to the splenium of the corpus callosum and consist mainly of fibres travelling to and from the entorhinal cortex and presubiculum (253).

### 1.4.1.4. Major Hippocampal Pathways

In the late 19th and early 20th centuries, anatomist *Santiago Ramon y Cajal* (261, 262) and his compatriot *Rafael Lorente de No* (263) used the Golgi method to conduct seminal neuroanatomical studies; these were key to the forming the first functional hippocampal circuit diagram and to characterising the different hippocampal cell types and subregions (264). Through the annotation of his illustrations *Ramon y Cajal* proposed a unidirectional flow of information through the hippocampal formation in a 'loop-like' system (*Figure 1.13*).

Image redacted for copyright reasons

**Figure 1.13 Horizonal section of the rat hippocampus.** This illustration by Ramon y Cajal depicts the cell morphology and connectivity of the hippocampal formation. Inset: overview of the proposed hippocampal circuitry (EC, entorhinal cortex; DG, dentate gyrus; CA, cornu ammonis subfield; Sub, subiculum). Figure taken from *http://neuronbank.org.*

The regions within the hippocampal formation are connected in a loop by a (mostly) unidirectional, excitatory pathway: the entorhinal cortex (EC) provides the main input to the hippocampus via the dentate gyrus (DG), which in turn sends inputs to CA3. From here CA3 projects to CA1, and finally CA1 to the EC and subiculum (*Figure 1.13, inset*). These are the main

output structures and project onwards to the neocortex and subcortical structures (259, 265).

Historically the first three links of this 'loop' have been collectively referred to as the *tri-synaptic loop* (266):

EC -> DG (synapse 1); DG -> CA3 (synapse 2); CA3 -> CA1 (synapse 3).

The projections between these regions have been assigned specific names. The *perforant path* arises from layers II and III of the EC and projects to the granule cells of the dentate gyrus and pyramidal cells in CA3. It provides the main input to the hippocampus proper and it is in this pathway that LTP was first discovered (244). The principal cells of the DG give rise to *mossy fibres* which project to pyramidal cells in CA3. These cells in turn provide input to CA1 via *Schaffer collaterals* (*Figure 1.14*).

Our understanding of hippocampal circuitry is now more nuanced; the trisynaptic loop represents only part of the functional circuitry in the hippocampal formation, with additional projections since identified including those from CA1 to the subiculum and entorhinal cortex, and a projection from layer III of the EC directly to the CA1 subregion of the hippocampus proper (the *temporoammonic pathway*). In addition, there is now an ever-growing appreciation of the important role played by local inhibitory interneurons (267). However, despite more recent advances, the concept of a strong excitatory circuit within the hippocampal formation in which sensory information is relayed from node to node in a largely unidirectional fashion appears to hold true (268). In the following sections the trisynaptic loop is used as a framework, and each component is discussed in turn, beginning with the EC.

Image redacted for copyright reasons

**Figure 1.14** *Major hippocampal pathways and circuitry.* A diagram of the hippocampal neural network. The classic components of the 'tri-synaptic' loop are shown by solid lines (PP, perforant pathway; Mossy fibres; Schaffer collaterals), and more recently identified projections by dashed lines (layer II component of the perforant pathway; TP, temporoammonic pathway). CA1-3, cornu ammonis 1-3; EC, entorhinal cortex; I – VI indicates layers of the EC). Figure from (269).

### *1.4.1.5. The Entorhinal Cortex*

### *1.4.1.5.1. History and overview*

As its name suggests, the entorhinal cortex (EC) is partially enclosed by the rhinal (olfactory) sulcus (270). Early descriptions by *Ramon y Cajal* highlighted the strong interconnections between the EC and the hippocampus leading him to propose that the functions of the two regions were closely aligned (271). Indeed, it is now thought that the unique position and connectivity of the EC enables it to function as the major input/output node between the hippocampus and the neocortex. Interest in the EC grew following the discovery that this site is affected by AD pathology at very early stages of the disease process (2), and when spatially modulated grid cells were identified in this region (50, 272).

### 1.4.1.5.2. Laminar structure

The EC has a laminar organisation in which different layers can be identified through their cytoarchitectonic features. *Ramon y Cajal* described six layers within the EC (271); four of these are cellular (II, III, V, VI) and two have very few or no cells (I, IV). The layers closest to the pial surface are termed the superficial layers (I – III), and those furthest away the deep layers (IV – VI). The principal cells of the EC are pyramidal cells and large multipolar neurons called stellate cells (273), both of which are excitatory and glutamatergic (274). GABAergic inhibitory interneurons are also present making intrinsic, local connections, and these can be distinguished based on their morphology (multipolar, bipolar, basket and chandelier cells) and immunoreactivity (they may stain for parvalbumin, cholecystokinin or somatostatin) (273). The EC is generally considered to be an input/output node for the hippocampus. The superficial layers (II/III) provide the main afferents to the hippocampus via the perforant (-> CA3 and DG) and temporoammonic (-> CA1) pathways, whereas layers V and VI send the major output projections, relaying information from CA1 and the subiculum.

### 1.4.1.5.3. Regional organisation

The EC is classically divided into two wedge-shaped subregions: the lateral entorhinal cortex (LEC) and the medial entorhinal cortex (MEC) (*Figure 1.15*). The LEC has a dorsal border with the perirhinal cortex and lies more rostro-laterally than the MEC, whereas the MEC has a ventral portion which extends rostro-caudally along the medial aspect of the LEC and curves to form a dorsal border with the parasubiculum. The LEC and MEC were first distinguished by Brodmann (areas 28a and 28b respectively) on the basis

of differences in cell morphology and density (275, 276), for example, the border between layers II and III is much clearer in the MEC than the LEC (273). Subsequent tracing studies have identified distinct patterns of connectivity and this is now regarded as the primary means of distinguishing between the two subregions (277). These distinct connectivity patterns are reflected in the different but related functions subserved by the LEC and MEC. Both the LEC and MEC receive input from a diverse array of cortical and subcortical brain regions including multimodal sensory areas (273, 278). While there is some overlap in connectivity, the LEC has strong connections with perirhinal cortex, olfactory cortex, insular cortex and the amygdala, whereas the MEC receives stronger input from visual association areas, postrhinal cortex, presubiculum and retrosplenial cortex and (274).



Image redacted for copyright reasons

*Figure 1.15 Anatomy of the MEC and LEC.* Left-hand image: Schematic lateral view of the rat left hemisphere showing the position of structures in the hippocampal formation (HF, hippocampal formation; LEC, lateral entorhinal cortex; MEC, medial entorhinal cortex; PaS, parasubiculum; PER, perirhinal cortex; POR, postrhinal cortex; rf, rhinal fissure (equivalent to rhinal sulcus). Right-hand image: Horizontal section from dotted region in left-hand image indicating the neuronal architecture of the rat hippocampal formation (labels as for left-hand image; DG, dentate gyrus; S, subiculum). Image taken from (274).

The LEC and MEC differ in their projections to the remainder of the hippocampal formation; while layer II/III EC neurons from both the LEC and MEC synapse onto the same cell populations of the DG and CA3 via the perforant path, the reciprocal projections to CA1 and the subiculum target

distinct cell populations (274). On the basis of their distinct connectivity, the MEC and LEC have been proposed to respectively process spatial (where) and non-spatial (what) information (279).

### 1.4.1.5.4. Topology of projections

The connectivity of the EC varies in a layer-specific manner but also exhibits a striking topographical organisation. This topology follows a dorsolateral-to-ventromedial gradient, running between the rhinal fissure and the EC/hippocampal border *(Figure 1.16)*; the dorsolateral regions of the EC which lie closest to the rhinal fissure project to the septal areas of the hippocampus proper, and ventromedial areas project to regions near the temporal pole (273, 277, 280).

Image redacted for copyright reasons

**Figure 1.16 Topographical connectivity of rat entorhinal cortex**. *A*: Posterolateral view of the rat entorhinal cortex with the yellow line indicating the separation between LEC and MEC. The gradient of connectivity is indicated by the colour scale with magenta corresponding to the dorsolateral bands of the entorhinal cortex, and blue the more ventromedial bands, running parallel to the rhinal fissure (dotted line). Neurons located within these bands project to the correspondingly coloured regions of the hippocampal formation (*B*) along a hippocampal septotemporal gradient. The cortical and subcortical connections of the EC follow a topographical organisation (*C*). Projections to/from the LEC are shown in dark green font and to/from the MEC in light green. The arrow direction indicates whether projections are afferent/efferent. White arrows indicate organisation of the intrinsic connections of the EC whereby regions within the same 'band' are preferentially interconnected. Figure taken from (274).

Cortical and subcortical projections to the EC also display a topographical organization with multimodal sensory cortical areas preferentially projecting to a band of the EC that lies adjacent to the rhinal sulcus. Areas of the EC that are further from the rhinal sulcus receive a different class of afferent information, for example input from the olfactory cortex, piriform cortex and amygdala (274). The outputs from the EC are organised following similar principles.

### 1.4.1.6. Dentate Gyrus

The dentate gyrus (DG) is a key node in the trisynaptic loop situated between the EC and the CA3 subregion of the hippocampus proper. It receives its major input from the EC via the perforant path (281), and in turn sends projections to the CA3 subregion of the hippocampus, thus providing the primary input to the hippocampus proper (282).

The DG, along with hippocampal subfields CA1-3, curves round from its septal pole rostrally to its temporal pole caudally. In a transverse section of the hippocampal formation the three layers of the dentate gyrus appear to form a V-shape (septally) or a U-shape (temporally) which interlinks with the hippocampus proper (*Figure 1.17*). The DG has no subregions and there is little variation in its trilaminar structure along the septotemporal axis. The three layers of the DG are the superficial *molecular layer* which contains relatively few cells alongside the terminal fibres of the perforant path (253, 283), the *granule cell layer*, and the *polymorphic cell layer*, also known as the hilus.

**Figure 1.17 Laminar structure of the hippocampus and dentate gyrus**. A schematic of a horizontal section of the rat hippocampal formation. Figure taken from (558). Grey indicates the principal cell layers of the hippocampus and dentate gyrus, i.e., the pyramidal cell layer and the granule cell respectively. SO, stratum oriens; SR, stratum radiatum; SML, stratum lacunosum moleculare; SL, stratum lucidum; ML, molecular layer; GL, granule layer; H, hilum (equivalent to polymorphic cell layer).

The *granule cells* are the principal cells of the DG and, along with granule cells in the olfactory bulb, continue to be generated throughout adulthood (284). The unmyelinated axons of the granule cells, called *mossy fibres* (261), form synapses with the proximal dendrites of pyramidal cells in the CA3 (285, 286). This *mossy fibre pathway* is the main distinguishing feature between hippocampal subregions CA3 and CA2 (283), and is the only output projection from the rat DG (253). The unusually large presynaptic boutons of the mossy fibres (mossy fibre expansions) (287), each of which has multiple release sites, ensures that the mossy fibre pathway is highly efficient and enables DG granule cells to exert a strong influence over the firing of CA3 pyramidal cells (253). Granule cells receive their primary innervation from ocean-stellate cells in layer II of the EC with a minor component from layers V and VI, via the perforant path (281, 288); afferents from the LEC terminate in the outer third of the molecular layer, with those from the MEC terminating in the middle third (289, 290).

The other main excitatory cell type in the DG is the *mossy cells* which are found within the polymorphic cell layer and can be distinguished by their architecturally complex dendritic spines (thorny excrescences) (291, 292). Reciprocal projections between the mossy cells and ipsilateral granule cells create a disynaptic feedback loop which links granule cells along the septotemporal axis of the DG (282). In addition several types of interneuron are found within the DG including the pyramidal basket cell (288).

### 1.4.1.7. The hippocampus proper

#### 1.4.1.7.1. Laminar structure

The laminar organisation of the hippocampus is similar across all subfields comprising five layers (*Figure 1.17*). The principal cell layer is the *stratum pyramidale* which contains the somata of pyramidal neurons along with several different classes of interneuron. Deep to this lies the *stratum oriens* which contains CA3-CA3 and CA1-CA1 association fibres. The layers superficial to the *stratum pyramidale* contain the apical dendrites of the pyramidal neurons and interneurons. From deep to superficial, these layers are the *stratum lucidum*, the *stratum radiatum* and the *stratum lacunosum moleculare*. The *stratum lucidum* is present only in the CA3 subregion and contains mossy fibres from the granular cell layer of the dentate gyrus. The *stratum radiatum* is the layer in which the majority of the CA3 -> CA1 schaffer collaterals are located (253). The *stratum lacunosum moleculare* contains axon terminals from layer III of the EC and a range of interneurons.

## 1.4.1.7.2. Hippocampal subregions

The hippocampus proper has three subfields based on the early neuroanatomical studies of *Lorente de No*: CA1, CA2 and CA3 (263). These can be distinguished on the basis of their morphology, connectivity and neurochemical expression patterns (293).

CA3 receives its main input via mossy fibres originating from the granule cell layer of the dentate gyrus, and via the perforant path, which originates in the ocean-stellate cells of layer II of the EC (282). Pyramidal neurons in CA3 project to other CA3 pyramidal neurons via the longitudinal associational bundle, and to CA2 and CA1 pyramidal neurons via schaffer collaterals (263, 294), mainly targeting apical dendrites in stratum radiatum (295).

CA2 is a narrow, small zone between the CA3 and CA1 subfields, distinguished from CA3 through its lack of a stratum lucidum and the absence of mossy fibre innervation (263). CA2 receives a strong excitatory input from layer II/III of the EC onto distal apical dendrites, a connection which exhibits a high degree of plasticity, and weaker inputs from CA3 onto proximal dendrites (296). The majority of CA2 pyramidal cells project to CA1, targeting basal dendrites in the stratum oriens, and there are very few recurrent associational projections (293).

As outlined above, CA1 receives inputs from CA3 schaffer collaterals, and from CA2. It also receives direct projections from layer III of the EC onto the distal apical dendrites of pyramidal cells in the stratum lacunosum moleculare (282). Projections from island cells in layer II of the EC onto CA1 interneurons, which in turn synapse onto the distal dendrites of CA1

pyramidal cells, form a neural circuit which regulates the input from layer III of the EC via feed-forward inhibition (297). CA1 has sparse associational connections (298) but the majority of CA1 pyramidal cells axons project to the subiculum and deep layers of the EC (299).

### 1.4.1.8. Subicular complex

#### 1.4.1.8.1. The subiculum

The subiculum lies between the hippocampus proper and the EC, bordering CA1 proximally and the presubiculum distally. It is a trilaminar region with the transition from CA1 marked by a widening of the pyramidal cell layer and the disappearance of the stratum oriens (263). Superficial to deep its layers are: the *molecular layer* which contains the apical dendrites of pyramidal cells, the *pyramidal cell layer*, and a *polymorphic layer* (300). The subiculum has long been considered the penultimate step in the hippocampal processing loop, however, it is now thought to be additionally involved in information processing at an earlier stage (301, 302). It receives several inputs from both cortical and subcortical structures. The primary projection to the subiculum originates from CA1 and targets the deep portion of the molecular layer, with further cortical inputs from layer III of the EC via the perforant path terminating in the superficial portion of the molecular layer (282, 303). The key projections from the subiculum target the pre- and parasubiculum and the deep layers of the EC, but subicular efferents also project to additional cortical (304, 305) and subcortical regions (267).

#### 1.4.1.8.2. Pre- and parasubiculum

The *presubiculum* lies distal to the hippocampus and is located between the subiculum and the *parasubiculum*. The *pre-* and *parasubiculum* have

broadly similar laminar structures with six layers which are more distinct dorsally. The precise role played by these two regions in the hippocampal processing loop is not certain and neither area can be characterised exclusively as either an input or an output area to the hippocampus proper.

The majority of inputs to the pre- and parasubiculum target layer I and arise from the subiculum and EC (264). Both regions also have reciprocal connections with the peri- and postrhinal cortices (306) and receive input from the retrosplenial cortex, the medial septum, visual association areas and anterior thalamic nuclei (267). In terms of their outputs, both the pre- and parasubiculum send projections to the superficial layers of the EC; the presubiculum predominantly projects to layer III and the parasubiculum to layer II (307, 308) and the molecular layer of the dentate gyrus (267, 307). This pattern of efferents suggests that the pre- and parasubiculum may play a role in the provision of sensory input to the hippocampal formation, however these regions also project to the molecular layer of the subiculum and deeper layers of the EC, which are considered output structures (273, 307, 309).

## 1.4.2. Hippocampal electrophysiology

### 1.4.2.1. Oscillatory dynamics of the hippocampus

The local field potential (LFP) is the electrical potential in the extracellular space and can be obtained through low-pass filtering of the voltage traces recorded from the brain *in vivo* using implanted electrode arrays. The LFP is generated by transient imbalances in extracellular ion concentrations which likely reflects a combination of the synaptic transmembrane current,

ion flow through ligand and voltage-gated ion channels, and intrinsic membrane oscillations (310). Oscillations with a frequency ranging from 1 to 200Hz can be observed in the hippocampal LFP of freely moving rodents (310). These oscillations reflect temporally coordinated network activity (310) and include theta (6-12Hz), beta (12-20Hz), gamma (30 – 100Hz) and ripple (140 – 200Hz) oscillations in addition to small and large irregular amplitude activity (SIA and LIA respectively).

### 1.4.2.1.1. The theta rhythm

The hippocampal LFP exhibits a prominent oscillatory tendency in the theta range (6-12Hz) (311). This theta rhythm was first recorded in the rabbit hippocampus (312) and is particularly prominent during behaviours with a link to voluntary locomotion such as walking and running, and during REM sleep (264, 310). A strong correlation between theta frequency and running speed has been demonstrated across many studies (313, 314), and theta frequency has been shown to be reduced in novel environments (315). Hippocampal cells tend to fire at a preferred theta frequency (*see page 109*), and this phenomenon, theta *phase-locking*, is also observed in extrahippocampal regions including the subiculum, EC (316), cingulate cortex (317), perirhinal cortex and amygdala (318).

Theta activity can be divided into two subtypes, type I and type II, based on its pharmacological properties and behavioural correlates. Both types are present during movement, however, type I theta is also present when the animal is immobile and is associated with attention or arousal. Type I theta is abolished by atropine, whereas type II theta is atropine-resistant (264, 319). Lesions or inactivation of the medial septum diagonal band of Broca

(MS-DBB) abolishes the theta rhythm hence the medial septum is widely regarded as the *pacemaker* of the theta rhythm (320). Distinct pathways are involved in the generation of type I and type II theta. The posterior hypothalamic nucleus, which displays tonic neural activity synchronised to the theta rhythm, has been implicated in the generation of type I theta (321), whereas type II theta has been shown to be conveyed to CA1 and CA3 by afferents from layer III and layer II of the EC respectively (322). For a comprehensive review of the prominent models of theta generation please see (319).

The network properties of the hippocampal formation and the intrinsic oscillatory properties of hippocampal neurons also influence the theta rhythm (319). Theta oscillations appear to be more regular and have the greatest amplitude in the most superficial layer of CA1, the stratum lacunosum moleculare. The traditional view is that amplitude and phase of theta oscillations change according to the depth of the recording tetrode, whereas theta oscillations are synchronised within the same layer (*Figure 1.18*) (323), however, more recent evidence suggests that in CA1 theta oscillations are travelling waves that propagate along the septotemporal axis of the hippocampus (324).

A large number of hypotheses have been proposed regarding the functional relevance of the theta rhythm, including a role for theta in motivation (325), short term memory (326), sensory-inhibition (327), sensorimotor integration (328) and information processing (329). Within the hippocampus the theta rhythm is proposed to have three main functions (264). First, it is a means by which firing can be synchronised across the hippocampal formation,

allowing organisation of neural activity in each subregion with respect to other hippocampal subregions. Second, it provides a 'clock' mechanism for the timing of hippocampal spikes; the firing of place cells in relation to the theta rhythm encodes additional spatial information through the phenomenon of *phase precession* (330) (*see page 109*). Finally, the theta rhythm can influence the induction of LTP; stimulation of hippocampal afferents using theta-bursts has been shown to effectively induce LTP and there is evidence that the propensity of spike trains to elicit LTP is related to theta phase (331).
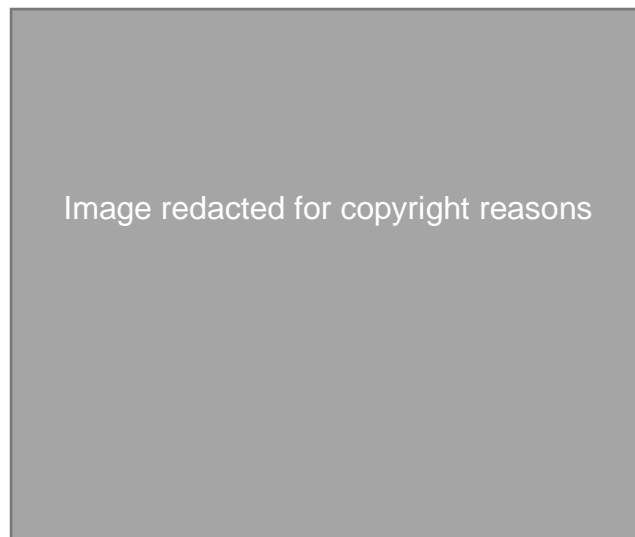


**Figure 1.18. Theta oscillations in the hippocampus. *A***: A 16 site silicon probe in the CA1-dentate gyrus axis. The numbers indicate the recording sites. Each site is 100μm apart. o, stratum oriens; p, stratum pyramidale; r, stratum radiatum; lm, stratum lacunosum moleculare; m, molecular layer of the dentate gyrus; g, granule cell layer; h, hilus. ***B***: Theta waves recorded from a rat during exploration. As the recording depth increases there is a gradual shift of theta phase and an increase in theta amplitude. The vertical scale bar indicates 1mV. Figure taken from (332).

*1.4.2.1.2. Sharp wave ripples*

During slow wave sleep and periods of immobility the LFP in the hippocampus changes: theta oscillations are markedly reduced and are replaced by large irregular amplitude (LIA) activity which features an irregular, high amplitude, low frequency oscillation called *sharp waves* (333). During sharp waves a high frequency (140 – 200Hz) oscillation,

*ripples,* occurs with a peak amplitude within the CA1 subfield. These ripples are associated with the simultaneous discharge of large numbers of neurons (183, 334, 335). Together these two oscillations are called *sharp-wave ripples* (SWRs).

SWRs are seen across species, including rodents and humans, and are thought to be an intrinsic property of the hippocampus since neo-decortication fails to abolish them (336-338). Due to the recurrent circuitry in CA3 it has been proposed that this is the region where SWRs are triggered. There is an increasing body of evidence supporting the contribution of SWRs to spatial cognition and memory, with the synchronous neuronal firing observed during SWRs proposed to represent the mechanism for consolidating new learning (339). In the context of this PhD thesis the relevance of SWRs is primarily related to their use as an important electrophysiological marker to enable correct tetrode positioning in the CA1 pyramidal cell layer, however, the proposed role of SWRs in memory consolidation, and the observation of sleep disturbances in patients with AD, make this an interesting avenue for future research.

### 1.4.2.2. Place cells

#### 1.4.2.2.1. Overview and historical context

Place cells are the principal cells of the hippocampus, found in the pyramidal cell layer of CA1 and CA3, and were discovered by *John O'Keefe* in 1971 in the hippocampus of the freely behaving rat (48). These cells fire in complex bursts and their activity is tuned to a specific location within the environment (340). Place cells have a low background firing rate throughout

the majority of the environment (0.1 – 2 Hz) but as the animal travels through a circumscribed region, called the *place field*, they emit a burst of action potentials with firing rates increasing several-fold, reaching rates as high as 30 – 50 Hz (341, 342). The rate of place cell firing therefore encodes the animal's location and this spatial firing pattern is best visualised using a firing rate map in which the mean firing rate in each location within the environment is represented by a colour, with hotter colours representing higher firing rates (*Figure 1.19*). Place cells are not unique to rats (48) and have been recorded in many other species including mice (343), bats (344) and non-human primates (345) . Recordings made in the temporal lobes of epileptic patients during planned neurosurgical procedures have also provided evidence for the existence of place cells in humans (206).

Image redacted for copyright reasons
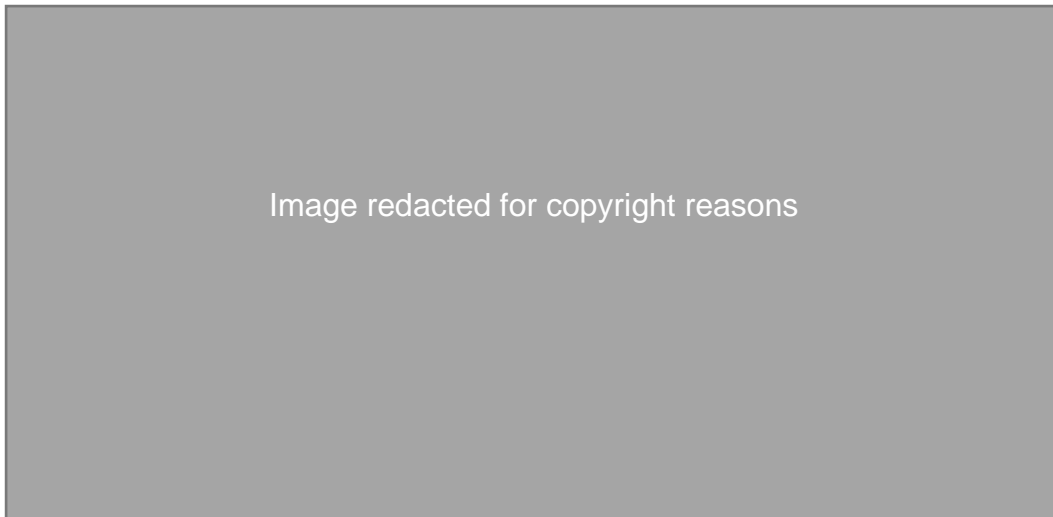
**Figure 1.19 Four types of spatial cell.** Examples of a place cell (A), head direction cell (B), grid cell (C) and boundary vector cell (D). The top row images show the locational firing rate maps (A, C, D) with hot colours representing higher firing rates, and a polar plot showing the preferred firing direction (B). The number in the top left of each image indicates the peak firing rate in Hz. The lower row of images shows the path of the animal within a four-walled environment (black line) with the locations at which spikes were recorded shown superimposed in green. Image adapted from (346).

### 1.4.2.2.2. Place cells and spatial selectivity

Different place cells are tuned to different locations in the environment and therefore in any given location there is a subset of place cells which fire together. The firing of these cells represents a sparse and distributed neural code which signifies the animal's location (339, 347). As a result, by recording the activity of a small population of place cells it is possible to accurately 'decode' the location of an animal (339, 348). Unlike brain regions such as the primary motor and sensory cortices, the hippocampus does not display topographical organisation, that is, anatomically proximal cells do not have adjacent place fields in physical space (349). Place field properties vary along the dorsoventral axis of the hippocampus, with a lower proportion of spatially modulated cells found near the temporal pole, and place cells in this region exhibiting larger place fields and more out-of-field activity than those located near the septal pole (350, 351).

Place cells exhibit place fields on first exposure to an environment (352) and can have stable firing patterns across long periods of time with one study finding that some place fields were maintained when a rat was exposed to the same environment 153 days later (353). More recent work has demonstrated that place coding across a large population of place cells is a more dynamic process than previously thought, with the relatively small subset of cells which maintain stable place fields over long time periods being sufficient for the animal to retain an accurate spatial representation over many weeks (354). Not all place cells are active in every setting with one study finding that the majority of place cells are silent within any given environment (355).

*1.4.2.2.3. Rate coding and temporal coding: an overview*

Place cells use two strategies to encode spatial locations. These two forms of coding, rate coding and temporal coding, can operate independently and encode an animal's speed of movement through a place field and its location within that place field respectively (356). As alluded to above, the firing rate of a place cell in any given location in the environment encodes spatial information. Hippocampal place cells fire both simple spikes, and complex spike bursts consisting of two to six spikes of decreasing amplitude separated by intervals of less than 6ms (340, 357). The distribution of place field firing rates is approximately Gaussian under most circumstances, which means that, due to its symmetrical nature, the rate code cannot distinguish, for example, between the beginning and end of a place field on a linear track.

Place cells also encode information about spatial location through the timing of their firing in relation to the hippocampal theta rhythm. During locomotion the prominent hippocampal oscillation is the theta rhythm at 4 – 12Hz (*page 92*), and as a rat crosses the place field of a given cell, the cell fires spikes at progressively earlier phases of successive theta cycles. This phenomenon is called theta *phase precession* (330) and, unlike the rate code described above, is a linear code, leading to proposals that the phase code might encode the proportion of the place field traversed by the animal (358, 359) . Phase precession is discussed further below (*see page 109*).

*1.4.2.2.4. Stability and remapping*

The pattern of place cell firing within the same environment can be stable over multiple exposures, and is robust even under a wide range of

experimental manipulations such as the removal of cues (49), turning off the lights (360) and even changing the shape of the environment (361). However, place cells may change the location of their firing fields, or *remap*, if the animal is introduced to a novel environment (49), or if there are sufficient alterations in the sensory attributes of the familiar environment that the animal no longer recognises it as familiar (188). During remapping the location in which a place cell fires in the novel environment is not related to its firing location in the original environment in any consistent way, and the sensory cues in the environment cannot accurately predict how a place cell will remap (188).

*Rate remapping* is a distinct phenomenon in which the firing rate within a cell's place field is altered, despite the overall spatial tuning of the cell remaining unchanged. This can occur with subtle manipulations of external sensory cues such as changes to the odour or colour of the testing environment (362, 363).

*1.4.2.2.5. Determinants of place cell firing*

A great deal is known regarding the determinants of place cell firing, including the role of exteroceptive and idiothetic cues. The key relevant findings are briefly outlined below and, unless stated otherwise, all the studies discussed were conducted in rats.

*Visual cues*

A large variety of visual landmarks and cues, including intra-environmental cues and more distal, extra-environmental cues, can exert an influence on place cell activity. In a controlled environment with four fixed visual cues it was found that place cell activity could depend on one or two individual

cues, or a more complex combination of several cues (49). Rotation of all four visual cues resulted in a corresponding rotation in place field locations, although in some instances place fields were unaffected by the movement of just one or two individual cues. Since this initial finding, it has been confirmed in subsequent studies that the rotation of a single polarising cue results in an equal rotation of the firing fields of individual place cells (*Figure 1.20*) (188, 364-366). The exception to this was if the rat had learned that the rotated cue was unstable, whether through seeing the cue being moved, or if the magnitude of the rotation was too large (364, 367, 368). Interestingly, the removal of the salient cue did not disrupt place cell firing, indicating that place cells did not solely rely upon the salient cue to localise their place fields.



**Figure 1.20 The influence of cues and boundaries on place cell firing. *A***: Example rate maps for two place cells whose firing fields rotate in conjunction with the rotation of a distal cue, represented by the black curved line. Figure adapted from (361). ***B***: Examples of the rate maps of two place cells whose firing is modulated by the insertion of a barrier (black line, central column). The field in cell 1 disappears when the barrier is inserted, and reappears again once it is removed, whereas cell 2, which has a place field along the east wall of the enclosure duplicates it field when the barrier is inserted (369).

The influence of cues on place cell firing has been linked to the experimental task being undertaken and the behaviour of the animal. In one study place cells remapped in the same environment when a rat switched from a random foraging task to a directed searching strategy to locate hidden food (370). Another study showed disruption of place fields occurred when conflicting distal and local cues were presented to rats randomly foraging for food, but when the rats were performing a navigational task in the same environment, place fields were unaffected by the same cue manipulation (371). It has subsequently been shown there is a strong interaction between the type of navigational task being undertaken and the response of place cells to cue rotations (372).

Some visual cues appear to be of more importance than others, with landmarks near the boundaries of the experimental arena found to exert a much greater control over place field location than cues located near the centre of the environment (373, 374). A possible explanation for this finding is that, unlike centrally placed cues, objects located at the peripheries of an environment are only perceived in a limited number of configurations and therefore using these cues as landmarks is less computationally demanding. The relationship between cues is also important, with one study showing that as intra-environmental cues were moved further apart the place fields were distorted in a topological fashion (366).

Distal cues (external to the experimental arena) and local cues (within the experimental arena) can both influence place cell firing. In a series of studies, manipulation of distal and local cues by rotating them, reordering them, or changing the relationship between them, showed that simultaneously recorded place cells could respond in different ways: some

became silent, others rotated their fields with respect to the distal or the local cues, some maintained their fields with respect to the experimental arena regardless of the cue manipulations, and others remapped (375-378). Studies which have translocated the experimental enclosure within the experimental room have shown that place fields tend to maintain their locations relative to the local enclosure rather than the distal cues in the experimental room, however when the distal cues were rotated the place fields also rotated, indicating that despite the dominance of local cues, distal landmarks were perceptible to the rats and could still exert an influence on place cell firing (379, 380).

*Olfactory, tactile, and auditory cues*

Although visual cues clearly exert an important influence over place cell firing, they are not necessary for place cell activity. Place cells still exhibit spatial tuning in complete darkness (335) and congenitally blind rats have been shown to have normal place cell firing patterns (381). This suggests that the firing of place cells depends on other cues in the absence of visual information. Changes in other environmental variables such as odour have been shown to elicit changes in the firing rates of place cells (362, 363). In one study cleaning of the floor in an experimental enclosure devoid of cues removed olfactory cues and resulted in reduced place field stability in both light and dark conditions (382). Global remapping of place fields has been observed when the odour of a familiar environment is changed (362) and in the absence of visual cues, distinct olfactory cues can be used to learn spatial contexts and form stable place fields which rotate when the olfactory cues are rotated, and remap when these are scrambled (383).

Tactile cues also influence place cell activity in the absence of other sensory cues (384). Blockade of tactile transmission in the rat through the application of lidocaine to the whisker pad resulted in an expansion of place fields recorded in an enriched tactile environment devoid of other sensory cues. Furthermore, when the tactile cues within this environment were rotated the majority of place fields also rotated (385).

The role of auditory cues is less well defined, although it has been shown that auditory cues alone were not sufficient to guide place navigation in a water maze task, but did support place navigation when associated with a visual cue (386). In another study on a dry maze rats were able to navigate to a reward location in complete darkness when guided by auditory cues (384).

*Ideothetic cues and path integration*

*Path integration*, also described as *dead reckoning*, describes the process by which an animal can locate its current position from its starting location using estimations of its speed, heading direction and course over time. Path integration relies on *idiothetic*, or internal, cues which include vestibular inputs, optic flow, and proprioception/self-motion cues. The importance of vestibular input for path integration was highlighted by a study in which gerbils were required to navigate to the centre of the arena to retrieve their pups, and then return to their home cage located on the periphery of the arena. When the gerbils were rotated at speeds too slow to trigger a vestibular response their home-bound trajectories had an angular displacement which was proportional to the degree of rotation (387). Additional studies have shown the importance of vestibular signals for path integration across species (388-390).

A role for path integration in place cell firing was initially proposed in 1978 (49), and has gained traction following observations that place cell firing is not abolished by the removal of cues. Observations that place cells rapidly form stable firing fields in new environments, and that place cell firing correlates with running speed support this thesis (339, 391), along with the discovery of grid cells (*see page 117*), which provide a major projection to the hippocampus and are thought to play a crucial role in path integration. Additional studies provide direct evidence for the role of path integration in place cell firing. *Gothard et al.* ran rats on a linear track with a fixed reward site at one end and a moveable reward site at the other. On the initial portion of their journey, when rats were running away from the moveable reward site, their place fields fired at consistent distances from the moveable reward site, regardless of its location, implying that the location of the place field must be updated by path integration (392).

Finally, there is evidence that vestibular inputs, optic flow, and self-motion cues all contribute to place cell activity. A number of studies have investigated the effects of rotating the floor or walls of an enclosure, or the animals themselves, below and above the acceleration threshold of the vestibular system, finding that slow rotations resulted in a corresponding rotation in the locations of place fields in contrast to fast rotations where the place fields remained constant in relation to the external laboratory environment (367, 368, 393, 394). Lesion studies have confirmed the importance of vestibular inputs to place cell firing; studies of rats with bilateral labyrinthectomies have shown a severe impairment in the spatial firing activity of CA1 pyramidal cells (395) and a disruption of the hippocampal theta rhythm (396). The observation that place cells fire when

animals have run specific distances on a running wheel suggest that in addition to external sensory inputs, internal self-motion cues can also influence place cell firing patterns (397). This is consistent with previous findings (392), and recent studies using virtual reality environments to decouple the influence of environmental visual information and physical self-motion signals have found that both factors affect CA1 place cell activity, although the place cell population is more strongly influenced by visual inputs (398, 399).

*Environmental features*

Various attributes of the experimental environment, such as its size and geometry, can influence place cell firing. Place cells may have multiple place fields, and this is more likely to be the case if the environment is larger. For example, in 2008 *Fenton et al.* found that in larger environments place cells had larger fields, and some cells had multiple fields spread across the environment in an irregular fashion (347). As the size of the environment increases there is also a lower proportion of silent place cells as more CA1 pyramidal cells exhibit place fields (400).

Altering the boundary walls of an environment has been shown to reliably elicit changes in the location of a cells place field in a predictable fashion (361). In 1996, *O'Keefe and Burgess* found that when a rat was foraging in a square arena stretching this arena along one axis to form a rectangle resulted in a corresponding elongation or duplication of place fields in the place cells which had fields along that axis (401). In another study, when a new boundary was introduced into a familiar environment, place fields which originally encoded locations overlapping with the new boundary were

abolished, whereas the firing of place cells with fields distant from the new boundary was unaffected (188) (*Figure 1.20*). Removing the number of boundaries within an environment has been shown to cause a degradation in place cell firing (369), although objects which do not impede movement were not found to have the same effect (373).

In open enclosures place cells are *omnidirectional*, firing irrespective of the direction an animal is travelling when it crosses the place field (402). However, on narrow linear tracks or mazes when the behaviour of the rat is highly stereotyped place cells can become *directional,* only having an elevated firing rate within their place field when the rat travels through it in a preferred direction (391). Even in the open field place cells can develop a directional preference if the animal is trained to run on a stereotypical path (370). Enriching a linear track environment with multimodal sensory cues can induce a significant proportion of place cells to become *bidirectional*, i.e. to have place fields in both running directions along the track (403). Given the above, it has been proposed that the trajectory of the animal's path is the major influence on whether the firing of a place cell is directional or omnidirectional (264); experiments where the animal crosses the same region of an environment via two different paths has shown that place cell activity depends on which route is chosen (404-406).

It has also been reported that as a rat runs along a linear track the firing features of its place cells change with experience; on each successive run through the place field it was observed that place fields expanded and the centre of mass of the field shifted opposite to the direction of movement (407). In addition, one study found that the Gaussian distribution of firing rates became more negatively skewed as a function of experience within a

given day (408), however this finding did not persist across days, and other studies have failed to replicate it (409, 410).

*Non-spatial cues*

In addition to the cues described above which all relate to spatial measures such as distance or direction, several studies have shown that non-spatial cues may influence place cell activity. Examples of these include findings that place cells encode information about goals (411), rewards (412), conspecifics (413), future trajectories (405) and time (414). These findings have been interpreted as evidence supporting theories of a broad hippocampal function in which all information is processed in an equivalent manner, regardless of type/content, in opposition to the cognitive map theory of hippocampal function (*see page 60*) which posits that the primary purpose of the hippocampus is the representation of spatial information, and the encoding of all non-spatial information occurs within this spatial framework (179). However, some of these seemingly non-spatial cues clearly have spatial components, and it has recently been suggested that the responses of place cells to non-spatial cues could represent *feature-in-place* signals. *O'Keefe and Krupic* argue that experiments in which non-spatial cues are presented in only one location or context are not able to demonstrate the spatial component of the place cell response (415).

### 1.4.2.2.6. Out-of-field firing

During slow wave sleep the hippocampal LFP is dominated by SWRs and the hippocampal pyramidal cells are far more likely to fire, and do so in a fashion which is independent of the location of the animal (49, 416). This *out-of-field firing,* which can also occur during periods when the animal is

awake but immobile, has been shown to represent the reactivation of place cells in sequences which were present during past wakeful experiences (349, 417). These reactivations form the basis of the phenomenon known as hippocampal *replay*, and occur in a compressed time scale, at approximately ten to twenty times the original rate. Place cell sequences can be replayed in the order in which the cells originally fired (forward replay) or in the reverse order (reverse replay). Hippocampal replay can occur when an animal is actively engaged in a task, so called *online* replay, or during periods of sleep or quiet wakefulness, *offline* replay. Both online and offline replay have been hypothesized to represent the neural correlate of memory consolidation through a Hebbian learning process (417-419), and online replay has also been proposed to play a role in navigational planning (420). Finally, some studies have shown that future place cell sequences are *pre-played* before an animal enters a novel environment which could be interpreted as a preparation for future navigation (421). For a review of replay please see (264, 420).

Out-of-field firing does not only occur during periods of quiescence, but also during activity, for example when an animal is engaged in a navigational task. In 2007, *Johnson and Redish*, observed that as a rat ran close to the choice point on a T-maze, CA3 place cell ensembles representing trajectories down either the right or left arm appeared to fire in quick succession (422). These 'sweeps' were associated with theta, rather than SWRs, and the authors speculated that they represented the neural correlate of the rat's decision-making process. However, an alternative explanation is that these theta sequences arise as a result of phase precession (*see page 109*), although it has been shown that phase

precession alone cannot predict the presences of theta sequences to the extent to which they actually occur (423).

*1.4.2.2.7. Place cell firing and the theta rhythm*

As briefly mentioned above place cells can encode spatial information through their firing in relation to the hippocampal theta rhythm.

*Phase-locking*

Hippocampal pyramidal cells and interneurons have been shown to consistently fire at preferred theta phases (288, 424-426). The extent of this theta *phase-locking* is influenced by the animal's internal state, for example, theta phase-locking may be greater during tonic REM sleep compared with wakefulness (427). Across the CA1 pyramidal cell population in mice, a bimodal distribution of preferred theta firing phase has been observed, with individual cells tending to phase-lock to the peak or the trough of the theta rhythm (428). This was found to reflect a segregation in the preferred theta phases of cells in the pyramidal cell layer according to their anatomical location; pyramidal cells in more superficial layers tended to fire closer to the theta trough, whereas cells located deeper in the layer fired near the theta peak (428).

*Phase precession*

Place cells encode spatial information through a rate-based code and a temporal code, also known as a phase code. The relative timing of a place cell's spikes in relation to the theta rhythm of the local field potential can signify the animal's location within the place field of that cell (330). As an animal runs across the place field, the place cell emits a burst of action potentials with spikes emitted at successively earlier phases of the theta rhythm (*Figure 1.21*). The first spike of a place cell within the place field

tends to occur at a fixed phase of the theta cycle, indicating a preferred onset firing phase, and the amount of precession which occurs as the animal progresses through the place field never exceeds 360°. The theta phase of firing has been shown to correlate better with the position of the animal than with related variables such as the time spent in the field. This phenomenon is termed theta *phase precession* (358, 429).
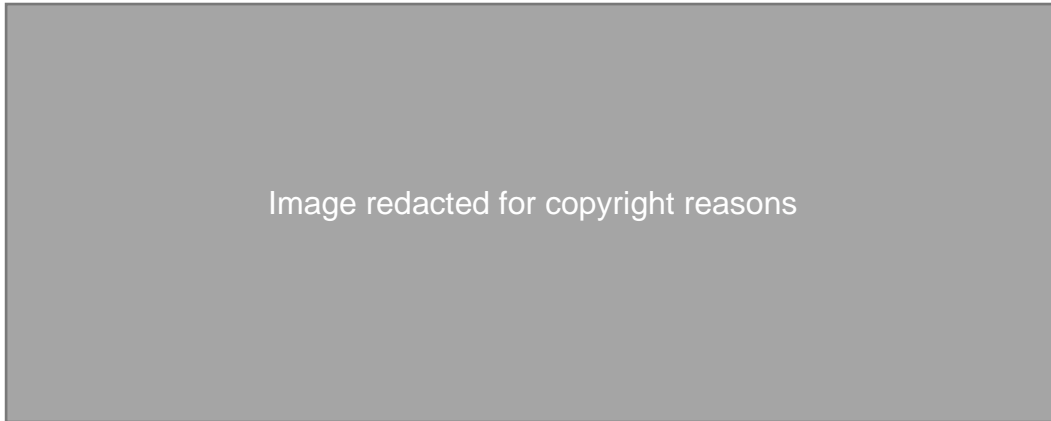


**Figure 1.21 Theta phase precession.** Phase precession can be seen from an example place cell as a rat runs along a linear track (***A-C***). The portion of the track analysed lies between the vertical lines in ***A***. ***B***: the rate map for an example place cell with the peak rate indicated in Hz. The cell has a field on the right half of the track. ***C***: Within the place field of this cell a raster plot shows the occurrence of individual spikes (black vertical lines) in relation to the theta rhythm of the LFP (shown in blue). ***D***: a scatterplot of theta phase versus track position shows a significant negative correlation, indicative of theta phase precession. Figure adapted from (430).

Phase precession was first observed in a linear track environment (330) but has subsequently been identified in two-dimensional environments, confirming it is not an artefact occurring secondary to stereotyped behaviour on the linear track (358, 359). It is also a feature of CA1 inhibitory interneurons (431). Since the frequency of theta oscillations in the hippocampus and the rate of place cell firing, are both known to increase with the running speed of the animal (314, 315, 339) phase precession can be explained by models where the place cell firing rate increases with running speed at a faster rate than the increase in theta frequency. A

discussion of such oscillatory interference models is included in the next section.

Structures beyond the hippocampus are likely to contribute to the phenomenon of phase precession. In one study by *Zugaro et al.* of rats running on a linear track, a brief electric shock applied to the ventral hippocampal commissure temporarily inhibited hippocampal pyramidal cells and reset the phase of hippocampal theta. The authors showed that when place cells resumed their firing they did so at a phase of theta which was appropriate to their location on a linear track, indicating that extra-hippocampal structures not influenced by the electric shock may play a key role in phase precession (432). A prime candidate is the EC which directly projects to CA1 and CA3 pyramidal cells, exhibits phase precession itself in its grid cell population (315), and was shown in this study to be largely unaffected by the electric shock applied to the ventral hippocampal commissure.

### *1.4.2.2.7. Models of place cell firing*

Various computational models have been proposed to explain the location-specific firing of place cells. Early models suggest place fields arise solely from convergent sensory information, specifically theoretical inputs encoding the distance and angular deviation of the animal from distal sensory cues (433, 434).

*The Boundary Vector Cell model*

In 1996 it was observed that stretching a rectangular enclosure along one dimension (by lengthening two walls of the environment) resulted in the receptive fields of some place cells elongating along the same axis (401).

This experiment suggested that place cells fire at fixed distances from the boundaries of the environment and led to the development of models emphasising sensory inputs indicating the presence of environmental boundaries (401). *O'Keefe and Burgess* proposed that "*the place field is formed by the summation of gaussian tuning curves, each oriented perpendicular to a wall and peaked at a fixed distance from it*" (401). This model has been updated several times, once to predict the existence of a new type of spatial cell, the *boundary vector cell* (435, 436), and subsequently to incorporate Hebbian learning and account for changes in place cell activity over time (369).

Simulations of place cell activity based on predictions from the boundary vector cell model have been shown to replicate experimental findings (*Figure 1.22*) such as the response of place fields to the addition of a barrier, and the deterioration of fields as environmental boundaries are removed (188, 369). Additional evidence supporting its validity came from the subsequent discovery of boundary vector cells, as predicted by the model. The boundary vector cell model is consistent with place cells firing in the dark (335), since non-visual cues can indicate the presence of a boundary within the environment, but it does not explain the updating of place cell receptive fields in response to self-motion cues (i.e. path integration) (392). Alternative computational models focus on self-motion inputs, as opposed to external sensory inputs, and fall into two main categories: continuous attractor network models and oscillatory interference models. (435, 437)

Image redacted for copyright reasons

**Figure 1.22 The Boundary Vector Cell model of place cell firing. *A***: Boundary vector cells (BVCs) fire in response to the presence of a boundary at a preferred allocentric direction and distance from the animal. The firing rate, illustrated by the bar charts (***A, right***), is maximal when the direction and distance of the animal align with the boundary vector cell's preference, i.e., when the centre of its receptive field (red) overlaps the boundary. ***B***: BVCs tuned to barriers further away have broader receptive fields. ***C***: The firing of the BVC with the receptive field as illustrated on the left produces the firing rate map on the right. Both images show that the BVC responds to boundaries a short distance to the east of the animal. ***D***: The BVC inputs to a place cell (top right, inset) can be predicted from its firing patterns in different shaped environments (top left). The inputs can then be used to predict the place cell firing patterns in novel environments (bottom right). As illustrated (bottom left) the BVC model can predict the pattern of place cell activity in novel environments. ***A-C*** adapted from (433). ***D*** adapted from (437).

*Continuous attractor network models*

In continuous attractor network models, individual place cells are viewed as

nodes with excitatory interconnections that can settle into a stable pattern

113

of firing. In one such model the connection strength between any two place cells in a two-dimensional continuous attractor network has been proposed to correlative inversely with the distance between the respective place fields (438, 439). If place cells are considered to be organised topographically in a hypothetical *abstract plane,* then this connectivity pattern, in conjunction with global inhibition, gives rise to a localized *activity packet* or *bump* of activity, the centre of which corresponds with the location of the animal's head. The authors proposed that this bump of activity can be shifted around the abstract topographical plane through asymmetric excitatory projections originating from populations of hypothetical neurons which encode movement direction or speed at specific locations and together provide information regarding the animal's velocity (438, 439) (*Figure 1.23*).

Image redacted for copyright reasons
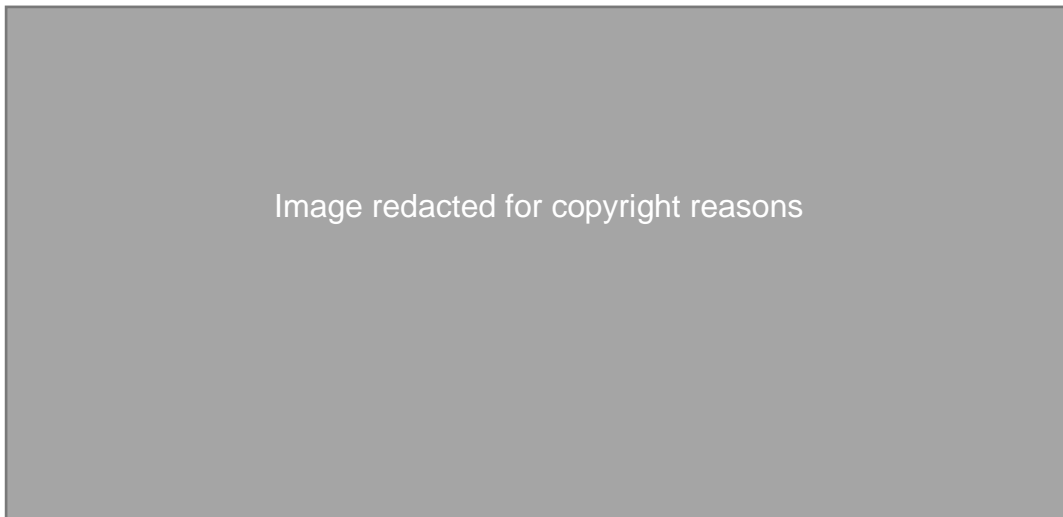
**Figure 1.23. A two-dimensional continuous attractor model of place cell firing.** Each coloured circle in *A* represents a place cell, with cells ordered on a hypothetical plane according to the location of their place fields. Interconnections between place cells, or 'nodes', decline in strength monotonically with distance (red arrows). Global feedback inhibition maintains the net neural activity within a narrow range, leading to a 'bump' of activity somewhere on the plane (*B*, bump shown in red). This bump of activity can move according to the rat's motion using an intermediate layer of cells which encode position on the plane and heading direction. The model requires the activity of these 'conjunctive' place and head direction cells to be positively modulated by running speed, and to project asymmetrically to the corresponding side of the cells in the attractor layer from which they receive input, according to the head direction encoded (green arrow). These conjunctive cells are proposed to be silent when the rat is not moving. Figure adapted from (440).

This model explains how place cells could perform path integration (441). Experimental evidence in support of this model includes the discovery of theta modulated place-by-direction cells in the pre- and para-subiculum which encode both the location and the heading direction of the animal (442). Against a continuous attractor network model is the observation that place cells which have overlapping receptive fields do not remap in the same way when certain sensory attributes of the environment are manipulated (49). Another criticism of continuous attractor models is that if place cell firing is underpinned by a pure path integration mechanism it will inevitably accumulate error. This has led to the proposal that external sensory inputs may be used to reset noise in the system.

*Oscillatory interference models*

An alternative way of modelling place cell firing is through oscillatory interference models which can provide an explanation both for the observed phenomenon of phase precession and the ability of place cells to exhibit spatial tuning in the absence of sensory cues. Theta phase precession can be explained by models in which place cell firing is modulated at a higher frequency than the LFP theta frequency, with the difference between these two frequencies increasing with the running speed of the animal (330). Specifically, the membrane potential of the place cell may oscillate at a frequency slightly faster than the theta rhythm, with the place cell being more likely to fire at the peak of its own membrane oscillation. These two oscillators are synchronised as an animal enters a place field, but the difference in their relative frequencies results in the place cell firing at progressively earlier phases in successive theta cycles as the animal travels

through the place field. As the animal runs faster and the difference between the two oscillator frequencies increases the amount of phase precession per unit time also increases correspondingly. This results in the encoding of the distance travelled by the animal through the place field, rather than the time spent in the place field (330) (*Figure 1.24*).
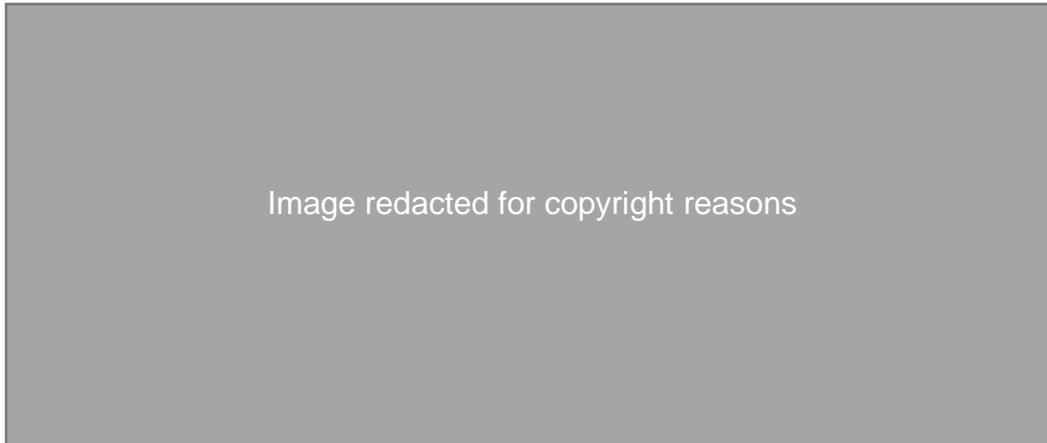


**Figure 1.24 The Detuned Oscillators Model of phase precession. *A:*** As a rat runs along a linear track the place field for the place cell of interest is shown in blue. ***B:*** The membrane potential of the place cell (light blue trace) oscillates faster than the theta rhythm (dark blue) within the firing field. Spikes (numbers 1 to 5) fire at positive peaks of the membrane potential. When the rat enters the place field the membrane oscillator is synchronised with the theta rhythm, but as it travels through the field the spikes begin to anticipate theta cycles resulting in phase precession. Figure adapted from (441).

In a similar fashion oscillatory interference models could also account for spatial tuning of place cells using only self-motion cues. For example, place cell firing could be determined by a membrane potential which is equivalent to the interference pattern of dual oscillators, the frequencies of which are both modulated to a different extent by the animal's running speed. The phase offset between these two oscillators determines the firing probability of the cell and encodes the running speed of the animal in such a fashion that the membrane potential of the cell reflects the distance travelled by the animal; when the two oscillators are in phase their summation will exceed the firing threshold of the neuron and an action potential will be fired in the cells place field (443). Although this type of model does provide an

explanation for some of the observed place cell characteristics, it also predicts that place cells should exhibit periodicity in their firing fields due to the dual oscillators moving in and out of phase as an animal moves; periodic firing fields are observed in grid cells (*see page 117*) but not commonly in place cells.

*A combination of models?*

In isolation none of the models described can fully account for all features of place cell activity, specifically phase precession and the influence of both exteroceptive cues and idiothetic cues on place cell firing. However, these models may not be mutually exclusive; an interaction between sensory cues and path integration, through boundary vector cell and continuous attractor inputs, could account for place cell firing. Place cells could be arranged in a continuous attractor plane according to their inputs from boundary vector cells, allowing place cells to switch strategies depending on the cues available in the environment. This arrangement could co-exist with a dual oscillator model which accounts for phase precession.

### 1.4.2.3. Other spatial cells in the hippocampal formation

Place cells are not the only cells in the hippocampal formation which encode spatial information. *Head direction cells*, first discovered in the dorsal presubiculum, have increased firing rates when an animal is facing in a particular direction in the horizontal (yaw) plane within an environment (189) (*Figure 1.19, page 97*). These cells are tuned to a particular allocentric heading direction and increase their firing rates when the head of the animal is aligned with this preferred direction regardless of whether the animal is moving or stationary. Head direction cells have also been identified in the

EC, and in areas outside the hippocampal formation such as the thalamus and the retrosplenial cortex (346).

In 2005 *grid cells* were discovered in the rat MEC, and they have since been identified in the pre- and parasubiculum (50, 444). Similarly to place cells, grid cells exhibit spatial firing patterns, but unlike place cells each grid cell has multiple firing fields (*Figure 1.19, page 97*). These firing fields tesselate the environment, producing a repeating pattern with six-fold symmetry. Three properties can be used to describe grid cell firing fields (*Figure 1.25*): grid phase (the location of the fields along the x and y axis of an environment), grid scale (the distance between the firing rate peaks of adjacent fields), and grid orientation (the angle of the grid field axes relative to an external reference line). The grid scale changes along the dorsoventral axis of the MEC with smaller fields which are close together in the dorsal MEC, and larger fields with a bigger grid scale in the ventral MEC (50, 445). Grid cells appear to be organised in discrete modules marked by abrupt changes in grid scale (446). Within these modules there appears to be distinct combinations of grid scales and orientations (447). There is evidence that grid cells are also present in humans; a grid-like signal can be identified using functional MRI as human participants navigate in a virtual reality environment (207).

The predominant hypothesis of grid cell function posits that grid cells represent a universal metric for space (449). The periodic firing pattern of grid cells appears to be stable despite changes in running speed and direction and it is widely thought that activity in the grid cell network underlies path integration (346). However, a challenge to this view is that

the observation that the properties of grid fields are not invariant across environments in all circumstances; grid scale has been shown to expand in novel environments (450) and grid orientation, scale and symmetry are permanently affected by environmental geometry with grid symmetry being broken in highly polarised environments (451).
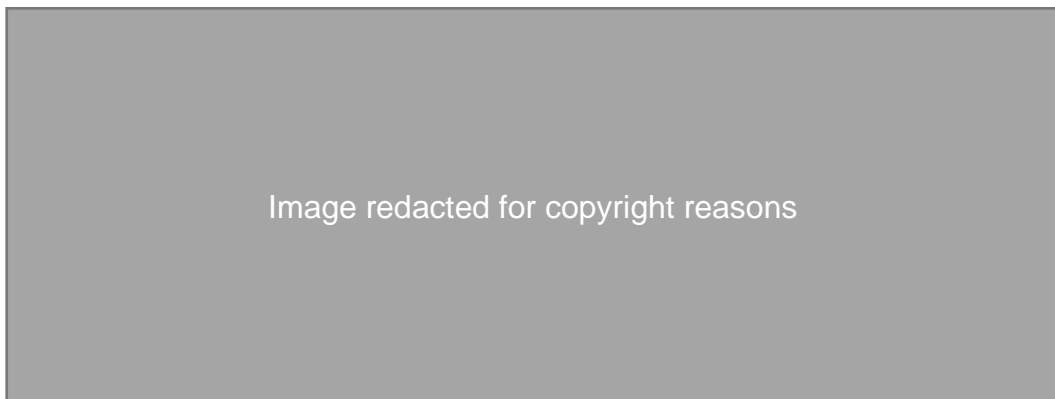


**Figure 1.25 The properties of grid fields.** Grid cell firing fields can be described in terms of their phase (the x-y location of the firing fields), scale (the distance between individual adjacent fields) and orientation (the angle of the grid axes relative to an external reference e.g., the wall of the recording environment). The schematics show the simulated fields of two grid cells (blue and green) with different phases, scales, and orientations. Figure taken from (448).

*Boundary vector cells*, whose existence was predicted by the boundary vector cell model of place cell firing, have been identified in the subiculum (190, 369) and MEC (452). These cells fire at a fixed allocentric direction and distance from boundaries within the environments, including walls, obstacles and edges (190) (*Figure 1.19, page 97*). Further characterisation of these cells has shown that they respond in a similar manner to vertical barriers and drop edges (453).

## 2. General Method

This chapter describes the general methods used to collect the data presented in this thesis including animals and their housing, surgical procedures, single cell recording techniques and histology. Further methodological details are included in the methods sections of each data chapter.

### 2.1. Animals and animal housing

All experiments undertaken were performed in accordance with British Home Office Regulations and the terms of the Animals (Scientific Procedures) Act 1986. The Project License was reviewed by the Animal Welfare and Ethical Review Board at University College London. University College London/ Sainsbury Wellcome Centre guidelines were adhered to throughout all experiments.

#### 2.1.1. Rats

Rats were used in the experiments conducted on the Honeycomb Maze (*Chapter 3, page 133*). Rats were male Lister hooded rats purchased from Charles River Laboratories aged between 12 and 16 weeks at the start of behavioural testing and weighing between 310 and 374g. Rats were housed in open caging along with their littermates, in groups of three to four. Housing consisted of open cages under a 12:12 inversed light-dark cycle, with two, one-hour half-light periods simulating dawn and dusk. Following surgery, if applicable, rats were housed individually thereafter and received a one-week post-operative recovery period with 72 hours of oral analgesia. Prior to behavioural testing on the Honeycomb Maze rats were put on a

calorie-restricted diet with a target weight of 90% of their free-feeding weight.

### 2.1.2. Mice

Mice were either tested on the Honeycomb Maze (*Chapter 3, page 133*) or used in electrophysiology studies (*Chapter 4, page 178*). Mice tested on the Honeycomb Maze did not receive a surgical intervention. Mice were initially housed communally in Perspex cages under a 12:12 inversed light-dark cycle, with two, one-hour half-light periods simulating dawn and dusk, and free access to food and water. Animals receiving surgery were individually housed following this in enriched cages with 72 hours of oral analgesia and received a recovery period of at least one week, until they returned to their pre-surgical weight, during which time they had free access to food and water. Prior to both behavioural and electrophysiology experiments all mice were put on a restricted calorie diet with the aim of reducing their weight to 85 – 90% of their free-feeding weight.

Homozygous APP$^{NL-G-F}$ knock-in mice were used as a model of AD. These were bred on a C57BL/6J background (stock from The Jackson Laboratory). The colony was maintained using heterozygous breeding pairs to enable the use of wild-type (WT) littermate controls. All mice used came from this colony. Male and female WT mice were used in the Honeycomb Maze studies (*Chapter 3*), and female APP$^{NL-G-F}$ mice and WT littermate controls in the electrophysiology studies (*Chapter 4*).

## 2.2. Microdrives

Custom built microdrives were used for electrophysiological recordings. The design allowed tetrodes to be advanced *en masse* through the brain in steps

of 30µm. Microdrives comprised 32 HM-L coated 17µm platinum-iridium (90% platinum, 10% iridium) electrodes (California Fine Wire, CA, USA). Four electrodes were twisted together at a pitch of two turns/mm to form a tetrode, and each microdrive had a total of eight tetrodes. These were wired to two 18-pin Omnetics connectors (Omnetics Connector Corp., MN, USA) which were fused onto a drive mechanism (Axona Ltd., St Albans, UK) using dental cement. This allowed the tetrodes to be advanced into the brain following initial implantation surgery through the turning of a screw located on top of the drive mechanism (*Figure 2.1*). Prior to surgery electrode tips were electroplated in a platinum iridium solution until each channel had an impedance of less than 150 kOhms at 1kHz.
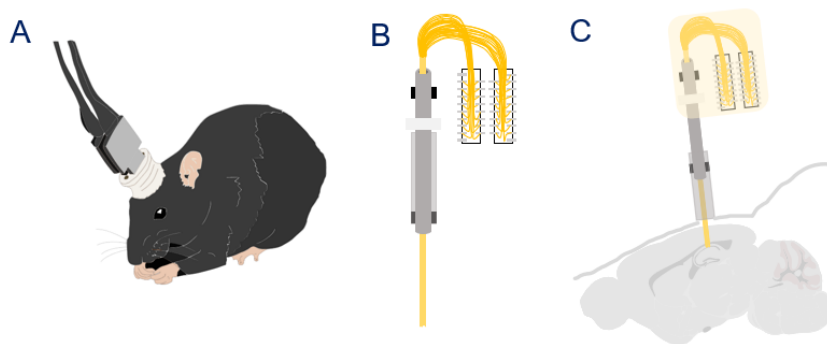


**Figure 2.1 Microdrive configuration.** *A*. Mice foraged freely while recordings were made via a head-mounted hippocampal implant. *B–C*. Microdrives loaded with 8 tetrodes (32 channels) were surgically implanted via a craniotomy into the cortex overlying the CA1 subfield of the left hippocampus. Post-operatively drives were advanced in 25–100 µm increments until the pyramidal layer of CA1 was reached. Mouse and mouse brain images sourced from *https://scidraw.io/*.

## 2.3. Surgeries

### 2.3.1. Lesion surgeries in rats

All surgeries were performed under sterile conditions with isoflurane anaesthesia (isoflurane 2-3% / oxygen 4L/min). Throughout surgery the respiratory rate was monitored and Viscotears® Liquid Gel (carbomer) was

applied to prevent corneal drying. The rat was rested on an isothermal heat pad and its head fixed in a stereotactic frame (Kopf instruments). Prior to incision the head was shaved, and the skin cleaned with Betadine® (10% iodine solution). Subcutaneous Carprieve® (caprofen 0.5%) was administered as an analgesic and Baytril® (enrofloxacin 2.5% 1ml/kg) as a prophylactic antibiotic.

A midline sagittal incision was performed to expose the skull and bilateral craniotomies drilled with a 0.7mm drill bit. To create neurotoxic hippocampal lesions, pressure injections of 50–100nl of ibotenic acid (10μg/μl, Sigma-Aldrich) were made into fourteen injection sites per hemisphere using borosilicate glass pipettes (World Precision Instruments) (*Table 2.1*). Sham lesions that caused no neural damage were made by insertion of a borosilicate glass micropipette at the same coordinates without injection. Lesions of the MEC were made by performing pressure injections of ibotenic acid at eight sites per hemisphere as outlined in *Table 2.2*. Sham MEC lesions were made by lowering pipettes to the same coordinates without injecting ibotenic acid. Following this the skin and scalp muscles were sutured, and topical amoxicillin applied to the wound. Rats were monitored post-surgery in a heated cage and once they returned to their home cage were provided with a cube of jelly containing Metacam® analgesia (meloxicam) and Baytril®. These were administered for at least 72 hours and the rat's recovery monitored closely with daily weights and free access to food for at least one week.

| Site | AP (mm) | ML (mm) | DV (mm) | IBO (µl) |
|------|---------|---------|---------|----------|
| 1 | - 2.4 | 1.0 | 3.0 | 0.05 |
| 2 | - 3.0 | 1.4 | 2.1 | 0.05 |
| 3 | - 3.0 | 1.4 | 2.9 | 0.05 |
| 4 | - 3.0 | 3.0 | 2.7 | 0.10 |
| 5 | - 4.0 | 2.6 | 1.8 | 0.05 |
| 6 | - 4.0 | 2.6 | 2.8 | 0.05 |
| 7 | - 4.0 | 3.7 | 2.7 | 0.10 |
| 8 | - 4.9 | 4.6 | 6.5 | 0.05 |
| 9 | - 4.9 | 4.1 | 3.5 | 0.05 |
| 10 | - 4.9 | 4.1 | 7.2 | 0.10 |
| 11 | - 5.9 | 4.3 | 3.9 | 0.10 |
| 12 | - 5.9 | 5.1 | 4.5 | 0.08 |
| 13 | - 5.9 | 5.1 | 5.3 | 0.08 |
| 14 | - 5.9 | 5.1 | 6.1 | 0.08 |

**Table 2.1 Hippocampal lesion sites.** AP, anteroposterior with respect to bregma; ML, mediolateral with respect to bregma; DV, dorsoventral with respect to the brain surface; IBO, ibotenic acid.

| Site | ML (mm) | DV (mm) | AP coordinates |
|------|---------|---------|----------------|
| 1 | 4.6 | 1.7 | Angle: 22° along |
| 2 | 4.6 | 2.2 | AP axis pointing |
| 3 | 4.6 | 2.7 | rostrally |
| 4 | 4.6 | 3.2 | |
| 5 | 4.6 | 3.7 | Site: close to |
| 6 | 4.6 | 4.2 | transverse sinus |
| 7 | 4.6 | 4.7 | (without inflicting |
| 8 | 4.6 | 5.2 | damage) |

**Table 2.2 MEC lesion sites.** AP, anteroposterior with respect to bregma; ML, mediolateral with respect to bregma; DV, dorsoventral with respect to the brain surface.

### 2.3.2. Microdrive implantation in mice

A total of eight animals were included in electrophysiological studies and each received a single microdrive implant into the left hippocampus, specifically the CA1 subregion. This surgical procedure was performed under isoflurane anaesthesia (an isoflurane (4%) / oxygen mix at a flow rate of 1.5–3 litres/min). Mice received a subcutaneous injection of Carprieve® (Caprofen) at the start of surgery at a dose of 5mg/kg for analgesic purposes, and Viscotears® Liquid Gel (carbomer) were applied to the eyes regularly throughout the surgery to prevent corneal damage. A heated water pad was used to maintain a constant body temperature and the animal's breathing was checked regularly throughout surgery. The mouse's head was shaved and fixed into a Kopf stereotaxic frame using ear bars. After cleaning the scalp with Betadine® a longitudinal midline incision was made running anterior to posterior to expose the skull. The skull was cleaned with hydrogen peroxide (3%) and saline to obtain a clear view of the anatomical landmarks (bregma and lambda) and enable levelling of the skull in the horizontal plane. Six 0.7mm diameter screw holes were drilled in the skull, one in the frontal bone for the ground screw, and four others in the frontal, parietal and occipital regions to provide anchor points to stabilise the microdrive. A craniotomy was then drilled over the left hemisphere to enable insertion of electrodes into the cortex overlying the CA1 subregion of the left hippocampus. The ground screw and stabilising screws were inserted using a jeweller's screwdriver until they just touched the surface of the dura and the microdrive was positioned using the stereotaxic frame so that the electrodes could be implanted 2.0mm posterior to bregma and 1.8mm to the

left of the midline. The dura was removed at the insertion site and the electrodes inserted vertically (no angular deviation) to a depth of 0.8mm. A metal sheath was then lowered around the electrodes to protect them and allow them to be moved further into the brain post-surgery. The craniotomy site was protected with a layer of sterile Vaseline® and then a layer of Superbond® applied to the skull and around the screws. Dental cement was applied to fix the microdrives to the skull and screws. All surgeries were performed under sterile conditions using aseptic techniques with instruments autoclaved prior to use. Following surgery mice were kept in a heated recovery chamber until they regained consciousness. Their post-operative weights were closely monitored, and they received a soft diet and 72 hours of oral analgesia in the form of metacam jelly (containing meloxicam at a dose of 5mg/kg).

## 2.4. Single unit and LFP recording

The DACQ USB recording system (Axona Ltd., St. Albans, UK) was used to acquire positional and single unit data. A *headstage* was connected to the omnetic connectors on the implanted microdrive and comprised an RC-coupled unity gain operational amplifier. This was connected to the recording system via lightweight cables suspended above the animal using elastic cords attached to the ceiling of the experimental room. The local field potential (LFP) recorded from each of the 32 channels of the microdrive were passed through the headstage and into the Axona 'DACQ USB' recording system (http://www.axona.com) which consists of a preamplifier and a system unit. Each channel was amplified 9000 to 20,000 times, bandpass filtered (360 – 7000Hz) and recorded differentially using a

channel on a separate tetrode as a reference. Spikes for which the amplitude exceeded a user-defined trigger threshold (selected individually for each tetrode but set at approximately 60-80µV) were recorded at 48kHz and time stamped with a 96kHz clock signal. In each mouse the channel which was the quietest, i.e., had the fewest and lowest amplitude individual units, was chosen to be low-pass filtered (< 500Hz) and was recorded continuously at 250Hz and 4.8KHz without referencing to another channel to provide a LFP trace. The same LFP channel was used for each mouse across each recording day. A single infra-red light-emitting diode (LED) was mounted on the headstage which was attached to the head of the mouse during recording. This LED was detected by a ceiling-mounted video camera positioned directly above the experimental enclosure. The image was digitized and sampled at a rate of 50Hz via the DACQ USB software enabling tracking of the animal's position. Head direction was inferred from the animal's trajectory.

## 2.5. Spike sorting

Spike sorting was performed offline. Collected spikes were assigned to putative clusters using KlustaKwik (454), a custom-designed program for unsupervised classification of multidimensional continuous data. KlustaKwik operates by fitting a Gaussian mixture model with unconstrained covariance matrices to sort spikes into clusters. Putative clusters were then manually analysed using the data analysis suite TINT (Axona Ltd, St Albans, UK) to correct for over-clustering and coordinate clusters across the different experimental trials. The parameters used to manually sort spikes were primarily the peak-to-trough amplitude and the shape of the recorded

waveforms across the four tetrode channels, in addition to temporal auto-correlation characteristics (*Figure 2.2*).
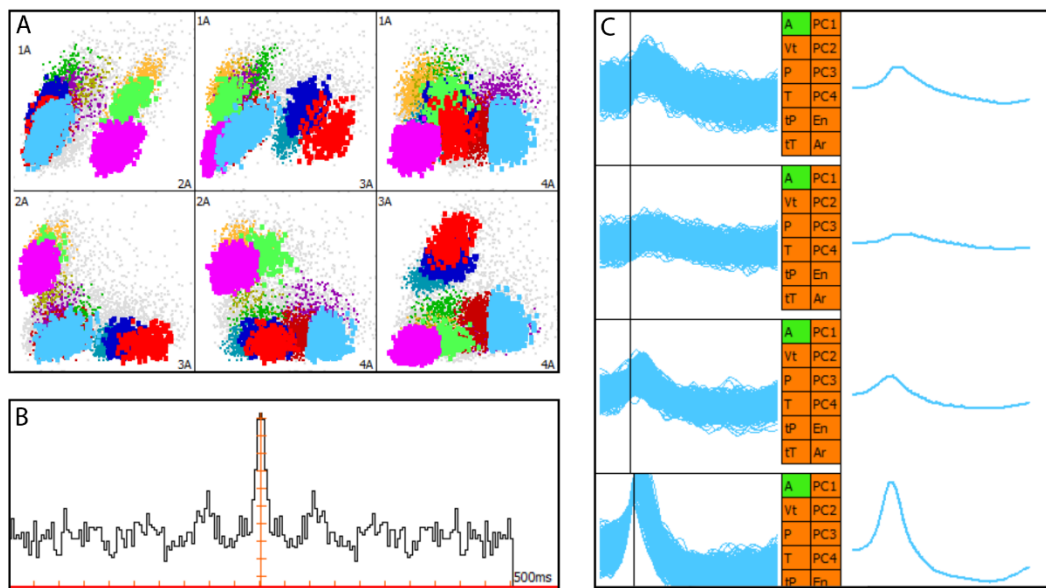


**Figure 2.2 Spike sorting using the TINT data analysis suite (Axona Ltd).** *A*. The peak-to-trough amplitude (µV) of each spike recorded on each channel is plotted against its amplitude on the other three channels of the tetrode. *B.* The temporal autocorrelogram for the blue cluster in A is shown. This histogram indicates the probability of encountering spikes with a time lag in the range -500 to + 500 ms. This cell shows peaks at approximately 10Hz indicating that it is theta modulated. **C.** The waveforms for the multiple spikes (action potentials) comprising the blue cluster in A. are shown in the left column, as recorded on each of the four channels of the tetrode. The mean waveform for each channel is shown in the right column.

Spike sorting was performed by an experimenter blinded to genotype. Once cells clusters had been assigned the experimenter was unblinded for subsequent analyses.

## 2.6. Histology

### 2.6.1. Tissue fixation and staining

Once data collection was complete animals were anaesthetised (4% isoflurane and 4L/min oxygen) and injected intra-peritoneally with an overdose of Euthatal® (sodium pentobarbital). Brain tissue was fixed via transcardial perfusion with saline and then a 4% paraformaldehyde solution

(PFA). Brains were removed and stored in PFA. This was replaced with a 4% PFA solution in phosphate buffered saline (PBS) with 20% sucrose 48 hours prior to sectioning.

In the Honeycomb Maze studies (*Chapter 3*) frozen brain tissue from rats with hippocampal lesions, or sham hippocampal lesions, was cut in horizontal sections of 40µm using a cryostat and mounted on gelatinized slides. In rats with MEC lesions or sham MEC lesions brains were embedded in gelatin prior to cutting 40µm sagittal sections using a cryostat. All sections were stained with cresyl violet acetate. In the electrophysiology study (*Chapter 4*) mouse brain tissue was cut in coronal sections of 40µm using a vibratome. Alternating sections were stained with cresyl violet acetate, and with Thioflavin S and DAPI. Thioflavin S/DAPI slides were stored in the fridge between 2 and 8°C. Images of the sections were acquired using the ZEISS Axio Scan.Z1 within 2 weeks of staining.

### 2.6.2. Lesion quantification *(Chapter 3)*

Hippocampal lesion volume was quantified by a blinded observer via manual tracing of the hippocampus on every fourth section using ImageJ (455). The remaining volume of hippocampal tissue in rats with lesions was expressed as a percentage in relation to the measured volume of a typical operated control rat with a sham hippocampal lesion. For presentation purposes the background was subtracted from each image and the contrast enhanced. Each image was processed using the same parameters.

### 2.3.3. Track identification *(Chapter 4)*

Each cresyl violet section was examined for evidence of a track formed by the tetrode bundle. The anteroposterior coordinates of the tetrode position

from bregma was estimated by comparing the coronal section where the tetrode track was visible with the coordinates in the Allen Brain atlas (456). The dorsoventral position of the tetrode tips on the day of recording was estimated by measuring the depth of the tetrode track and subtracting the distance the microdrive had been moved following the day of recording. This allowed an estimation of the layer in which the tetrode tips were located at the time of recording.

### 2.3.4. Quantification of Aβ pathology in APP$^{NL-G-F}$ mice

40μm coronal sections stained with Thioflavin S/DAPI were used to assess the presence of Aβ plaques in all mice, and to quantify fibrillar Aβ burden in the APP$^{NL-G-F}$ mice (*Figure 2.3*). Of note, Thioflavin S only stains fibrillar forms of Aβ and as such, oligomeric, soluble forms and pre-fibrillar diffuse Aβ plaques were not visualised or quantified by this staining. Image processing and analysis was performed using Image J (455). To quantify Aβ plaque burden, the left and right hippocampal formations were manually traced on ten evenly spaced coronal sections between approximately -1.65mm and -3.18mm posterior to bregma. Sections selection was guided by the Allen Brain atlas (456) to ensure comparable anteroposterior coordinates were used for each mouse, and DAPI stained sections were used to avoid being biased by the presence of Aβ plaques. The corresponding Thioflavin S images were then thresholded using an Otsu threshold to produce a binary image (the same method was used for all sections across all mice). Two regions of interest per section, corresponding to the left and right hippocampal formation as traced on the DAPI image, were transposed onto the corresponding thresholded Thioflavin S image,

and the plaque area and total hippocampal area measured. The total Aβ plaque burden was expressed as a percentage of the area of the left and right hippocampal formations and was calculated by taking a mean of the percentage coverage of the left hippocampal formation and the right hippocampal formation for each coronal section (i.e., a mean of twenty measurements).

## 2.7. Statistics

Across all studies data were tested for normality using Shapiro-Wilk and/or Kolmogorov-Smirnov testing. If data were not normally distributed then a non-parametric test was selected. If the assumption of sphericity was violated a Greenhouse-Geisser correction was performed. The specific statistical tests used are outlined in the methods sections of the respective data chapters (*Chapters 3 and 4*).
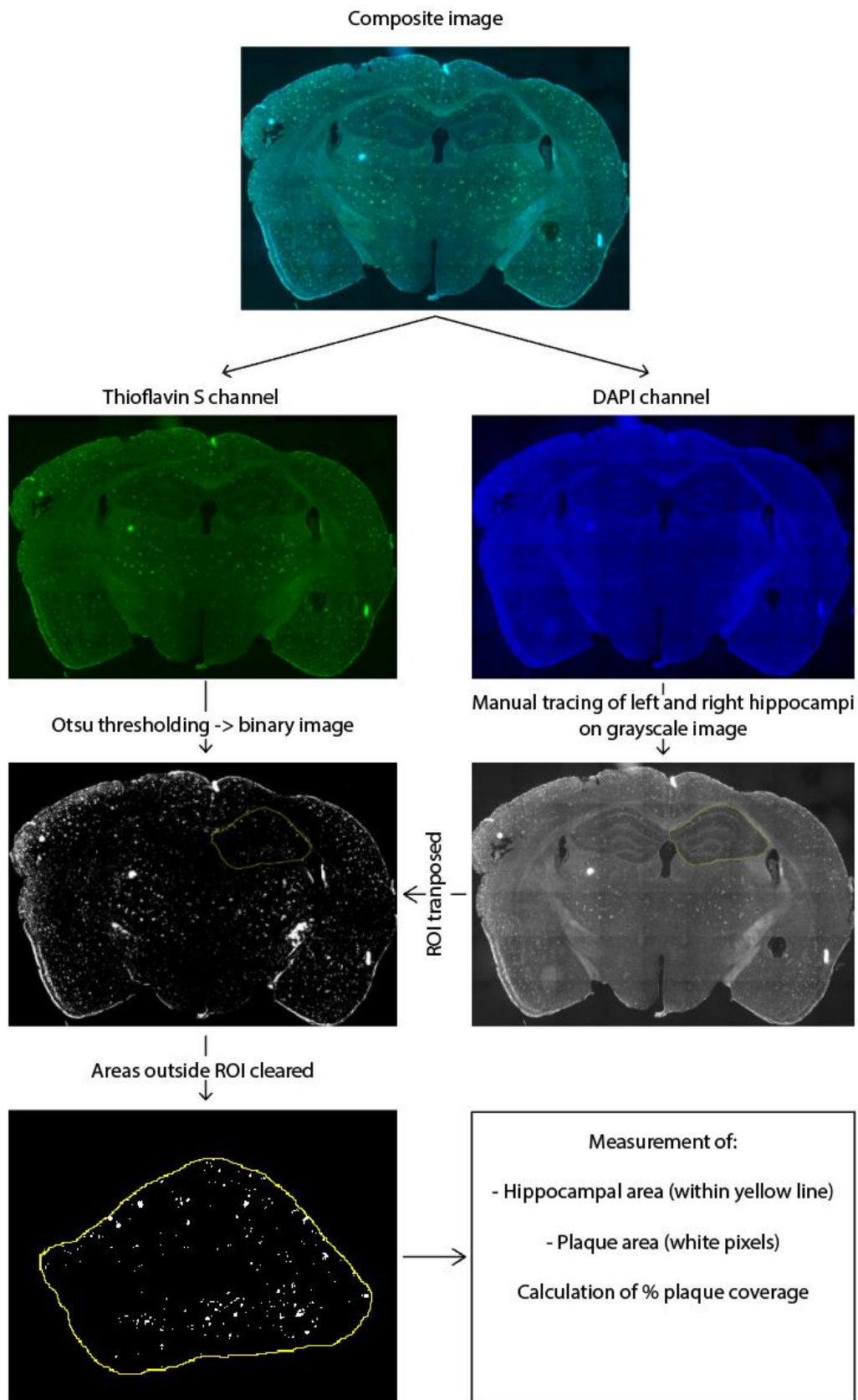
**Figure 2.3 Quantification of amyloid β plaque burden.** DAPI, 4′,6-diamidino-2-phenylindole); ROI, region of interest.

## 3. Honeycomb Maze Studies

### 3.1. Introduction

#### 3.1.1. Study rationale

Rodent models are indispensable tools for the study of Alzheimer's disease (AD), facilitating both investigation of AD pathogenesis and the testing of potential therapeutic strategies. The validity of a mouse model of disease is intrinsically linked to its ability to replicate signs of the disease, and cognitive decline in AD models is an important outcome measure in AD treatment trials. Other outcome measures include histopathological measures, such as $A\beta$ plaque burden, however, if a reduction in plaque burden is not accompanied by an improvement in or stabilisation of cognitive decline then arguably the treatment being trialled may be of limited clinical value when translated into human subjects. Cognitive tests available for use in mice can probe several memory domains, with spatial memory being the foremost choice due to the role of the hippocampal formation in spatial cognition and its vulnerability to AD pathology. As discussed in Chapter 1, spatial memory, particularly allocentric spatial memory, is affected early in AD. A test of allocentric spatial memory, which is sensitive to hippocampal impairment, and produces a parametric output which can track disease progression in mouse models of AD, would therefore be a valuable research tool. Ideally such a test would also offer the opportunity to create an analogous task in humans, allowing comparison of results across species.

Current tests of spatial memory in rodents have been reviewed in the introductory chapter (*see page 66*). Except for the Morris Water Maze, these tests share a common limitation in that they do not force the animal to use

a single identifiable spatial strategy. In addition, none of the tasks can be scaled in difficulty which may limit their utility in tracking progressive hippocampal impairment. The Morris Water Maze is the test which is most commonly used to assess allocentric spatial memory and has been used to validate a number of AD mouse models (4, 219, 222), however, despite being the gold standard test for spatial navigation, it has limitations. *Richard Morris* himself stated that the Morris water maze "abandon(s) the necessity for choice-point decisions by forcing the spatial localization system of the animal to guide him to the exact location of the goal" (457). This could be considered an advantage, for example, this type of task may closer replicate the navigational behaviour of an animal in the wild, in contrast to the artificial presentation of choices often used in other maze tasks. However, a problem arising is that during free navigation in the Morris Water Maze the lack of independence of the animal's heading direction at each instant means the animal is not making a series of discrete independent choices at each location, and therefore this task does not test the animal's knowledge of the goal location from all locations along its chosen path. The lack of a limited number of discrete, independent choices also means performance is difficult to score. Standard methods include calculating the total distance travelled by the animal between the starting position and goal, or measuring the time taken for the animal to locate the goal. However, when using these scoring measures it is challenging to ascertain what level of performance corresponds with chance, so instead surrogate measures such as performance of the animal when navigating to a visible goal or to a random goal location are used (179). An additional issue is the aversive nature of

water to rodents which can make the task stressful; some never swim but simply float, generating no useful data.

Finally, recording hippocampal cellular activity during a spatial navigation task would be a powerful research tool providing a means of directly correlating the activity of single neurons with spatial behaviour in AD mouse models. Such data could potentially provide an explanation for the allocentric spatial memory impairment observed in AD. The Morris Water Maze is not a favourable environment to undertake concomitant electrophysiology for two reasons. First, recording cellular activity in an aqueous environment is challenging, although there are examples where this has been successfully achieved (458, 459). In both instances, however, considerable modification of standard techniques was required. Second, to fully characterise the spatial properties of cells such as place cells and head direction cells, the animal needs to sample the entire recording environment in a relatively homogenous fashion. Achieving full coverage of the environment is challenging in the water maze since the animal rapidly learns the location of the hidden goal and develops a preference for this location and a preferred heading direction. Areas of the environment not situated on the direct path between the starting locations and the goal are therefore rarely visited. This uneven sampling of the environment prohibits correlation of single cell activity and spatial behaviour on a trial-by-trial basis.

The Honeycomb Maze is a new behavioural apparatus specifically designed by *John O'Keefe* to study spatial cognition in rodents and overcome the limitations of the spatial memory tasks discussed above. In particular, the Honeycomb Maze was intended to enable testing of spatial memory in rodents while constraining them to a single navigational strategy. Its flexible

design is intended to permit scaling of task difficultly and allows egocentric or allocentric spatial memory paradigms to be run using the same apparatus. The maze itself requires animals to make a series of independent navigational choices to reach an unmarked goal location. This results in a parametric behavioural output which is potentially useful for tracking progressive spatial memory impairment as is seen in several animal models of neurodegenerative disease.

This chapter describes experiments undertaken to validate the Honeycomb Maze as a novel behavioural test of spatial memory, and to assess its potential for application as a test in rodent models of AD.

### 3.1.2. Objectives

The main objectives of this study were as follows:

1. To test task feasibility and ensure that 'normal' control rats and mice were able to successfully learn the Honeycomb Maze task

2. To establish which parameters within the testing paradigm influenced performance on the maze and could therefore be used to scale task difficulty

3. To determine the extent to which the hippocampus and/or EC contributed to performance on the Honeycomb Maze
(Since these are the regions most vulnerable to AD pathology, behavioural tests which are sensitive to damage in these brain areas will be particularly useful in studies of AD.)

These objectives were addressed in four experiments which tested different cohorts of animals on the Honeycomb Maze:

Experiment 1: Control rats (Objectives 1 and 2)

Experiment 2: Hippocampal lesioned rats (Objective 3)

Experiment 3: Entorhinal lesioned rats (Objective 3)

Experiment 4: Wild-type mice (Objective 1)

### 3.1.3. Hypotheses

1. Wild-type rats and mice will learn the location of an unmarked goal on the Honeycomb Maze.

We predicted that wild-type (WT) rats would learn the goal location on the Honeycomb Maze task based on its similarity to the Morris water maze which rats learn rapidly (219). In addition, pilot studies on the Honeycomb Maze had indicated that rats could safely move between the maze platforms. We also predicted that WT mice should be able to learn the goal location on the Honeycomb Maze provided modifications were made to account for species differences, such as their reduced weight and increased propensity to startle.

2. The difficulty of choices in the Honeycomb maze task can be scaled by altering maze parameters.

We predicted that task difficulty on the Honeycomb maze could be scaled by altering the parameters of the choices the animal was required to make to reach the goal. Early work examining the performance of rats in maze environments identified two factors which contribute to successful navigation: the 'goal-gradient' factor (460) and the 'goal-orientation' factor (461) (*see discussion for more detail, page 170*). These two factors

predicted that performance on the Honeycomb Maze would improve for navigational choices where the animal was located closer to the goal, and where one of the choice options offered oriented him more directly towards the goal. We also predicted that when making a navigational choice on the maze, an increased separation between the two options offered would make the choice easier for the animal, whereas offering two choices which were very similar in terms of their orientation to the goal would be more challenging.

## 3. Hippocampal and medial entorhinal lesions will impair performance on the Honeycomb maze.

We predicted that rats with bilateral hippocampal lesions would show an impaired performance on an allocentric spatial memory task on the Honeycomb Maze. The task which bears the most resemblance to the Honeycomb Maze is the Morris water maze which also relies on the animal using an allocentric strategy to navigate to the goal. Rats with chemical and electrolytic lesions of the hippocampus have been shown to have impaired place navigation on the water maze (4, 462).

As the main source of afferents to the hippocampus, the MEC is a key component of the brains navigational network. Lesion studies investigating the effect of EC damage on performance in the Morris water maze have shown that these animals have an impaired performance, but that this impairment is less robust than is seen in animals with hippocampal lesions (463-465).

## 3.2. Method

### 3.2.1. Description of the maze apparatus

#### 3.2.1.1. Honeycomb Maze 1.0

The Honeycomb Maze consists of 37 hexagonal platforms which tessellate in a larger hexagonal configuration (*Figure 3.1A*). Each platform is mounted on a pneumatic tube, allowing it to be raised and lowered independently of the other platforms (*Figure 3.1B*, *Figure 3.2*). This enables the maze to have a variety of configurations and this flexibility allows the apparatus to be used to conduct different behavioural paradigms.

Each individual hexagonal platform measures 11.5cm along each side and consists of three layers, the bottom of which contains six microswitches which detect the presence of the animal on the platform. The platforms are arranged with 1cm gaps between them, and the total maze diameter is 145.5cm. When raised each platform sits 81.5cm above the base of the maze, and 49cm above the base when in a lowered position. Each platform has a cylindrical plastic skirting underneath, around the top of the pneumatic tubes, to protect the wires and tubes which lie underneath the platforms.

A B
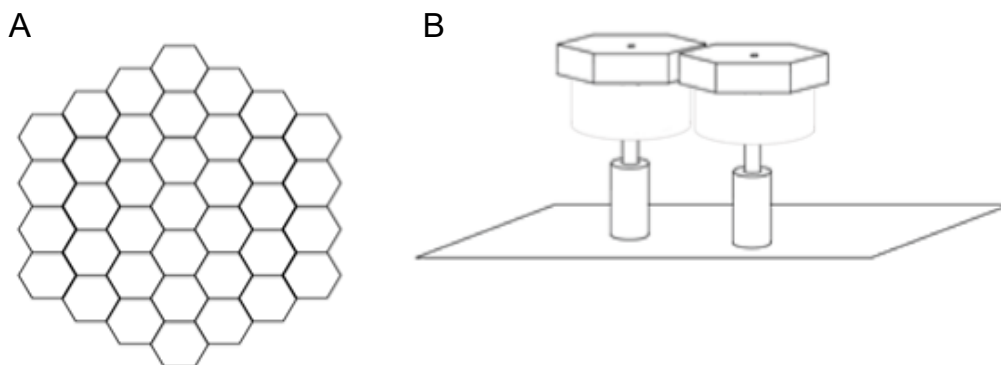


**Figure 3.1 Schematic of Honeycomb Maze components**. *A.* Aerial view of the Honeycomb Maze showing the overall hexagonal configuration of the 37 tessellating platforms. *B.* Two hexagonal maze platforms sitting atop pneumatic tubes with cylindrical skirting underneath protecting the wires and tubes beneath the platforms.
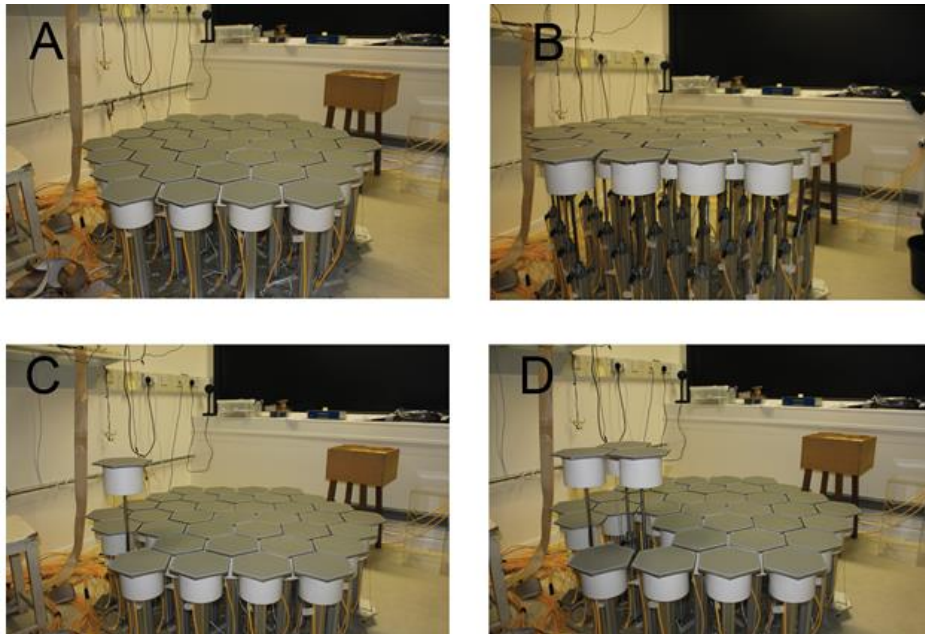
**Figure 3.2 The Honeycomb Maze Apparatus.** The Honeycomb Maze with no (**A**), all (**B**), one (**C**) and three (**D**) platforms raised.

The maze itself is situated in a standard behavioural laboratory with abundant extra-maze cues which can be used by the animal for navigation (*Figure 3.3*). Platforms are raised and lowered using custom-made software written in Labview®. The programme monitors the platform switches so that platforms can be raised and lowered based on the animal's location. Only platforms which are not occupied are moved.
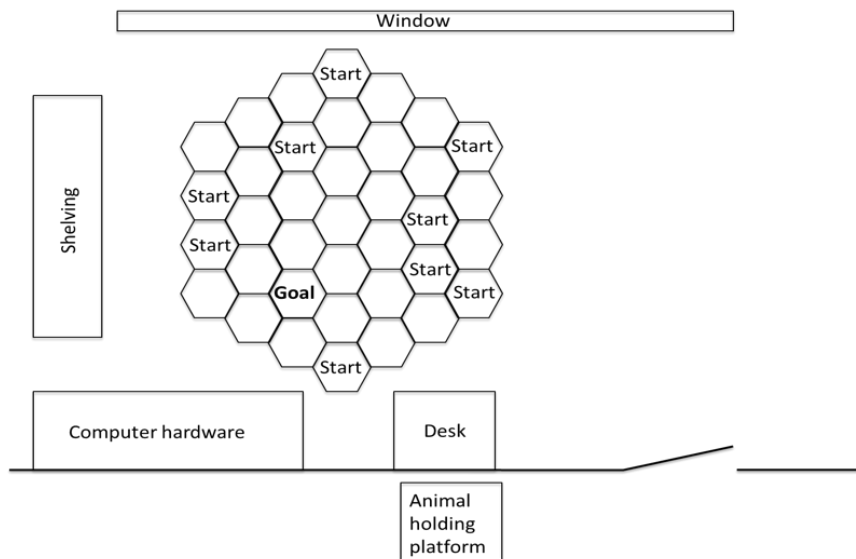


**Figure 3.3 Honeycomb Maze experimental set-up.** The Honeycomb Maze was situated in a lab with shelving, computer hardware, a blacked-out window, and a desk, along with other standard laboratory items, which all acted as extra-maze cues during experiments.

### 3.2.1.2. Honeycomb Maze 2.0

A newer version of the Honeycomb Maze was developed to enable testing of mice as well as rats (466). The key changes which permitted this were the substitution of pneumatic tubes with linear actuators, which reduces the noise associated with raising and lowering platforms, and the use of load cells (RobotShop, cat. # RB-Phi-117) rather than microswitches, to detect the presence of an animal on each platform. The signal from these load cells is amplified using a custom-made circuit and is sensitive enough to detect the presence of a 25 - 30-gram mouse.

As with the original version, Honeycomb Maze 2.0 consists of tessellated hexagonal platforms, each measuring 11.5cm along a side, in an overall hexagonal configuration, however, the newer version has 61 platforms, rather than 37, and is therefore much larger with a diameter of approximately 200cm.

### 3.2.2. Spatial navigation paradigm

In the experiments presented in this chapter a spatial navigation paradigm was used on the Honeycomb Mazes. In this paradigm the animal's objective is to locate, and navigate to, an unmarked goal platform (*Figure 3.4*, black hexagon) where, after a short delay, he receives a food reward. To do this the animal must make a series of binary choices, at each point in the maze choosing between two platforms adjacent to the platform he is currently occupying. The correct choice is the platform which provides the most direct path to the goal i.e., the choice which provides the smallest angular deviation from the goal direction. The animal continues to be offered pairs of platforms to choose between until the goal is reached. To ensure the

animal must use a place learning strategy, and approaches the goal from different directions, several different start platforms are used.
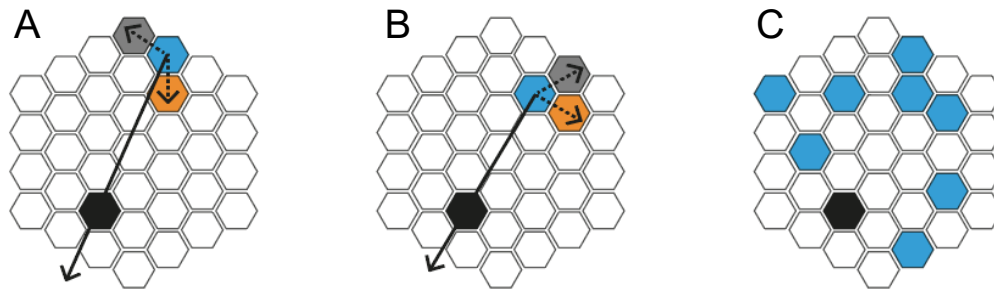


**Figure 3.4 Navigation on the Honeycomb Maze.** ***A***: At any given starting location (blue) two choices are offered: the correct choice (orange) possesses a smaller angle with respect to the goal heading direction (black) than the incorrect choice (grey). ***B***: The previously chosen platform becomes the new 'occupied' platform (blue), and two further platforms are presented as choices. ***C***: Illustration of eight potential starting platforms (blue).

### 3.2.3. Choice parameters on the Honeycomb Maze

Each choice in the navigation paradigm described above can be characterised by several parameters (*Figure 3.5*):

- The <u>distance</u> of the choice from the goal: this is the distance of the occupied platform from the goal in terms of the number of platforms (1–5) to be traversed on the direct route to the goal.

- The angle between the goal heading direction and the best choice (<u>angle α</u>). This could vary between 0° and 135°. The smaller angle α the more direct the route to the goal. In some instances, the correct choice may take the animal further away from the goal (i.e., angle α > 90°) and the animal must choose the 'least bad' platform.

- The angle between the correct and the incorrect choice (<u>angle β</u>). Choice platforms may be adjacent to one another (angle β = 60°) or separated by one (angle β = 120°) or two (angle β = 180°) platforms.

- The angle between the goal direction and the incorrect choice (<u>angle γ</u>).
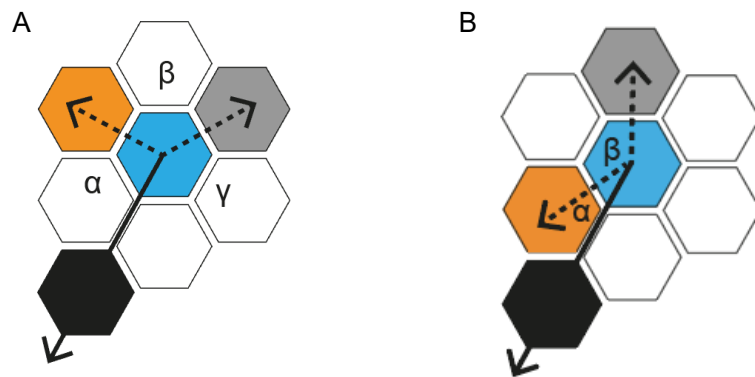


**Figure 3.5 Angles of the Honeycomb Maze.** Each choice can be described by three angles. The occupied platform is shown in blue and the goal in black. The animal must choose between the correct orange platform and the incorrect grey platform. The goal heading direction is indicated by the solid black arrow whereas the paths to the choice platforms are represented by the dashed arrows. Angle α is the angle between the goal heading direction and the correct choice, angle β is the angle between the correct and incorrect choices, and angle γ is the angle between the goal direction and the incorrect choice. ***A&B:*** The relationship between angles α, β and γ is not fixed. In ***A*** angle γ = 360° - (angle α + angle β), whereas in ***B*** angle γ = angle α + angle β.

### 3.2.4. Behavioural testing on the Honeycomb Maze

#### *3.2.4.1. Rats on Honeycomb Maze 1.0 (Experiments 1 - 3)*

Control rats were tested on the Honeycomb Maze in experiment 1, and hippocampal and MEC lesioned rats in experiments 2 and 3. In the lesion experiments the experimenter was blinded to lesion status. Rats receiving surgical interventions were given at least one week of recovery and free access to food before commencing behavioural testing. All rats were food-restricted to reduce their weight to 90% of their free-feeding weight before training. They were habituated to the sounds made by the maze platforms being raised and lowered while sitting on a holding platform in an antechamber adjacent to the maze room a week prior to testing. There was no period of maze exploration before training on the task began. At the beginning of each trial, the rat was placed on a start platform and after a

delay of four seconds, two of the six adjacent platforms were raised. When the rat chose one of these two platforms, the previously occupied and non-chosen platforms were lowered and after an interval of four seconds, two new platforms were raised. This process was fully automated. If the rat did not make a choice within one minute, he was gently guided onto a platform, which was alternately chosen as correct or incorrect. The choice was then scored as incorrect and the next choice in the sequence initiated. If the rat had not reached the goal within five minutes the trial was terminated, and the rat guided to the goal platform by the experimenter and given a food reward. The trial ended when the rat reached the goal, or after five minutes had elapsed. Upon reaching the goal, rats were given one Cheerio after a delay of approximately five seconds. Rats completed between 4 and 6 trials per day with an intertrial interval of 5 - 15 minutes. Between trials the rats rested on a holding platform with their littermates and the maze was cleaned with 70% ethanol to eliminate odour cues.

### 3.2.4.2. Mice on Honeycomb Maze 2.0 (Experiment 4)

Testing of mice using Honeycomb Maze 2.0 was very similar to the procedure used on the original Honeycomb Maze. Mice were put on a calorie restricted diet to reduce their weights to 85-90% of their free-feeding weights. In contrast to the experiments on Honeycomb Maze 1.0, one group of mice received training on the maze prior to testing (*see page 148*). At the beginning of each trial the mouse was placed onto a raised start platform and the trial was initiated by the experimenter. The choices made by the mouse were recorded once the mouse had triggered the load-cell system on a choice platform continuously for 5 seconds. Once a choice had been

made the other two platforms were lowered, and after a delay of 4 - 10 seconds further choice platforms were presented. If the mouse had not made a choice within 30 seconds the occupied platform was programmed to 'flutter' gently up and down to encourage the mouse to move. Once the mouse reached the goal platform it was rewarded with chocolate flavoured chow pellets. Between trials mice rested with their cage mates in a box containing bedding from their home cage. Every 4 trials the maze was wiped down with 70% ethanol.

### 3.2.5. Testing schedules on the Honeycomb Mazes

The design of the Honeycomb Maze permits many different spatial navigation schedules to be run using the same apparatus, from those most sensitive to hippocampal function to those least so (*Figure 3.6*). At the most sensitive end of the spectrum are schedules in which no trial sequence is ever repeated (for example testing schedule C*, page 148*), which prevents the animal from solving the task using non-hippocampal strategies. At the other end of the spectrum are fixed schedules, for example, always starting the animal from the same platform and offering the same sequence of choices, which could be solved using a stimulus-response or egocentric strategy.

### *3.2.5.1. Testing schedules on Honeycomb Maze 1.0*

Testing schedules were designed to incorporate several criteria. First, for each choice, the rat was never offered a platform it had just occupied to eliminate the strategy of avoiding the platform that had just been occupied. Second, to prevent the task being solved using an egocentric strategy, correct choices were selected so that there was an approximately equal

number that required the rat to turn left (or anticlockwise), when facing the goal, as there were right (or clockwise). Third, the starting platform changed between trials and the potential start platforms were distributed approximately equally around the maze. In order to meet these criteria, it was occasionally necessary to include some 'forced choices' in the testing schedules, where the rat was only offered one choice platform. Testing schedules A and B were used to test rats on Honeycomb Maze 1.0.
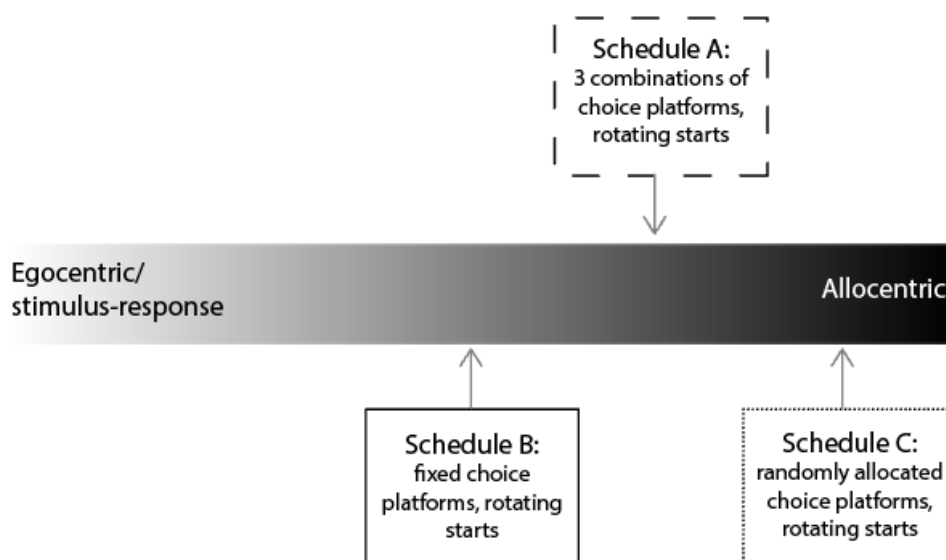


**Figure 3.6 Testing schedules on the Honeycomb Maze.** Different testing schedules may require different navigational strategies. All the schedules used in these experiments were designed to lie towards the 'allocentric' end of the spectrum since they use rotating start platforms and thus require a place learning strategy.

### 3.2.5.1.1. Testing schedule A

This testing schedule lies at an intermediate point along the schedule spectrum (*Figure 3.6*) and was specifically designed to investigate the effect of the three maze parameters (angle α, angle β and distance) on task performance. In this schedule, rats undertook three different types of trial, which we named *Angleβ_60*, *Angleβ_120* and *Angleβ_180*. In each trial angle β was fixed at either 60° (Angleβ_60), 120° (Angleβ_120) or 180° (Angleβ_180) degrees. The values of angle α were selected to ensure that for any given distance from the goal there were a range of values of angle

α for each choice. This maximized the number of choices with unique combinations of distance, angle α and angle β, which enabled the collection of a dataset with 50 such unique combinations. Rats were tested in groups of three. Each rat completed six trials per day, which consisted of two trials of each type, for twelve days. In the testing schedule, trial type was staggered to control for the effect of experience on performance. Start platforms were also rotated among eight different locations and the combinations of start platforms and trial type were counterbalanced. This testing schedule is illustrated in *Figure 3.7A*.
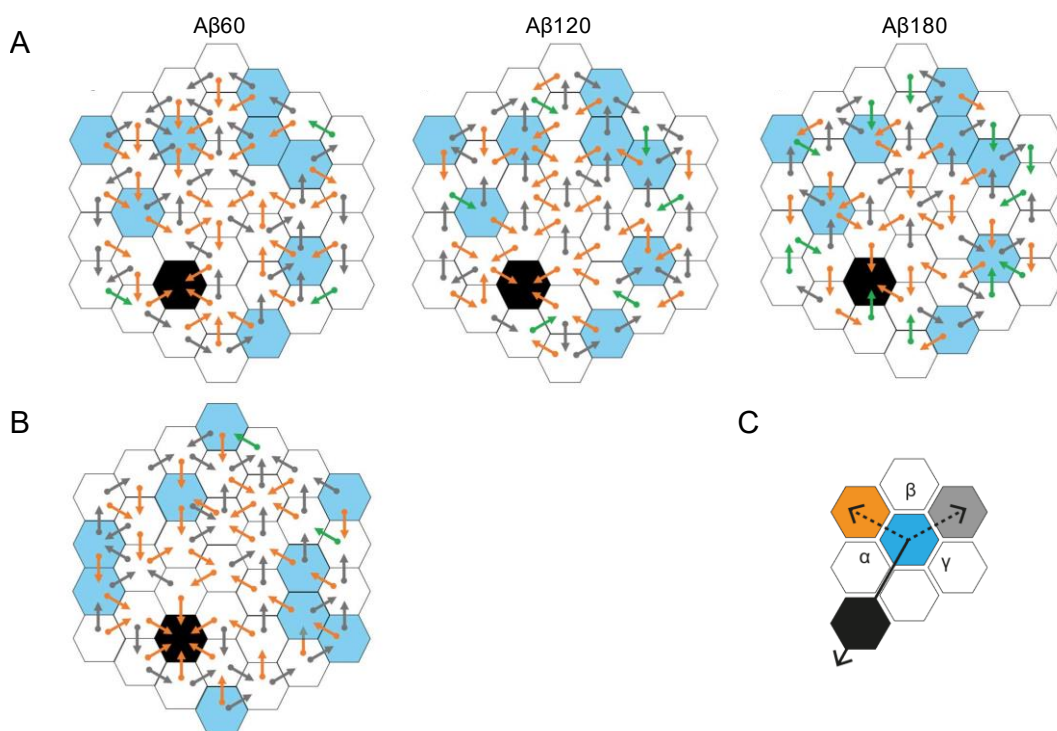


**Figure 3.7 Testing schedules on Honeycomb Maze 1.0.** *A&B*: Schedules A and B are illustrated. The goal platform is shown in black and start platforms are blue. The orange vectors show correct choices, and the grey vectors show incorrect choices. Forced choices, where the animal was only offered one platform, are indicated by green vectors. *A*: Schedule A consists of three trial types, 'Aβ60', 'Aβ120' and 'Aβ180', where the value of angle β is fixed at 60°, 120° and 180° respectively. A reminder of the maze angles is included (*C*). *B*: Schedule B consists of only one trial type where all values of angle β are used within the same trial.

*3.2.5.2.2. Testing schedule B*

Testing schedule B is a protocol designed to investigate whether there is a correlation between lesion size and task performance. At each location on

the maze the two choice platforms offered was constant (*Figure 3.7B*). Choice platforms were selected so that across the testing schedule there were choices with a combination of values of angle α and β. Nine different start platforms were used and rotated between trials. Rats tested on this protocol completed four trials a day over 17 days. They were then tested for a further ten days with a new goal location.

### 3.2.5.3. Testing schedule on Honeycomb Maze 2.0

*3.2.5.3.1. Testing schedule C*

Testing schedule C, which was developed as part of a separate study, was used to undertake pilot testing of WT mice on the newer version of the Honeycomb Maze. In this schedule the choice platforms offered to the mouse were pseudo-randomly selected by custom-written software with two stipulations. First, the mouse was always offered at least one platform which took her closer to the goal, and second, platforms which had not yet been visited were offered first, provided this did not violate the first stipulation. Under this testing schedule the mouse could be offered two platforms which took her equivalent distances from the goal. In these cases the choice was not scored. The start positions used in this testing schedule were rotated between trials and are illustrated in *Figure 3.8*. Mice completed six trials per day.

### 3.2.5. Cohorts tested on the Honeycomb Maze

As outlined in the introduction to this chapter, four experiments were conducted on the Honeycomb Maze.
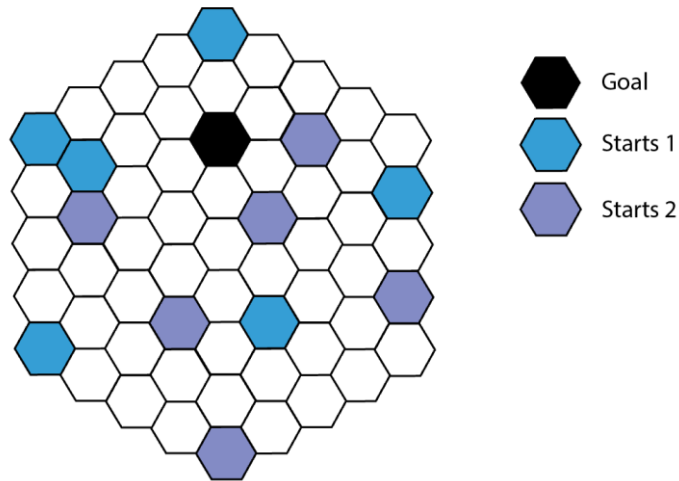
**Figure 3.8 Start platforms used in testing schedule C.** The goal location (black) and start platforms (blue) are indicated for testing schedule C which was used to test wild-type mice on Honeycomb Maze 2.0. Starting platforms were changed on alternate testing days between 'starts 1' and 'starts 2'.

### 3.2.5.1. Cohorts tested on Honeycomb Maze 1.0

Data for the first three experiments came from testing five cohorts of male rats aged between 12 and 16 weeks on the original Honeycomb Maze (*Figure 3.9*). Experiment 1, which investigated the factors affecting the performance of control rats on the Honeycomb Maze, used data from nine unoperated WT rats (cohort 1), and sixteen rats with sham hippocampal or entorhinal lesions (cohorts 3 and 5). Experiment 2, which examined the effect of hippocampal lesions on task performance, randomly assigned rats to an intervention group, which received hippocampal lesions (cohort 2, n = 8), or a control group, which received sham lesions (cohort 3, n = 8). Randomization was stratified to ensure that littermates were equally distributed between groups. Experiment 3, examining at the effects of MEC lesions on performance, assigned rats into two groups using the same method. In one group eight rats received lesions of the MEC (cohort 4), and in the other, eight had sham lesions (cohort 5). Cohort 1 was tested using

testing schedule A, and cohorts 2 – 5 were tested using testing schedule B (*Figure 3.9*).
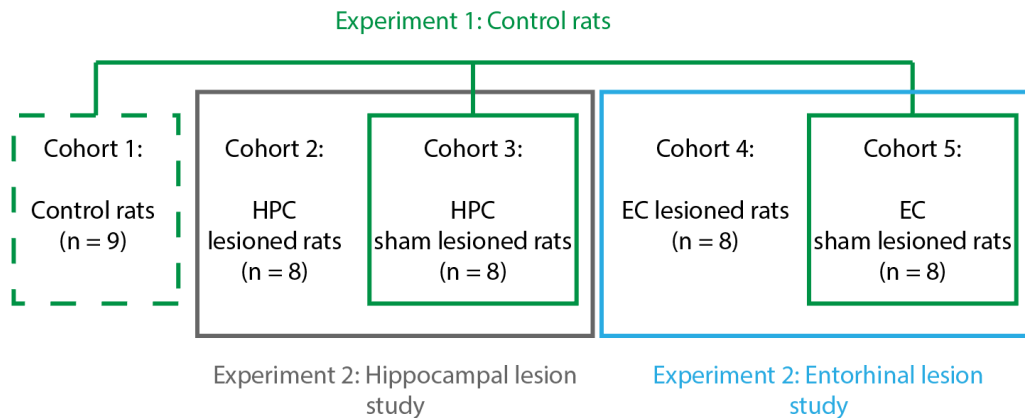


**Figure 3.9 Honeycomb Maze 1.0 cohorts.** An illustration of the cohorts of rats tested on Honeycomb Maze 1.0. Solid boxes indicate that rats were tested using testing schedule B, whereas the dotted box indicates rats that were tested using testing schedule A. As is indicated, data from cohorts 3 and 5 were used in two studies.

### 3.2.5.2. Cohorts tested on Honeycomb Maze 2.0

Data for the final experiment were collected from eight mice, four females and four males, aged between 16 and 24 weeks at the time of testing. These mice were tested on the newer version of the Honeycomb Maze using testing schedule C. Mice were run in two groups. Group 1 comprised the four female mice, and group 2 the four male mice. Group 1 mice were trained for three days prior to testing on an 'easy' version of the testing schedule. They were each given six trials a day where the start platforms were located relatively close to the goal, and the choice platforms offered both took them closer to the goal location. Following training, group 1 completed six trials per day for eight days. Group 2 received no prior training and completed six trials per day for twelve days.

For additional details about the animals used in these experiments, including housing and surgeries, please see Chapter 2 (*page 120*).

### 3.2.6. Scoring the trials and statistics

Choices were scored as correct if the animal selected the platform which provided the most direct path to the goal within one minute. Otherwise, a choice was scored as incorrect. 'Forced choices' where the animal was only offered one platform, or choices where both platforms were equal distances from the goal, were not included in the trial scores. The score for each trial was expressed as a percentage of correct choices. The daily score for each animal was a mean of their scores across all completed trials that day. The daily score for each cohort was a mean of the daily score for all animals in the cohort.

Differences in learning curves between the different groups (experiment 1: cohort 1 vs 3 vs 5; experiment 2: cohort 2 vs 3; experiment 3: cohort 4 vs 5) were assessed using a two-way mixed ANOVA. If day-by-lesion interactions are not reported they were non-significant. In experiment 1, a two-way repeated measures ANOVA was used to compare the performance of cohort 1 on trials with different values of angle $\beta$, with post hoc Bonferroni testing for pairwise comparisons. A two-way repeated measures ANOVA was also used to test for an interaction between angle $\alpha$ ('ahead' choices versus 'behind' choices) and distance, in trials in which choices consisted of adjacent platforms (i.e., Angle$\beta$_60 trials). One-way repeated measures ANOVAs were used to test for a relationship between performance and distance, and performance and angle $\alpha$, in cohort 1. Performance on 'ahead' choices (angle $\alpha < 90°$) versus 'behind' choices (angle $\alpha > 90°$) was compared using a paired t-test, and a one-sample t-test was used to determine whether performance on 'behind' choices was significantly better than chance. A multiple regression analysis was conducted to evaluate the

contributions of the three maze factors (angle α, angle β and distance) to performance in the cohort 1.

In experiments 2 and 3, two-way mixed ANOVAs were used to ascertain the effect of each maze variable (angle α, angle β and distance) on performance, and their potential interaction with lesion status. A Spearman correlation was used to correlate hippocampal lesion extent with performance. Differences in latencies between rats with hippocampal lesions and control rats over time were tested using a two-way mixed ANOVA, and a two-way mixed ANOVA was used to investigate the relationship between latencies, whether a choice was correct or incorrect, and lesion status.

In experiment 4 one sample t-tests were used to compare WT performance against chance. In situations where multiple t-tests were performed an FDR correction for multiple comparisons was made and q values presented. When comparing the performance across weeks, either a paired t-test (group 1) or a one-way repeated measures ANOVA (group 2) was used.

For all statistical tests, data were tested to ensure they met the necessary assumptions before proceeding to analysis. Shapiro-Wilk testing was used to assess normality, Levene's test to assess homogeneity of variances, and a Greenhouse-Geisser correction applied if the assumption of sphericity was violated. Tests were performed using SPSS and GraphPad (Prism).

## 3.3. Results

### 3.3.1. Experiment 1: Control rats on the Honeycomb Maze

In this study nine unoperated control rats (cohort 1) were tested on the Honeycomb Maze using testing schedule A. These rats completed three

trials per day on the first two days and six trials per day for the next eleven days (72 trials in total). Sixteen sham-lesioned control rats (cohorts 3 and 5) were tested using testing schedule B and completed four trials per day for seventeen days (68 trials in total). Across all cohorts the number of choices per trial varied between 2 and 37 according to the rat's success rate, with a median of 5 choices per trial. Testing schedule A, used for cohort 1, was a spatial navigation protocol specifically designed to minimize the interaction between the maze parameters being studied (distance, angle α and angle β) so that the effect of each could be examined. Testing schedule B, used for cohorts 3 and 5, was a modified spatial navigation protocol and was used to assess whether these groups could successfully complete the task, and also allowed them to act as controls for experiment 2.

### 3.3.1.1. All three control cohorts rapidly learnt the location of the goal

All three cohorts of control rats were able to learn the location of the goal platform rapidly, and despite slight variations in spatial navigation protocols (testing schedule A versus testing schedule B) there was no statistical difference between the learning curves of the three groups ($F_{2,22} < 0.001$, $p > 0.999$, two-way mixed ANOVA). After 28 trials all rats achieved a mean score of greater than 90% correct choices over four consecutive trials (*Figure 3.10A, page 156*).

### 3.3.1.2. Three maze parameters significantly influenced performance

The effect of three maze parameters, distance-to-goal, angle α and angle β, on performance on the Honeycomb Maze was investigated in cohort 1 (the unoperated controls). Performance declined with increasing distance of choice from goal ($F_{3,24} = 3.707$, $p = 0.025$, one-way repeated measures

ANOVA). The percentage of correct choices ranged from 88.4 ± 1.0% (mean ± s.e.m.) when platforms were adjacent to the goal, to 71.8 ± 6.1% when platforms were five platforms away from the goal (*Figure 3.10B, page 156*).

Performance improved when the correct choice was aligned more closely with the goal direction, i.e., when angle α was smaller ($F_{4,32} = 20.670$, $p < 0.001$, one-way repeated measures ANOVA). The percentage of correct choices ranged from 86.2 ± 1.3% for angles of 0–29°, to 61.1 ± 3.1% for angles greater than or equal to 90° (*Figure 3.10C, page 156*). Rats performed significantly better when the direction of the correct platform was less than 90° from that of the goal (*Figure 3.10C, inset, page 156*). Even when the correct choice was 90° or greater from the goal direction, all rats performed with rates of success above those that would be achieved by chance ($t_8 = 3.156$, $p = 0.013$, one sample t-test).

The rats performed best when choice platforms were separated by two others (angle β = 180°, 92.8 ± 1.1% (mean ± s.e.m.) correct choices) and their performance deteriorated when only one (angle β = 120°, 86.9 ± 1.2%) or no platform separated them (angle β = 60°, 85.8 ± 1.4%) (*Figure 3.10D, page 156*). There was a significant effect of both angle β and experience (day of testing) on performance, but there was no interaction between these (performance versus angle β: $F_{2,16} = 8.850$, $p = 0.003$; performance versus day of testing: $F_{11,88} = 11.361$, $p < 0.001$; angle β × testing day: $F_{22,176} = 1.438$, $p = 0.102$; two-way repeated measures ANOVAs). The differences between two-platform separations (angle β = 180°) and the rest (angle β = 120° or 60°) were significant (*Figure 3.10 D, inset, page 156*).

A multiple regression analysis was undertaken to establish the contributions of angle α, angle β and distance-to-goal to maze performance. This indicated that angle α, angle β and distance-to-goal were all significant predictors of performance and between them predicted 5.5% of the variance ($R_2$ = 0.055, $F_{3,391}$ = 7.608, p < 0.001). A large proportion of the remaining variance in performance is accounted for by experience (*Figure 3.10E*). Finally, there was evidence of an interaction between the effects of angle α and the distance-to-goal when choice platforms were adjacent to one another, i.e. when angle β was 60° ($F_{3,24}$ = 9.133, p < 0.001, two-way repeated measures ANOVA); at a distance of one platform from the goal the difference in mean scores between 'ahead' (angle α < 90°) and 'behind' (angle α > 90°) choices was 38.4%, whereas at four platforms distant there was virtually no difference between 'ahead' and 'behind' choices (1.2%). The angle-to-goal effect was seen to decrease as a function of the distance from the goal, such that performance improved with larger angles at greater distances (*Figure 3.10F, page 156*).

### 3.3.2. Experiment 2: Hippocampal lesioned rats on the Honeycomb Maze

In this experiment the performance of eight rats with bilateral hippocampal lesions (cohort 2) was compared with that of eight control rats with sham hippocampal lesions (cohort 3). Both groups were tested using testing schedule B, completing four trials per day.

#### *3.3.2.1. Rats with hippocampal lesions were deficient in learning the Honeycomb Maze task.*

Rats with hippocampal lesions were significantly deficient in learning the
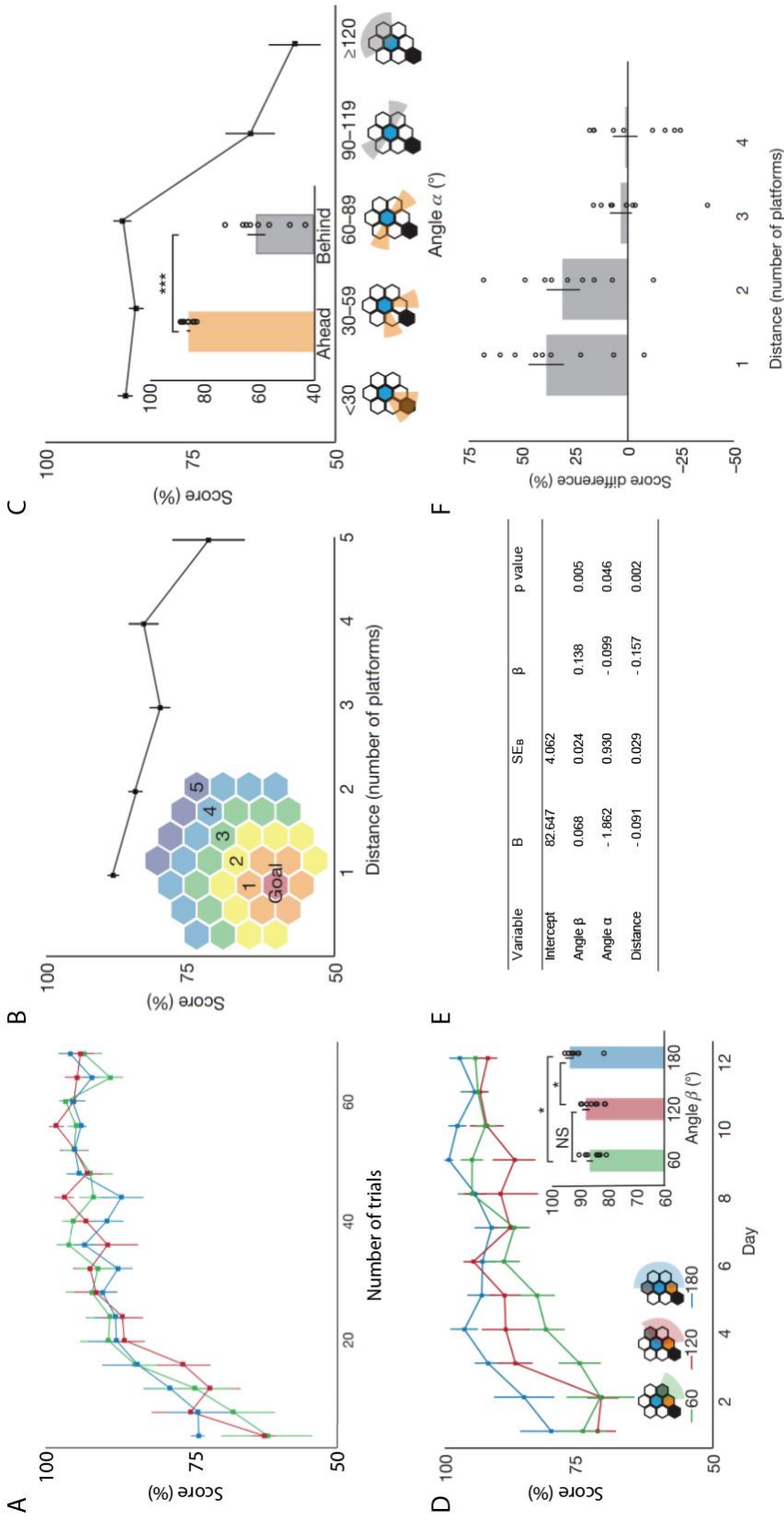
**Figure 3.10 Control rats on the Honeycomb Maze. A:** Learning curves for control cohorts on the Honeycomb Maze: cohort 1 (unoperated controls, n = 9, blue), cohort 3 (sham hippocampal lesions, n = 8, red) and cohort 5 (sham MEC lesions, n = 8, green). Each data point represents data from four trials. The schematic (inset) indicates distances-to-goal of 1 to 5 platforms. **C:** The effect of distance-to-goal on performance in cohort 1. Rats completed 68 - 72 trials over 13–17 days; data are shown for the first 68 trials. **B:** The effect of distance-to-goal on performance in cohort 1. Rats completed 68 - 72 trials over 13–17 days; data are shown for the first 68 trials. **B:** The correct) versus angle α (30° bins). *Inset:* scores were higher for choices that were 'ahead' (angle α < 90°, orange) of the rat compared to choices 'behind' (angle α > 90°, grey). **D:** The effect on angle β (choice platform separation) on performance in cohort 1. *Main graph:* learning curves for cohort 1 on Angleβ_60 trials (green), Angleβ_120 trials (red) and  Angleβ_180 trials (blue). 6 trials were undertaken per rat per day. *Inset:* mean score for trials with different values of angle β across all days (individual data points shown), with pairwise comparisons from a post-hoc Bonferroni test: 60° vs 180°, mean difference = 7.0%, p = 0.034; 120° vs 180°, mean difference = 5.9%, p = 0.044; 60° vs 120°, mean difference = 1.1%, p = 1.000. **E:** Regression model for the contributions of distance-to-goal, angle α and angle β to performance in cohort 1. B, unstandardized regression coefficient; SEB, standard error of the coefficient; β, standardized coefficient. **F:** The interaction between distance-to-goal and angle α in Aβ60 trials. The y axis shows the difference in mean performance for 'ahead' and 'behind' choices. Individual data points are shown for each animal. For A-F: *p < 0.05, ***p < 0.001. Error bars indicate s.e.m.

156

Honeycomb Maze task relative to controls ($F_{1,14}$ = 10.240, p = 0.006, two-way mixed ANOVA; *Figure 3.11A*). Control rats, but not hippocampal lesioned rats, showed learning within the first day, performing above chance on the first day of testing (controls: $t_7$ = 3.758, p = 0.0071; lesioned: $t_7$ = 0.8289, p = 0.4345; one sample t tests), although both groups performed at chance on the first trial (controls: $t_7$ = 2.049, p = 0.0796; lesioned: $t_7$ = 0.6831, p = 0.5165; one sample t-tests).
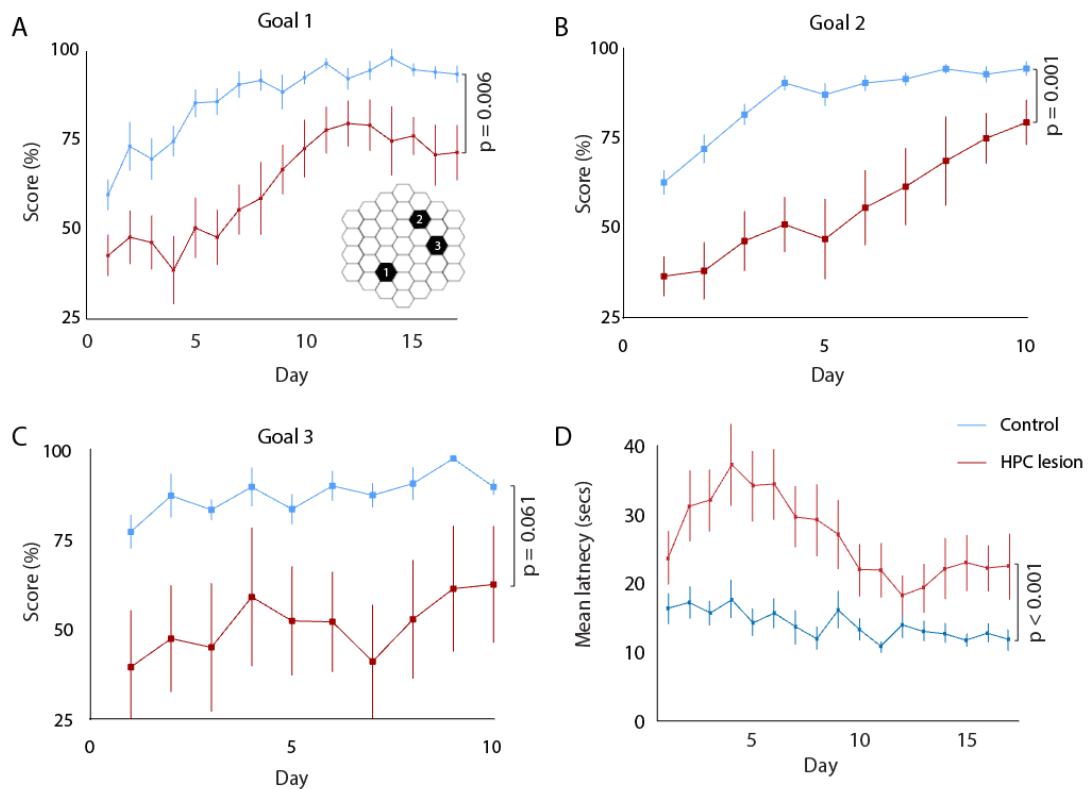


**Figure 3.11 Hippocampal lesioned rats on the Honeycomb Maze. *A:*** Rats with hippocampal lesions (red, n = 8) were impaired compared to sham-lesioned controls (blue, n = 8). Rats completed four trials per day. *Inset:* schematic of the goal locations used in ***A-C***. Hippocampal lesioned rats were also impaired in learning the location of a second (***B***, n = 8), and a third (***C***, n = 4) goal. ***D***: Rats with hippocampal lesions (red, n = 8) had longer choice latencies than sham-lesioned controls (blue, n = 8). For ***A-D*** error bars indicate s.e.m.

Rats with hippocampal lesions were also slower to make choices than sham-operated controls ($F_{1,14}$ = 11.103, p = 0.005; *Figure 3.11D*). Choice latencies were significantly longer for incorrect choices than correct choices across all rats ($F_{1,14}$ = 23.839, p < 0.001); this effect was larger for rats with

lesions ($F_{1,14}$ = 4.956, p = 0.043, two-way mixed ANOVA). Latencies also changed as a function of experience (day) ($F_{16,224}$ = 5.612, p < 0.001) with a significant day-by-lesion interaction ($F_{16,224}$ = 2.464, p = 0.002, two-way mixed ANOVA).

### 3.3.2.2. Rats with hippocampal lesions showed impaired reversal learning.

After 17 days of testing the goal location was changed (*Figure 3.11A, inset*). Hippocampal lesioned animals showed impaired reversal learning compared to controls ($F_{1,14}$ = 10.784, p = 0.005, two-way mixed ANOVA; *Figure 3.11A*). As with the first goal, controls performed significantly above chance within the first day of testing ($t_7$ = 3.670, p = 0.0080; one sample t-test) unlike hippocampal lesioned rats who performed at chance level ($t_7$ = 2.068, p = 0.0630; *Figure 3.11B.*). Half the rats were subsequently trained to locate a third goal location (*Figure 3.11C*; n = 4 in each group). The hippocampal lesioned rats achieved lower scores than controls, although, perhaps due to the smaller sample size and high variability in the performance of lesioned rats, the learning curves were not significantly different ($F_{1,6}$ = 5.281, p = 0.061, two-way mixed ANOVA). After ten days of testing the hippocampal lesioned rats were still performing at chance level ($t_3$ = 0.7643, p = 0.5003) whereas the control rats had learned the location of the third goal ($t_3$ = 18.32, p = 0.0004, one sample t-tests).

### 3.3.2.3. Maze parameters had a greater effect on performance in hippocampal lesioned rats.

As in the unoperated control group (cohort 1), the performance of rats with hippocampal lesions (cohort 2) and their controls (cohort 3) was related to three variables (*Figure 3.12B-D*): distance-to-goal, angle of the correct

choices to the goal direction (angle α), and separation between choice platforms (angle β). The effect of these variables on performance was analysed in data where the rats were learning the location of the first goal.
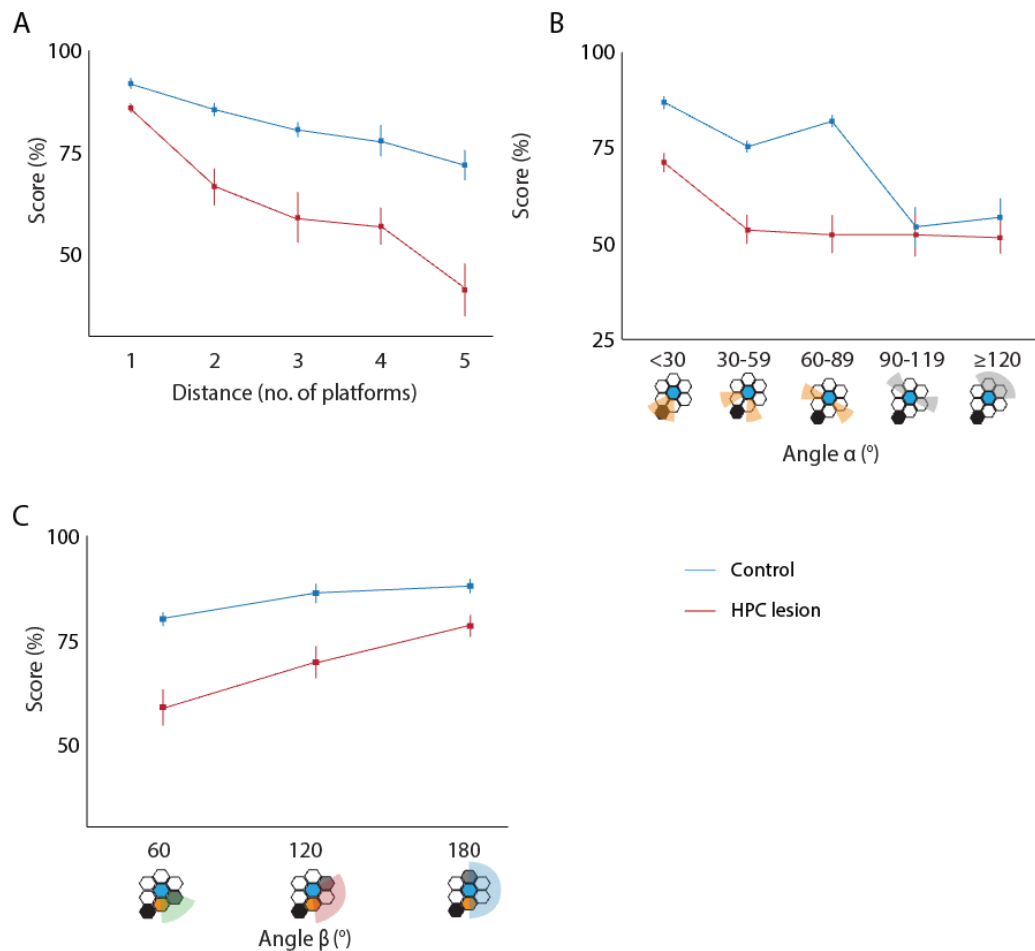


**Figure 3.12 Maze parameters in hippocampal lesioned rats.** Performance in rats with hippocampal damage (cohort 2, red, n = 8) was significantly more influenced than control performance (cohort 3, blue, n = 8) by distance-to-goal (**A**), angle to goal (**C**, angle α) and separation between choice platforms (**D**, angle β). Error bars indicate s.e.m.

Rats with hippocampal damage were significantly more influenced than controls by distance from the goal (*Figure 3.12B*; $F_{4,56} = 34.740$, p < 0.001, two-way mixed ANOVA), angle to goal (*Figure 3.12C*; angle α; $F_{2.3,32.8} = 28.812$, p < 0.001, two-way mixed ANOVA) and separation between choice platforms (*Figure 3.12D*; angle β; $F_{2,28} = 40.024$, p < 0.001, two-way mixed ANOVA). There was a significant interaction between all three variables and

lesion status (distance × lesion status, $F_{4,56}$ = 4.999, p = 0.002; angle α × lesion status, $F_{2.3,32.8}$ = 8.431, p = 0.001; angle β × lesion status, $F_{2,28}$ = 6.981, p = 0.003; two-way mixed ANOVAs).

### 3.3.2.4. There was a trend towards a negative correlation between hippocampal lesion size and task performance.

Hippocampal damage in the lesioned rats ranged from 48% to 94% (*Figure 3.14, page 161*). Preserved tissue was observed primarily in the ventral hippocampus with small incidental damage to the caudate and putamen in all rats. Minor additional damage to the dorsal subiculum, medial geniculate nucleus and pre- and parasubiculum was found in a subset. Maze performance decreased as hippocampal damage increased, although this trend was not statistically significant (n = 8 rats, $\rho_6$ = 0.452, p = 0.260; Spearman's correlation), possibly owing to a floor effect as half of the rats with lesions scored at chance level (*Figure 3.13*).
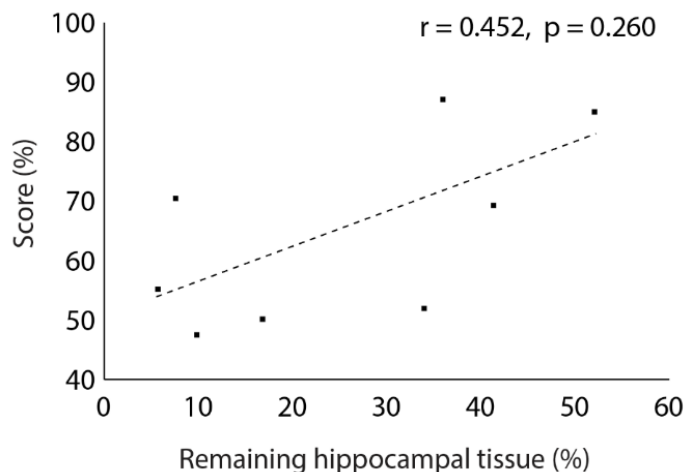


**Figure 3.13 Maze performance and hippocampal damage.** There was a non-significant correlation between remaining hippocampal volume in the lesioned rats (n=8) and performance on the Honeycomb Maze.

160
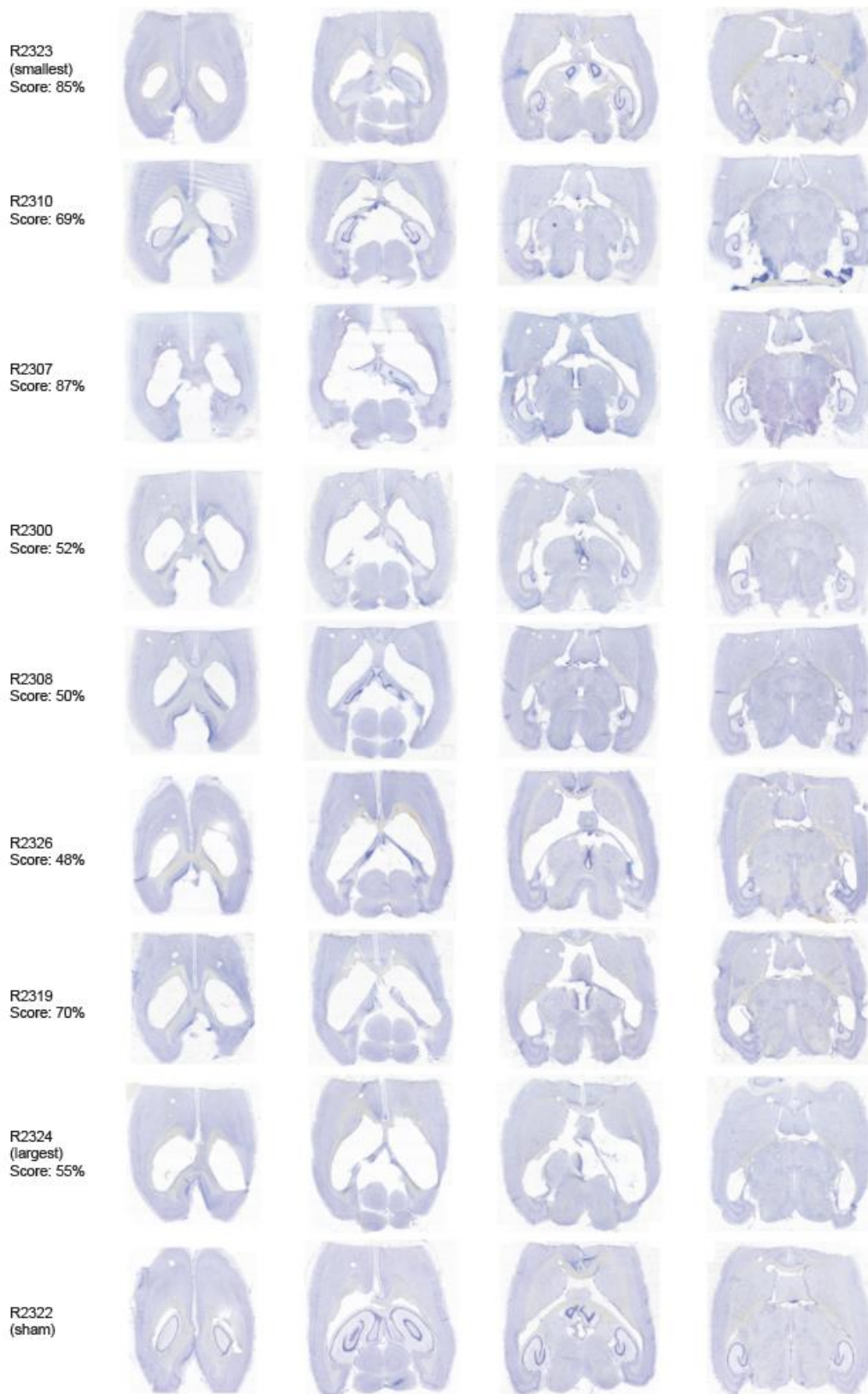
**Figure 3.14 Histology of hippocampal lesioned rats.** Representative horizontal sections from the brains of rats with hippocampal lesions, and one operated control with a sham hippocampal lesion (R2322), are shown alongside the rats score on the Honeycomb Maze (left column). Subjects are arranged in order of increasing lesion size. Horizontal sections (40μm) are stained with cresyl violet.

### 3.3.3. Experiment 3: Rats with MEC lesions on the Honeycomb Maze

In this experiment the performance of eight rats with bilateral MEC lesions (cohort 4) was compared with eight control rats with sham MEC lesions (cohort 5). Both groups completed four trials per day on testing schedule B.

### *3.3.3.1. Rats with MEC lesions could successfully navigate the Honeycomb Maze.*

Rats with lesions of the MEC were able to learn the goal location on the Honeycomb Maze (*Figure 3.15A*). The learning curve for MEC lesioned rats lay below that of the control group but there was no statistically significant difference in performance across all 17 testing days ($F_{1,14} = 4.005$, $p = 0.065$, two-way mixed ANOVA; *Figure 3.15A*). After 17 days of testing the goal location was changed (see *Figure 3.15A, inset*). There was no difference in reversal learning between the two groups, and the performance appeared more similar than when testing on the first goal location ($F_{1,14} = 0.566$, $p = 0.464$, two-way mixed ANOVA; *Figure 3.15B*).
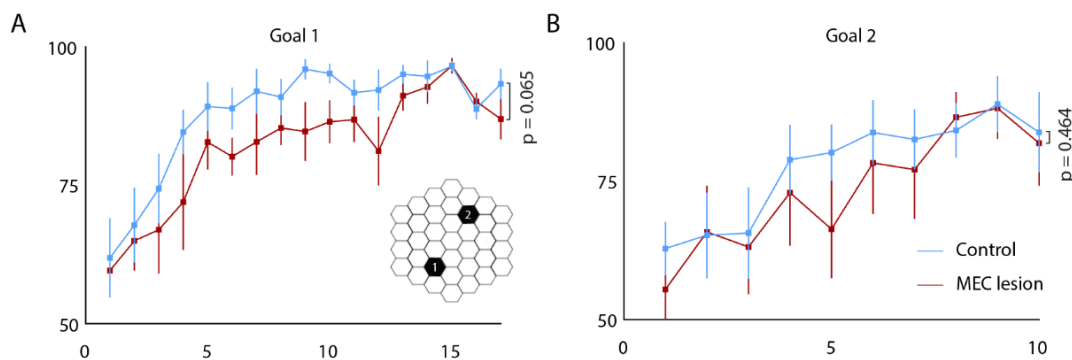


**Figure 3.15 Rats with MEC lesions on the Honeycomb Maze.** *A:* Rats with lesions of the MEC (cohort 4, red, n = 8) were not significantly impaired compared to sham-lesioned controls (cohort 5, blue, n = 8). Rats completed four trials per day. *Inset:* schematic of the goal locations used. *B*: MEC lesioned rats did not show an impairment in reversal learning. Error bars indicate s.e.m.

### 3.3.3.2. Maze parameters affected the performance of rats with MEC lesions and controls to a similar extent.

When learning the location of the first goal the performance of both the MEC lesioned rats and the sham-lesioned controls was significantly affected by the distance-to-goal, angle-to-goal (angle α) and the choice platform separation (angle β) parameters (*Figure 3.16*).
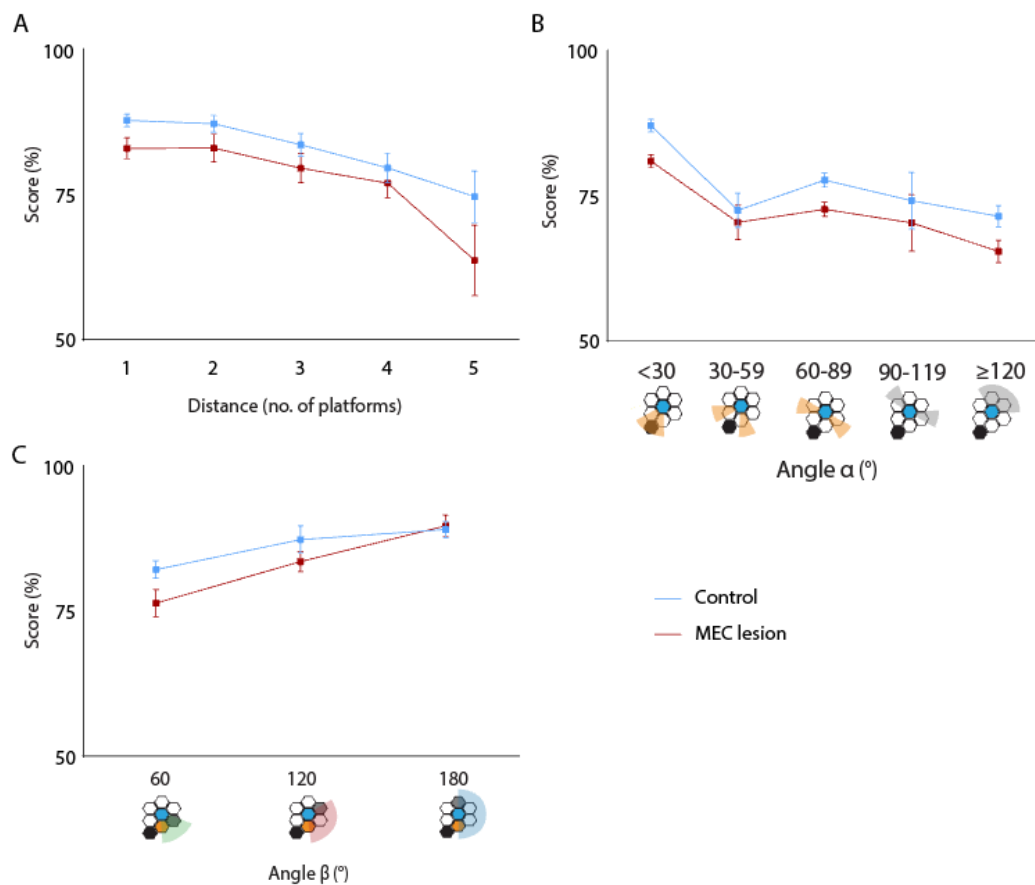


**Figure 3.16 Maze parameters in rats with MEC lesions.** Performance of rats with MEC lesions (red, n = 8) and their controls (blue, n = 8) was significantly influenced by distance-to-goal (***A***), angle to goal (***B***, angle α) and separation between choice platforms (***C***, angle β). The separation between platforms appeared to have a greater effect on performance in the MEC lesioned rats, however there was no significant interaction between angle β and lesion status. Error bars indicate s.e.m.

In both groups, performance declined at distances further from the goal ($F_{1.6,22.1}$ = 15.381, p < 0.001, two-way mixed ANOVA) and there was no interaction between lesion status and distance ($F_{1.6,22.1}$ = 0.915, p = 0.394,

two-way mixed ANOVA; *Figure 3.16*A). As the angle-to-goal (angle α) increased performance declined in both groups ($F_{4,56}$ = 13.769, p < 0.001, two-way mixed ANOVA; *Figure 3.16B*), again with no interaction with lesion status ($F_{4,56}$ = 0.253, p = 0.821, two-way mixed ANOVA).

Finally, the greater the separation of the choice platforms (angle β) the better the performance in both groups ($F_{2,28}$ = 26.842, p < 0.001, two-way mixed ANOVA; *Figure 3.16C*). On inspecting the plots of angle β versus performance (*Figure 3.16C*) it appeared that the separation of choice platforms had a greater effect on performance in the MEC-lesioned rats; MEC-lesioned rats performed significantly worse than controls when choice platforms were adjacent to one another (angle β = 60°; $t_{14}$ = 2.118, p = 0.050) but not when choice platforms were separated by two other platforms (angle β = 180°; $t_{14}$ = -0.225, p = 0.825, independent samples t-tests), however an interaction between lesion status and angle β fell short of reaching statistical significance ($F_{2,28}$ = 2.727, p = 0.083, two way mixed ANOVA).

### 3.3.3.3. Histology

Histological examination of the fixed, stained brain tissue of MEC lesioned rats confirmed the presence of MEC damage (*Figure 3.17*), however MEC lesion size was difficult to quantify due to methodological difficulties. Despite embedding tissue in gelatin prior to sectioning, tissue was friable, and the peripheral location of the MEC on brain sections meant that tissue was lost on several sections. This difficulty was compounded by the presence of the MEC lesions which further affected tissue integrity. From the sections available it appeared that the MEC lesions were very large and were

associated with substantial volume loss. Damage was frequently seen in adjacent areas, including the perirhinal cortex, parasubiculum and the posterior hippocampus although, again, due to the challenges described above was difficult to quantify
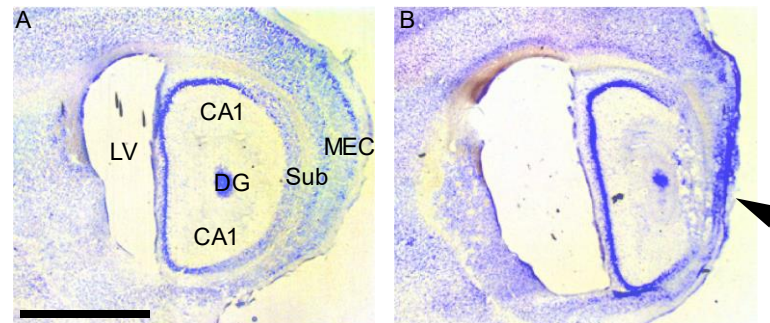


**Figure 3.17 Histology from a sham lesioned and MEC lesioned rat.** An example of an MEC lesion (**B**) compared to a sham lesioned control (**A**) in 40µm sagittal sections stained with cresyl violet. The arrowhead indicates extensive MEC damage which extends into the posterior hippocampus. Scale bar is 500 µm. LV = lateral ventricle; CA1 = CA1 hippocampal subfield; DG = dentate gyris; Sub = subiculum; MEC = medical entorhinal cortex.

### 3.3.4. Experiment 4: Pilot testing of mice on Honeycomb Maze 2.0

In this feasibility study, eight wild-type mice, aged between 12 and 16 weeks, were tested on a newer version of the Honeycomb Maze. The first group (female mice) received three days of training, followed by eight days of testing using testing schedule C. The second group (male mice) received no training and completed 12 days of testing using the same testing schedule.

### *3.3.4.1. WT mice with prior training can successfully navigate to a hidden goal location on the Honeycomb Maze*

In Group 1 no individual mouse scored significantly better than chance (50%) on the first day of testing, but by the final testing day all four appeared to have learned the goal location and performed significantly better than chance (group mean on final testing day +/- s.e.m. = 81.1 +/- 6.6%; *Table*

*3.1*, FDR corrected one sample t-tests). No learning effect was seen when comparing mean scores between the two testing weeks suggesting that a degree of learning may have occurred during the initial training period ($t_3$ = 1.004, p = 0.3895, paired t-test; *Figure 3.18, page 167*). To investigate this further, the performance of the whole group on the first testing day was compared against chance. Although mice did not perform better than chance on an individual level, on a group level performance was significantly better than chance on the first day of testing ($t_3$ = 5.695, p = 0.0107, one sample t-test).

| | Mouse | Day 1 score (%) | Score vs. chance | Final day score (%) | Score vs. chance |
|---|---|---|---|---|---|
| **Group 1** | M898617 | 66.9 | $t_3$ = 1.479, q = 0.3070 | 76.7 | $t_5$ = 4.356, **q = 0.0146** |
| | M898623 | 70.0 | $t_3$ = 1.507, q = 0.4576 | 95.2 | $t_5$ = 9.500, **q = 0.0008** |
| | M908826 | 58.8 | $t_3$ = 1.328, q = 0.2761 | 70.0 | $t_5$ = 3.000, **q = 0.0301** |
| | M908827 | 72.5 | $t_3$ = 2.029, q = 0.5416 | 82.4 | $t_5$ = 3.600, **q = 0.014** |
| **Group 2** | M930428 | 64.1 | $t_5$ = 1.675, q = 0.2063 | 62.7 | $t_5$ = 1.585, q = 0.1738 |
| | M930430 | 66.0 | $t_5$ = 3.068, q = 0.1116 | 85.3 | $t_5$ = 4.572, **q = 0.0240** |
| | M930431 | 77.4 | $t_5$ = 2.368, q = 0.1282 | 77.7 | $t_5$ = 2.874, **q = 0.0464** |
| | M930426 | 63.7 | $t_5$ = 1.156, q = 0.3121 | 79.2 | $t_5$ = 3.416, **q = 0.0378** |

**Table 3.1 Honeycomb Maze performance in mice on the first and last day of testing.** Seven out of eight mice were able to learn the goal location by the last day of testing. q values are from one-sample t-tests, testing the score obtained versus a chance score of 50%. All values are FDR-corrected for multiple comparisons.

### 3.3.4.2. WT mice with no prior training can successfully navigate to a hidden goal location on the Honeycomb Maze

No mouse in Group 2 performed above chance on the first day of testing, but by the final day of testing all mice, except one (M930428), achieved scores which were significantly better than chance (75.5 +/- 4.8 % (s.e.m.); *Table 3.1*). This finding in M930428 may have been due to over-training since this mouse achieved a maximum score of 86.3% on day nine of testing, with his daily scores then dropping to 62.7% on the final day of

testing. Mice in group 2 completed four consecutive days of testing per week. Analysis of scores by week of testing, rather than by day, indicated that M930428 did perform at a level significantly better than chance over the final week of testing ($t_3 = 4.989$, $p = 0.0155$, one sample t-test). When analysing the performance of all mice in group 2, a significant learning effect was seen across weeks ($F_{2,6} = 6.208$, $p = 0.0346$, one-way repeated measures ANOVA; *Figure 3.18 D*).
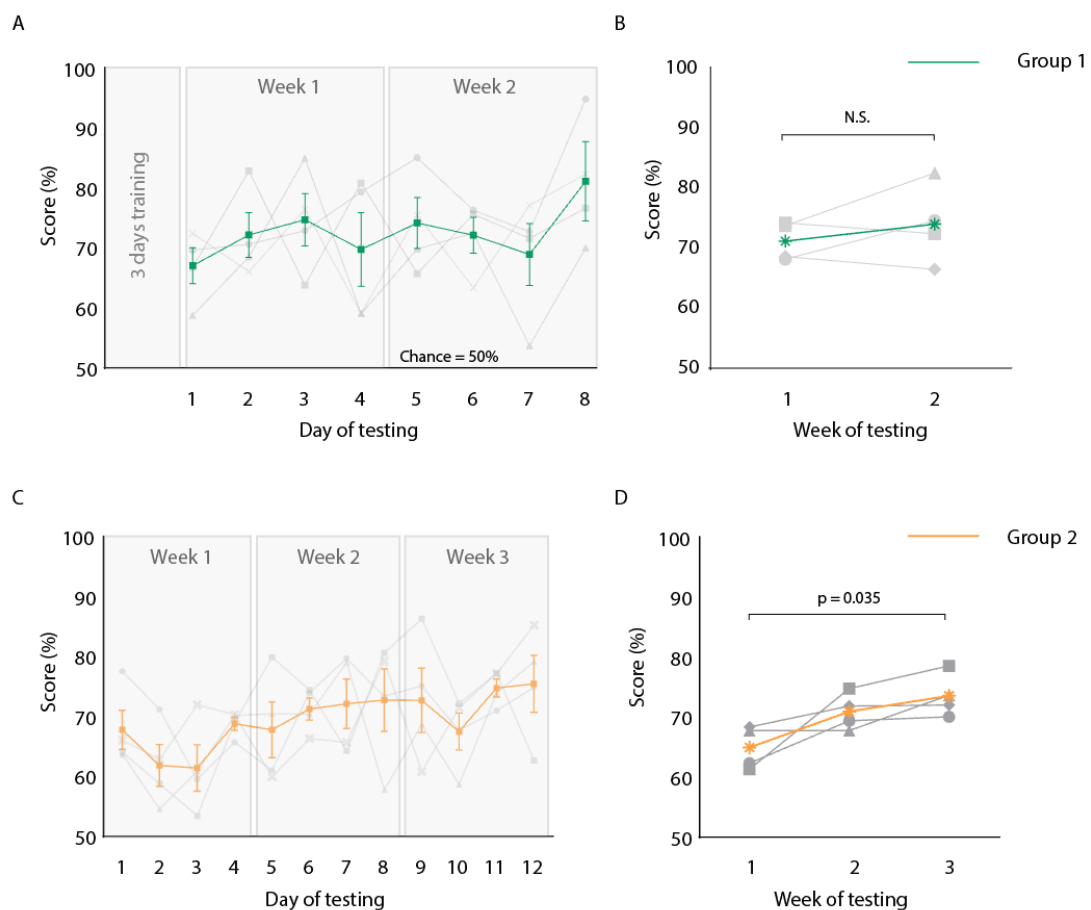


**Figure 3.18 Mice can learn to navigate to the goal platform on the Honeycomb Maze.** Learning curves are shown for the mice in group 1 (*A*) and group 2 (*B*) across testing days. The learning curves of individual mice are shown in light grey, with the coloured line indicting the group mean. Error bars indicate standard error of the mean. The performance of mice over weeks are shown in (*B*) and (*D*). p values are calculated using a paired t-test in *B*, and a one-way repeated measures ANOVA in *D*.

## 3.4. Discussion

### *3.4.1. WT mice and rats can learn the Honeycomb Maze*

The first experiment confirmed that control rats can rapidly learn a spatial navigation task on the Honeycomb Maze. The lack of a significant difference in performance between the three control groups, despite testing on different occasions and using subtly different testing schedules indicates that performance on the maze is consistent and reliable. Pilot testing in experiment four demonstrated that mice can also successfully navigate to an unmarked goal platform on a newer version of the Honeycomb Maze. The performance of both groups of mice was significantly above chance by the final day of testing, and a learning effect was seen across weeks of testing in the group which had received no prior training on the maze. These data are encouraging and suggest that the Honeycomb Maze 2.0 could be a suitable apparatus to test hippocampal function in mouse models of AD. Unpublished data from the O'Keefe lab have shown that rats can also successfully navigate on the newer version of the Honeycomb Maze (467). The Honeycomb Maze therefore provides a powerful research tool as a paradigm which can be used to test spatial memory across species. Although this is also true of the Morris Water Maze, it has been observed that the prevalence of anxiety-related behaviours in the water maze, such as floating rather than swimming, and thigmotaxis, is higher in mice compared to rats (468). The design of the Honeycomb Maze precludes thigmotaxis and, during the testing of mice on the maze, no freezing was observed, and all eight mice were able to navigate to the goal platform by the end of the testing schedule. Mice and rats were able to complete the

task using the same experimental apparatus; this contrasts with other tasks, such as the Morris water maze and the T-maze, in which different sizes of environment are frequently used to test rats and mice.

The results of these experiments provide insights into how testing paradigms should be designed in future experiments using the Honeycomb Maze. Of note, neither mice nor rats required any prior training to learn the task. One potential issue is that mice achieved a narrower range of scores than rats and had more variability in their performance, with lower scores attained on the final day of testing; rats achieved scores of 94.5 +/- 2.3%, 93.3 +/- 2.7% and 95.0 +/-1.4% on the final day of testing (cohorts 1, 3, and 5 respectively; mean +/- s.e.m.) whereas mice achieved scores of 81.1 +/- 6.6% and 75.5 +/- 4.8% (groups 1 and 2 respectively). The scores achieved by mice on the Honeycomb Maze are higher or similar to those observed when mice undertake other spatial memory tasks, such as those measuring spontaneous alternation; spontaneous alternation rates in normal mice are reported as approximately 75% in standard versions of the T-maze task (221). However, a narrow performance range could make identifying and tracking progressive hippocampal impairment in mice more challenging. This narrower range of scores could be due to species differences or may reflect the different testing schedules used and the increased size of Honeycomb Maze 2.0. Mice were tested on the 61-platform version of the maze, rather than the 37-platform version, and therefore had to travel further to reach the goal. In addition, testing schedule C, was a 'pure allocentric' task since the choice platforms offered to the mice at each point on the maze were selected in a pseudo-random fashion, and therefore the maze may have been more difficult to solve. Testing mice on the newer maze with the

outer ring of platforms excluded, and using testing schedule B, may result in mice achieving higher scores. The increased variability of scores in mice also suggest that larger cohorts may be needed in future studies looking for group differences.

### 3.4.2. Task difficulty on the Honeycomb Maze is scalable and provides an insight into the mechanisms underlying spatial navigation.

In the first experiment, three maze parameters were identified which increased choice difficulty: increased distance-to-goal, increased deviation of the correct choice platform from the goal (angle α) and decreased separation of choice platforms (angle β). The difficulty of a choice on the maze can therefore be set by adjusting these three parameters, and this provides opportunities for creating bespoke paradigms using the maze apparatus for application in future studies.

As alluded to briefly in the introduction to this chapter, direction and distance factors were noted in early research on maze learning. The *goal-orientation factor* refers to the observation that in mazes rats displayed a greater tendency to enter blind alleys pointing in the direction of the goal than those oriented away from it (469-471). *Dashiell* demonstrated that rats running in a maze quickly develop an orientation preference for the general direction of the goal and that this plays an important role in their ability to learn, enabling them to reach the goal via routes they had not previously encountered (461). Subsequent studies by *Yoshioka* (472), *Gengerelli* (473) and *Tolman and Honzik* (474) confirmed these findings, and it has since been proposed that the direction factor is generated by the hippocampal cognitive map (179). In accordance with the *goal-orientation factor,*

performance on the Honeycomb Maze was improved on choices where the correct choice platform pointed more directly towards the goal (i.e., when angle α was smaller).

The *goal-gradient factor* describes the tendency for animals to make fewer errors when they are nearer the goal (469), and this led *Hull*, amongst others, to conclude that a maze may be learned from the goal backwards (460, 475, 476). He hypothesised that the motivation to reach a goal increases with proximity (either spatially or temporally) to the goal along a logarithmic gradient (460). *Spence* summarised the goal-gradient factor as follows: "*there is considerable evidence of some backward order principle of learning operating in the maze situation. In general, the blinds are more difficult the farther they are from the goal…*" (469). These findings are in line with observations on the Honeycomb Maze that rats are more prone to errors on platforms that are further away from the goal.

The early maze studies do not specifically refer to the separation between choices in a maze although observations in the Honeycomb Maze are intuitive; one would expect choices with a greater separation (i.e., a greater value of angle β) to be easier for the animal since the two choices presented will appear less similar to one another and may therefore have more distinct neural representations which are less susceptible to noise.

The finding that maze parameters influence choice difficulty provides an insight into the mechanisms used by the brain to solve the Honeycomb Maze task. Control rats were able to identify the better of two directions even when neither was directly aligned with the goal. This suggests that they may be using vector computations to solve the task. *John O'Keefe* has previously proposed that the cognitive map within the hippocampal formation contains

a set of place representations based on the direction and distance between locations, and that these directions and distances can be represented by vectors which are used for spatial navigation (477). An adapted version of this vector model can explain the observed effects of the maze parameters on performance (*Figure 3.19*).
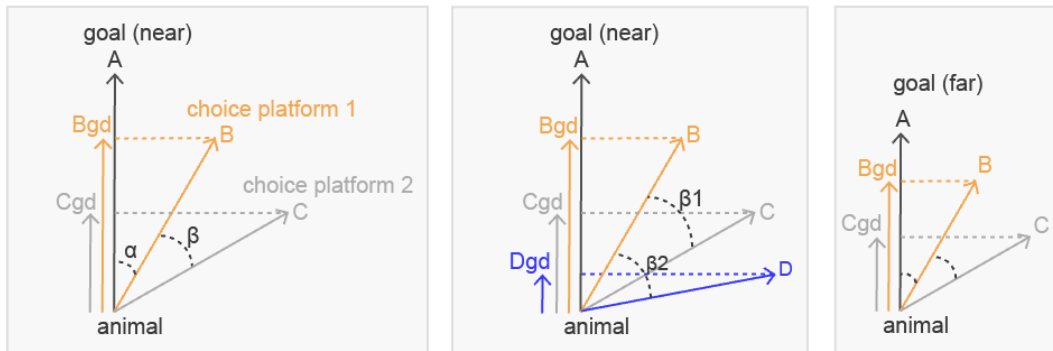


**Figure 3.19 Vector-based navigation schema**. *Left*: In this model the hippocampus represents a goal-direction vector pointing from the rat to the goal (vector A, black). The navigation system within the brain computes the projection of each choice platform vector, the correct choice (B, orange) and the incorrect choice (C, grey), onto this goal-direction vector (inner product, Bgd, Cgd). The larger of the two is then selected as the correct choice. *Middle*: The choice is easier when the angle between choices (angle β) is greater, due to the consequent increased difference in the magnitudes of the projection vectors. If a rat were choosing between a correct choice (B, orange) and an incorrect choice (D, blue), separated by angle β2 (where β2 > β1), the difference between the projection vectors Bgd and Dgd is greater than if choosing between choices B and C separated by angle β1, with projection vectors Bgd and Cgd. *Right*: When the animal is further from the goal, or if the correct choice takes the animal away from the goal (i.e., angle α > 90°), the magnitude of the vector representation may be smaller (whether due to reduced motivation or another factor). This would mean that the absolute difference in the choice projection vectors is reduced and therefore more vulnerable to noise.

### 3.4.3. The hippocampus makes a key contribution to successful navigation on the Honeycomb Maze.

Data from experiment 2 indicates that the hippocampus plays a key role in solving the Honeycomb Maze task; rats with hippocampal lesions took longer to learn the goal location and never attained the same level of competence as sham-operated controls. Rats with hippocampal lesions also took longer to make choices than control animals, which may reflect an increased level of uncertainty due to a navigational impairment, or a

reduced level of motivation. The former argument is supported by the fact that rats had longer latencies for incorrect choices than for correct choices. A degree of learning was observed in hippocampal-lesioned rats and this may reflect residual function in the remaining hippocampal tissue or represent the use of an alternative non-hippocampal navigational strategy. In further support of an important role for the hippocampus in solving this task, a trend towards a correlation was observed between hippocampal lesion size and performance, however this was not statistically significant, possibly due to a small sample size or a floor effect. The clear contribution of the hippocampus to solving the Honeycomb Maze task suggests that this may be a useful paradigm for detecting impaired hippocampal function in rodent models of AD.

All three maze parameters, distance-to-goal, angle α and angle β, were found to affect the performance of rats with hippocampal damage to a greater extent than sham-operated controls.  If the vector model proposed above (*Figure 3.19*) is a true approximation of how the brain solves the Honeycomb Maze task, and these vector computations are performed within the hippocampus itself, it would be expected that hippocampal lesions should equally impair the animal's ability to make easier and more difficult choices, with the animal performing at chance in both cases. However, the results suggest that the easier, and potentially less computationally demanding, choices have a lesser reliance on hippocampal processing and can potentially be solved using alternative strategies, whereas the harder choices are more dependent on an intact, functioning hippocampal network. An alternative explanation is that all choices require the same degree of computation (as per the proposed vector model), but that lesioning the

hippocampus introduces noise into the system. More difficult choices would be more vulnerable to noise given the smaller absolute difference in their choice projection vectors compared to easier choices. The required vector computations could be performed either by the residual functioning hippocampal tissue, or within another brain region such as the parietal cortex which is dependent on receiving spatial information from hippocampal place cells.

### 3.4.4. The role of the MEC in navigating the Honeycomb Maze is unclear.

Data from experiment 3 indicated that lesioning the MEC had no significant effect on performance in the Honeycomb Maze, although the learning curve for the lesioned animals did lie below that of sham-operated controls, with the difference between the two falling just short of statistical significance. These results were unexpected; if spatial memories depend on an interaction between the hippocampus and the neocortex, MEC lesions would be expected to cause deficits in hippocampal-dependent memory to a similar extent as hippocampal lesions themselves. The results presented here could reflect a true finding or could be due to alternative explanations such as incomplete lesioning of the MEC, or the use of an alternative strategy by MEC lesioned animals.

Previous studies have found that electrolytic and neurotoxic lesions of the medial and lateral EC can result in impaired performance on the Morris Water Maze (464, 478, 479), as can lesions of the LEC alone (480) (but see (481)), and the MEC alone (463, 481). However, such findings have not been consistently replicated; some studies fail to find a spatial memory

impairment in EC lesioned animals (482-486), while others report that the effect of MEC lesions on spatial memory was less robust than that of hippocampal lesions (464, 465). This latter observation fits with findings that MEC lesions do not entirely abolish place cell firing but reduce their stability and fine-tuning; residual place cell activity may imply that hippocampal spatial representations remain somewhat intact, albeit in an impaired state, and this could be sufficient to enable performance at a level greater than chance. It may be that MEC lesions do impair performance on the Honeycomb Maze but that since this impairment is small in magnitude the current study was not sufficiently powered to detect it. An explanation for the weaker effect of MEC lesions in comparison to hippocampal lesions is that visuospatial information could reach the hippocampus via alternative routes (for a review see (487)), including sparser projections from the subicular complex (301), the peri- and postrhinal cortices (488) and subcortical structures (489). If these inputs were sufficient for the encoding and retention of spatial memories this would explain why lesioning the MEC does not significantly affect performance on the Honeycomb Maze.

The discordant results from previous EC lesion studies have been proposed to be due to methodological differences such as the lesion technique (for example, chemical, genetic and mechanical methods), and differing stereotactic coordinates, both of which potentially result in incomplete lesions or lesions of different entorhinal subregions. It is possible that in our study the MEC lesions were incomplete or spared neighbouring regions which could subserve the role of the MEC in task performance. There is increasing evidence that a simple 'what-where' functional dichotomy of the EC, where the LEC processes information regarding objects and the MEC

processes spatial information, is an oversimplification (490). For example, in one study the separate manipulation of distal or local environmental cues dissociated cellular activity in the MEC and the LEC respectively, indicating that both regions can play a role in spatial representation (491). The MEC and LEC are densely interconnected and project to common downstream targets and therefore it is possible that these regions have some overlapping functions (267).

An alternative explanation takes into consideration the modular organisation of the MEC in recurrently connected bands which run parallel to the rhinal fissure, each of which has a distinct pattern of connectivity. One study has shown that it is the dorsolateral band of the MEC which is critical for navigational performance, with lesions of this area completely disrupting spatial memory on the Morris water maze and preventing the learning of a new goal. In contrast, lesions of the ventromedial band of the MEC spared spatial memory (465). This fits with observations that the caudal portion of the dorsolateral band is the region of the MEC which contains spatial cells (272), and receives the majority of cortical visuospatial afferents (492).

Unfortunately, it was not possible to fully assess lesion extent in the histology obtained from our MEC lesioned rats to check for involvement of the LEC or the dorsolateral band of the MEC. The lesions were very large causing substantial damage to surrounding structures, including the hippocampus; this affected the integrity of the sections, despite embedding the brains in gelatine, and some friable tissue was lost. To fully characterise the contribution of the MEC to performance on the Honeycomb Maze task a repeat study using targeted MEC lesions, such as the method used in (465) would be warranted. During the course of the present study,

alternative techniques were explored, including the possibility of performing structural neuroimaging, such as MRI, in lesioned rats to quantify the extent of MEC lesions.

### 3.4.5. Summary

The results indicate that both mice and rats can navigate the Honeycomb Maze, and that successful performance on the maze involves the hippocampus. Maze difficulty can be scaled by altering the parameters of the choices offered to animals as they navigate the maze. Taken together these findings suggest that the Honeycomb Maze provides a reliable means of testing hippocampal function in rats and mice and has potential for use as a test of hippocampal function in rodent models of AD. Separate experiments undertaken by other members of the *O'Keefe* laboratory have shown that concurrent electrophysiological recordings can be performed in rats as they solve the honeycomb maze (466) (*Figure 3.20*), providing a means by which place cell activity and spatial memory could be co-investigated in the context of AD pathology. Further work remains to clarify the contribution of the MEC to solving the Honeycomb Maze.
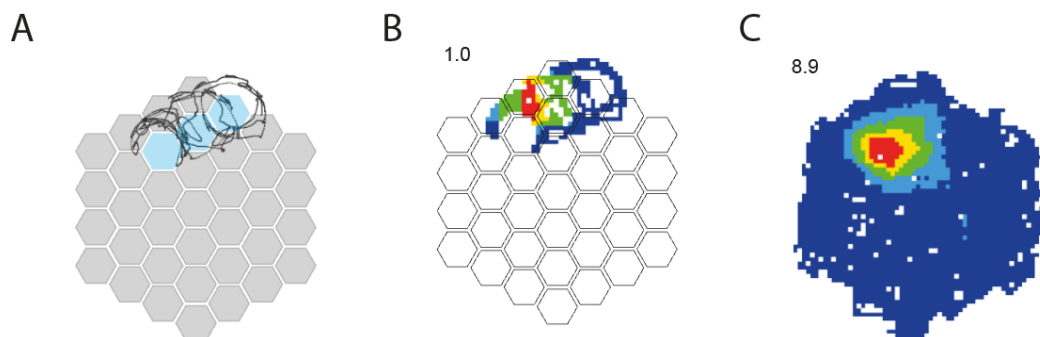


**Figure 3.20 A place cell recorded on the Honeycomb Maze.** Rate maps for a place cell recorded on the Honeycomb maze are shown for a single trial (**B**) and when a rat explored the whole maze with the platforms raised (**C**). The path of the rat in the trial is shown in **A** (black line).

# 4. CA1 electrophysiology in an APP knock-in mouse model of Alzheimer's disease

## 4.1 Introduction

### 4.1.1. Background

As discussed in the introductory chapter, the hippocampal formation is critically involved in the early stages of Alzheimer's disease (AD). Patients with AD have marked atrophy of the entorhinal cortices and hippocampi on MRI (30), and post-mortem studies show that these regions exhibit neurofibrillary tangles (NFTs) composed of hyperphosphorylated tau (Braak stages 1 and 2), and amyloid β (Aβ) pathology (Thal phase 2), relatively early in comparison to other brain areas (2, 3, 31). The hippocampal formation is a key node in the brain's spatial memory network, and spatial memory deficits, specifically impairments in allocentric spatial memory, have been consistently identified at the very early stages of AD (5, 21, 224, 228, 229, 233, 234, 237, 242). There is extensive evidence supporting the existence of an allocentric spatial representation within the hippocampus (48, 182, 493). Hippocampal place cells encode spatial information through their firing rates, which are increased within their place fields, and also through the timing of their activity in relation to the theta rhythm of the LFP (theta phase precession) (330). It is therefore logical to hypothesize that <u>AD pathology causes a disruption of hippocampal function which manifests as alterations of spatially-related single cell activity and behaviour.</u>

### 4.1.2. Studies of spatial cells in mouse models of Alzheimer's disease

Previous studies have investigated the effects both Aβ and tau on the function of hippocampal place cells in AD mouse models. In the first such study, the *O'Keefe* group demonstrated that Aβ plaque burden in the hippocampus of the Tg2576 (an APP overexpression model) correlated with a progressive disruption of place cell activity and spatial memory, as assessed using a forced choice T-maze alternation task (*Figure 4.1*) (494).

Image redacted for copyright reasons

**Figure 4.1 Rate maps of place cells recorded in Tg2576 mice**. Place fields appear normal in young and aged wild-type mice and in young Tg2576 mice. However, in aged Tg2576 there is a reduction in spatial information associated with increasing Aβ pathology. Some aged Tg2576 mice have place fields similar to wild-type controls e.g., Mouse 1, while others are clearly disrupted e.g., Mouse 4. Figure taken from (494).

Place cell abnormalities have since been reported in other mouse models of neurogenerative disease, including those with Aβ pathology (495, 496), mutant tau (497, 498) and both Aβ and tau pathology (496). Findings from these studies are summarized in *Table 4.1 (page 181)*. Taken together the results show a consistent reduction in the spatial information of place cells in the various mouse models used (494-496, 498, 499). Other findings in AD mouse models were less consistent but included an increase in place

field size (494) (but see (498)) , a reduction in place cell stability (495), a decreased proportion of place cells (496), a reduction in the mean and peak firing rates of place cells (495, 499) (but one study also reported a decreased running speed (499)), and a decrease in phase locking of place cell activity to the theta and slow gamma rhythms of the LFP (499). One study has examined the effects of tau pathology on the function of grid cells in the entorhinal cortex. In the EC-tau mouse, which overexpresses mutant human tau (P301L) in layer II of the EC (148), the accumulation of tau pathology is associated with reduced grid field periodicity and firing rates (500) (*Figure 4.2*).



Image redacted for copyright reasons
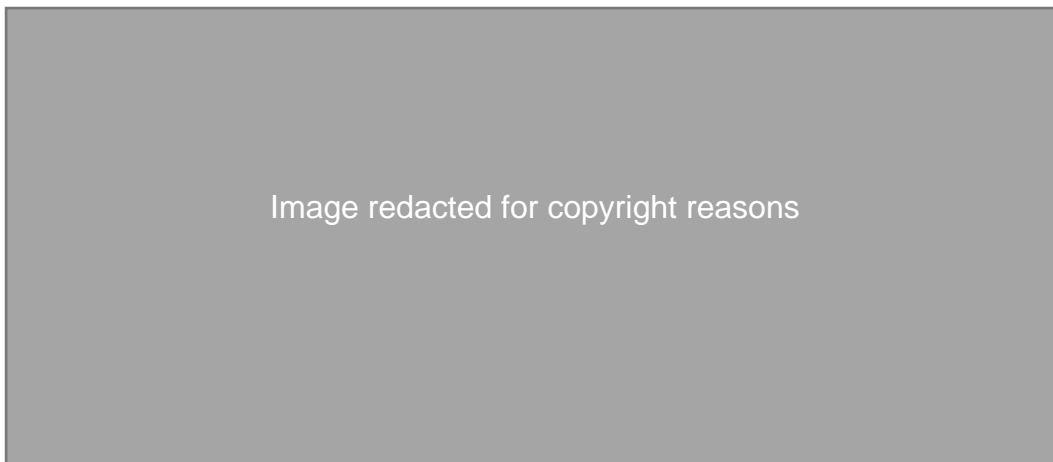
**Figure 4.2 Grid cells in aged EC-tau mice.** Medial entorhinal cortex grid cell rate maps (with peak firing rate in Hz) and their autocorrelations (with grid scores, GS) are shown for 14-month EC-tau mice and 30+-month EC-tau mice along with age-matched controls. A: Activity maps and autocorrelations were unchanged in the 14-month EC-Tau mice compared to controls. (b) Activity maps and autocorrelations were severely affected in 30+-month EC-Tau mice when compared to age-matched controls. Figure taken from (500).

Taken together the results of these studies suggest that both Aβ and tau pathology can disrupt place cell function in the hippocampus, and that tau pathology can cause grid cell dysfunction in the EC.

| Mouse model | Overexpression of: | Pathology | Key findings |
|---|---|---|---|
| Tg2576 (491) | APP (Swedish) | Aβ plaques | ↓ spatial information in place cells<br><br>↑ place field size<br><br>Spatial memory deficits (forced-choice T maze alternation) correlated with place cell changes<br><br>Behavioural + place cell deficits correlated with Aβ pathology |
| TetO-APP Swelnd (495) | APP (Swedish, Indiana) | Aβ plaques (Tet-On condition) | Familiar environments: ↓ spatial information, ↓ stability + ↓ peak firing rates in place cells<br><br>Novel environments: place fields formed at the same rate as in controls |
| APPPS1 (496) | APP (Swedish)<br>PSEN1 (L166P) | Aβ plaques | ↓ proportion of place cells<br><br>↓ spatial information in place cells |
| 3xTg (499) | APP (Swedish)<br>MAPT (P301L)<br>PSEN1 (M146V) | Aβ plaques<br><br>MAPT immuno-reactivity in CA1 | ↓ place field stability<br><br>↓ spatial information in place cells<br><br>↓ mean firing rates (but ↓running speeds)<br><br>↓ place cells locked to theta + slow gamma rhythms |
| rTg4510 (497, 498) | MAPT (P301L) | NFTs<br>Neuronal loss | CA1 pyramidal cells had no stable place fields but did fire in robust sequences (497)<br><br>↓ spatial information in place cells but no difference in field size (498) |

**Table 4.1 Studies investigating the effects of Aβ and tau on place cell function in mouse models.** APP, amyloid precursor protein; Aβ, amyloid β; PSEN, presenilin; MAPT, microtubule associated protein tau; CA1, hippocampal subfield; NFTs, neurofibrillary tangles.

## 4.1.3. Limitations of current studies

The studies investigating the effects of Aβ on place cell function share a common limitation: all are conducted in mouse models which overexpress mutant APP, with or without the overexpression of additional mutant genes

(494-496, 499). It has been argued that such models may produce artificial phenotypes since they overproduce other APP fragments in addition to Aβ (153). Additional issues include the destruction of endogenous genes when the transgene is inserted, unphysiological levels of APP expression due to the use of artificial promoters, and transgene expression across cells not resembling endogenous APP expression patterns (*see page 49*). Alternative knock-in mice models are now available which harbour APP with the Swedish and Beyreuther/Iberian mutations, either with (NL-G-F) or without (NL-F) an additional Arctic mutation (153). Such mouse models provide the opportunity to study the effects of Aβ pathology on place cell properties without the limitations of overexpression models, and this is the rationale behind the selection of the APP$^{NL-G-F}$ knock-in mouse model for the present study.

Studies of the effects of tau pathology on place and grid cell function have used mouse models overexpressing P301L mutant tau (497-500), since this leads to an accumulation of phosphorylated tau in NFTs. However, it is important to note that no MAPT mutations have been linked to AD and so although these models allow research into the effects of mutant tau pathology on cell function they should, strictly, be considered models of frontotemporal dementia and not AD. Furthermore, the native human 3R/4R ratio is not preserved in these models since the transgenic mice express tau cDNA with no modulation of alternative splicing. Although beyond the scope of this project, which focuses on the effects of Aβ pathology on place cell function, these limitations could be addressed by using alternative models,

such as the humanised tau (htau) mouse model (501), or mice injected with tau extracts isolated from the brains of patients with AD (502).

### 4.1.4. Study rationale and objectives

The main objective of the present study is to investigate hippocampal (dys)function, specifically place cell electrophysiology, in the APP$^{NL-G-F}$ mouse model, to gain an insight into how the presence of Aβ pathology influences spatial representations within the hippocampus. Neural activity will be examined on both a single cell and population level.

During the course of the research presented in this chapter, another study was published which examines place cell function in the same APP knock-in model (503). This study focused on place cell remapping and reported impaired remapping in 7–13-month APP$^{NL-G-F}$ mice. Place cells were described as 'mildly impaired' and fewer place cells were identified in APP$^{NL-G-F}$ mice compared to controls. Other findings included an impairment of spatial tuning in MEC grid cells, and an impairment in the fast gamma oscillatory coupling between the MEC and CA1. The limitations of this study included the use of non-littermate controls, and a relatively low yield of pyramidal cells from a large number of mice (218 pyramidal cells from 20 mice).

Despite this recent study, place cell electrophysiology has not yet been fully characterised in the APP$^{NL-G-F}$ mouse model. Further questions remain regarding place cell function, including scope for a full characterisation of the spatial properties of place cells, such as directionality on the linear track, place cell coherence, and firing in relation to local cues. The relationship

between place cell firing and the theta oscillation of the LFP in the APP$^{NL-G-F}$ model also warrants investigation, in particular examination of phenomena such as theta modulation and theta phase precession. A thorough evaluation of place cell function in the APP$^{NL-G-F}$ mouse is important, not least because this model is increasingly being used in other AD studies, and also because this will help to differentiate which (if any) effects seen in previous studies of place cell function are artefacts secondary to the use of APP overexpression models. Such in-depth probing of place cell function may also provide additional clues as to the mechanisms underlying the spatial memory impairments which are observed in AD patients.

### 4.1.5. Hypotheses

Given that hippocampal place cells are a vital component of the brain's spatial network, and spatial memory impairment is a prominent early feature of AD, the central hypothesis of this study is that place cell function will be impaired in the APP$^{NL-G-F}$ model, and this impairment will correlate with Aβ pathology. Place cell function could be disrupted in several different ways. In the hippocampus, pyramidal cells encode spatial aspects of an animal's environment or behaviour using both rate coding and temporal coding (356). Rate and temporal codes have been shown to be dissociable and both could be affected by Aβ pathology. This chapter aims to address the following hypotheses:

1. Rate coding of spatial information by CA1 pyramidal cells will be impaired in APP$^{NL-G-F}$ mice.

Evidence from previous studies in APP overexpression models and in the APP$^{NL-G-F}$ model, support the hypothesis that rate coding of spatial information will be impaired in APP$^{NL-G-F}$ mice. On a single cell level, the precise firing pattern, or rate coding, of each place cell may deteriorate resulting in a decreased spatial information content, and larger, less distinct place fields with lower within field firing rates. The peak firing rates of place cells may also be decreased, and place cells may have reduced stability and spatial coherence. On the linear track place cells may be less effective at encoding the direction of travel. A consequence of the deterioration in the rate coding of hippocampal place cells would be that a lower proportion of pyramidal cells would be identified as place cells due to their lower spatial information content. There may also be a reduction in the stability of firing patterns across place cell ensembles, in addition to reduced stability at a single cell level.

## 2. Temporal coding of spatial information will also be impaired in APP$^{NL-G-F}$ mice.

In WT mice the firing of place cells in relation to the theta oscillation of the LFP encodes additional spatial information on a finer scale. The relationship between hippocampal place cell activity and the theta rhythm may be disrupted or distorted in the APP$^{NL-G-F}$ model due to the presence of Aβ pathology. Scant data are available regarding the effects of Aβ pathology on the temporal coding of spatial information in the hippocampus. In a triple transgenic mouse model of AD (3xTg) place cells in the CA1 subregion of the hippocampus showed reduced phase-locking to the theta rhythm of the LFP suggesting that temporal coding could be affected by Aβ pathology

(499). However, since the 3xTg model contains APP, PSEN1 and MAPT mutations, it cannot be certain whether finding was attributable to Aβ or tau pathology.

Temporal coding requires a place cell to have a well-defined field, and a stable theta oscillation to be present in the LFP. Both these features may be altered in the APP[NL-G-F] model and have a secondary effect on temporal coding. Place fields are known to be partially degraded in the APP[NL-G-F] mouse (503) and Aβ pathology in regions which play a role in the generation of hippocampal theta, such as the superficial layers of the EC, Schaffer collateral input from CA3, and the medial septum, may result in changes in theta dynamics including a reduction in theta power and stability. CA1 pyramidal cells are normally theta modulated, exhibit a preference to fire at a particular theta phase, and show theta phase precession (504). All these processes could be disrupted in the APP[NL-G-F] model. It is possible that an impairment in temporal coding could precede alterations in rate coding although to determine this, experiments would need to be undertaken in a range of age groups.

## 3. Aβ plaque burden in APP[NL-G-F] mice will correlate with measures of place cell dysfunction.

Aβ plaques are surrounded by 'toxic haloes' of oligomers (505, 506) which encompass dystrophic and dysfunctional neurites (507, 508). A correlation between Aβ plaque burden and measures of place cell dysfunction is therefore expected in APP[NL-G-F] mice. Such a correlation was found in a previous study of the Tg2576 mouse model of AD where increased

hippocampal plaque burden correlated with place cell deficits and impairment of spatial behaviour (494).

## 4.2 Method

Please see *Chapter 2 (page 120)* for details of animal housing, surgical procedure, basic recording technique, spike sorting and histology.

### 4.2.1 Animals

Eight experimentally naïve, female mice aged 54 to 61 weeks at the time of surgery and weighing between 27 and 52 grams were used in this study. Four were WT littermate controls (C57BL/6J bred from stock from The Jackson Laboratory), and four were homozygous APP$^{NL-G-F}$ knock-in mice on the same C57BL/6J background. The mouse colony was set up by breeding homozygous APP$^{NL-G-F}$ mice with C57BL/6J mice. Subsequently heterozygote breeding pairs were used to allow the use of homozygote APP$^{NL-G-F}$ mice with WT littermate controls.

Mice of a single sex were selected to avoid introducing an additional, and potentially confounding factor, especially given the finding that female APP$^{NL-G-F}$ mice have more extensive Aβ deposition than their male counterparts. Female mice were selected due to availability of mice within the specified age range from our breeding colony. Mice of an advanced age, and therefore mice presumed to have a high Aβ burden, were chosen in order to maximise the chance of identifying the hypothesized Aβ -induced changes in CA1 pyramidal cell function.

## 4.2.2. Experimental apparatus

The experiment took place in two recording environments: a circular arena and a linear track. Mice also rested on a holding platform between recording sessions (*Figure 4.3*). The circular arena was made of wood and painted matte black, with a cleanable black polypropylene floor, and wall height and internal diameter of 48cm. There were no intra-arena visual cues but polarising extra-arena cues were available including a black curtain to the south of the arena, and a light grey blind to the north. To optimise position tracking and to create a non-aversive environment, low light levels were used with illumination provided by dimmable overhead lights and ground level lamps placed evenly around the arena.
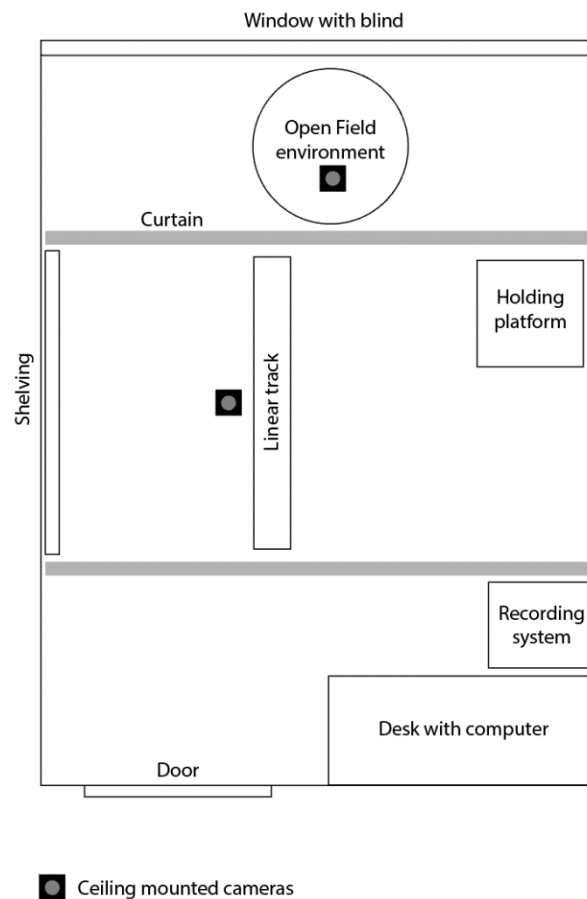


**Figure 4.3 Experimental room layout.** A diagram of the experimental room indicating the relative positions of experimental apparatus, including the two recording environments and the holding platform.

188

The linear track was situated in the same experimental room but was screened from the circular arena by a black curtain. It was made from dark grey matte acrylic and measured 10 x 130 cm, with walls 20cm high. Black metal pillars, floor struts and textured panels made from grey polystyrene sheets, provided intra-maze cues and standard laboratory equipment provided extra-maze cues (*Figure 4.4*). The holding platform where mice rested measured 40 x 40 x 30cm (L x W x H), was made from MDF and contained bedding from the mouse's home cage.
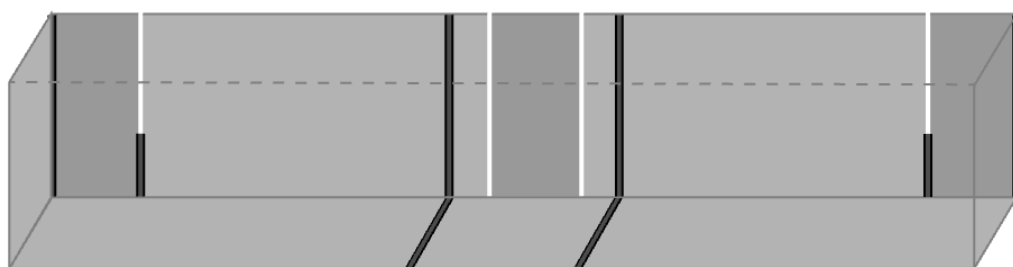


**Figure 4.4 Linear track intra-maze cues.** A view into the linear track which had several intra-maze cues on both the floor and walls. Black lines indicate metal pillars, white lines small gaps in the walls, and grey panels regions of different textures or shades of grey.

### 4.2.3. Experimental protocol

#### *4.2.3.1. Habituation*

Mice received a week-long post-operative recovery period and, provided they had maintained or reattained their pre-surgical weight, habituation then began. Mice were handled and exposed to the holding platform in the experimental room daily for sessions of 20 minutes until they were deemed to be comfortable in the environment and tolerated being connected to a headstage.

### 4.2.3.2. Training and monitoring of electrophysiological parameters

Following habituation (a minimum of three sessions), mice were trained to forage for a liquid food reward (a 1:1 ratio of Aptamil® Soya milk and Nesquik® strawberry powder) in the circular arena. Each day the mice were placed in the arena for two sessions of 10 - 15 minutes with a 5-minute rest period in between. The microdrive was advanced in increments of 30-125µm per day until electrophysiological markers indicated that the electrode tips were in, or close to, the pyramidal cell layer of the CA1 hippocampal subfield. These markers included prominent theta rhythmicity of the LFP, theta modulation of recorded units, sharp wave ripples, pyramidal waveforms, and complex spikes. Once these markers were identified, experimental sessions were recorded using the protocol outlined below and the drives were advanced in smaller increments or not at all. All animals received at least seven days of training prior to the commencement of recording sessions although the exact timing of recording sessions depended on when the electrodes were deemed to be in the correct recording position.

### 4.2.3.3. Recording protocol

The daily recording protocol consisted of three trials in the circular arena. "Trial a" lasted 5 minutes and allowed optimisation of electrophysiological recording parameters. Two further trials, "trial b" and "trial c", lasted 10 - 15 minutes each with the exact timing depending on whether adequate coverage of the environment was achieved in the initial 10 minutes, and whether the mouse was visibly tired. Each mouse subsequently completed two 10-minute trials on the linear track ("linear track a" and "linear track b").

Between each trial the mouse rested for five minutes on a holding platform (*Figure 4.5*).
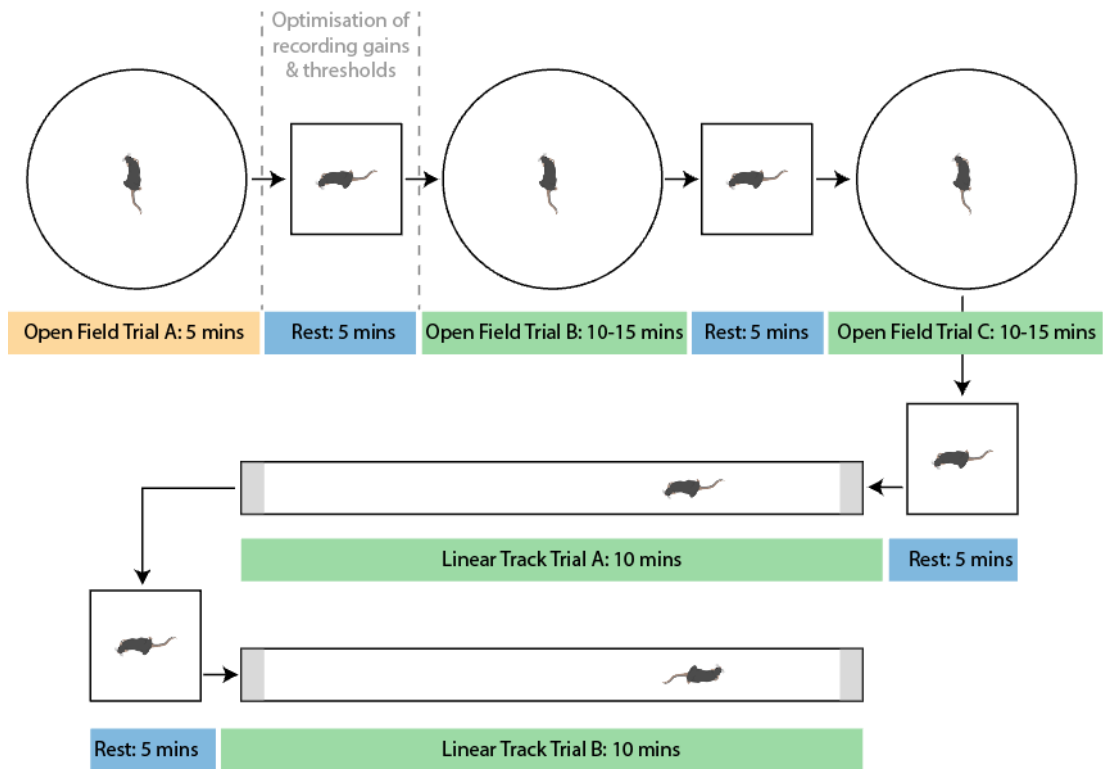


**Figure 4.5 Recording protocol.** Each mouse completed three trials in the circular arena and two on the linear track. Data from trials underlined in green were included in the analysis. Rest sessions are indicated in blue. Data from trial A was not included in the analysis as the recording settings were altered between Open Field Trial A and B.

Prior to each trial the floor of the environment was cleaned. When recording in the circular arena the mouse was initially placed in the centre and the experimenter moved around the circumference in a pseudorandom fashion distributing drops of liquid food reward to encourage the mouse to evenly sample the environment. On the linear track the mouse was placed in the centre and a drop of liquid reward placed at each end of the track. Each drop was replaced when the mouse was visiting the other end of the track. In both environments the tether for the headstage was suspended from the ceiling using a pulley system and/or elastic so that the animal was not required to support its weight and the centre of mass moved freely with the

animal so as not to influence its behaviour. If the mouse was immobile for a prolonged period she was encouraged to move by the experimenter. Across all recording sessions two WT mice required prompting during the open field trials, whereas no APP$^{NL-G-F}$ mice required an additional incentive to move around the environment. The two WT mice which required prompting were also the mice with the highest presurgical weights and therefore may have been less motivated by the edible reward.

Daily recordings continued provided putative place cells were still identifiable in the initial 5-minute screening trial (trial a). Locational firing fields were not used as a means of identifying putative place cells at this stage since it was not known whether APP$^{NL-G-F}$ mice would have cells with fields. Instead, recordings continued if pyramidal cells with complex spikes and theta modulation were identified by eye on screening. If no putative place cells were identifiable, or the same cells had been recorded over three consecutive days then the tetrodes were advanced further into the brain to look for new place cells. Recordings were stopped if no further putative place cells were found, or if 10 or more days of putative place cell data had been collected.

## 4.2.4 Recording session selection

Data were analysed from open field trials b and c and linear track trials a and b. Data from open field trial a was not included since the recording settings were optimised between open field trial a and b. Data were analysed from the 'best' day of recording for each animal. This day was manually selected to achieve the best compromise between three desirable criteria:

1. a similar level of exposure to the recording environments between animals,

2. the best possible sampling of the circular arena during the open field trials with the least number of prompts, and

3. as many cells as possible recorded from the CA1 pyramidal cell layer.

Between groups there was no significant difference in the prior experience of the recording environments on the best day (mean$_{WT}$ +/- s.e.m.$_{WT}$ = 14 days +/- 2.3, mean$_{NLGF}$ +/- s.e.m.$_{NLGF}$ = 10 days +/- 3.2; $t_{(6)}$ = 1.152, p = 0.2930; *Figure 4.6C*), or in the age of the mice (mean$_{WT}$ +/- s.e.m.$_{WT}$ = 60.2 +/- 1.4 weeks, mean$_{NLGF}$ +/- s.e.m.$_{NLGF}$ = 61.6 +/- 2.1 weeks; $U$(N$_{WT}$ = N$_{NLGF}$ = 4) = 6, p =0.6286; Fig. 4.6A), the weight of mice (Mdn$_{WT}$ = 35.9g, Mdn$_{NLGF}$ = 28.7 grams; $U$(N$_{WT}$ = N$_{NLGF}$ = 4) = 2, p = 0.1143; *Figure 4.6B*) or the degree of weight loss (a percentage of the pre-surgical free-feeding weight; Mdn$_{WT}$ = 87.6%, Mean$_{NLGF}$ = 86.2%; $U$(N$_{WT}$ = N$_{NLGF}$ = 4) = 7, p =0.8857) on the best day.
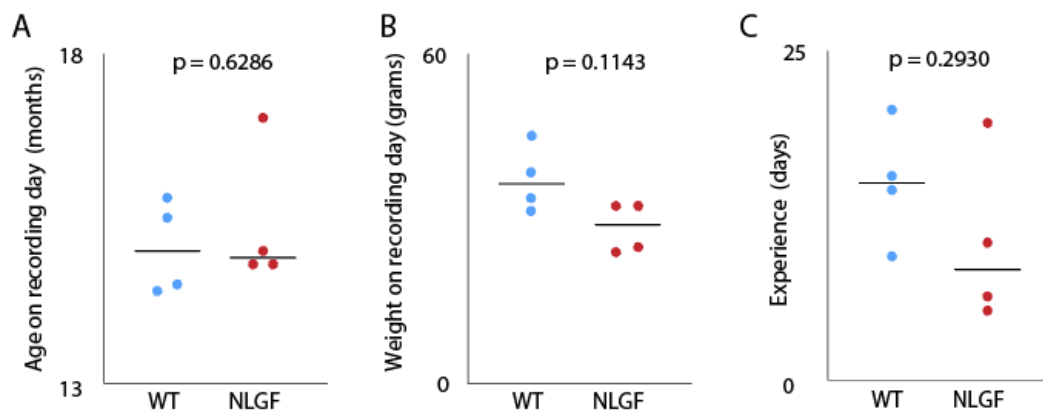


**Figure 4.6 Mouse baseline characteristics**. Mice did not differ significantly in terms of age (*A*), weight (*B*), or experience on the recording day (*C*). WT data are shown in blue and APP$^{NL-G-F}$ data in red. Solid black bar indicates the mean. Statistical tests were selected based on whether the data were parametric. p values from Mann Whitney U testing (*A, C*) and unpaired t-testing (*B*).

### 4.2.5. Analysis

#### 4.2.5.1 Post-processing of position data

For position data recorded in both environments, data points lying outside the environmental boundaries were excluded as mis-tracked points. Raw position tracking data was speed filtered to remove jumpy points. Instantaneous speed was estimated at every 20ms time bin. Speeds greater than 1m/s were deemed to be physiologically impossible and linear interpolation was used to provide surrogate values for mis-tracked coordinates. Position data were smoothed using a boxcar of width 0.4s.

#### 4.2.5.2 Identification of neurons across the two recording environments

Putative clusters were first identified in data from open field trial b using the spike sorting method described in *Chapter 2 (page 127)*. The centres of these clusters were then used to identify the same neurons recorded in open field trial c, and in the linear track trials (using the 'centre cut' command in TINT). Some manual cluster cutting was required to correct for any drift, or to identify cells which fired in only one of the two environments. For each cell observed to fire in both recording environments, the shape of the waveforms and locations of clusters in the cluster space were closely compared to identify clusters which represented two distinct neurons.

#### 4.2.5.3 Neuronal inclusion criteria

Data from neurons where fewer than 100 spikes were collected during the session being analysed were excluded. Neurons were also excluded from analysis if more than 0.25% of spikes violated a 2ms refractory period as

determined by examining the interspike intervals. When analysing theta modulation of pyramidal cell firing, autocorrelograms were only examined for cells in which at least 250 spikes were recorded.

### 4.2.5.4 Classification of pyramidal cells and interneurons

Exploratory scatterplots of variables known to differ between pyramidal cells and interneurons, as recorded in the open field, indicated that mean firing rate and peak-to-trough width were promising candidates to classify cells into these two groups (*Figure 4.7*). Cells were primarily labelled as either pyramidal cells or interneurons based on the peak-to-trough width (spike width) of the highest amplitude mean waveform (*Figure 4.7*). The peak-to-trough width was calculated as the distance in microseconds between the peak of the highest amplitude waveform and the trough occurring after this peak. 300µs was used as a threshold to classify neurons as pyramidal cells or interneurons in accordance with *Cacucci et al.* 2008 (494). Visual inspection of the probability histograms of spike widths for all recorded WT and APP[NL-G-F] cells indicated that this was a reasonable threshold (*Figure 4.7E*). Two curves were fitted to the probability histogram of spike widths across all cells for both genotypes using a Gaussian mixture model on the probability density functions ("fitgmdist" in MATLAB). The point of intersection between the two gaussian curves was 298µs, providing further corroboration for a threshold of 300µs (*Figure 4.7G-I*).
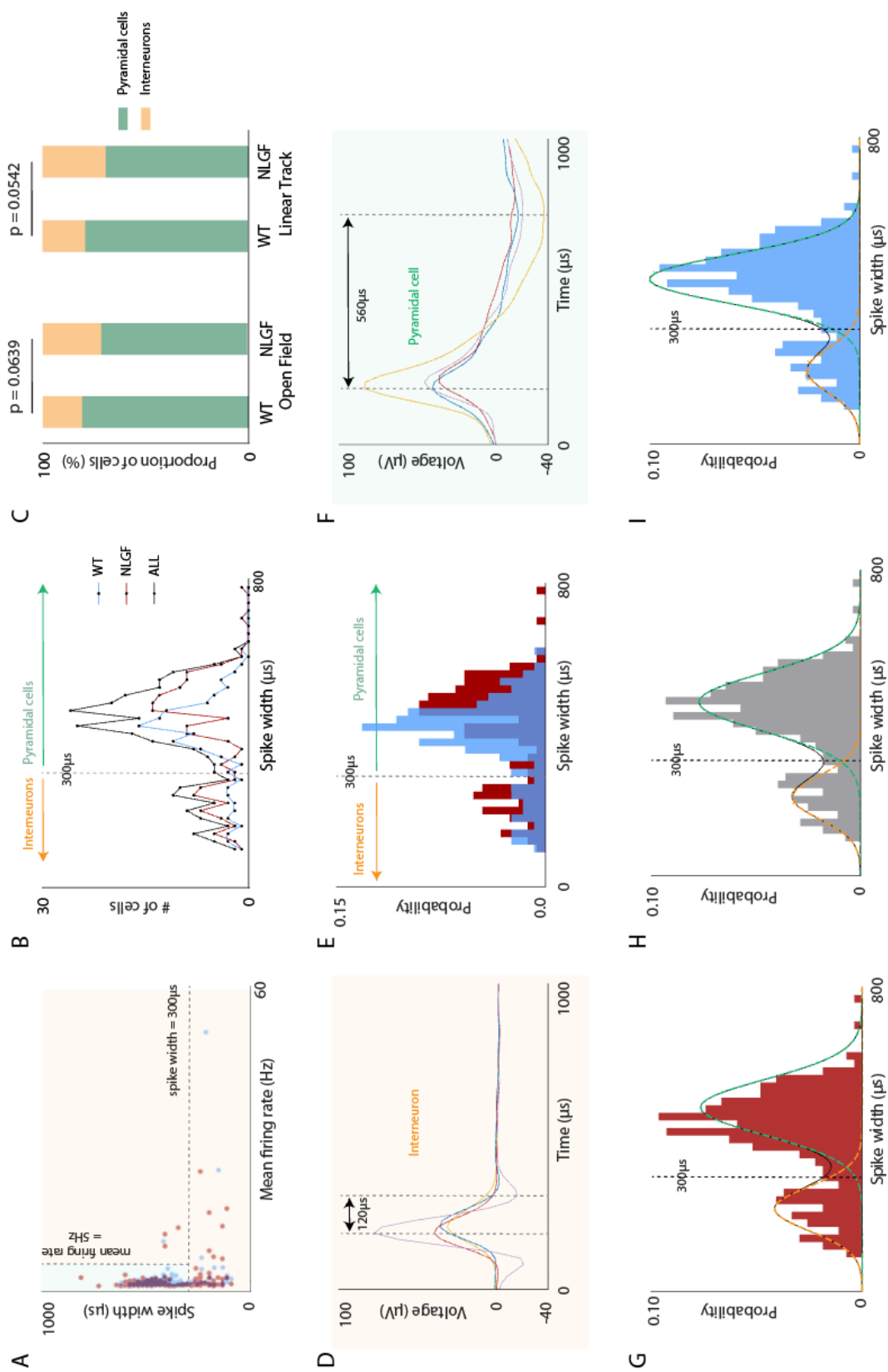
**Figure 4.7 Classification of pyramidal cells and interneurons.** *Full legend page 197.*

196

**Figure 4.7 Classification of pyramidal cells and interneurons.** *A*: Scatterplot of mean firing rate (Hz) versus spike width (μs, peak-to-trough width) for cells recorded in the open field ($N_{WT}$ = 119, blue; $N_{NLGF}$ = 151, red). Cut off values indicated by dotted lines: spike width = 300μs, taken from (491), mean firing rate = 5Hz chosen after scatterplot inspection. Pyramidal cell cluster shaded green ($N_{WT}$ = 96; $N_{NLGF}$ = 107), interneurons shaded yellow ($N_{WT}$ = 96; $N_{NLGF}$ = 107). *B & E*: Spike width histograms for WT (blue) and APP$^{NL-G-F}$ (red) cells, with all cells included in B (black line). *D & F*: Examples of waveforms from a recorded interneuron and pyramidal waveform respectively. Spike width (peak-to-trough width) indicated between the dotted grey lines. **G - I**: spike width probability histograms fitted with a Gaussian mixture model for APP$^{NL-G-F}$ cells (*G*), WT cells (*I*) and all cells (*H*). *C*: There were no significant differences in the proportion of cells classified as pyramidal (green) and interneurons (yellow) in WT and APP$^{NL-G-F}$ mice either in the open field, or on the linear track. P values from Mann Whitney U testing for non-parametric data.

When examining the distributions of spike widths for WT and APP$^{NL-G-F}$ mice there was a significant difference between the two distributions (KS test, D = 0.2323, p = 0.0015), and a significant difference in the mean spike width (mean$_{WT}$ +/- s.e.m.$_{WT}$ = 387 +/- 10.3μs vs mean$_{NLGF}$ +/- s.e.m.$_{NLGF}$ = 403 +/- 11.5μs; $U$($N_{WT}$ = 119, $N_{NLGF}$ = 151) = 7654, p = 0.0365). When fitting separate Gaussian mixture models to the WT and APP$^{NL-G-F}$ spike width distributions the points of intersection between the two Gaussian curves were 283μs and 327μs respectively (*Figure 4.7G,I*). The chosen cut-off of 300μs lies between these two values. On inspection of the scatterplot of mean firing rate (Hz) versus spike width it was noted that there were a small number of outliers from the main pyramidal cell cluster that would be excluded by applying a mean firing rate threshold of 5 Hz (*Figure 4.7A*). Cells with a mean firing rate of greater than 5 Hz were therefore classified as interneurons. Of note, it is possible that cells recorded which did not fulfil the criteria to be considered as pyramidal cells represent axons rather than interneurons, however, currently there are no established methods of differentiating between these two possibilities.

*4.2.5.4.1. Pyramidal cells and interneurons on the linear track*

The same criteria were used to classify cells as pyramidal cells or interneurons on the linear track. When comparing cells recorded in the circular arena with those on the linear track, 5.5% (11/200) of cells were not classified in the same way across the two environments. For these cells the spike widths fell either side of the 300µs cut off. Based on visual inspection of the mean waveforms a decision was made whether to classify each cell as pyramidal or interneuron for the purposes of comparing cells between environments. This resulted in 8 cells being reclassified on the linear track (5 as pyramidal and 3 as interneurons) and 3 in the open field (2 as pyramidal and 1 as interneurons).

### 4.2.5.5. Rate maps

Position estimates were based on the tracking of an LED on the head stage of the mouse and position data processed as outlined above. Position data were speed filtered and only epochs with running speeds of greater than 0.5cm/s were included in the construction of rate maps; at speeds below this, animals were deemed to be stationary.

*4.2.5.5.1. Rate maps in the open field*

When constructing rate maps from data recorded in the circular arena the tracked positions of the mouse were assigned to 2 x 2 cm bins covering the whole environment. Rate maps for each cell were calculated by dividing the number of spikes fired in each bin of the environment by the total time the animal spent in that bin during the trial (the occupancy). Prior to plotting, rate maps were smoothed using a boxcar average over the surrounding 5 x

5 bins, with the firing rate in each bin being equal to the number of spikes in the kernel centred on that bin, divided by the occupancy in the kernel. Rate maps were scaled from a firing rate of zero (dark blue) to the maximum rate of that cell (red) with each colour representing a 10% band of the peak firing rate. Unvisited bins were shown in white. The peak firing rate of the smoothed rate map is shown next to each rate map.

### 4.2.5.5.2. Rate maps on the linear track

When constructing rate maps on the linear track, the speed-filtered spike and position data were used, as for the open field analysis. From the two-dimensional positional data, a one-dimensional coordinate, $\varphi$, was extracted using Pythagoras's theorem, and this represented the mouse's location during the trial in terms of her distance from the left (west) end of the linear track. Neuronal activity recorded during left-bound (west) and right-bound (east) runs on the track were considered separately. Head direction data were used to construct directional rate maps with spike and position data separated according to the heading direction of the mouse. A mouse with a heading direction of 315 - 45° was deemed to be moving east (right-bound runs), and a mouse with a heading direction of 135 - 225° degrees west (left-bound runs). Data were sorted into 2cm bins and individually smoothed using a boxcar moving average over 5 adjacent bins. For each cell, and each direction, the number of spikes firing in each 2cm bin was divided by the occupancy to provide a firing rate. The resultant one-dimensional directional rate map was smoothed, using a boxcar moving average over 5 adjacent bins, prior to plotting with the same colour map/scaling as for ratemaps in the open field.  6cm sections (equivalent to

3 bins) at each end of the track were excluded from further analysis since these regions were poorly tracked and more affected by electrical artefact due to contact between the headstage and the end walls.

### 4.2.5.6. Classification of spatial cells

Pyramidal cells were classified as spatial or non-spatial based on the spatial information content of the cell's rate map.

#### 4.2.5.6.1. Spatial cells in the open field

All pyramidal cells were considered potential '*spatial cells*'; no cells were excluded on the basis of peak firing rate as has been performed in other studies (for example, (494)) since the effect of the APP$^{NL-G-F}$ genotype on neuronal firing properties is largely unknown. Spatial information values were calculated using adaptive smoothing on the unsmoothed rate maps (509). This adaptive binning procedure developed by *Skaggs et al.* (359) was designed to optimize the trade-off between spatial resolution and sampling error; it involves iterating through each bin of an unsmoothed rate map and expanding a circle centred on each bin until the following criterion is met (359):

$$N_{spikes} > \frac{\alpha}{N_{occ}{}^2 \, r^2}$$

(1)

where $N_{spikes}$ is the number of spikes within the circle, $N_{occ}$ is the dwell time of the mouse within the circle, r is the radius of the circle in bins and $\alpha$ is a scaling parameter, set to 200. The value within each bin is set at $Rs \dfrac{N_{spikes}}{N_{occ}}$ where Rs signifies the position sampling rate. The spatial information was computed for each pyramidal cell following *Skaggs et al.* (509):

$$I_{sec} = \sum_x \lambda(x) log_2 \frac{\lambda(x)}{\lambda} p(x) dx$$

(2)

where $I_{sec}$ is the spatial information of the cell in bits per second, x is the spatial location of the animal, p(x) is the probability density of the mouse being at location x, $\lambda(x)$ is the mean firing rate when the mouse is in location x, and $\lambda$ is the overall mean firing rate of the cell calculated as follows:

$$\lambda = \sum_x \lambda(x) p(x) dx$$

(3)

The spatial information in bits per spike was then calculated for each cell where:

$$I_{spike} = \frac{I_{sec}}{\lambda}$$

(4)

Spatial cells were defined as cells with spatial information scores ($I_{spike}$) above chance level (as in (510)). To determine whether a pyramidal cell was significantly spatial the calculated spatial information value was compared with a shuffled distribution. To generate this distribution, which was unique to each cell, a randomly generated number, ranging from 0 to the maximum timestamp, was added to the timestamp of the spikes recorded (wrapping around at the end of the trial). This served to preserve the temporal architecture of neuronal firing but shift the locations at which the cell was deemed to have fired. A spatial information value was then calculated for this shuffled data. This process was repeated one thousand times for each cell to generate a distribution of shuffled spatial information values. If the true spatial information value of a pyramidal cell lay above the 99th

percentile of its shuffled distribution then it was deemed to be significantly spatial (*Figure 4.8*). Since each cell had a unique shuffled distribution, some cells were classified as spatial even if they had spatial information values which were lower than other non-spatial cells.
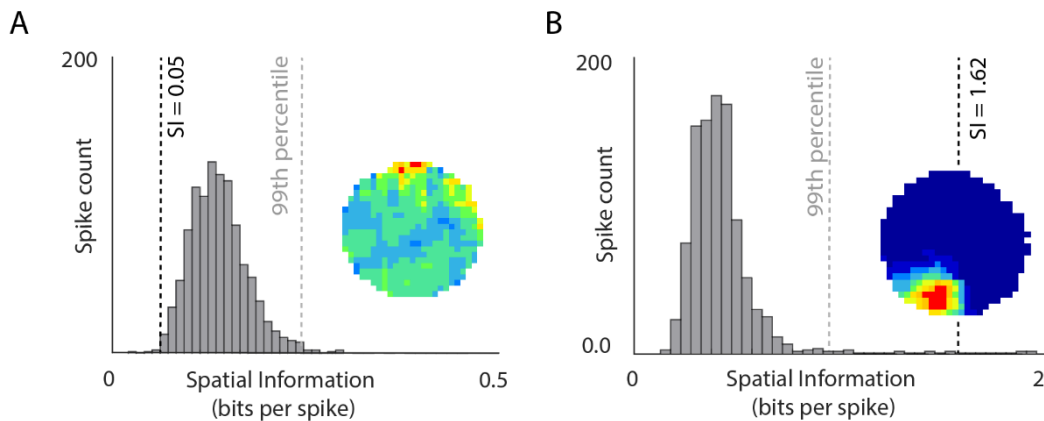


**Figure 4.8 Classification of spatial cells in the open field**. An example of the spatial information value (SI – dotted black line) for a non-spatial (**A**) and a spatial cell (**B**) overlying a shuffled distribution of spatial information values. Grey dotted lines indicate the 99th percentile of the distribution. Smoothed rate maps are inset for each cell.

### *4.2.5.6.2. Spatial cells on the linear track*

For linear track data, spatial information values were calculated separately for left-bound (west) runs and right-bound (east) runs, as is convention, and also for the concatenated left- and right-bound runs to allow a direct comparison of the number of significantly spatial cells in each recording environment. Spatial information values were calculated from smoothed one-dimensional rate maps. To determine whether pyramidal cells had a significantly spatial firing pattern the same shuffling method was used as for the open field data on the concatenated left- and right-bound rate maps. A pyramidal cell was classed as a *spatial cell* if the spatial information value of the rate map from the concatenated left- and right-bound runs lay above the 99th percentile of its shuffled distribution. A *spatial run* was used to describe the significantly spatial firing of a pyramidal cell in one direction

along the track. Not all pyramidal cells with a spatial run in one running direction met the criteria to be classified as a spatial cell (*Figure 4.9*). In analyses where data from both running directions along the track were considered separately the number of spatial runs was used as a primary outcome measure, whereas the number of spatial cells was used when comparing the firing of pyramidal cells across the two recording environments (open field versus linear track).
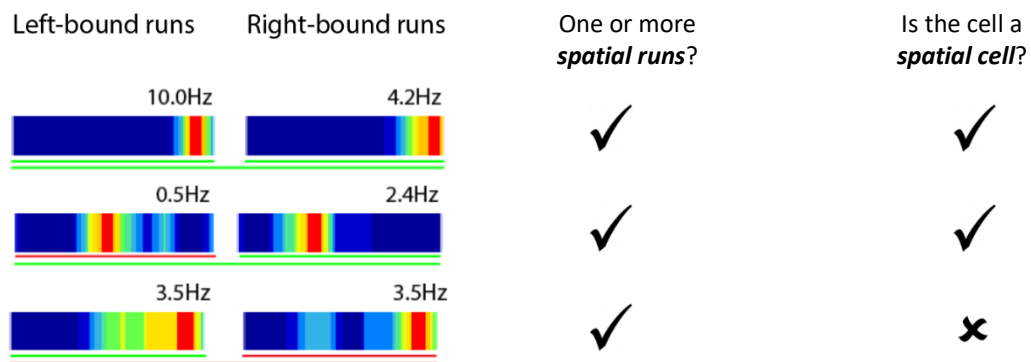


**Figure 4.9 Classification of spatial cells on the linear track**. An illustration of a spatial run versus a spatial cell. Rate maps are presented in pairs (left- and right-bound runs) and scaled from a firing rate of zero (dark blue) to the maximum rate of that cell (red) with each colour representing a 10% band of the peak firing rate (shown above each rate map). Significantly spatial runs are underlined in green, and non-spatial runs in red. The colour of the line extending below both left- and right-bound runs indicates whether the concatenated left- and right-bound rate map, and therefore the cell, was significantly spatial.

### 4.2.5.7. Directionality of cells on the linear track

On narrow linear tracks place cells can be highly directional (330, 392). A cell was defined as bidirectional if it exhibited significantly spatial firing in both directions along the linear track. To determine the extent to which a cell's firing was influenced by the direction of travel a method was used derived from *Battaglia et al.* (403). For each cell that was significantly spatial on both the left- and right-bound runs, the overlap (r) between the unsmoothed rate maps (P(x)) for left-bound runs and the unsmoothed rate

map for right-bound runs, shifted by s bins, was computed according to the following equation (403):

$$r(s) = \frac{2 \sum_\varphi \min (\acute{P}_{right}(\varphi + s), \acute{P}_{left}(\varphi))}{\sum_\varphi (\acute{P}_{right}(\varphi) + \acute{P}_{left}(\varphi))}$$

(5)

where,

$$\acute{P}_{right,left}(\varphi) = \frac{N_{bins} \, P_{right,left}(\varphi)}{\sum_\varphi (P_{right,left}(\varphi)}$$

(6)

$P_{right,left}$ = unsmoothed direction-filtered rate map, $\varphi$ = one-dimensional coordinate along the linear track and $N_{bins}$ = number of bins along the length of the linear track.

The overlap, r, was calculated for values of s (the alignment parameter) ranging from -15 to +15 bins (+/- 30cm), where r values of 0 indicated no overlap and values of 1 complete overlap. For each spatial cell the maximum value of $r_{(s)}$, R, and the value of s at which this occurred, S, were recorded. Spatial cells were classified as unidirectional if the calculated overlap value between left-bound and right-bound runs (R) lay below the 5th percentile of the overlap values (R) from a shuffled distribution. This shuffled distribution was calculated using the same method as that used to determine whether a cell was significantly spatial, except that only data from the left-bound runs was shuffled, and then this was compared to the actual data from right-bound runs to obtain a shuffled distribution of overlap values (400).

### 4.2.5.8. Cell properties

#### 4.2.5.8.1. Spike width and firing rate

Properties compared between WT and APP$^{NL-G-F}$ cells included spike width (peak-to-trough width as previously described), mean firing rate (the number of spikes fired when the animal was moving > 0.5cm/s divided by the trial time in seconds), and the peak firing rate (calculated by taking the bin of the smoothed rate map with the highest firing rate for each cell). The peak firing rate on the linear track when comparing spatial cell populations was taken to be the bin with the highest firing rate in the concatenated left-bound and right-bound rate maps.

#### 4.2.5.8.2. Burstiness

All included neurons were classified as *'bursty'* or *'non-bursty'* based on the interspike interval (ISI) histograms, and a burstiness score was assigned. The method and underlying rationale is outlined in *Ebbesen et al.* (511). The interspike intervals between 0 and 60ms were binned into 2ms bins, and the area of the histogram was normalised to 1 to produce a probability distribution histogram for each neuron (*Figure 4.10, page 202*). This allowed comparison between neurons. A principal components analysis (PCA) was performed on the matrix of the ISI probability distributions of all neurons (0 - 60ms) (MATLAB, 'pca'). Neurons were then assigned to two clusters using a k-means clustering algorithm on the first three principal components (MATLAB, 'kmeans) (*Figure 4.10C, page 202*). Four cells were not classified due to insufficient data.

Following the method outline by *Ebbesen et al.* (511), a linear discriminant analysis performed in MATLAB ('classify') was undertaken to determine the

optimal linear discriminant (Fishers Linear Discriminant) i.e., the plane which best separated the two clusters in a three-dimensional scatter plot of the principal components. Training on 80% of the data and testing on the remaining 20% resulted in a good separation of the two clusters. A burstiness score was assigned to each neuron which was calculated by computing the shortest distance between the plotted point for each neuron in the three-dimensional cluster space (principal components 1,2 and 3), and the plane separating the two clusters (i.e., the optimal linear discriminant). To ensure the distribution of these burstiness scores was bimodal, reflecting the presence of two classes of neuron ('bursty' versus 'non-bursty'), probability density functions for Gaussian mixture models with between one and four underlying Gaussian curves were fitted and the fit of each compared using the Akaike information criterion (AIC) (512) ('fitgmdist' in MATLAB). The model with the best fit was bimodal ($AIC_{unimodal}$ = 1599.9, $AIC_{bimodal}$ = 167.1, $AIC_{trimodal}$ = 1577.9, $AIC_{quattromodal}$ = 1599.5). The criteria for a guard zone were selected based on the two Gaussian distributions underlying the burstiness distribution; excluding cells where the burstiness score was between -3.65 and -2.75 resulted in a 95% probability of correctly classifying a neuron as bursty or non-bursty (method adapted from *Latuske et al.* (513)) (*Figure 4.10E*). The proportion of bursty CA1 pyramidal cells, as determined by the linear discriminant analysis and burstiness score, was compared between WT and APP$^{NL-G-F}$ mice using a $\chi^2$ test of equal proportions. Burstiness scores of CA1 pyramidal cells were compared between WT and APP$^{NL-G-F}$ mice using a Mann Whitney U test.
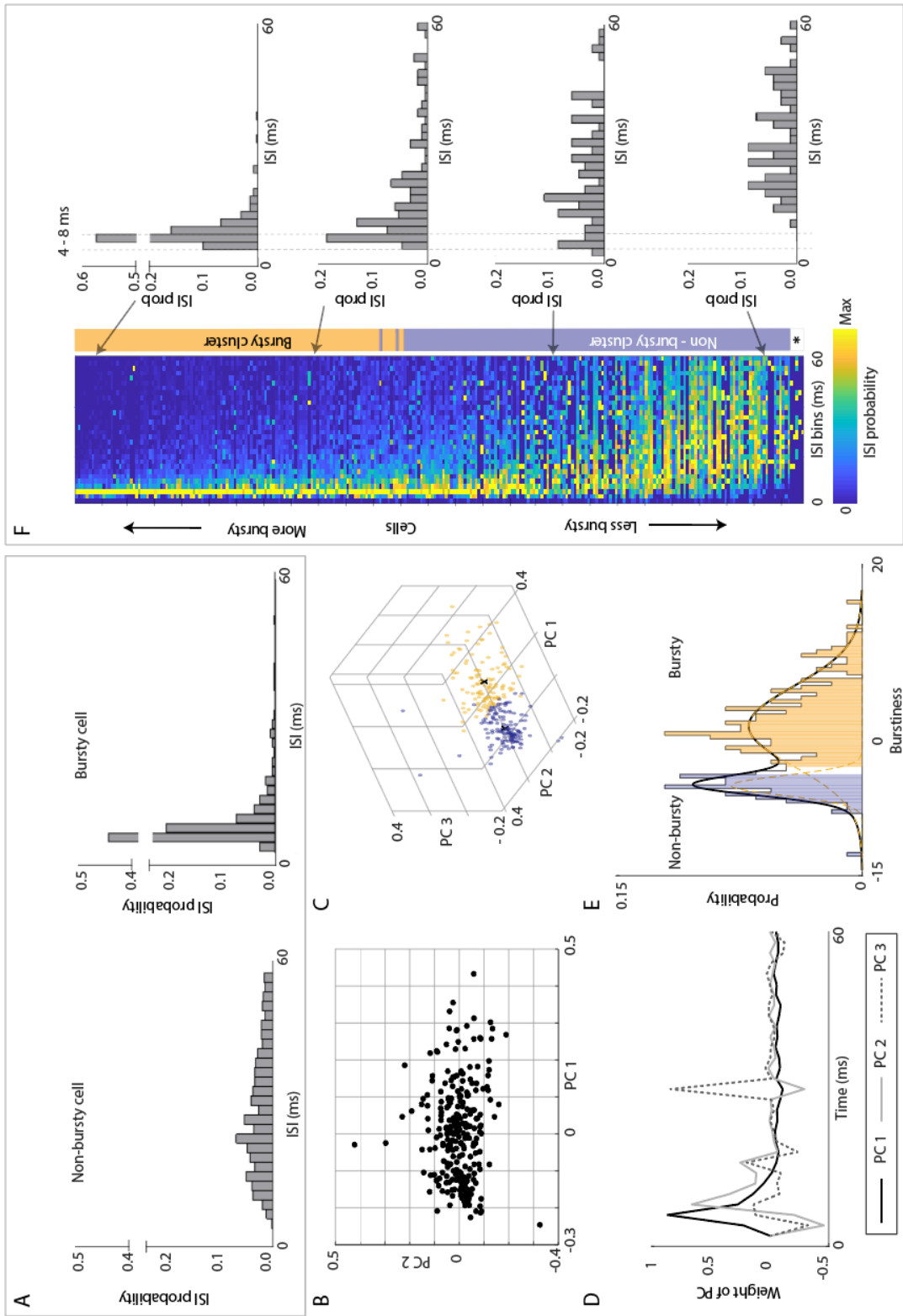
**Figure 4.10 Classification of cells as bursty and non-bursty.** *Full legend page 208.*

**Figure 4.10 Classification of cells as bursty and non-bursty.** *A*: Representative probability density functions of the distribution of interspike intervals (ISI) for a non-bursty (left) and a bursty (right) neuron (bin width, 2ms). *B*: Scatterplot of the first two principal components (PC1 and PC2) obtained from a Principal Components Analysis of ISI distributions (black dots). *C*: Three-dimensional scatterplot of the first three principal components, assigned to two clusters using a *k*-means clustering algorithm. The centre-of-mass of the bursty neurons (yellow) and non-bursty neurons (blue) are indicated by black crosses. *D*: the first three principal components of the ISI histograms. *E*: Projection of ISI distributions onto the optimal linear discriminant of the two clusters (burstiness) revealed a bimodal distribution of bursty (yellow) and non-bursty (blue) neurons. *F*: *Left*. ISI histograms of all classified neurons, sorted by burstiness (scaled to the maximum probability for each neuron for visibility). * Indicates 4 neurons which were not classified due to insufficient data. *Right*. Example ISI histograms for neurons with varying degrees of burstiness. Bursty neurons tend to fire bursts at 125 - 250Hz (4 - 8ms intervals).

### *4.2.5.9. Place fields*

#### *4.2.5.9.1. Place fields in the open field*

The presence of one or more place fields was determined by looking for contiguous bins of the smoothed rate maps which exceeded a given firing rate threshold. Previous studies have used different rate thresholds; in their study of place cells in a mouse model of AD *Cacucci et al.* used a threshold of the mean firing rate (494), whereas other studies have used alternative thresholds, including 20% of the peak firing rate (356, 398) and 50% of the peak firing rate (442).

An exploratory analysis was undertaken to determine the optimal firing rate threshold and minimum field size to use to define a place field in the open field. Specifying a minimum field size prevents small, isolated regions with spurious high firing rates being identified as fields. Cell identifiers for all WT and APP$^{NL-G-F}$ spatial cells were removed and data for these cells were pooled. Place fields were identified using a range of firing rate thresholds and minimum field size in bins. The relationship between total field size and spatial information ($I_{spike}$) was evaluated through the inspection of scatter

plots and calculation of the Pearson correlation coefficient (R). It was expected that, in most cases, smaller place fields would be identified in pyramidal cells with a higher spatial information value, and this observation helped guide the choice of place field criteria; a lower firing rate threshold, and a smaller minimum field size, provided a stronger negative correlation between these two variables (*Table 4.2*). Inspection of the rate maps, annotated with the fields identified, indicated that a compromise needed to be struck, since a lower firing rate threshold and smaller minimum field size resulted in the labelling of small regions of spurious firing as fields (*Figure 4.11, page 211; Figure 4.12, page 212*).

| Rate threshold | Minimum Field Size (% of total environment) | | |
|---|---|---|---|
| | 0% | 5% | 10% |
| 10% x PFR | -0.90 | -0.89 | -0.89 |
| 20% x PFR | -0.79 | -0.77 | -0.76 |
| 30% x PFR | -0.69 | -0.68 | -0.68 |
| 50% x MFR | -0.91 | -0.90 | -0.90 |
| 100% x MFR | -0.81 | -0.77 | -0.73 |
| 200% x MFR | 0.66 | 0.62 | 0.50 |

**Table 4.2 Defining place fields in the open field.** Pearson R values for the correlation between field size and spatial information (bits/spike) for different place field thresholds. PFR, peak firing rate; MFR, mean firing rate.

The optimal mean firing rate criteria (100% x mean firing rate, minimum field size 5% of the environment) were then compared to the optimal peak firing rate criteria (20% of the peak firing rate, minimum field size 5% of the environment) (*Figure 4.13, page 214; Figure 4.14, page 215*). The peak

firing rate criteria were selected to define place fields in the open field; although both criteria appeared to identify place fields with a similar degree of accuracy, significant differences were identified between the mean firing rates of WT and APP$^{NL-G-F}$ spatial cells but not the peak firing rates (*see later, page 234*) suggesting that criteria based on the peak firing rate may be more appropriate.

The number, field size and within-field firing rate were calculated for each spatial cell identified in the open field. The size of the field was defined as the percentage of the environment covered by the field. The mean within-field firing rate was calculated by dividing the number of spikes fired within the boundaries of the field when the animal was moving, by the total time spent by the animal within the field (occupancy). Data from unvisited bins were not included when calculating field width or mean rate in field.

### 4.2.5.9.2. Place fields on the linear track

Place fields were defined on the linear track in a similar way to the open field. Left- and right-bound runs were analysed separately, and a field was defined as three or more contiguous bins (covering approximately 5% of the environment) in which the firing rate exceeded a pre-determined threshold. This criterion was relaxed if there was a single bin where the firing rate dipped below the threshold provided the rate exceeded this threshold in both adjacent bins. For the majority of analyses the firing rate threshold was defined as 20% of the peak firing rate, as in the open field analysis, to ensure results were broadly comparable. However, for the phase precession analysis alternative rate thresholds were explored (*page 222*).
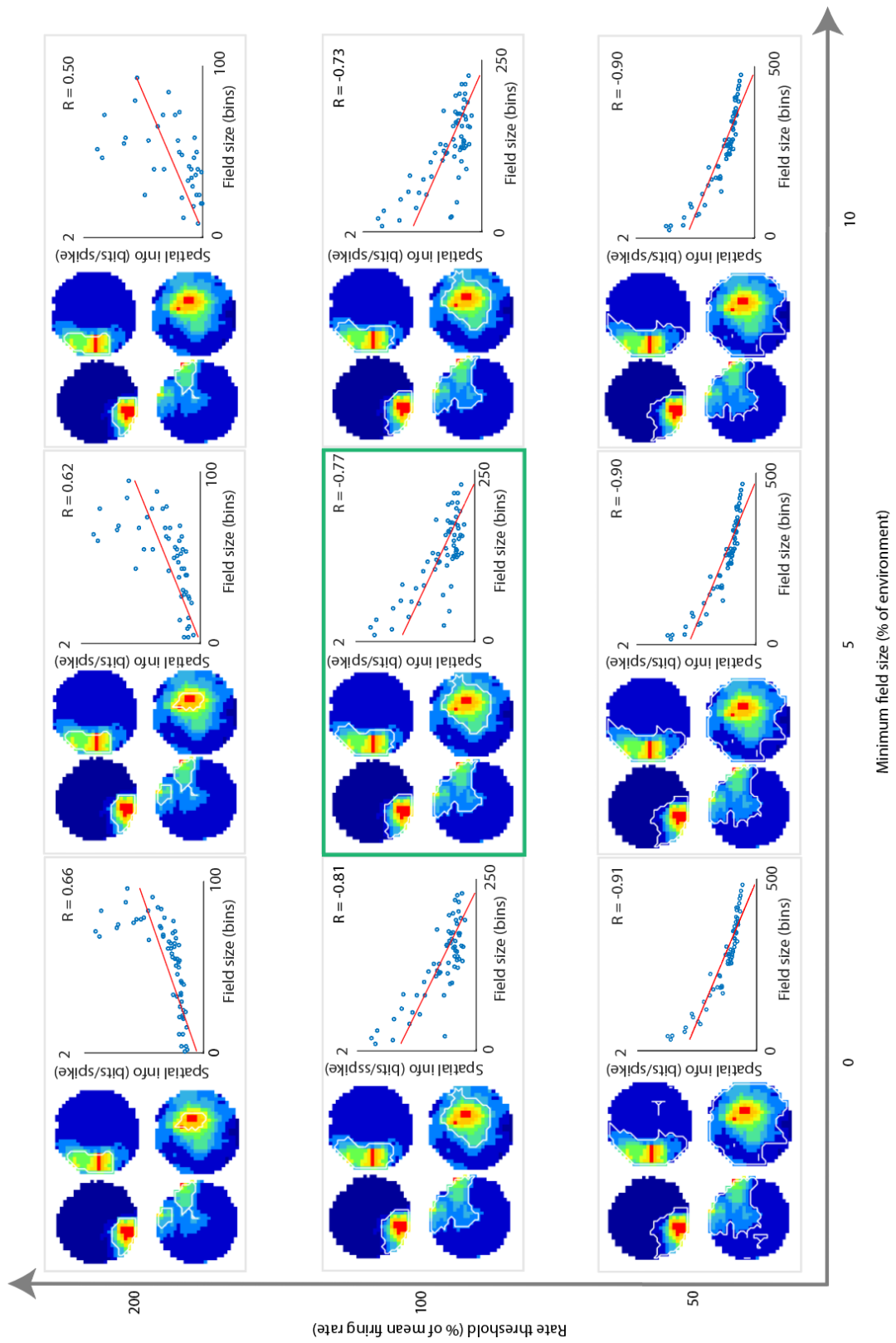
**Figure 4.11 Classification of place fields using a mean firing rate threshold.**
*Full legend page 213.*

211

**Figure 4.11 Classification of place fields using a mean firing rate threshold.** An



**Figure 4.12 Classification of place fields using a peak firing rate threshold.**
*Full legend page 213.*
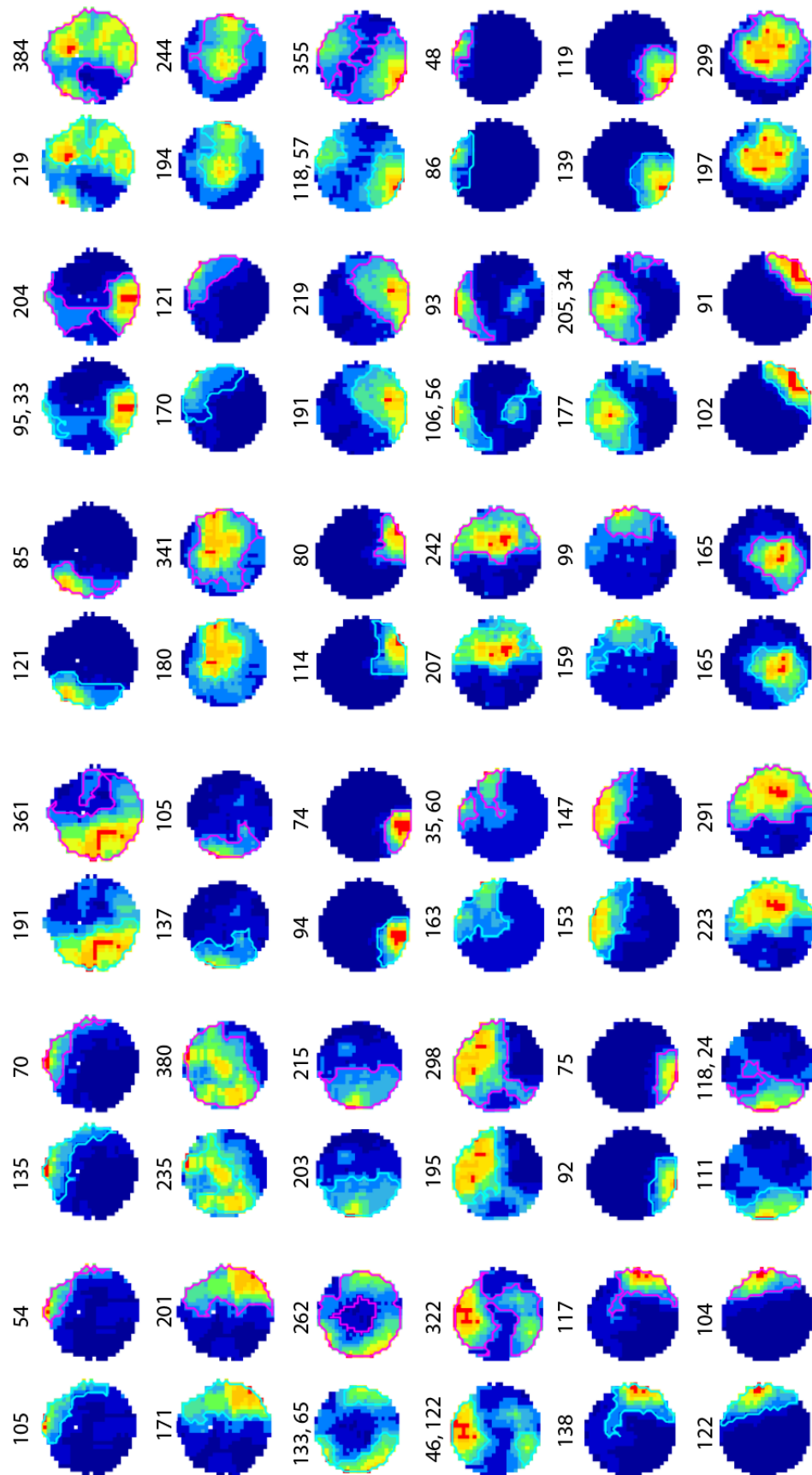
**Figure 4.13 A comparison of the optimal mean and peak firing rate criteria for place fields in wild-type mice.** *Full legend page 213.*

213
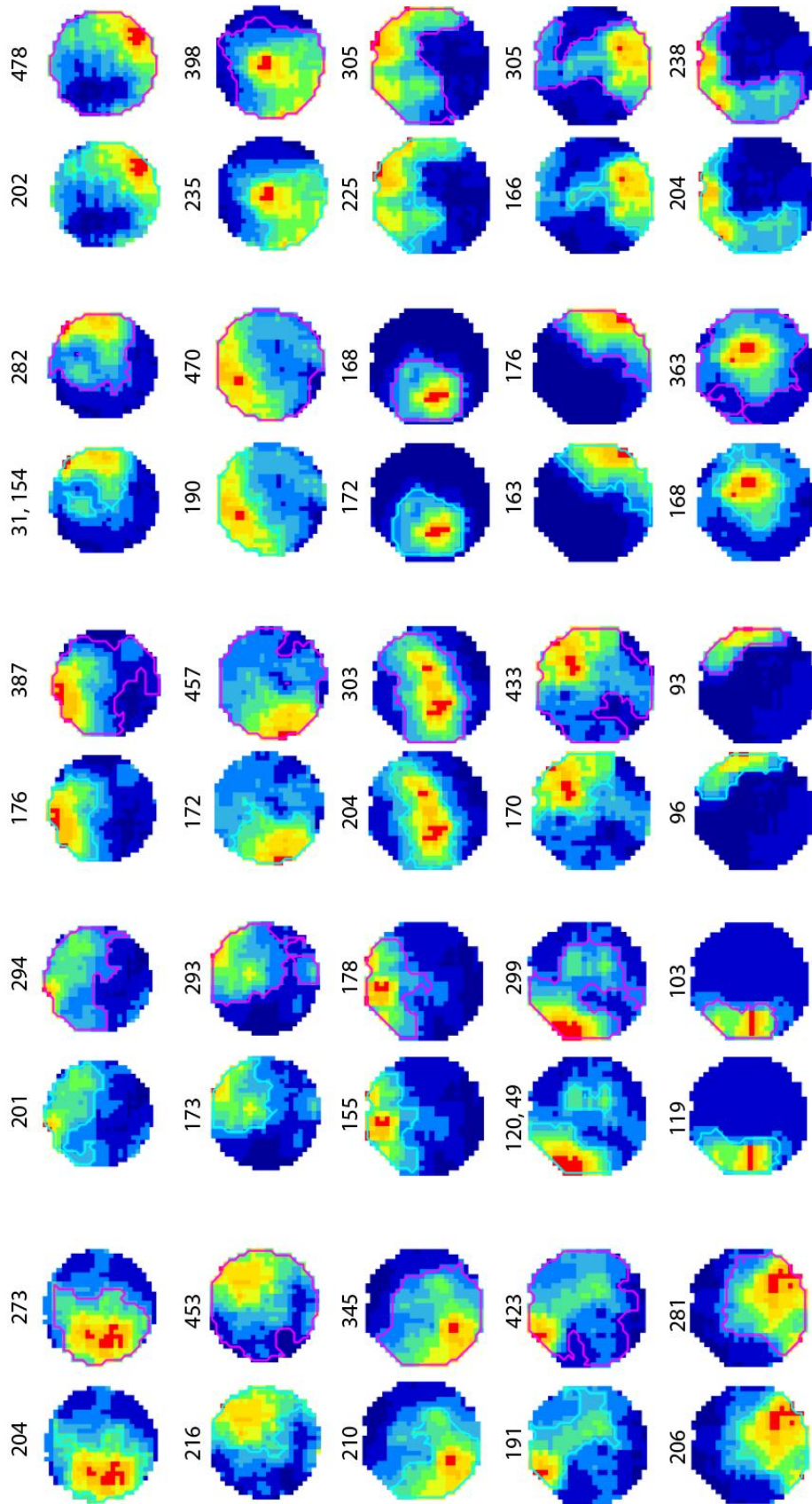
**Figure 4.14 A comparison of the optimal mean and peak firing rate criteria for place fields in APP^NL-G-F mice.** *Full legend page 213.*

214

The field centroid (centre of mass) on the linear track was defined as a function of the rate map, i.e., the dwell time weighted spike distribution (396). Each position bin within a field was weighted according to the firing rate within that bin, and the mean of this distribution (expressed in bin number) was taken to be the centre of mass of the field:

$$\sum_{i=1}^{n} x_n f(x_n) / \sum_{i=1}^{n} f(x_n) \tag{7}$$

, where f($x_n$) is the firing rate in the bin at $x_n$.

### 4.2.5.10. Spatial correlations

Since mice completed two trials in each recording environment, it was possible to examine the stability of cells by calculating the spatial correlation between the rate maps generated in each of the trials (as in 396). A spatial correlation was computed for all cells where at least 100 spikes were recorded during each of the trials. Bins were not included if they were unvisited in either trial, or if there was a firing rate of zero within the bin across both trials. A Pearson correlation was performed on the paired rate maps. For spatial correlations on the linear track, left- and right-bound rate maps were considered separately.

### 4.2.5.11. Spatial coherence

Spatial coherence, a measure of the smoothness of the place field, was calculated for pyramidal cells by taking an unsmoothed rate map and calculating the Pearson correlation of all occupied bins with the mean of their neighbouring bins (514).

### 4.2.5.12. Population Vector Correlation Analysis

To compare the stability of the population-level activity of WT and APP[NL-G-F] cells, a population vector correlation analysis was conducted comparing the firing of neurons between paired trials (trial b versus trial c in the open field, linear track trial a versus linear track trial b on the linear track). This method involves stacking the rate maps from the chosen cell population and calculating the correlation of the rates of all cells in each bin of the map between the two trials (*Figure 4.15*) (360). Cells with a higher firing rate may, therefore, have a larger effect upon the result than cells with a lower firing rate. A population vector correlation of -1 indicates that the population of recorded neurons display completely distinct firing patterns between the two trials, whereas a score of +1 indicates identical firing patterns between the two environments (363).
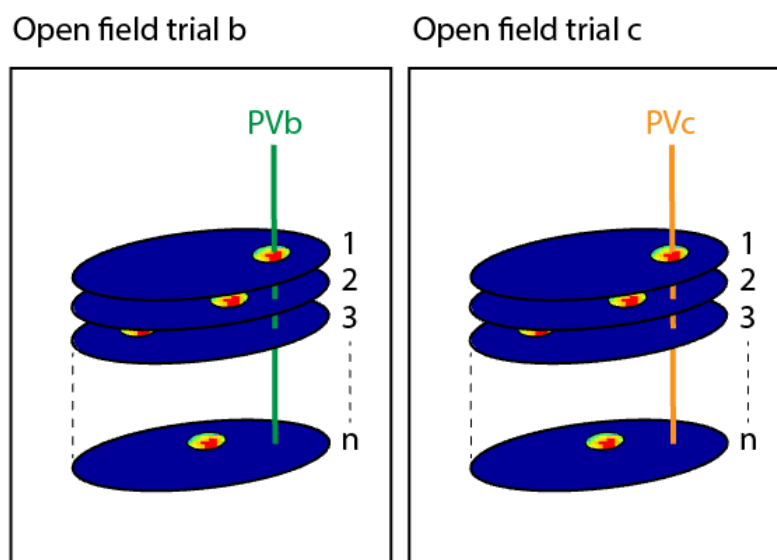


**Figure 4.15 Population vector correlation analysis.** The rate maps from the cell population of interest are stacked from 1 to n (where n is the number of cells in the population). The firing rates in the same bin across all rate maps corresponds to a single population vector (PVb and PVc). The correlation between the population vectors in open field trial b and open field trial c provides a measure of the stability of the population-level activity.

### 4.2.5.13. Analysis of the Local Field Potential

The power in the LFP at different frequency bands was assessed for each mouse using data from linear track trials a and b on the 'best day' of recording. Local field potentials recorded at 4.8KHz were down sampled to 1.2KHz, converted into volts using the known gain settings for the recorded channel, and a power spectrum constructed for each mouse using a fast Fourier Transform (FFT). This was smoothed using a Gaussian filter with kernel width 2Hz and σ of 0.5Hz. These parameters were chosen since they have been used as standard in publications both from the O'Keefe group and collaborators (for example see (515)). To examine theta power, only LFP data where the mouse was non-stationary (i.e., travelling at speeds of greater than 0.5cm/s) were included. A lower speed threshold was selected than in other studies from our group to account for the older age of the mice tested and their low running speeds when compared to younger mice. To control for impedance differences between tetrodes and to allow comparison of power spectra between mice, the speed-filtered power spectra were normalised to the total power in the 4-125Hz band. This normalisation envelope was selected following inspection of the raw power spectra for all mice and identification of the frequencies corresponding to the first trough (MATLAB 'findpeaks' on smoothed data, *Figure 4.18, page 217*). The aim was to exclude the initial peak, representing noise, from the normalisation envelope. The peak theta frequency was calculated for each mouse by finding the frequency with maximal power in the range 4 - 12Hz, and the theta power index was determined by calculating the total power

within a 2Hz bin centred on the peak theta frequency and dividing this by the total power in the remaining 4 - 125Hz power spectrum.

### 4.2.5.14. Theta modulation

Theta modulation was examined in speed-filtered data collected from the linear track trials on the 'best day' of recording. Temporal autocorrelograms were constructed for each pyramidal cell by summing the number of spikes firing within each 5ms bin from 0 to 500ms, in relation to a spike firing at time 0ms. These values were then divided by the trial length to provide the rate of occurrence for each interval in spikes per second. Cells which fired fewer than 250 spikes were not included in the theta modulation analysis. Temporal modulation of firing in the theta frequency range was assessed using two methods.

First, a theta modulation index (TMI) was calculated as described in (516). The TMI was defined as the difference between the theta modulation trough (the mean of autocorrelogram bins 50 – 70ms) and the theta modulation peak (the mean of autocorrelogram bins 100 – 140ms) divided by their sum (*Figure 4.16A*). If there were no spike occurrences within either range the TMI was not computed.

Second, a method was devised for calculating the a measure of theta power in relation to power in the remaining power spectrum. A power spectrum was constructed for each temporal autocorrelogram using a FFT and smoothed using a Gaussian filter with kernel width 2Hz and σ of 0.5Hz. A 'theta signal-to-noise ratio' was calculated for each pyramidal cell as follows: the total power within the 'theta peak', i.e., a 2Hz bin centred on the peak of the temporal autocorrelogram power spectrum within the theta range (4 -

12Hz), was computed and then divided by the sum of the 4 – 125Hz temporal autocorrelogram power spectrum excluding the theta peak (*Figure 4.16B*). The theta peak was identified using the MATLAB function 'findpeaks', and a minimum peak width was specified as 0.023Hz (10 bins) to prevent small baseline oscillations being spuriously identified as peaks. If no peak was identified within the theta range the maximum power within the range, and the corresponding frequency, were used instead.
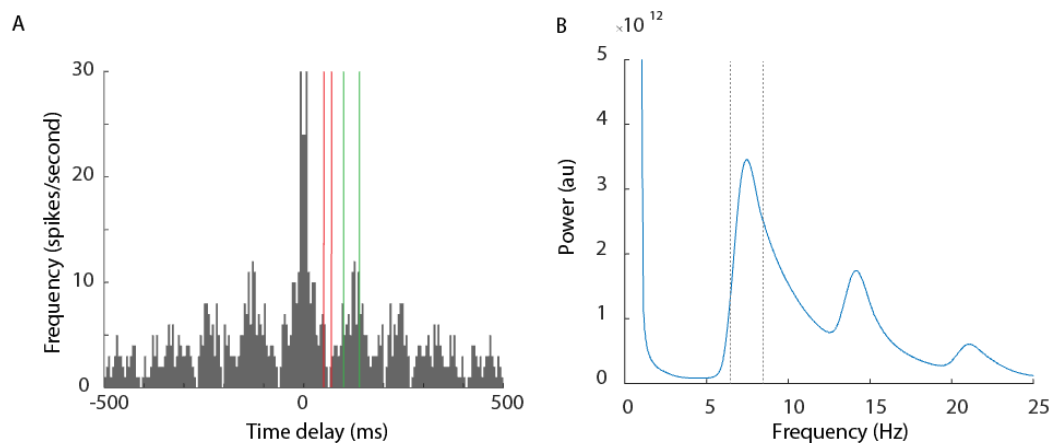


**Figure 4.16 Theta modulation index and theta signal-to-noise ratio.** An example of how the theta modulation index (TMI) (***A***) and theta signal-to-noise ratio (***B***) are calculated for a spatial theta-modulated cell (M719648 5_15). ***A.*** A temporal autocorrelogram showing theta modulation with the theta peak lying between the green lines (100 – 140ms) and the theta trough between the red lines (40 – 70ms). The TMI is the difference between the mean of the theta peak and the theta trough, divided by the sum of the two. **B.** A power spectrum of the temporal autocorrelogram of the same cell showing a peak for the frequencies corresponding to theta and two theta harmonics. The theta signal-to-noise-ratio was calculated as the power within the theta peak (indicated by the grey dotted lines) divided by the power in the remaining 4 – 125Hz spectrum excluding the peak.

### *4.2.5.15. Bandpass filtering of the LFP for theta frequencies*

Local field potentials, previously down sampled to 1.2KHz and converted into volts, were detrended and digitally filtered for theta (6 -10Hz) (as in (398)) using a 1200-tap, Blackman windowed, bandpass filter with a passband of 4-12Hz (Matlab function 'fir1') (*Figure 4.17*). An analytic signal was constructed using the Hilbert transform (517), taking the form:

$$s_a(t_k) = s(t_k) + iH[s(t_k)]$$

(8)

where H specifies the Hilbert transform, $s(t_k)$ is the filtered LFP signal, $t_k = k\Delta$, where $k = 1,...,k$ indexes the time-step and $\Delta$ is the inverse of the sampling rate. This was used to assign a phase angle to each spike with 0 radians corresponding to the positive to negative crossing of the EEG.
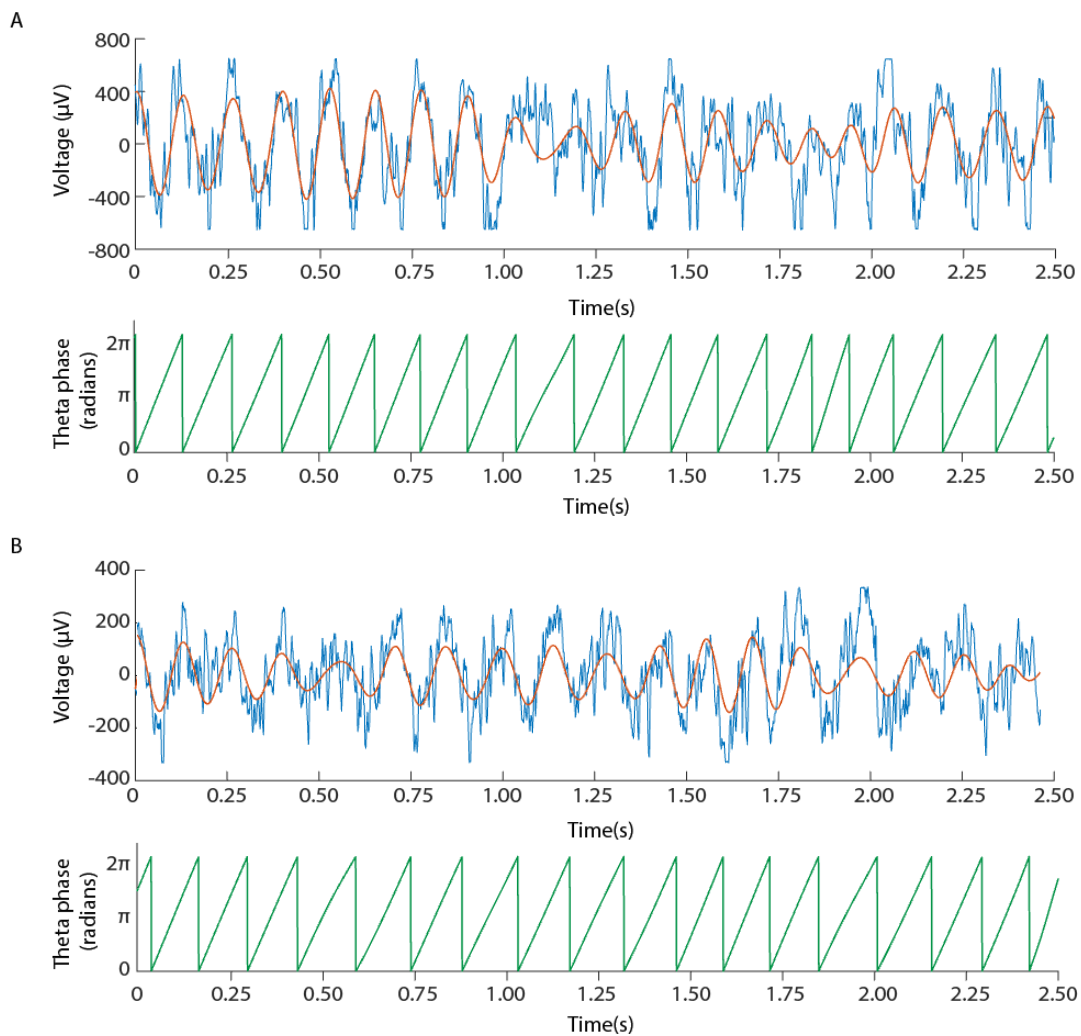


**Figure 4.17 Filtering the LFP for theta frequencies.** Raw LFP traces (blue trace, upper plot) were filtered for theta in the 6 - 10Hz range. An analytic signal was constructed using the Hilbert transform (red trace, upper plot) and this was used to assign a phase angle (green trace, lower plot). Examples are shown for a WT (**A**) and APP$^{NL-G-F}$ (**B**) mouse.
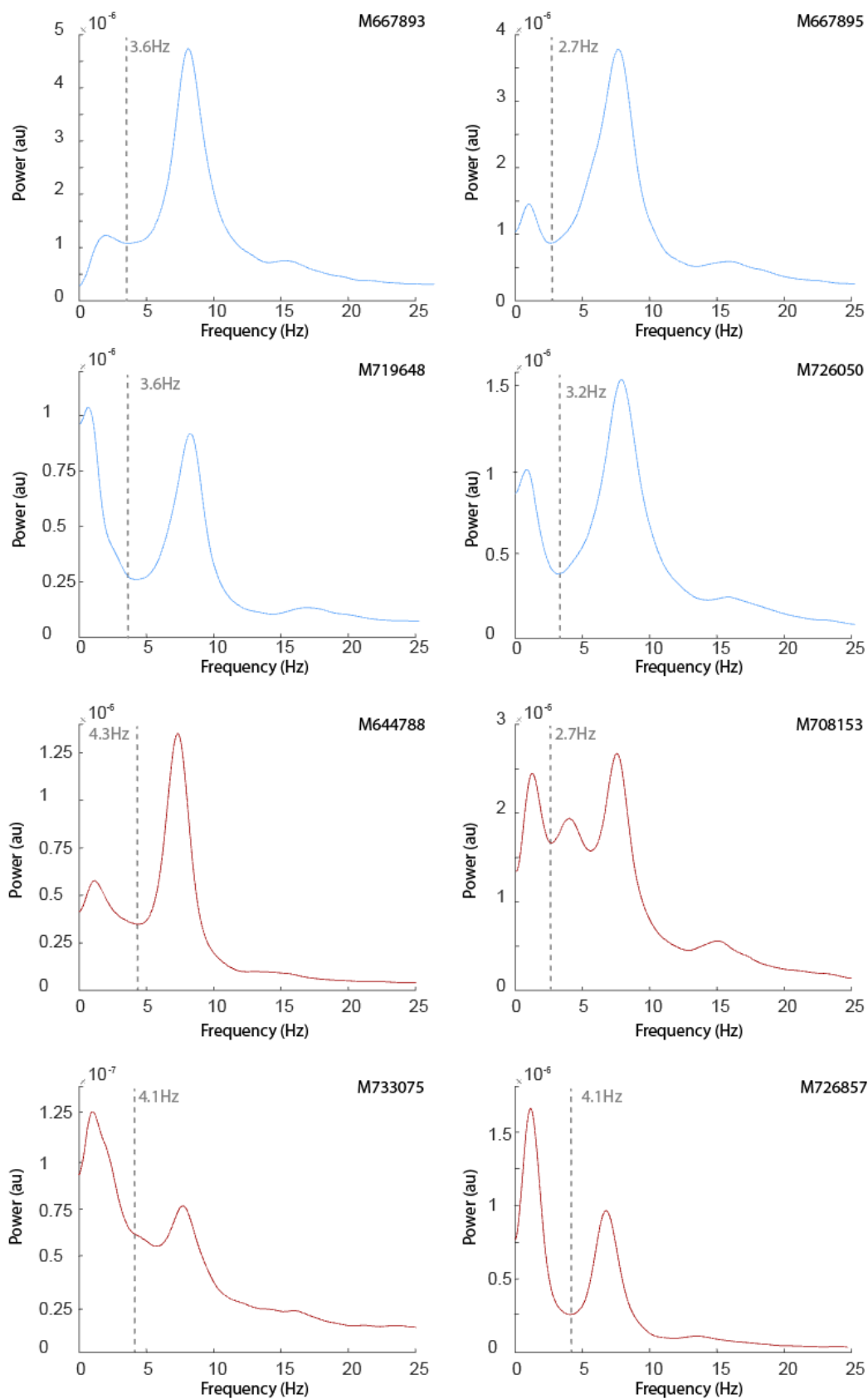
**Figure 4.18 Raw power spectra: selecting the normalisation envelope.** Raw power spectra are shown for all mice in the range 0 – 125Hz (prior to normalisation). Data were speed filtered at 0.5 cm/s. Mouse ID is shown at the top right of each plot. The dotted grey line corresponds to the first trough in each spectrum.

### 4.2.5.16. Phase-locking analysis

Data from the linear track recordings were used to analyse phase-locking in pyramidal and spatial cells. For the purposes of this analysis, phase-locking was quantified as the circular concentration of the resulting phase vector distribution (407). This was defined as the mean resultant vector calculated from N unit-length vectors with phase angles equal to the theta phase angles to which each of the N spikes from the cell were aligned ('circ_r' in MATLAB CircStat toolbox (518)). The length of the resultant vector reflected the *phase concentration*, which represented the extent to which a cell was phase-locked and ranged from 0 (no phase-locking) to 1 (perfect phase-locking) (519). The angle of the resultant vector was equivalent to the circular mean of all N phase angles and represented the phase of preferred firing ('circ_mean' in MATLAB CircStat toolbox). To determine whether a cell was significantly phase-locked, Rayleigh's test was performed to ascertain whether the distribution of spike phase angles deviated significantly from the von Mises distribution. A p value of less than 0.01 was required for statistical significance as is standard when using this test (520). To compare the preferred theta phases of pyramidal cells, a multi-sample test for equal means, the equivalent of a one-way ANOVA for circular data, was performed ('circ_wwtest' in MATLAB CircStat toolbox).

### 4.2.5.17. Phase precession analysis

Data were used only from linear track trials for simplicity of analysis. Speed-filtered data were used, and data were only included when the animal was travelling left or right along the track (i.e., when the heading direction of the animal was between 315 – 45 degrees, or 135 – 225 degrees).

As a starting point, the same definition of a place field was adopted as used in previous analyses, i.e., a cell's place field was defined as three or more contiguous bins on the linear track (covering >5% of the environment) in which the firing rate of that cell exceeded 20% of its peak firing rate. Data were analysed from all significantly spatial runs (i.e., each cell could contribute up to two data points) with left- and rightwards runs considered separately. In addition, each field was initially considered separately, with a normalised in-field position calculated for each spike within a given field. This took into consideration the width of the field and the direction of travel, such that a value of 0 indicated that an animal was just entering the place field, and a value of 1 that an animal was just leaving the place field. Place fields in which the cell fired fewer than ten spikes were not included in further analyses.

It was unclear when using this method whether or not to include data from significantly spatial runs where the width of the identified place field (or the combined width of place fields) occupied a large proportion of the linear track. The use of alternative place field definitions was investigated, and the analysis repeated using a new place field definition. More detail is provided alongside the results (*page 282*). In all analyses a spatial field was always defined as three or more contiguous bins on the linear track (covering >5% of the environment) in which the firing rate of that cell exceeded the chosen firing rate threshold.

Phase precession analysis methods followed the principes of those outlined in Schmidt et al. 2009 (407). In plots of spike phase versus in-field position, a best fit line was found using a circular linear regression method as outlined

in (521). Using this method, a linear regression model was fitted to circular-linear data by minimising the circular error between the measured and predicted phase angles. The slope of the resulting regression line was then used to scale the linear variable and transform it into a circular variable. A correlation coefficient was calculated based on the phase angles unwrapped around the best fit line. A p value was generated by calculating the correlation coefficients for 10,000 random permutations of phase angle versus in-field position/ time through field. The true correlation coefficient was then compared to the distribution of the simulated values to generate a p value. A cell was considered significantly phase-precessing if it had a p value of less than 0.05 and a negative circular correlation coefficient.

## 4.3. Results

Electrophysiology recordings were performed in the left CA1 hippocampal subregion of 8 freely moving mice ($N_{WT} = 4$; $N_{NLGF} = 4$) as they explored a circular arena (open field) and ran lengths of a linear track. Data were analysed from the best day of recording.

### 4.3.1. Histology

#### *4.3.1.1. Locations of recording tetrodes*

Histological examination of all 8 mice confirmed that tetrodes were implanted into the CA1 subfield of the hippocampus (*Table 4.3, Figure 4.19*). In one mouse (M667893) the tetrodes had been lowered through the stratum radiatum of the CA1 subfield into the polymorph layer of the dentate gyrus, however, by reviewing when the microdrive was moved it was

calculated that on the best recording day the tetrode tips were located at the border of the CA1 pyramidal cell layer and the stratum radiatum.
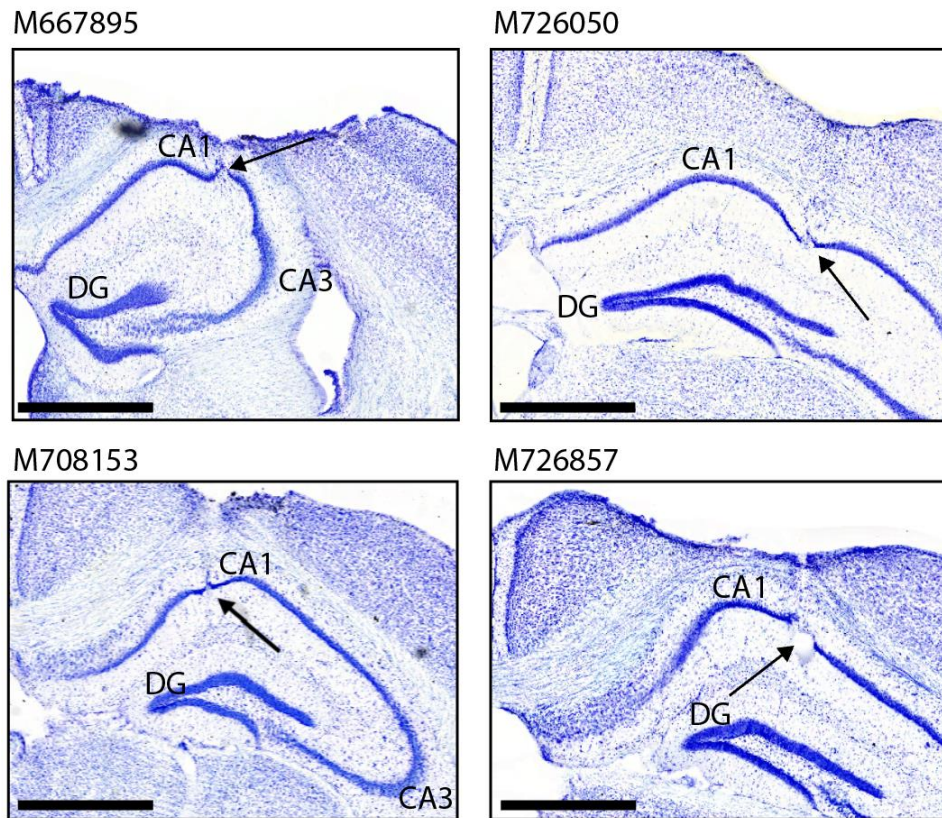


**Figure 4.19 Locations of recording tetrodes.** The locations of tetrodes are shown for two WT (top row) and two APP$^{NL-G-F}$ mice (bottom row) in cresyl violet coronal sections of the dorsal hippocampus. Tetrode tracks are indicated by black arrows. Scale bars are 1000μm and hippocampal subfields are labelled as follows: CA1, cornu ammonis 1; CA3, cornu ammonis 3; DG, dentate gyrus.

| Mouse ID | Hemisphere | Estimated final recording layer | Estimated recording location from bregma (mm) |
|---|---|---|---|
| M667893 | Left | CA1 stratum radiatum | - 2.1 AP |
| M667895 | Left | CA1 pyramidal layer/ stratum radiatum | - 1.5 AP |
| M719648 | Left | CA1 stratum oriens | - 2.0 AP |
| M726050 | Left | CA1 pyramidal layer/ stratum radiatum | - 2.1 AP |
| M644788 | Left | CA1 stratum oriens | - 2.1 AP |
| M708153 | Left | CA1 pyramidal layer/ stratum radiatum | - 2.3 AP |
| M726857 | Left | CA1 stratum radiatum | - 2.3 AP |
| M733075 | Left | CA1 pyramidal layer | - 2.1 AP |

**Table 4.3 Locations of the recording tetrodes.** AP = anteroposterior.

### 4.3.1.2. Amyloid beta pathology

Histological staining with Thioflavin S, which binds to the characteristic β-pleated sheet conformation of Aβ, identified Aβ plaques in the brains of all APP$^{NL-G-F}$ mice. In contrast no plaque-like staining was seen in WT controls (*Figure 4.21*). In APP$^{NL-G-F}$ mice Aβ plaques were visible in all subfields of the hippocampal formation and surrounding some blood vessels (*Figure 4.20*).
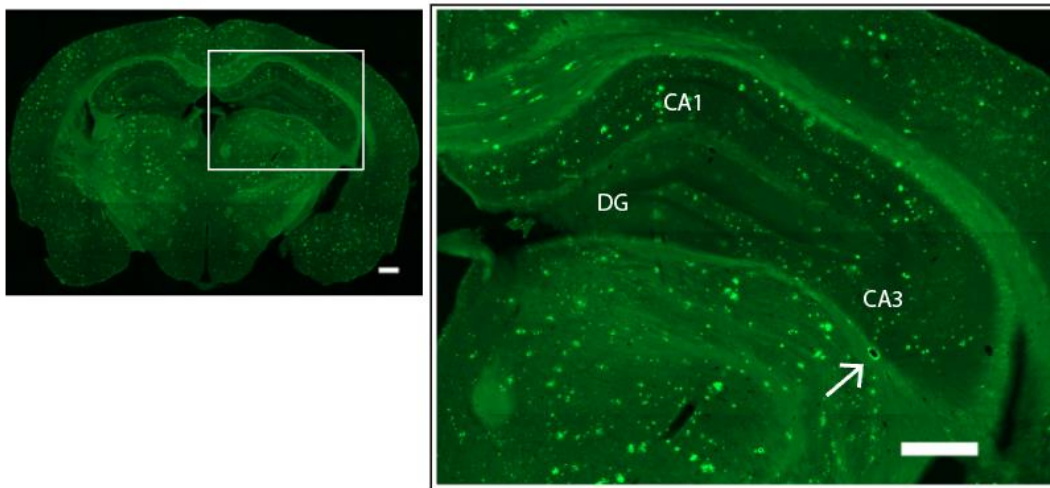


**Figure 4.20 Aβ plaques were seen in all hippocampal subfields and surrounding some blood vessels in APP$^{NL-G-F}$ mice.** Thioflavin S staining of a 40μm coronal section of an APP$^{NL-G-F}$ mouse (M733075) approximately 2.4mm posterior to bregma. Scale bars are 500μm. Hippocampal subfields are labelled, and the white arrow indicates Aβ surrounding a blood vessel.
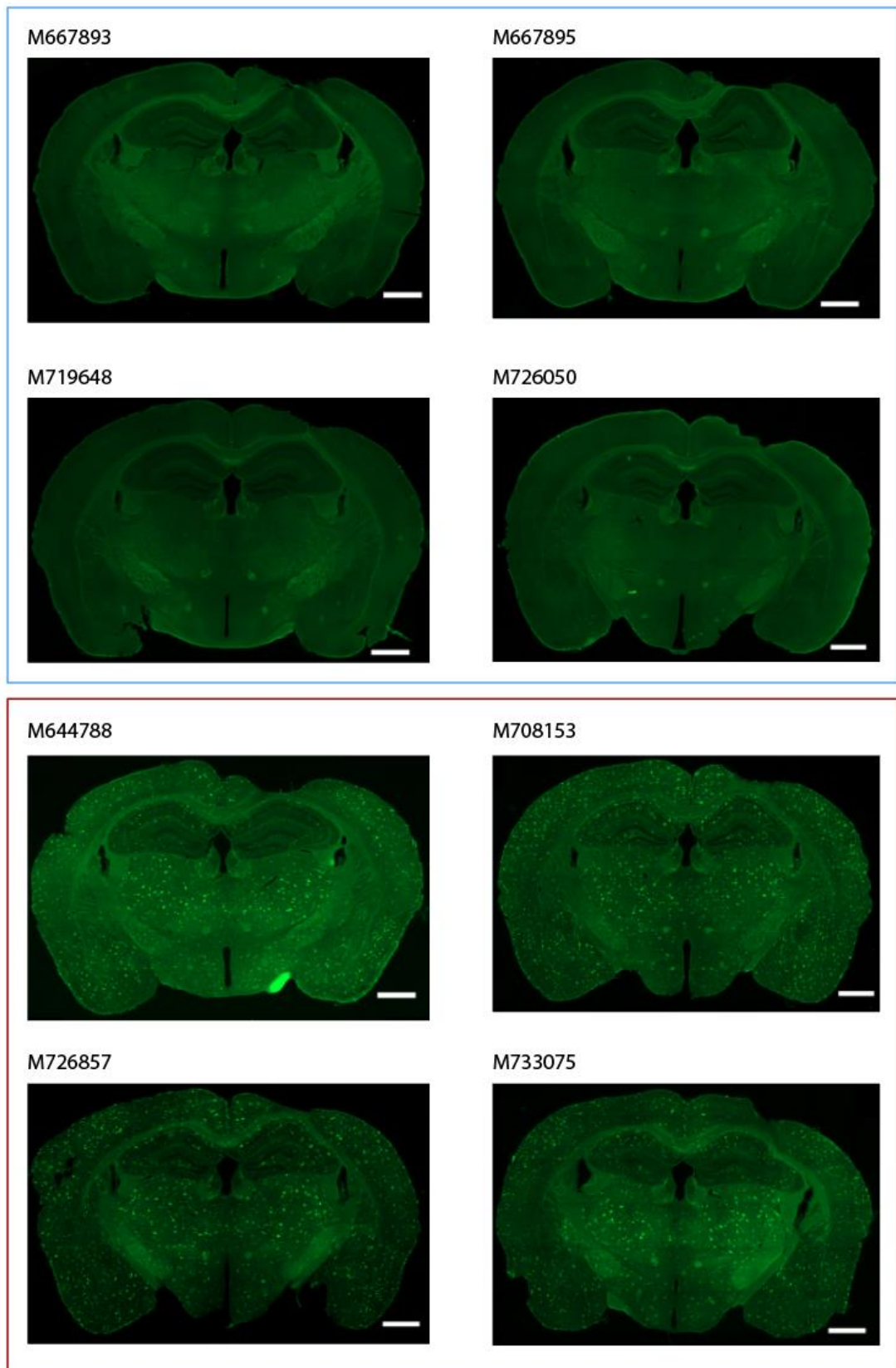
**Figure 4.21 Aβ plaques were seen in APP$^{NL-G-F}$ but not WT mice.** Thioflavin S staining of 40µm coronal sections from WT (blue box) and APP$^{NL-G-F}$ (red box) mice approximately 1.8mm posterior to bregma. Scale bars are 1000µm. Mice IDs are shown above each image.

227

## 4.3.2. Behaviour during recording sessions

Behavioural measures were compared between WT and APP$^{NL-G-F}$ mice (n=8) to ensure that any observed differences in hippocampal electrophysiology were not due to underlying differences in behaviour (*Figure 4.22, page 230; Figure 4.23, page 231*). When combining data from open field trials b and c there were no significant differences between groups in terms of the total distance travelled (mean$_{WT}$ +/- s.e.m$_{WT}$ = 76.85 +/- 8.36 metres  vs. mean$_{NLGF}$ +/- s.e.m.$_{NLGF}$ = 108.8 +/- 16.81 metres; $t_{(6)}$ = 1.700, p = 0.1400), speed (mean$_{WT}$ +/- s.e.m$_{WT}$ = 5.2 +/- 0.37 cm/s vs. mean$_{NLGF}$ +/- s.e.m$_{NLGF}$ = 6.9 +/- 0.80 cm/s; $t_{(6)}$ = 2.031, p = 0.0885), or the proportion of time the animal spent stationary (Mdn$_{WT}$ = 13.90% vs. Mdn$_{NLGF}$ = 11.90%; $U$(N$_{WT}$ = N$_{NLGF}$ = 4) = 6, p = 0.6857). There was, however, a significant difference when comparing the distribution of speed across trials b and c combined, with WT mice spending a greater proportion of time running at slower speeds than APP$^{NL-G-F}$ mice (KS D = 0.2350, p < 0.0001).

On the linear track there were no significant differences in behaviour. WT and APP$^{NL-G-F}$ mice travelled similar distances (Mdn$_{WT}$ = 60.27 metres, Mdn$_{NLGF}$ = 61.50 metres, $U$(N$_{WT}$ = 4, N$_{NLGF}$ = 4) = 7.0, p = 0.8857), and there were no differences in speed (Mdn$_{WT}$ = 5.448 cm/s, Mdn$_{NLGF}$ = 5.811 cm/s, $U$(N$_{WT}$ = 4, N$_{NLGF}$ = 4)  = 8, p  > 0.999), time spent stationary (Mdn$_{WT}$ = 89.52 secs, Mdn$_{NLGF}$ = 159.9, $U$(N$_{WT}$ = 4, N$_{NLGF}$ = 4)  = 7.0, p = 0.8857), peak speed (Mdn$_{WT}$ = 42.77 cm/s, Mdn$_{NLGF}$ = 33.80 cm/s, $U$ (N$_{WT}$ = 4, N$_{NLGF}$ = 4) = 6.0, p = 0.6857), or time spent on left-bound (west) versus right-bound (east) runs (mean$_{WT}$ +/- s.e.m.$_{WT}$ = 341.1 /- 5.22 secs,  mean$_{NLGF}$ = 370.4 +/- 6.21 secs, $F_{(1,12)}$ = 0.9907, p = 0.3392).
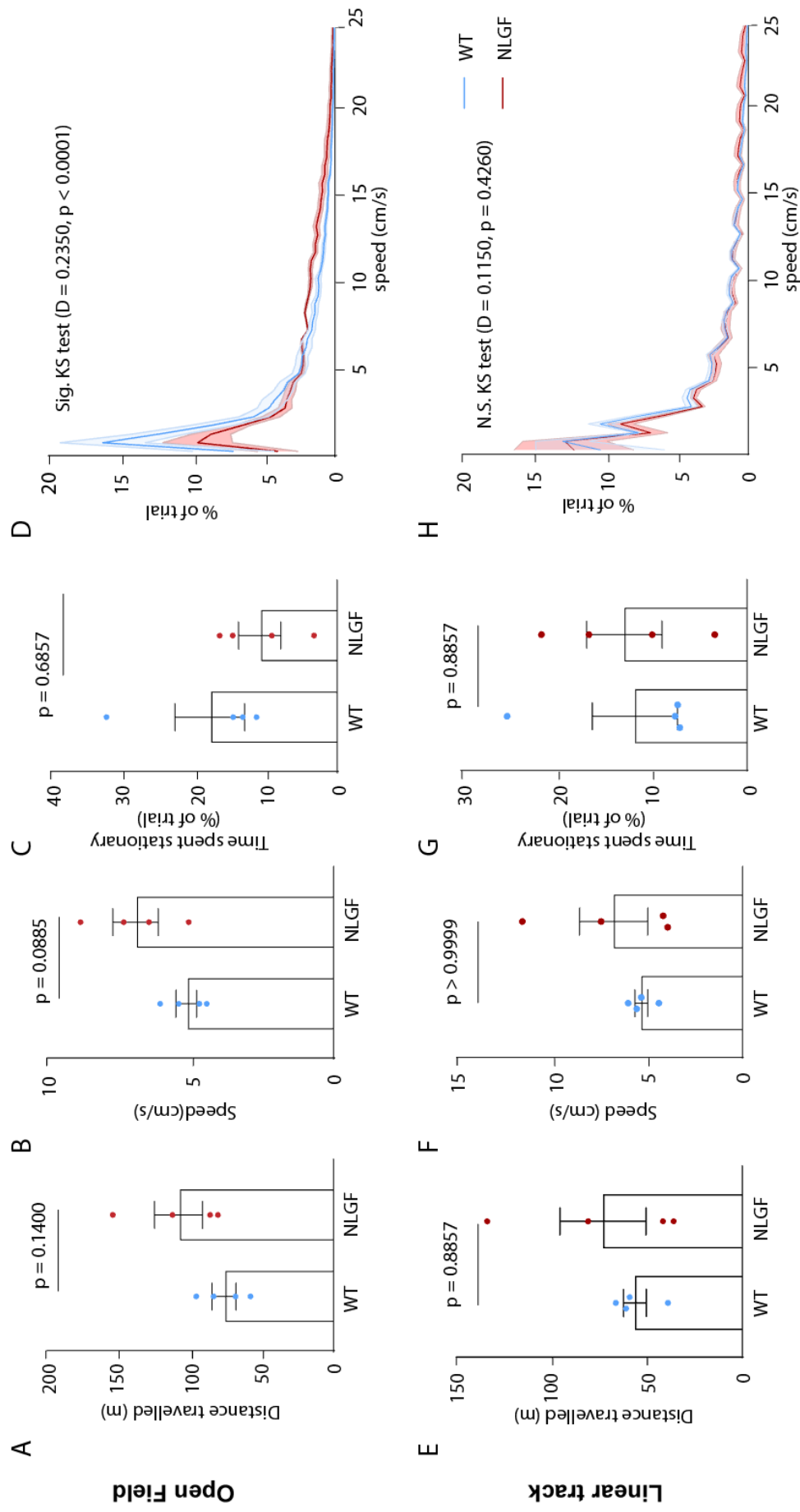
**Figure 4.22 Mouse behaviour.** Behavioural measures from open field trials b and c combined (*A-D*), and linear track trial a and b combined (*E-H*). WT data are shown in blue and APP$^{NL-G-F}$ in red. Bar height indicates mean values, and error bars the standard error of the mean. p values were calculated using paired t-tests for parametric data and Mann Whitney U tests for non-parametric data. Far right: speed histograms (bins of 0.5 cm/s) for each trial. Bold lines indicate the mean with the shaded error envelope representing the standard error of the mean. Distributions were compared using a Kolmogorov-Smirnov test.
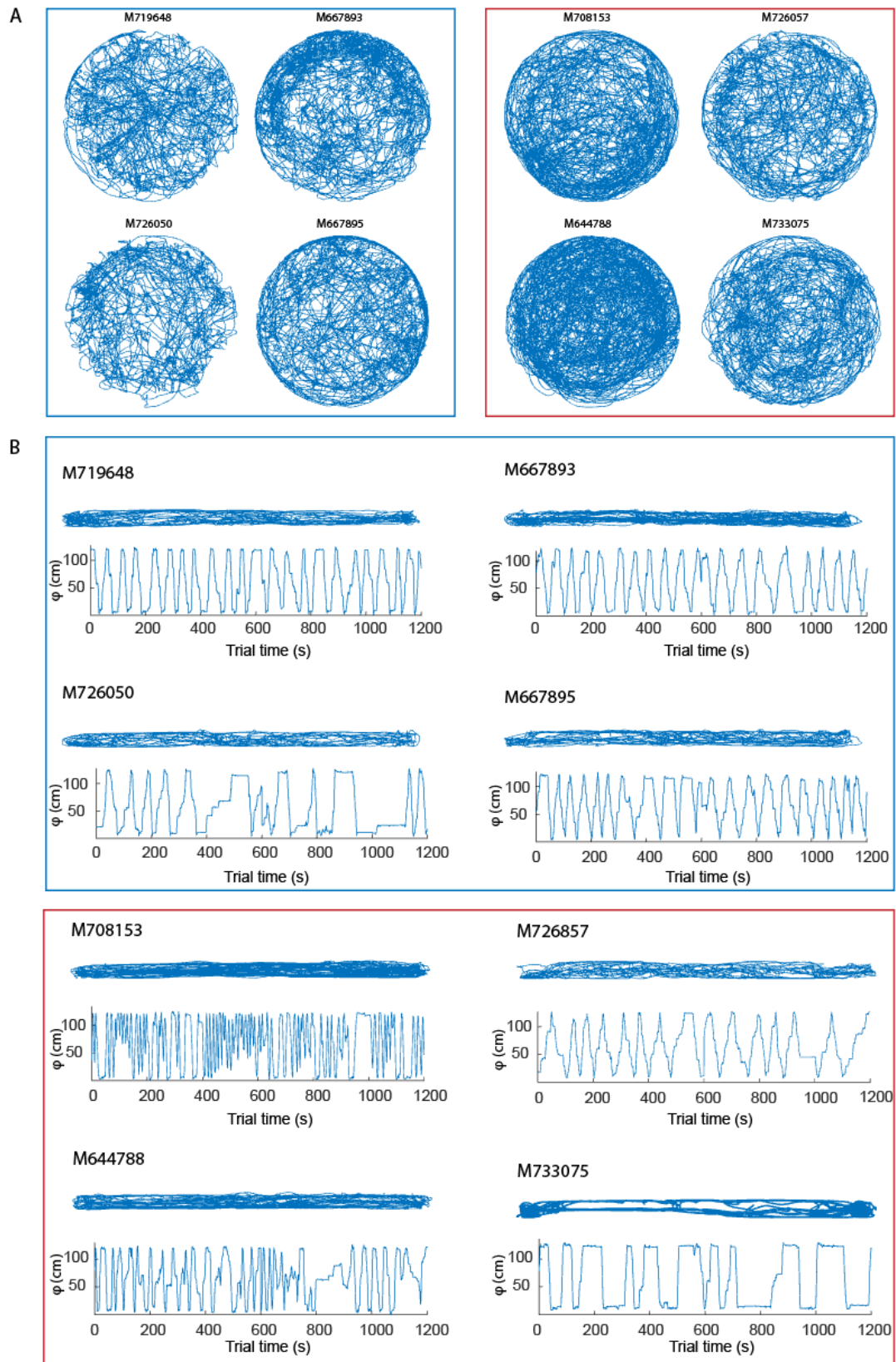
**Figure 4.23 Paths of mice in the open field and on the linear track.** ***A.*** Paths of all WT (blue box) and APP$^{NL-G-F}$ (red box) mice (n = 8) in the circular arena (open field trials b and c). ***B.*** Paths of all WT (blue box) and APP$^{NL-G-F}$ (red box) mice on the linear track shown in 2-dimensions (upper plot; x versus y position) and 1-dimension (lower plot, φ versus time (s)).

### 4.3.3. Cells recorded

### *4.3.3.1. Similar proportions of CA1 pyramidal cells and interneurons were recorded in WT and APP$^{NL-G-F}$ mice.*

Data from 270 cells recorded in the open field were eligible for inclusion in the analysis ($N_{WT}$ = 119; $N_{NLGF}$ = 151). Similar proportions of pyramidal cells and interneurons were recorded in each group (WT: $N_{pyr}$ = 96/119 (80.7%), $N_{int}$ = 23/119 (19.3%); APP$^{NL-G-F}$: $N_{pyr}$ = 107/151 (70.9%), $N_{int}$ = 44/151(29.1%); $\chi^2_{(1)}$ = 3.434, p = 0.0639; *Table 4.4*; *Figure 4.24*). On the linear track 263 cells met the inclusion criteria with approximately equal numbers recorded from WT and APP$^{NL-G-F}$ mice ($N_{WT}$ = 128 and $N_{NLGF}$ = 135). As was found in the open field, similar proportions of pyramidal cells and interneurons were recorded in each group (WT: $N_{pyr}$ = 104/128 (81.3%), $N_{int}$ = 24/128 (18.8%); APP$^{NL-G-F}$: $N_{pyr}$ = 96/135 (71.1%), $N_{int}$ = 39/135 (28.9%); $\chi^2_{(1)}$ = 3.708, p = 0.0542; *Figure 4.24*). Despite no group difference, when comparing individual mice, it was noted that mouse M733075 had a relatively low proportion of pyramidal cells. One potential explanation is that contrary to its estimated location, the tetrode may have been some distance from the pyramidal cell layer.
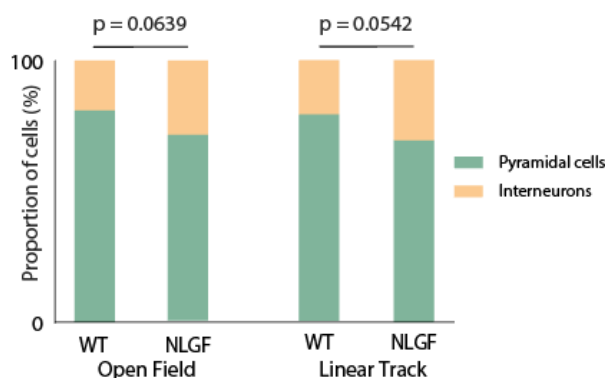


**Figure 4.24 Proportions of pyramidal cells and interneurons.** Similar proportions of pyramidal cells and interneurons were recorded in WT and APP$^{NL-G-F}$ mice across both recording environments**.** p values calculated using Mann Whitney U testing.

| Mouse ID | Measures on day of recording | | | Tetrode position | | Cells Recorded | | | Spatial information (bits per spike) | |
|---|---|---|---|---|---|---|---|---|---|---|
| | Age (months) | Open Field Experience (days) | Weight (grams) | Estimated CA1 layer | Estimated AP location (mm from bregma) | Total | Pyramidal | Spatial | Pyramidal | Spatial |
| M719648 | 14.4 | 14 | 36.4 | Oriens | -2.0 | 45 | 38 (84%) | 23 (60%) | 0.48 +/- 0.47 | 0.48 +/- 0.42 |
| M667893 | 15.5 | 20 | 29.8 | Radiatum | -2.1 | 40 | 36 (90%) | 7 (19%) | 0.12 +/- 0.10 | 0.23 +/- 0.06 |
| M726050 | 14.5 | 9 | 42.8 | Pyramidale/ Radiatum | -2.1 | 29 | 19 (66%) | 7 (37%) | 0.28 +/- 0.31 | 0.20 +/- 0.30 |
| M667895 | 15.8 | 15 | 32 | Pyramidale/ Radiatum | -1.5 | 5 | 3 (60%) | 0 (0%) | 0.07 +/- 0.02 | |
| **All WT mice** (mean +/- s.e.m.) | **15.1 +/- 0.4** | **14 +/- 2.3** | **35.3 +/- 2.9** | | | **119** | **96 (81%)** | **37 (39%)** | **0.29 +/- 0.19** | **0.33 +/- 0.20** |
| M726857 | 15.0 | 10 | 30.9 | Radiatum | -2.3 | 38 | 37 (97%) | 16 (43%) | 0.20 +/- 0.18 | 0.21 +/- 0.18 |
| M708153 | 14.8 | 6 | 23.9 | Pyramidale/ Radiatum | -2.3 | 34 | 30 (88%) | 6 (20%) | 0.07 +/- 0.06 | 0.08 +/- 0.06 |
| M644788 | 17.0 | 19 | 30.7 | Oriens | -2.1 | 25 | 19 (76%) | 4 (21%) | 0.11 +/- 0.10 | 0.11 +/- 0.03 |
| M733075 | 14.8 | 5 | 22.8 | Pyramidale | -2.1 | 54 | 21 (39%) | 1 (4.8%) | 0.07 +/- 0.07 | 0.1018 |
| **All APP$^{NL-G-F}$ mice** (mean +/- s.e.m.) | **15.4 +/- 0.5** | **10 +/- 3.2** | **27.1 +/- 2.2** | | | **151** | **107 (71%)** | **27 (25%)** | **0.12 +/- 0.07** | **0.25 +/- 0.10** |

**Table 4.4 Summary table: Open Field data.** Pre-cellular analysis measures and cells recorded in the open field are shown by group (WT, blue; APP$^{NL-G-F}$, red), and by individual mouse. AP = anteroposterior. The spatial information (bits/spike) is shown for pyramidal cells and spatial cells and values indicate the mean +/- the standard error of the mean. *The summary data for each group in rightmost two columns has been calculated with each recorded cell contributing a single data point rather than each mouse.

### 4.3.3.2. APP$^{NL-G-F}$ mice had a lower proportion of spatial cells.

In the open field a pyramidal cell was considered *spatial* if its spatial information value ($I_{spike}$) lay above the 99$^{th}$ percentile of a shuffled distribution. A significantly lower proportion of CA1 pyramidal cells recorded from APP$^{NL-G-F}$ mice were spatial, compared to those recorded from WT mice ($N_{WT}$ = 37/96 (38.5%) vs. $N_{NLGF}$ = 27/107 (25.2%); $\chi^2_{(1)}$ = 4.151, p = 0.0416; *Table 4.4, page 233*; *Figure 4.25G, page 237*). This trend was also present when analysing the data from individual mice, rather than pooling data from all recorded cells, however, due to the small sample size this approach was statistically underpowered (Mdn$_{WT}$ = 28.0%, Mdn$_{NLGF}$ = 5.0%, *U*($N_{WT}$ = 4, $N_{NLGF}$ = 4) = 4.0, p = 0.3429).

On the linear track, significantly fewer CA1 pyramidal cells in the APP$^{NL-G-F}$ mice were spatial ($N_{WT}$ = 48/104 (46.2%), $N_{NLGF}$ = 21/96 (21.9%); $\chi^2_{(1)}$ = 13.02, p = 0.0003; *Figure 4.26*). When considering the left- and right-bound runs separately, the firing of WT pyramidal cells was spatial on a greater proportion of runs than the firing of APP$^{NL-G-F}$ pyramidal cells ($N_{WT}$ = 114/208 (54.8%), $N_{NLGF}$ = 86/192 (44.8%); $\chi^2_{(1)}$ = 4.006, p = 0.0453; *Figure 4.26*).
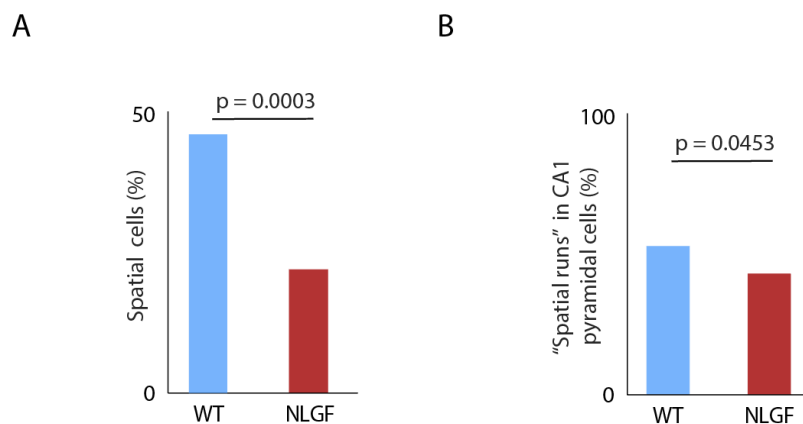


**Figure 4.26 Spatial cells on the linear track. *A***: The proportion of spatial cells in WT (blue) vs. APP$^{NL-G-F}$ (red) mice. ***B***: The proportion of spatial runs in WT vs. APP$^{NL-G-F}$ mice. p values from $\chi^2$ tests.

### 4.3.4. Firing properties of the recorded cells

### *4.3.4.1. CA1 pyramidal cells from APP$^{NL\text{-}G\text{-}F}$ mice had lower peak firing rates.*

In the open field, pyramidal cells from APP$^{NL\text{-}G\text{-}F}$ mice did not differ significantly from WT pyramidal cells in terms of their mean firing rates (Mdn$_{WT}$ = 0.3692 Hz vs. Mdn$_{NLGF}$ = 0.3851Hz; $U($N$_{WT}$ = 96, N$_{NLGF}$ = 106) = 4941, p = 0.6419), but had significantly lower peak firing rates (Mdn$_{WT}$ = 1.72 Hz vs. Mdn$_{NLGF}$ = 1.16 Hz; $U($N$_{WT}$ = 96, N$_{NLGF}$ = 107) = 3968, p = 0.0050; *Figure 4.27*). This finding was replicated on the linear track (peak firing rate: Mdn$_{WT}$ = 1.47 Hz, Mdn$_{NLGF}$ = 1.01 Hz; $U($N$_{WT}$ = 104, N$_{NLGF}$ = 96) = 3769, p = 0.0027; mean firing rate: Mdn$_{WT}$ = 0.45 Hz, Mdn$_{NLGF}$ = 0.37Hz; $U($N$_{WT}$ = 104, N$_{NLGF}$ = 96) = 4295, p = 0.0884; *Figure 4.27, page239*).

Since the activity of cells recorded from the same mouse are not strictly independent, the mean and peak firing rates of CA1 pyramidal cells were compared between WT and APP$^{NL\text{-}G\text{-}F}$ mice using each mouse as a data point, rather than each cell. Pyramidal cells recorded from APP$^{NL\text{-}G\text{-}F}$ mice had similar peak firing rates and mean firing rates to those recorded from WT mice when using this method, likely reflecting the small sample size (peak firing rate: Mdn$_{WT}$ = 2.24 Hz, Mdn$_{NLGF}$ = 1.53Hz; $U($N$_{WT}$ = 4, N$_{NLGF}$ = 4) = 4, p = 0.3429; mean firing rate: Mdn$_{WT}$ = 0.54Hz, Mdn$_{NLGF}$ = 0.52Hz; $U($N$_{WT}$ = 4, N$_{NLGF}$ = 4) = 6.500, p = 0.7429; *Table 4.5*).

| Mouse ID | Spike width (µs) | Peak firing rate (Hz) | Mean firing rate (Hz) |
|---|---|---|---|
| M719648 | 454 +/- 66 | 2.72 +/- 1.85 | 0.53 +/- 0.45 |
| M667893 | 407 +/- 52 | 2.44 +/- 3.47 | 0.61 +/- 0.62 |
| M726050 | 426 +/- 61 | 2.04 +/- 1.89 | 0.54 +/- 0.72 |
| M667895 | 480 +/- 69 | 0.72 +/- 0.47 | 0.23 +/- 0.13 |
| **WT mice (n = 4)** | **442 +/- 32** | **1.98 +/- 0.89** | **0.48 +/- 0.17** |
| M726857 | 483 +/- 76 | 1.83 +/- 1.56 | 0.53 +/- 0.38 |
| M708153 | 493 +/- 48 | 1.69 +/- 1.38 | 0.59 +/- 0.44 |
| M644788 | 475 +/- 61 | 1.37 +/- 1.10 | 0.50 +/- 0.53 |
| M733075 | 463 +/- 120 | 1.06 +/- 0.81 | 0.46 +/- 0.47 |
| **NLGF mice (n = 4)** | **478 +/- 13** | **1.48 +/- 0.34** | **0.52 +/- 0.05** |

**Table 4.5 Firing properties of CA1 pyramidal cells.** Firing properties of CA1 pyramidal cells from WT (blue) and APP$^{NL-G-F}$ (red) mice presented as mean values +/- the standard deviation of the mean. The summary data for each group in the shaded rows is calculated with each mouse contributing a single data point.

In the open field APP$^{NL-G-F}$ spatial cells had a higher mean firing rate than WT spatial cells (Mdn$_{WT}$ = 0.4753 Hz vs. Mdn$_{NLGF}$ = 0.7883 Hz; $U$(N$_{WT}$ = 37, N$_{NLGF}$ = 27) = 317, p = 0.0126), but there was no significant difference in peak firing rate (Mdn$_{WT}$ = 2.885 Hz vs. Mdn$_{NLGF}$ = 2.774 Hz; $U$(N$_{WT}$ = 37, N$_{NLGF}$ = 27) = 472, p = 0.7155; *Figure 4.28, page 239*). On the linear track there were no differences in the peak or mean firing rates of spatial cells between groups (peak firing rate: Mdn$_{WT}$ = 2.29 Hz, Mdn$_{NLGF}$ = 1.81; $U$(N$_{WT}$ = 48, N$_{NLGF}$ = 21) = 481, p = 0.7710; mean firing rate: Mdn$_{WT}$ = 0.5585 Hz; Mdn$_{NLGF}$ = 0.6536 Hz; $U$(N$_{WT}$ = 48, N$_{NLGF}$ = 21) = 418, p = 0.2660; *Table 4.5*). Taken together, these results suggest that CA1 pyramidal cells from APP$^{NL-G-F}$ mice have a reduced peak firing rate compared to WT controls, in the absence of a difference in mean firing rate (*Table 4.6*) which likely reflects the decreased prevalence of spatial cells amongst the APP$^{NL-G-F}$ pyramidal cell population.

**Figure 4.25 Spatial properties in the open field.** *A&D*: histogram of spatial information for WT (blue) and APP[NL-G-F] (red) mice, in CA1 pyramidal cells (*A*), and in spatial cells (*D*). Bin size 0.01 bits/spike. *B&E* Cumulative frequency distribution of spatial information for CA1 pyramidal cells (*B*) and spatial cells (*E*). p values from Kolmogorov-Smirnov testing. *C&F*: spatial information for WT and APP[NL-G-F] pyramidal cells (*C*), and spatial cells (*F*). Bar height indicates the mean, and error bars standard error of the mean. p values calculated using Mann Whitney U tests. *G*: Bar chart comparing the proportion of spatial cells in WT (blue) and APP[NL-G-F] (red) mice. p value from χ² testing.

236

In the open field APP$^{NL-G-F}$ spatial cells had a higher mean firing rate than WT spatial cells (Mdn$_{WT}$ = 0.4753 Hz vs. Mdn$_{NLGF}$ = 0.7883 Hz; $U$(N$_{WT}$ = 37, N$_{NLGF}$ = 27) = 317, p = 0.0126), but there was no significant difference in peak firing rate (Mdn$_{WT}$ = 2.885 Hz vs. Mdn$_{NLGF}$ = 2.774 Hz; $U$(N$_{WT}$ = 37, N$_{NLGF}$ = 27) = 472, p = 0.7155; *Figure 4.28, page 239*). On the linear track there were no differences in the peak or mean firing rates of spatial cells between groups (peak firing rate: Mdn$_{WT}$ = 2.29 Hz, Mdn$_{NLGF}$ = 1.81; $U$(N$_{WT}$ = 48, N$_{NLGF}$ = 21) = 481, p = 0.7710; mean firing rate: Mdn$_{WT}$ = 0.5585 Hz; Mdn$_{NLGF}$ = 0.6536 Hz; $U$(N$_{WT}$ = 48, N$_{NLGF}$ = 21) = 418, p = 0.2660; *Table 4.5*). Taken together, these results suggest that CA1 pyramidal cells from APP$^{NL-G-F}$ mice have a reduced peak firing rate compared to WT controls, in the absence of a difference in mean firing rate (*Table 4.6*) which likely reflects the decreased prevalence of spatial cells amongst the APP$^{NL-G-F}$ pyramidal cell population.

| Cell classification | Recording environment | Findings in APP$^{NL-G-F}$ mice | | |
|---|---|---|---|---|
| | | Mean firing rate | Peak firing rate | Spike width |
| Pyramidal | Open field | No difference | Decreased | Increased |
| | Linear track | No difference | Decreased | Increased |
| Spatial | Open field | Increased | No difference | Increased |
| | Linear track | No difference | No difference | Increased |

**Table 4.6 Firing properties of CA1 pyramidal and spatial cells: an overview.** The mean firing rate, peak firing rate and spike width (peak-to-trough width) were compared between WT and APP$^{NL-G-F}$ pyramidal and spatial cells in both recording environments. Yellow cells indicate circumstances where the measured value for APP$^{NL-G-F}$ cells was significantly increased compared to WT controls, and blue cells where it was significantly decreased. Findings remained significant following a Bonferroni correction for multiple comparisons (α = 0.025). p values obtained from Mann Whitney U testing.
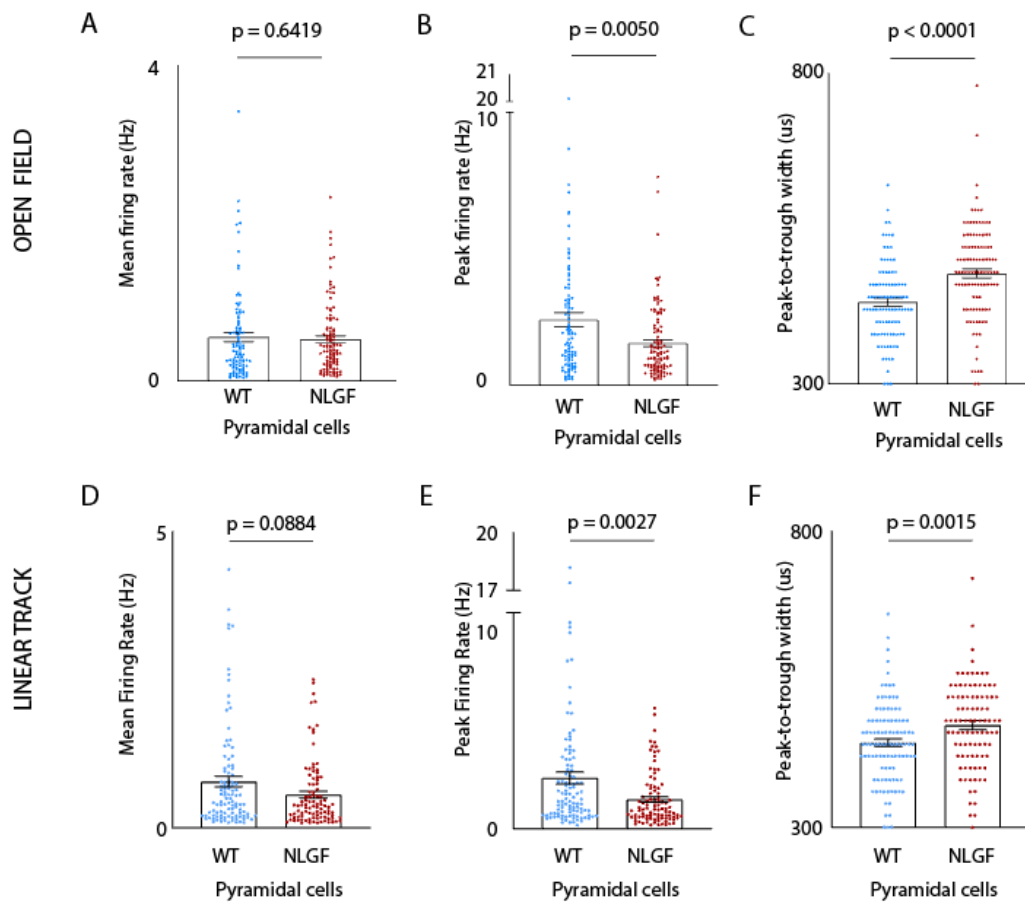
**Figure 4.27 Firing properties of WT and APP$^{NL-G-F}$ pyramidal cells.** **A&D**: mean firing rates of WT (blue) and APP$^{NL-G-F}$ (red) pyramidal cells, in the open field (**A**), and on the linear track (**D**). **B&E**: peak firing rates of WT and APP$^{NL-G-F}$ pyramidal cells, on the open field (**B**) and linear track (**E**). **C&F**: peak-to-trough width (spike width) of WT and APP$^{NL-G-F}$ pyramidal cells, in the open field (**C**), and on the linear track (**F**). p values are calculated using Mann Whitney U testing for non-parametric data (**A,B,D,E**) and paired t-tests for parametric data (**C,F**).
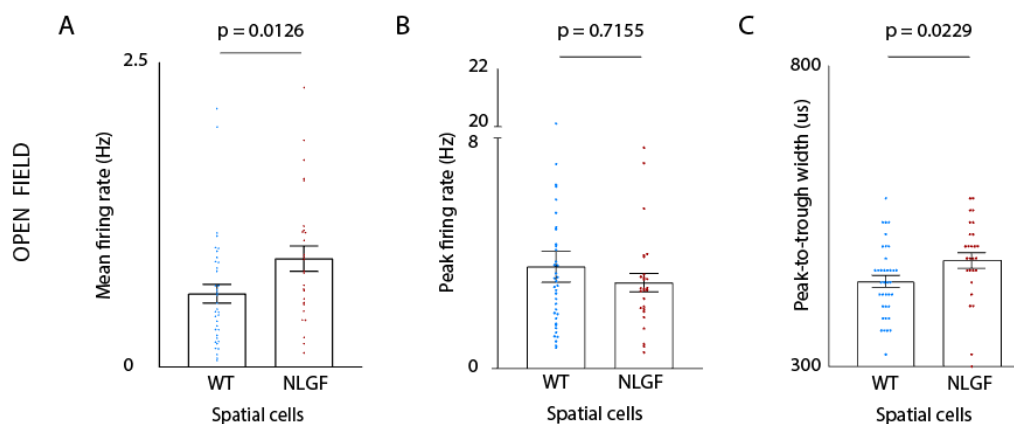


**Figure 4.28 Firing properties of WT and APP$^{NL-G-F}$ spatial cells in the Open Field.** **A**: mean firing rates of WT (blue) and APP$^{NL-G-F}$ (red) spatial cells. **B**: peak firing rates of WT and APP$^{NL-G-F}$ spatial cells. **C**: peak-to-trough width (spike width) of WT and APP$^{NL-G-F}$ spatial cells. p values are calculated using Mann Whitney U testing for non-parametric data (**A,B**) and paired t-tests for parametric data (**C**).

### 4.3.4.2. CA1 Pyramidal cells from APP$^{NL-G-F}$ mice had greater peak-to-trough widths than WT controls.

The peak-to-trough width (spike width) of the highest amplitude mean waveform was measured for each cell. When comparing the spike widths of pyramidal cells, those recorded from APP$^{NL-G-F}$ mice were greater than WT mice in both the open field (Mdn$_{WT}$ = 420µs vs. Mdn$_{NLGF}$ = 480µs; $U$(N$_{WT}$ = 96, N$_{NLGF}$ = 107) = 3051, p < 0.0001), and on the linear track (Mdn$_{WT}$ = 440µs, Mdn$_{NLGF}$ = 480µs; $U$(N$_{WT}$ = 104, N$_{NLGF}$ = 96) = 3707, p = 0.0015; *Figure 4.27*; *Table 4.6*). This was also the case for APP$^{NL-G-F}$ spatial cells, which had a greater peak-to-trough width than WT spatial cells in the open field (mean$_{WT}$ +/- s.e.m.$_{WT}$ = 442 +/- 9.8µs vs. mean$_{NLGF}$ +/- s.e.m.$_{NLGF}$ = 479 +/- 13.2µs; t$_{(62)}$ = 2.333, p = 0.0229; *Figure 4.28*; *Table 4.5*), and on the linear track (Mdn$_{WT}$ = 440µs, Mdn$_{NLGF}$ = 480µs; $U$(N$_{WT}$ = 48, N$_{NLGF}$ = 21) = 280.5, p = 0.0029; *Table 4.6*).

### 4.3.4.3. WT and APP$^{NL-G-F}$ CA1 pyramidal cells were equally bursty.

The burstiness of CA1 pyramidal and spatial cells in the open field was compared between WT and APP$^{NL-G-F}$ mice. Cells were designated as bursty or non-bursty based on a categorical classifier with a guard zone (*page 205*). When comparing the proportions of bursty and non-bursty cells in the WT and APP$^{NL-G-F}$ CA1 pyramidal cell populations there was no significant difference between the two groups ($\chi^2_{(1)}$ = 0.2310, p = 0.6308; *Figure 4.29C, page 242*). In both groups, CA1 pyramidal cells were predominantly bursty (82.3% (79/96) in WT vs. 79.6% (84/107) in APP$^{NL-G-F}$). To ensure that excluding data from cells in the guard zone did not have an effect, the burstiness scores of all CA1 pyramidal neurons in the WT and

APP$^{NL-G-F}$ mice were compared directly. There was no significant difference in burstiness scores between WT and APP$^{NL-G-F}$ pyramidal cell populations (mean$_{WT}$ +/- s.e.m.$_{WT}$ = 1.111 +/- 0.4570 vs. mean$_{NLGF}$ +/- s.e.m.$_{NLGF}$ = 1.635 +/- 0.4908; $t_{(202)}$ = 0.7763, p = 0.4385, two-tailed; *Figure 4.29D*). There was also no significant difference in the burstiness of spatial cells between groups. A similar proportion of WT and APP$^{NL-G-F}$ spatial cells were bursty (94.6% (35/37) WT vs 89.3% (25/28) APP$^{NL-G-F}$; $\chi^2_{(1)}$ = 0.6326, p = 0.4264; *Figure 4.29E*), and there was no significant difference in the burstiness score (mean$_{WT}$ +/- s.e.m.$_{WT}$ = 2.841 +/- 0.6163 vs. mean$_{NLGF}$ +/- s.e.m.$_{NLGF}$ = 3.046 +/- 0.8918; $t_{(63)}$ = 0.1957, p = 0.8454; *Figure 4.29F*). Across both groups pyramidal cells were found to be significantly more bursty if they were spatial. A two-way ANOVA showed a significant effect of being spatial on cell burstiness ($F_{(1,263)}$ = 11.09, p = 0.0010) but no effect of genotype ($F_{(1,263)}$ = 0.8695, p = 0.3519) and no significant interaction between the two ($F_{(1,263)}$ = 0.4128, p = 0.5211). Post-hoc pairwise comparisons using Tukey HSD testing revealed that while WT spatial cells were significantly more bursty than WT non-spatial cells (Bonferroni adjusted p value = 0.0313), APP$^{NL-G-F}$ spatial cells were not significantly more bursty than APP$^{NL-G-F}$ non-spatial cells (Bonferroni adjusted p value = 0.2002); *Figure 4.29H*).

**Figure 4.29 Burstiness of WT and APP$^{NL-G-F}$ cells.** *A&B*: Probability histograms of the interspike intervals (ISI) for WT (*A*) and APP$^{NL-G-F}$ (*B*) CA1 pyramidal cells. *C&E*: proportions of bursty (yellow), non-bursty (blue) and guard zone (white) pyramidal (*C*) and spatial (*E*) cells in WT and APP$^{NL-G-F}$ mice. *D&F*: burstiness scores of pyramidal (*D*) and spatial (*F*) cells in WT (blue) and APP$^{NL-G-F}$ (red) mice. *G&H*: proportions of bursty cells (*G*) and burstiness (*H*) in spatial and non-spatial pyramidal cells in WT and APP$^{NL-G-F}$ mice. *Post hoc* pairwise comparisons in *H* calculated using Tukey HSD testing corrected for multiple comparisons. p* indicates the p value has been adjusted for multiple comparisons using a Bonferroni correction. The black traces in A and B represent the boundaries of the 95% confidence interval of the median ISI probability.
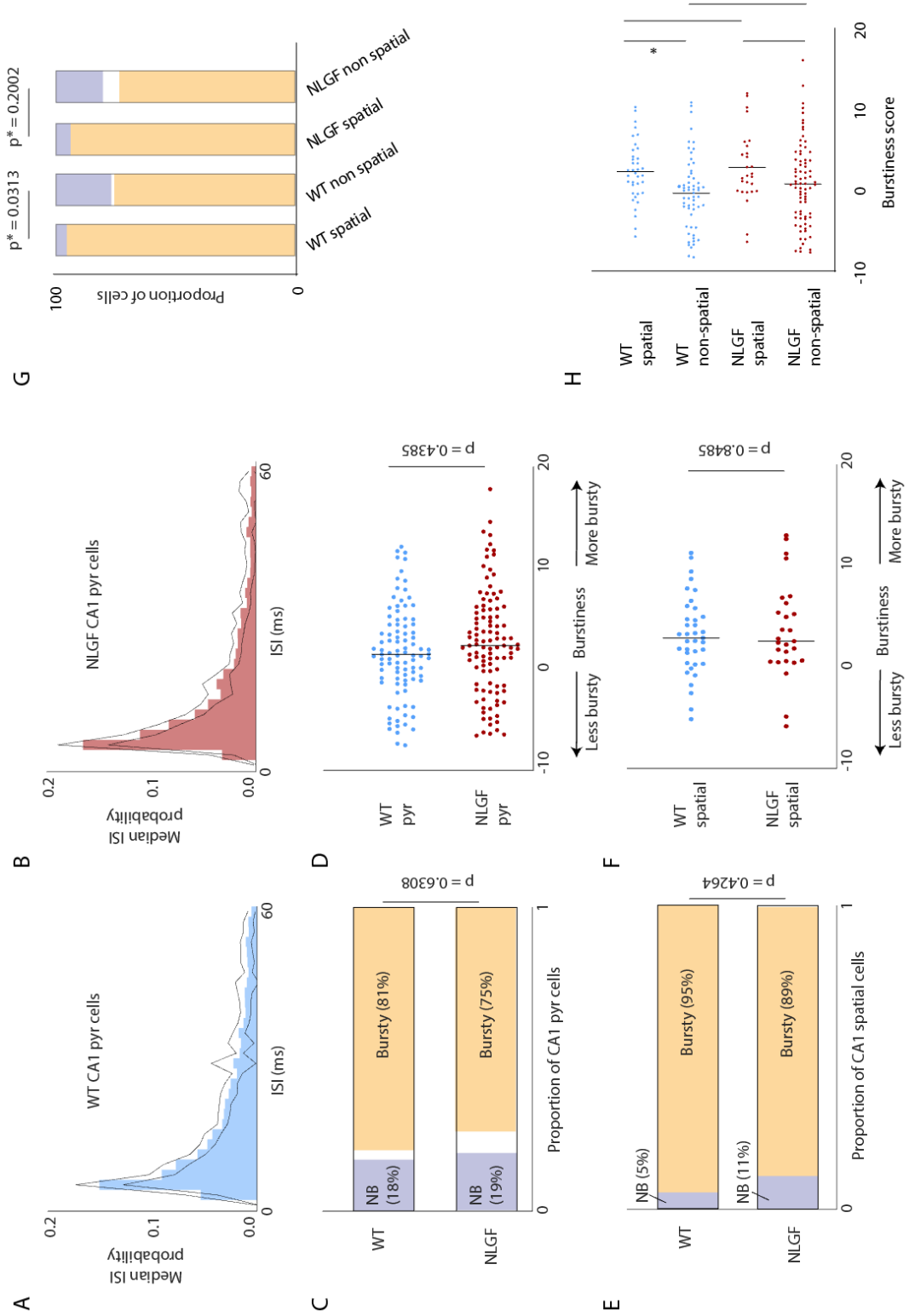
**Figure 4.29 Burstiness of WT and APP$^{NL-G-F}$ cells.** *Full legend page 241.*

### 4.3.5. Rate coding of spatial information was impaired in APP$^{NL-G-F}$ mice compared to WT controls.

#### 4.3.5.1. CA1 pyramidal and spatial cells from APP$^{NL-G-F}$ mice had a lower spatial information content.

The spatial information content of the rate maps of WT and APP$^{NL-G-F}$ pyramidal cells, both in the open field (*Figure 4.30*), and on the linear track (*Figure 4.31*), were calculated and compared. In the open field, CA1 pyramidal cells in WT mice had a significantly higher level of spatial information ($I_{spike}$) than those in the APP$^{NL-G-F}$ mice (Mdn$_{WT}$ = 0.2348 vs. Mdn$_{NLGF}$ = 0.1261; $U$(N$_{WT}$ = 96, N$_{NLGF}$ = 107) = 3326, p < 0.0001; *Figure 4.25A-C*). This was also the case for WT and APP$^{NL-G-F}$ spatial cells recorded in the open field (Mdn$_{WT}$ = 0.4304 vs. Mdn$_{NLGF}$ = 0.268; $U$(N$_{WT}$ = 37, N$_{NLGF}$ = 27) = 228, p = 0.0001; *Figure 4.25D-F, page 237; Figure 4.30*).
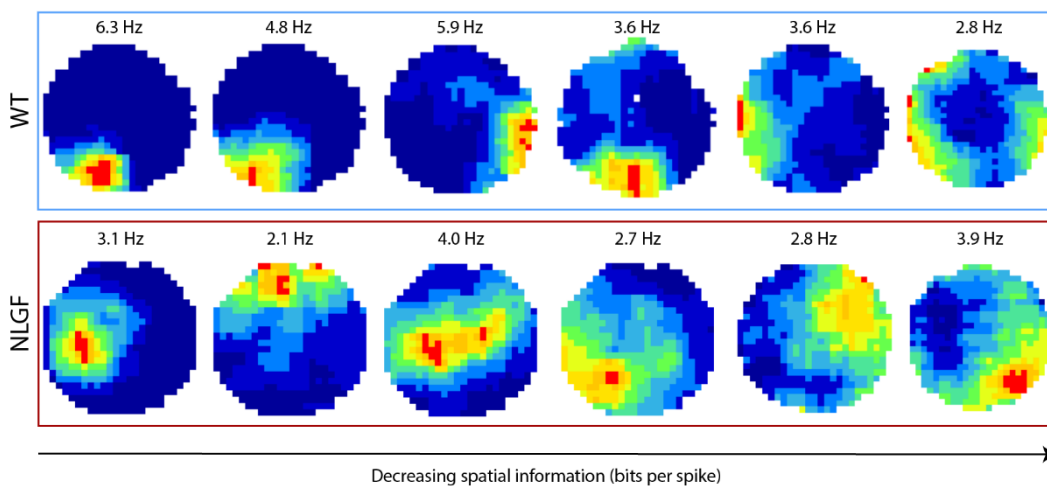


**Figure 4.30 Rate maps from WT and APP$^{NL-G-F}$ spatial cells in the open field.** Representative rate maps for WT (*top row*) and APP$^{NL-G-F}$ (*bottom row*) spatial cells. Rate maps were ordered by their spatial information values and examples selected at evenly spaced intervals. Rate maps are scaled from a firing rate of zero (dark blue) to the maximum rate (red) with each colour representing a 10% band of the peak firing rate. Unvisited bins are shown in white. The peak firing rate is shown above each rate map.

On the linear track, spatial information values were calculated from the concatenated left- and right-bound rate maps. Pyramidal cells recorded from WT mice had a significantly higher spatial information content than pyramidal cells recorded from APP$^{NL-G-F}$ mice (Mdn$_{WT}$ = 0.2223, Mdn$_{NLGF}$ = 0.1004; $U$(N$_{WT}$ = 104, N$_{NLGF}$ = 96) = 3197, p < 0.0001; *Figure 4.32D-F, page 239*). Pyramidal cells which had one or more significantly spatial run also had a lower spatial information content in APP$^{NL-G-F}$ mice (Mdn$_{WT}$ = 0.2851, Mdn$_{NLGF}$ = 0.1187; $U$(N$_{WT}$ = 74, N$_{NLGF}$ = 66) = 1420, p < 0.0001; *Figure 4.32D-F, page 245*), as did spatial cells from APP$^{NL-G-F}$ mice (Mdn$_{WT}$ = 0.4352, Mdn$_{NLGF}$ = 0.1896; $U$(N$_{WT}$ = 48, N$_{NLGF}$ = 21) = 214, p < 0.0001).
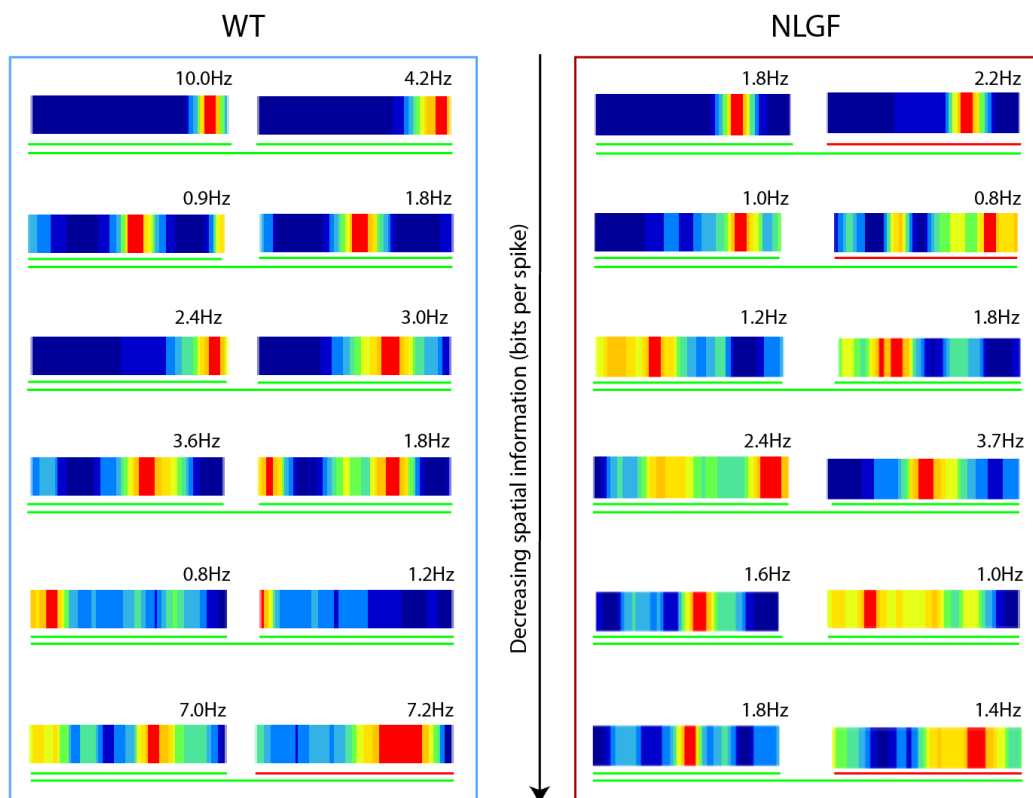


**Figures 4.31 Rate maps from WT and APP$^{NL-G-F}$ spatial cells on the linear track**. Representative rate maps for WT (*left*) and APP$^{NL-G-F}$ (*right*) spatial cells. Rate maps were ordered by their spatial information values and example rate maps selected at evenly spaced intervals. Rate maps are scaled from a firing rate of zero (dark blue) to the maximum rate (red) with each colour representing a 10% band of the peak firing rate. The peak firing rate is shown above each rate map. Rate maps are presented in pairs with the left-bound run on the left, and the right-bound run on the right. Runs underlined in green were significantly spatial compared to a shuffled distribution, and those underlined in red were not. The line extending underneath both rate maps signifies whether the concatenated left- and right-bound rate map, and therefore the cell, was significantly spatial.
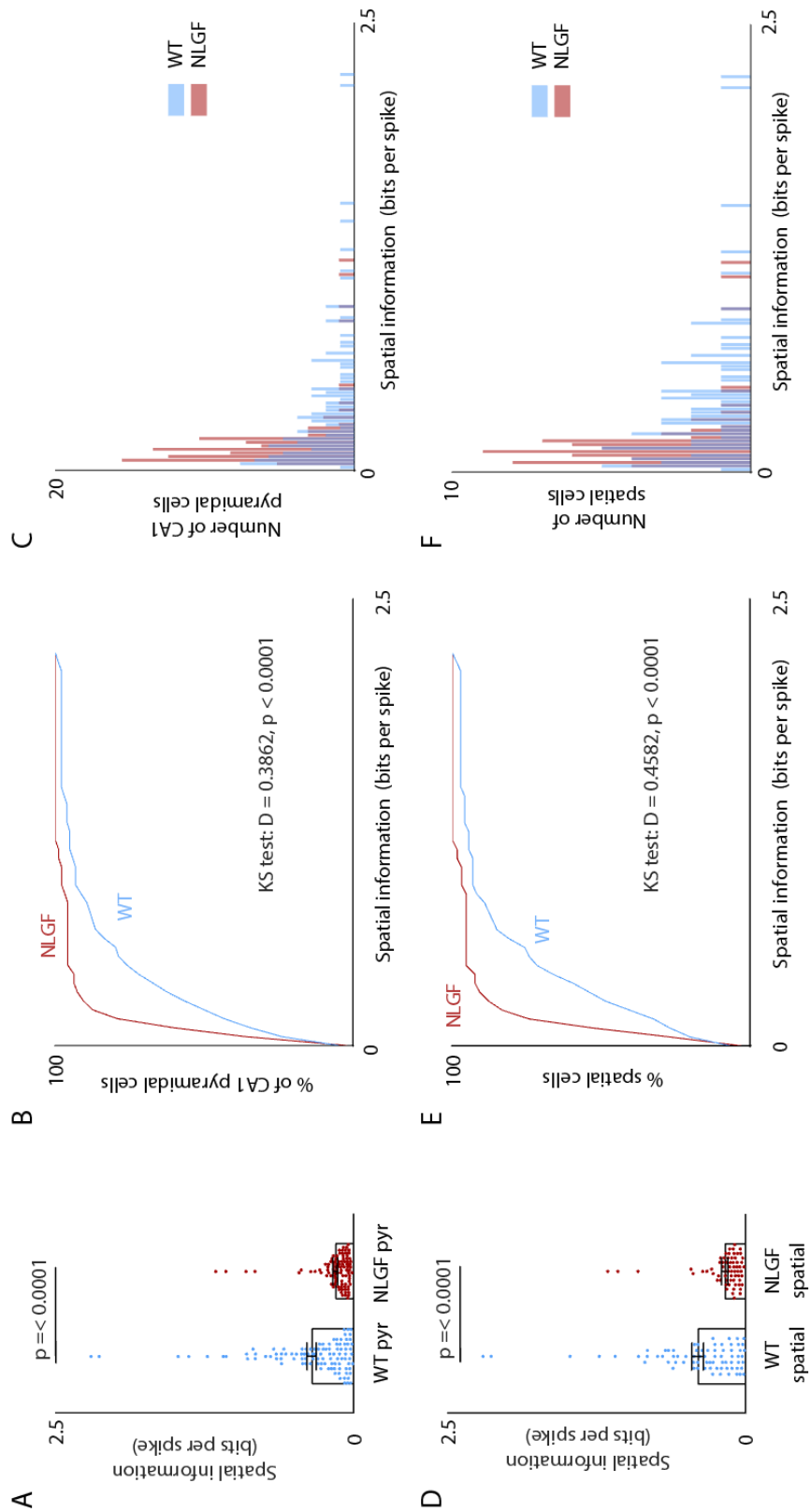
**Figure 4.32 Spatial properties on the linear track.** *A&D*: Spatial information from all pyramidal cells with at least one spatial run (*D*). Bar height indicates the mean value and error bars the standard error of the mean. p values from Mann Whitney U tests. Spatial information for cells with one or more spatial runs (*D*) was calculated from the concatenated left- and right-bound runs of spatial cells. *B&E*: Cumulative frequency distributions of spatial information for CA1 pyramidal cells (*B*), and cells with one or more spatial runs (*E*). p values calculated using Kolmogorov-Smirnov testing. *C&F*: Spatial information histograms for pyramidal cells (*C*), and cells with one or more spatial runs (*F*).

### 4.3.5.2. APP$^{NL-G-F}$ pyramidal cells with a spatial component were more likely to be unidirectional than WT cells.

WT pyramidal cells with one or two significantly spatial runs on the linear track were more likely to be spatial in both directions (*bidirectional*) than cells from APP$^{NL-G-F}$ mice which were more likely to be *unidirectional*; in WT mice 46.0% (34/74) of these cells were unidirectional, and 54.1% (40/74) were bidirectional, compared to 69.7% (46/66) unidirectional, and 30.3% (20/66) bidirectional cells in the APP$^{NL-G-F}$ mice ($\chi^2_{(1)}$ = 8.036, p = 0.0046; *Figure 4.33*).
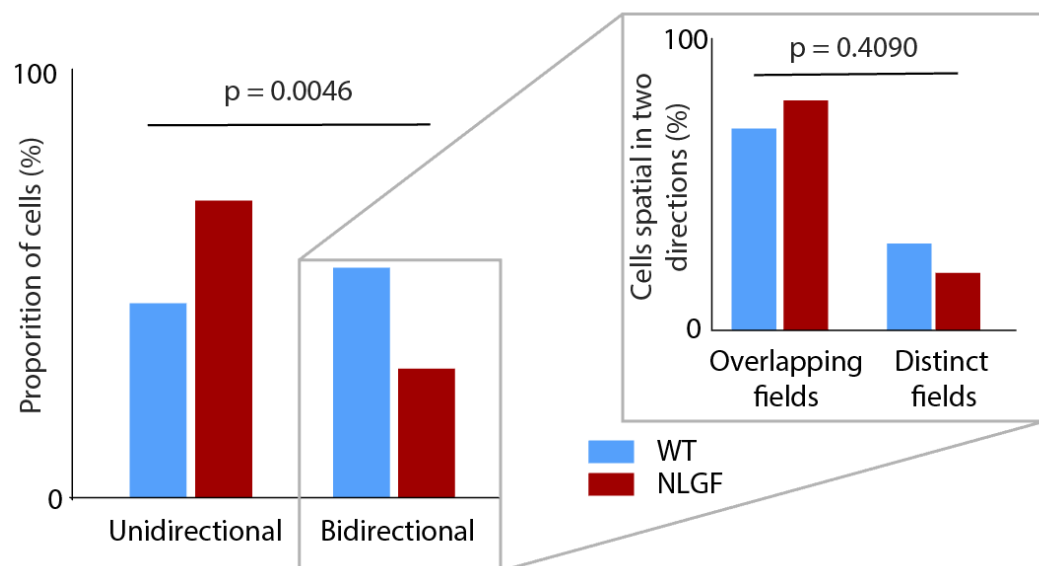


**Figure 4.33 Directionality on the linear track**. The proportion of pyramidal cells with at least one spatial run which were spatial in one direction (unidirectional) vs. both directions (bidirectional) are shown for WT (blue) and APP$^{NL-G-F}$ (Red) mice. *Inset*, the proportion of bidirectional cells which represented distinct or overlapping locations on the left- and right-bound runs.

Next, it was investigated whether the difference observed in the proportion of *bidirectional* cells was related to differences in firing rates on left- and right-bound runs. The difference in the peak firing rates between left- and right-bound runs was calculated for each pyramidal cell with one or more spatial runs, and normalised by dividing by the sum of the peak firing rates.

This produced a value between 0 and 1, where 0 indicates that there was no difference in the peak firing rates and 1 that there was a maximal difference. The same procedure was followed for the mean firing rates. Given that a lower proportion of APP$^{NL-G-F}$ cells were bidirectional, it might be expected that a greater difference would be seen between left- and right-bound peak firing rates compared to WT mice, however this was not the case (Mdn$_{WT}$ = 0.1967, Mdn$_{NLGF}$ = 0.1748, $U$ (N$_{WT}$ = 74, N$_{NLGF}$ = 66) = 2231, p = 0.6456; *Figure 4.34A*). There was also no difference observed in the difference in mean firing rate between left- and right-bound runs when comparing WT and APP$^{NL-G-F}$ spatial cells (Mdn$_{WT}$ = 0.1613, Mdn$_{NLGF}$ = 0.1590, $U$(N$_{WT}$ = 74, N$_{NLGF}$ = 66) = 2171, p = 0.2597; *Figure 4.34B*).
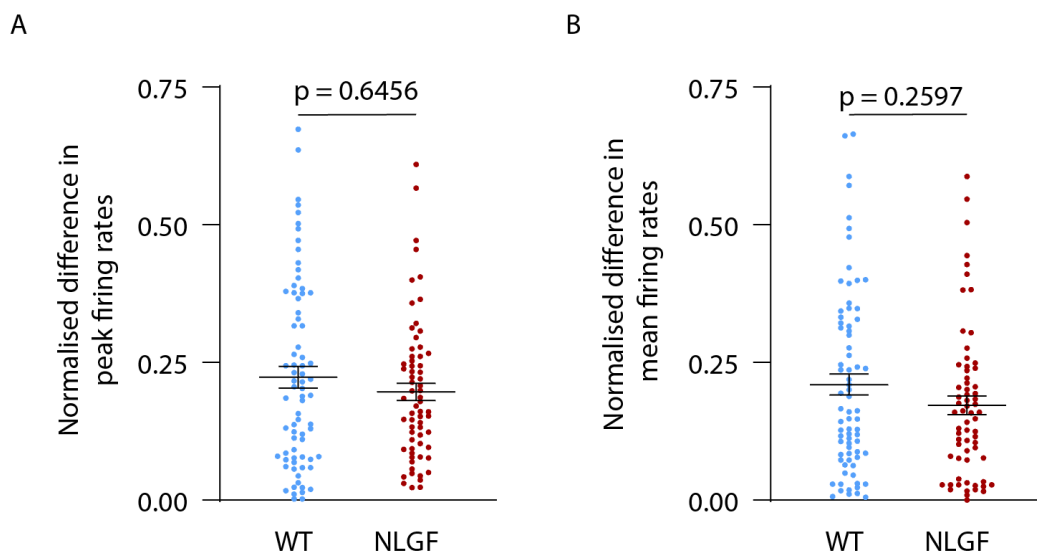


**Figure 4.34 Differences in firing rates between left- and right-bound runs on the linear track in pyramidal cells with a spatial component.** There were no significant differences between WT (blue) and APP$^{NL-G-F}$ (red) pyramidal cells with one or more spatial runs, in terms of the difference in peak firing rates (*A*) or mean firing rates (*B*) between left- and right-bound runs. Solid black bars indicate the mean, and error bars the standard error of the mean. p values from Mann Whitney U testing.

For *bidirectional* cells, i.e., cells which exhibited spatial firing in both directions along the linear track, the degree of overlap of the rate maps was calculated and compared to a shuffled distribution to determine whether the cell represented the same or distinct locations in the two directions. In the

WT mice, 30% (12/40) of bidirectional cells encoded distinct locations compared to 20% (4/20) in the APP$^{NL-G-F}$ mice, with no significant difference between the two groups ($\chi^2_{(1)}$ = 0.6818, p = 0.490; *Figure 4.33, page 246*).

### 4.3.5.3. Place fields were degraded in *APP$^{NL-G-F}$* mice.

Place fields were analysed in cells recorded in the open field and on the linear track using a firing rate threshold of 20% of the peak firing rate to identify a place field (*see page 208*). When analysing the properties of place fields on the linear track each run was considered separately and only data from the runs that were significantly spatial were included ($N_{WT}$ = 114, $N_{NLGF}$ = 86).

### *4.3.5.3.1. Place fields were larger in APP$^{NL-G-F}$ mice.*

In the open field, spatial cells from APP$^{NL-G-F}$ mice had significantly larger place fields than those from WT mice ($Mdn_{WT}$ = 33.67% vs. $Mdn_{NLGF}$ = 62.24%; $U(N_{WT}$ = 37, $N_{NLGF}$ = 27) = 220, p < 0.0001; *Figure 4.35D*). Using the chosen place field criteria, fields could also be identified in the non-spatial cell populations, although these tended to be large, often filling nearly the entire environment. When comparing the size of place fields across all pyramidal cells (spatial and non-spatial cells included), those in the WT group were significantly smaller ($Mdn_{WT}$ = 58.78% vs. $Mdn_{NLGF}$ = 83.67%; $U(N_{WT}$ = 96, $N_{NLGF}$ = 107) = 3035, p < 0.0001; *Figure 4.35A*). This difference in field size does not purely reflect the increased proportion of spatial cells amongst the WT pyramidal cells, since it was also present when looking only at non-spatial pyramidal cells ($Mdn_{WT}$ = 74.49% vs. $Mdn_{NLGF}$ = 90.41%; $U(N_{WT}$ = 59, $N_{NLGF}$ = 80) = 1605, p = 0.0012).

**Figure 4.35 Place field properties of WT and APP^NL-G-F cells in the Open Field.** ***A&D***: Field size in pyramidal cells (***A***), and spatial cells (***D***) in WT (blue) and APP^NL-G-F (red) mice. ***B&E***: Proportions of pyramidal (***B***), and spatial (***E***), cells with different numbers of fields. ***C&F***: Within-field firing rates for pyramidal (***C***) and spatial (***E***) cells in WT and APP^NL-G-F mice. In all bar graphs bar height indicates the mean value and the error bar represents the standard error of the mean. p values from Mann Whitney U tests.
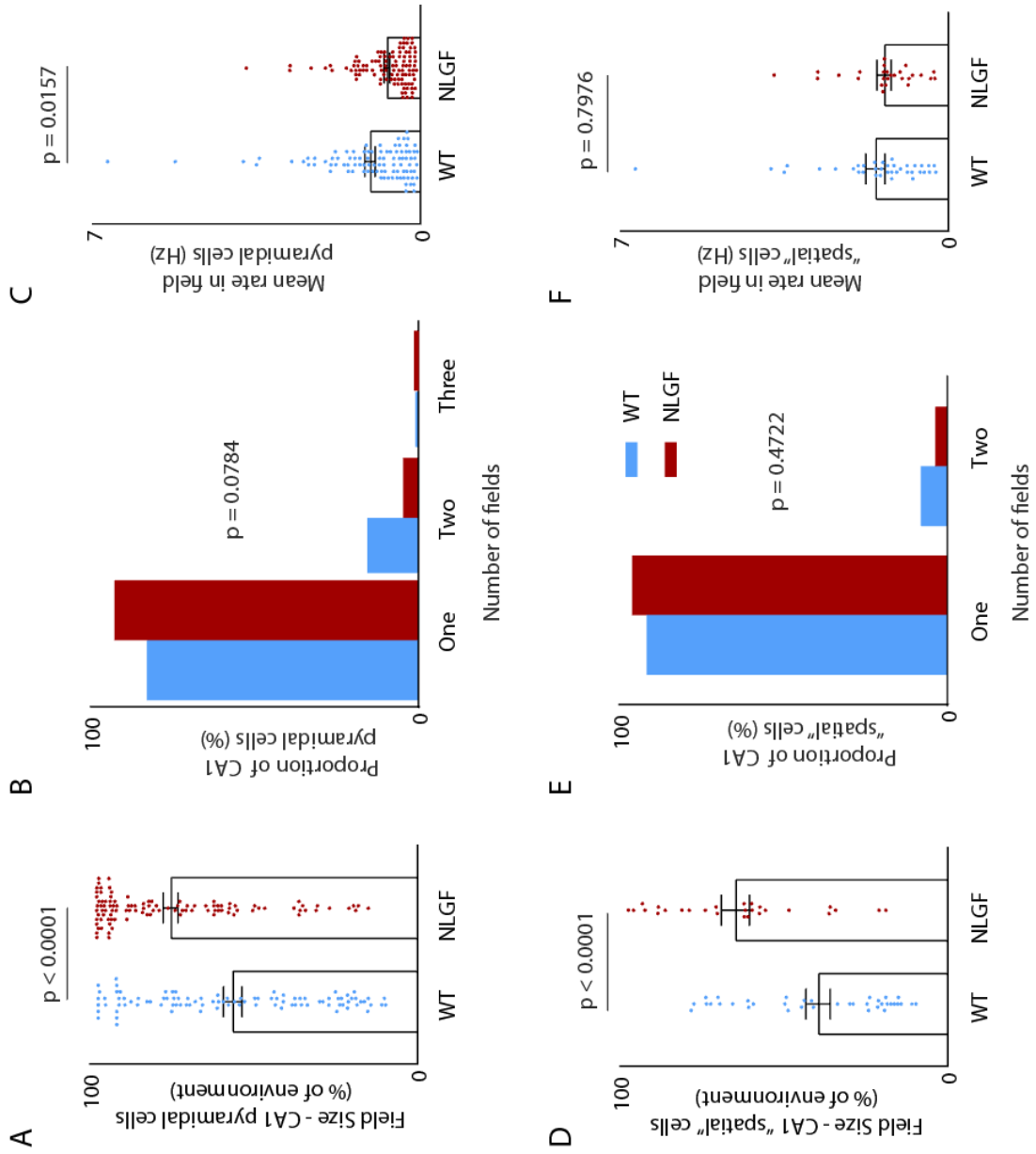
When comparing the width of place fields on significantly spatial runs recorded on the linear track, place fields were found to be significantly wider in the APP$^{NL-G-F}$ mice (Mdn$_{WT}$ = 64.4%, Mdn$_{NLGF}$ = 88.5%; $U$(N$_{WT}$ = 114, N$_{NLGF}$ = 110) = 3493, p < 0.0001; *Figure 4.36B*). Of note, using this place field definition on the linear track (*see page 210*) resulted in the identification of wide fields; even in WT mice 65.8% (75/114) of place fields identified covered more than half of the length of the linear track.
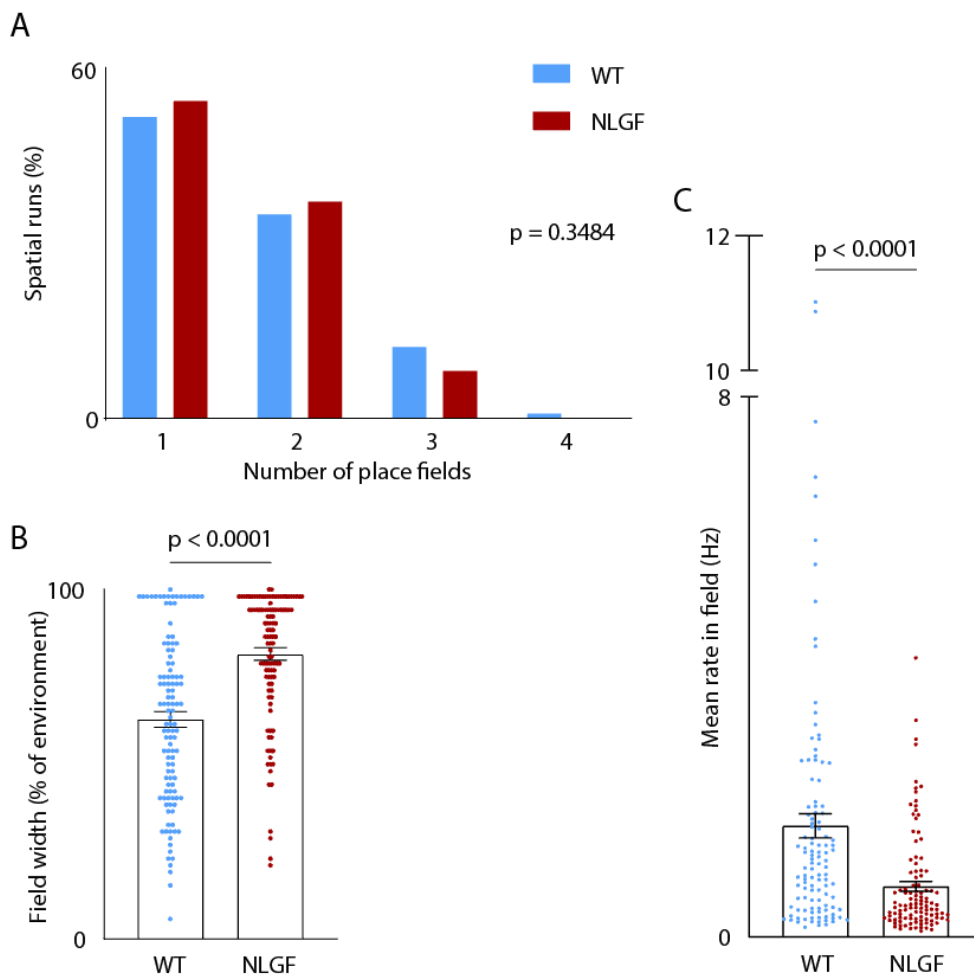


**Figure 4.36 Place field properties in WT and APP$^{NL-G-F}$ spatial runs on the linear track.** **A**: Proportions of spatial runs with different numbers of fields. p value from χ² test with trend. **B**: Field width in spatial runs from WT (blue) and APP$^{NL-G-F}$ (red) mice. **C**: Within-field firing rate for spatial runs in WT and APP$^{NL-G-F}$ mice. **B&C**: p values from Mann Whitney U testing, bar height indicates mean, error bars are standard error of the

### 4.3.5.3.2. There were no differences in the number of place fields in WT and APP$^{NL-G-F}$ mice.

In the open field some spatial cells had more than one identifiable place field; 8% (3/37) of WT spatial cells had two fields compared to 4% (1/27) of APP$^{NL-G-F}$ spatial cells, however the observed difference was not statistically significant ($\chi^2_{(1)} = 0.5168$, p = 0.4722; *Figure 4.35F, page 249*). On the linear track there were between one and four place fields per spatial run in the WT mice (only one run had four fields), and one to three fields per spatial run in the APP$^{NL-G-F}$s. There was no significant difference in the number of place fields when comparing spatial runs from WT and APP$^{NL-G-F}$ mice (mean$_{WT}$ +/- s.e.m. = 1.62 +/- 0.0687, mean$_{NLGF}$ = 1.54 +/- 0.0615; $\chi^2_{trend(1)} = 0.8794$, p = 0.3484; *Figure 4.36A, page 250*).

### 4.3.5.3.3. On the linear track APP$^{NL-G-F}$ spatial runs had a lower within-field firing rate.

In the open field there were no significant differences in the mean firing rate within the place fields of spatial cells when comparing WT and APP$^{NL-G-F}$ mice (Mdn$_{WT}$ = 1.297 vs. Mdn$_{NLGF}$ = 1.308; $U$(N$_{WT}$ = 37, N$_{NLGF}$ = 27) = 480, p = 0.7976; *Figure 4.35F, page 249*), although there was a significant difference when looking at the whole pyramidal cell population (Mdn$_{WT}$ = 0.7885 vs. Mdn$_{NLGF}$ = 0.4987; $U$(N$_{WT}$ = 96, N$_{NLGF}$ = 107) = 480, p = 0.0157; *Figure 4.35C*). For spatial runs on the linear track, the within-field firing rate was significantly reduced in APP$^{NL-G-F}$ mice compared to WT controls (Mdn$_{WT}$ = 1.09Hz, Mdn$_{NLGF}$ = 0.47Hz; $U$(N$_{WT}$ = 114, N$_{NLGF}$ = 110) = 3837, p < 0.0001; *Figure 4.36C*).

### 4.3.5.3.4. Spatial coherence was reduced in the CA1 pyramidal cells of APP$^{NL-G-F}$ mice compared to WT controls.

Spatial coherence is a measure of the degree to which a neuron's activity is spatially contiguous, i.e., it measures the smoothness of a place field. In the open field, pyramidal cells from WT mice exhibited significantly greater spatial coherence than those from APP$^{NL-G-F}$ mice (mean$_{WT}$ +/- s.e.m.$_{WT}$ = 0.3731 +/- 0.01684 vs. mean$_{NLGF}$ +/- s.e.m.$_{NLGF}$ = 0.2921 +/- 0.01435; t$_{(201)}$ = 3.682, p = 0.0003; *Figure 4.37A*), however there was no significant difference when comparing the spatial coherence between WT spatial cells and APP$^{NL-G-F}$ spatial cells (mean$_{WT}$ +/- s.e.m.$_{WT}$ = 0.5063 +/- 0.01993 vs. mean$_{NLGF}$ +/- s.e.m.$_{NLGF}$ = 0.4854 +/- 0.01620; t$_{(62)}$ = 0.7701, p = 0.4442; *Figure 4.37B*).

On the linear track, rate maps from spatial runs exhibited significantly reduced spatial coherence in APP$^{NL-G-F}$ mice compared to WT mice (Mdn$_{WT}$ = 0.9781, Mdn$_{NLGF}$ = 0.9469; $U$(N$_{WT}$ = 114, N$_{NLGF}$ = 110) = 3112, p < 0.0001; *Figure 4.37C*).
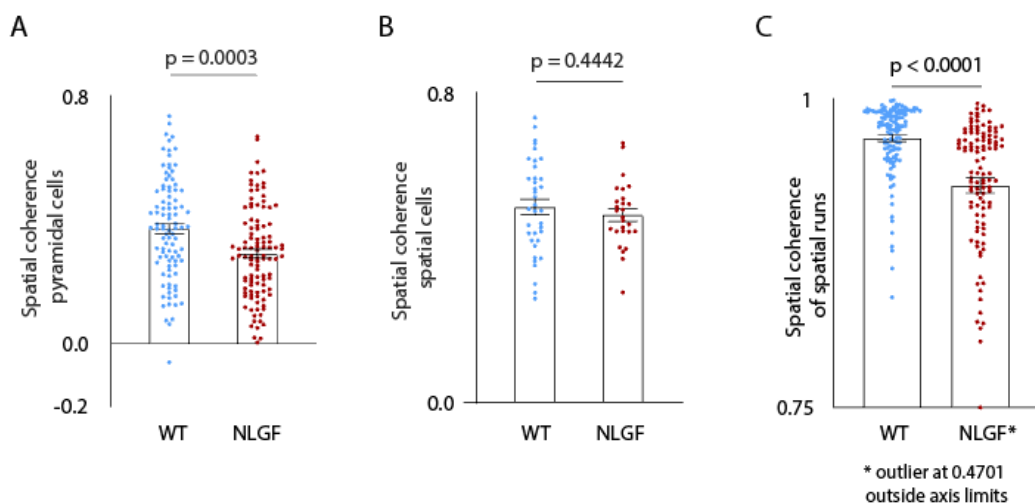


**Figure 4.37 Spatial coherence.** Spatial coherence for pyramidal (**A**), and spatial (**B**), cells in WT (blue) and APP$^{NL-G-F}$ (red) mice in the open field, and for spatial runs on the linear track (**C**). Bar height indicates the mean value and the error bar the standard error of the mean. p values from paired t-tests.

### 4.3.5.3.5. The influence of local cues on place fields differed in APP$^{NL-G-F}$ mice and WT controls.

For cells recorded on the linear track, the position of the centre of mass, or *centroid*, of each field was calculated for each spatial run, and the distribution of centroid locations examined. In both WT and APP$^{NL-G-F}$ mice field centroids were not evenly distributed on the track. In WT mice field centroids were more likely to be located at either end of the track or in the centre. This pattern was less distinct in APP$^{NL-G-F}$ mice (*Figure 4.38, page 255*).

Probability density functions were fitted to histograms of field centroid locations using Gaussian mixture models with between one and five underlying Gaussian curves, and the fit of each model was compared using the Akaike information criterion (AIC) (512). The model with the best fit for both left- and right-bound runs in WT mice was trimodal, whereas in APP$^{NL-G-F}$ mice left-bound runs were best fitted by a trimodal model and right-bound runs by a quattromodal model (*Table 4.7, page 254*). When combining left- and right-bound runs on the linear track, the WT field centroid histogram was best fitted by a trimodal model, whereas the APP$^{NL-G-F}$ histogram was best fitted by a quattromodal model (*Figure 4.38, right column*). When overlaying these histograms onto a scaled schematic of linear track, field centroids in WT mice appear to cluster around local cues, whereas this relationship appears distorted in the APP$^{NL-G-F}$ mice; while APP$^{NL-G-F}$ centroids appeared to cluster near the central cue on the track this was not as apparent for cues at either end of the linear track (*Figure 4.38, page 255*).

252

| Genotype and running direction | AIC values for Gaussian mixture models Number of components | | | | |
| --- | --- | --- | --- | --- | --- |
| | One | Two | Three | Four | Five |
| WT: left | 816.2 | 803.1 | **780.0** | 782.0 | 785.1 |
| WT: right | 718.0 | 702.0 | **684.1** | 689.0 | 687.1 |
| APP$^{NL-G-F}$: left | 734.6 | 720.1 | **717.8** | 719.5 | 721.3 |
| APP$^{NL-G-F}$: right | 614.3 | 616.2 | 603.3 | **601.3** | 606.9 |

**Table 4.7 AIC values for Gaussian Mixture Models of field centroid histograms.** The fit of various Gaussian mixture models to field centroid histograms is indicated by the AIC (Akaike information criterion) values. Highlighted values indicate the lowest AIC values, i.e., the model with the best fit.

To investigate this further, zones were defined on the linear track corresponding to the locations of the cues (*Figure 4.39, page 251*) and the proportions of field centroids falling within these zones was compared between groups. In the APP$^{NL-G-F}$ mice, a significantly lower proportion of field centroids were found in close proximity to cues at either end of the track; 30.8% (57/185) of field centroids from WT spatial runs were at either end of the track compared to 19.5% (33/169) of APP$^{NL-G-F}$ field centroids ($\chi^2_{(1)}$ = 5.931, p = 0.0149; *Figure 4.39*). There was, however, no significant difference between groups in the proportion of field centroids located near the central cue; 33.0% (61/185) of field centroids from WT spatial runs were at centre of the track compared to 38.5% (35/169) of APP$^{NL-G-F}$ field centroids ($\chi^2_{(1)}$ = 1.161, p = 0.2813; *Figure 4.39*).
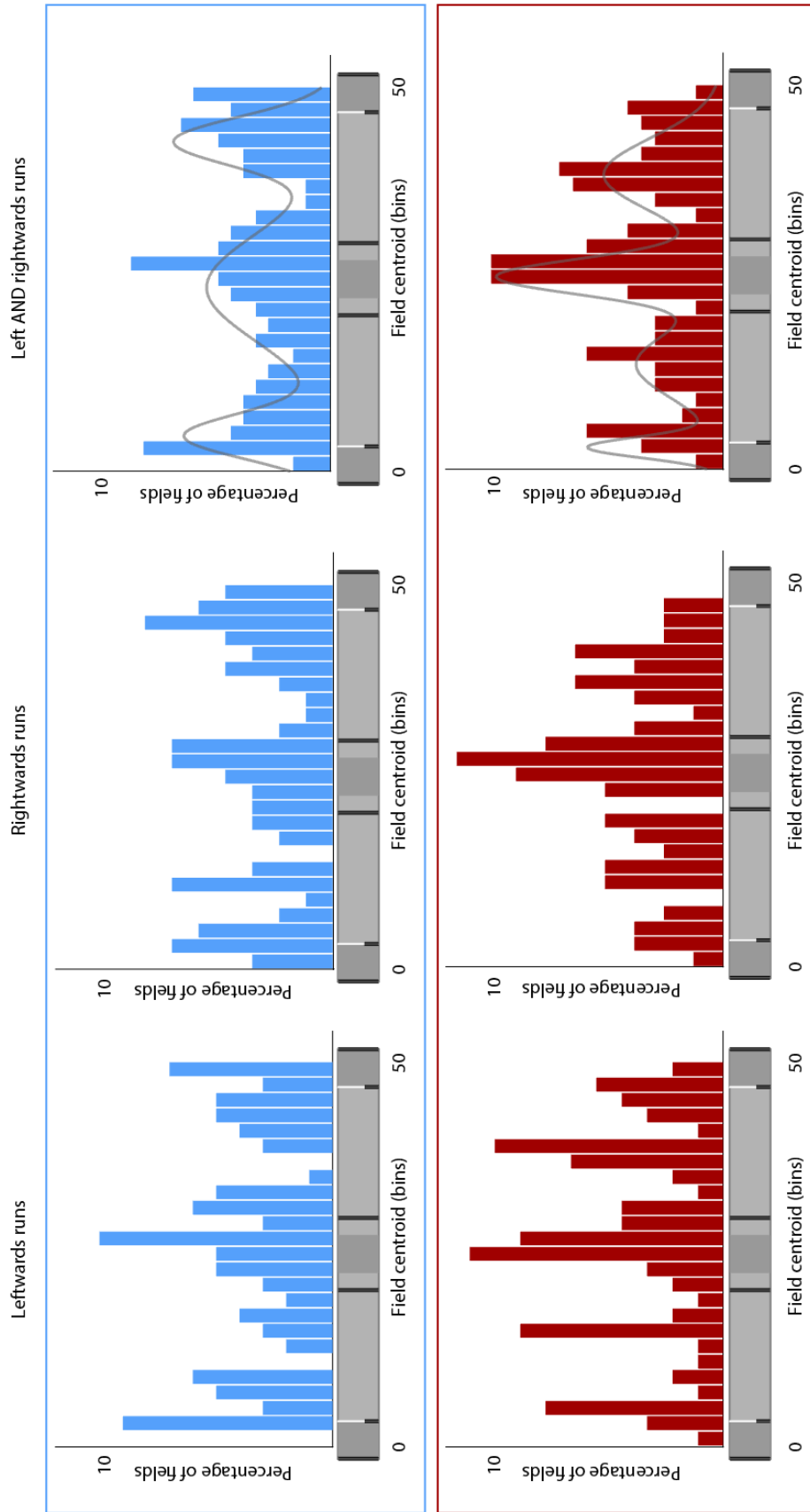
**Figure 4.38 Field centroid histograms.** Histograms illustrating the distribution of field centroids along the linear track for WT mice (*top row, blue box*) and APP[NL-G-F] mice (bottom row, red box). Histogram bin size 4cm. The grey line in the rightmost column illustrates the best fit Gaussian mixture model (trimodal for WTs, and quattromodal for APP[NL-G-F] APP[NL-G-F]s). A schematic of the linear track, indicating the position of local intra-environment cues, is presented under each histogram. This diagram is to scale, and the alignment indicates the relationship between the field centroids and local cues.

254
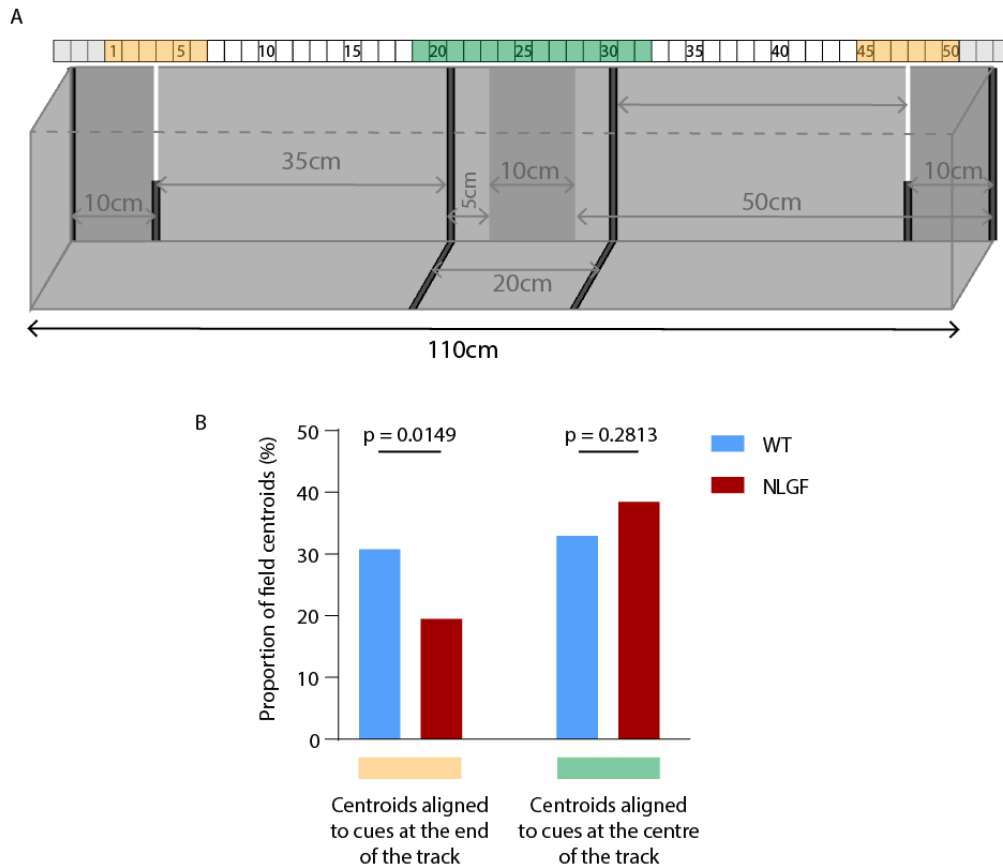
**Figure 4.39 Field centroids on the linear track.** *A*: A schematic of the linear track environment, to scale, indicating the zones corresponding to local cues at either end of the track (yellow) and in the centre of the track (green). Zones shaded in light grey in the scale bar indicate regions which were not included in the analysis (*see page 199*). *B*: The proportion of field centroids aligned with cues at either end of the linear track (yellow), and the central cues (green), are shown for WT (blue) and APP$^{NL-G-F}$ (red) mice. p values calculated from $\chi^2$ testing.

### 4.3.5.4. APP$^{NL-G-F}$ CA1 pyramidal cell activity was less stable.

### 4.3.5.4.1. APP$^{NL-G-F}$ spatial cells had lower spatial correlations on the linear track but not in the open field.

To assess the stability of cells across each recording environment, a spatial correlation was performed between the rate map from the first trial (i.e., open field trial b or linear track trial a) with the rate map from the second trial (i.e., open field trial c or linear track trial b). In the open field environment, there was no significant difference in the spatial correlation between paired rate maps when looking at WT versus APP$^{NL-G-F}$ cell

255

populations. This was the case for all pyramidal cells (mean$_{WT}$ +/- s.e.m.$_{WT}$ = 0.536 +/- 0.02926 vs. mean$_{NLGF}$ +/- s.e.m.$_{NLGF}$ = 0.4729 +/- 0.02971; t$_{(159)}$ = 0.9689, p = 0.3341) and for spatial cells (mean$_{WT}$ +/- s.e.m.$_{WT}$ = 0.7013 +/- 0.026 vs. mean$_{NLGF}$ +/- s.e.m.$_{NLGF}$ = 0.7269 +/- 0.02832; t$_{(54)}$ = 0.6633, p = 0.5100; *Figure 4.40*). However, on the linear track there was a significant difference between WT and APP$^{NL-G-F}$ spatial runs; spatial runs from WT mice had a significantly higher spatial correlation than those from APP$^{NL-G-F}$ mice (Mdn$_{WT}$ = 0.6889 vs. Mdn$_{NLGF}$ = 0.4989; $U$(N$_{WT}$ = 91, N$_{NLGF}$ = 75) = 2425, p = 0.0013; *Figure 4.40C*) indicating that the activity of WT pyramidal cells with a spatial component was more stable on the linear track than the equivalent cell population in APP$^{NL-G-F}$ mice.
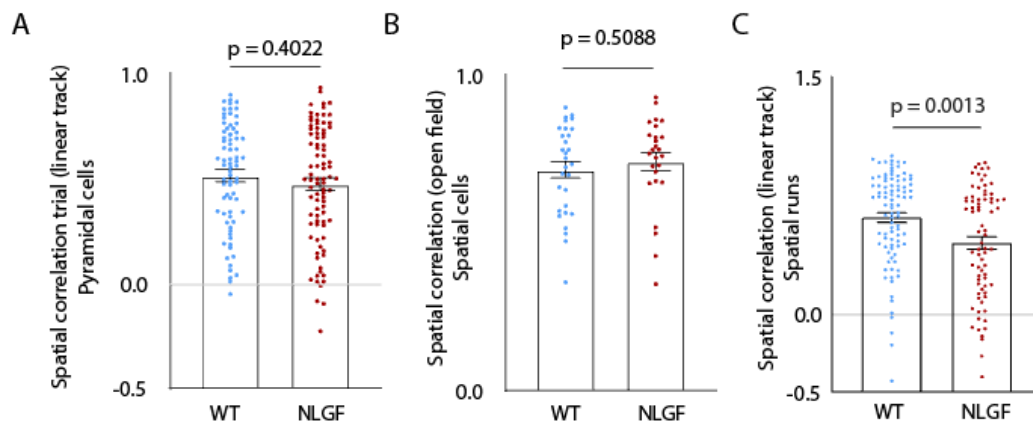


**Figure 4.40 Spatial correlations.** Spatial correlations are shown for pyramidal cells (**A**), and spatial cells (**B**), on the open field, and for spatial runs on the linear track (**C**). In all plots bar height indicates the mean, and error bars the standard error of the mean. p values calculated using paired t-tests. The Bonferroni adjusted α threshold is α = 0.0167.

*4.3.5.4.2. Neural activity across the pyramidal cell population was less stable in APP$^{NL-G-F}$ mice.*

To compare the stability of neural activity across WT and APP$^{NL-G-F}$ cell populations, rather than examining the stability of individual cells, a population vector correlation analysis was conducted. This method involves

performing a correlation between the population level activity in each bin of the environment (i.e., population vectors, see *page 216*). Values close to 1 indicate an increased stability in the neural activity on a population level. WT pyramidal cells displayed a significantly higher population vector correlation than APP[NL-G-F] pyramidal cells, indicating that, on a population level, WT pyramidal cells provided a more stable representation of the open field environment than APP[NL-G-F] pyramidal cells ($Mdn_{WT} = 0.8169$ vs. $Mdn_{NLGF} = 0.6693$; $U(N_{WT} = 340, N_{NLGF} = 389) = 15442$, $p < 0.0001$; KS D = 0.7035, $p < 0.0001$; *Figure 4.41A, top panel, page 259*).

Interestingly, in pyramidal cells recorded on the open field, it appeared to be the non-spatial pyramidal cells, which drove the observed difference in the population vector correlation (*Figure 4.41A*). Further analyses were undertaken to understand why there were different results for the spatial cells versus the whole pyramidal cell population. Due to the nature of a population vector correlation analysis, a single cell with a high firing rate can unduly influence the overall result. To ensure this was not the case subtraction analyses were conducted, i.e., the original analyses were repeated excluding cells with very high firing rates. This showed that no single cell had unduly influenced the findings. Another explanation is that this result is a consequence of how cells are classified as spatial in the open field. In support of this, it was found that WT 'non-spatial' pyramidal cells had significantly higher spatial information values than 'non-spatial' APP[NL-G-F] pyramidal cells ($Mdn_{WT} = 0.08813$ vs. $Mdn_{NLGF} = 0.05608$; $U(N_{WT} = 59, N_{NLGF} = 80) = 1725$, $p = 0.0066$).

**Figure 4.41 Population vector correlations.** Population vector correlations (PVCs) are shown for pyramidal cells in the open field (**A**, *top panel*), with a plot of population vectors (*left*) and a cumulative frequency distribution of population vectors (*right*), and for pyramidal cells on the linear track (**B**, *top panel*). PVCs are also shown for spatial and non-spatial cells in the open field (**A**, *lower panels*) and spatial runs on the linear track (**B**, *lower panel*). In all bar graphs individual points represent the population vectors, where n = the number of bins occupied in the environment, bar height indicates the mean value, and error bars the standard error of the mean. p values were calculated using Mann Whitney U tests (bar graphs) and a Kolmogorov-Smirnov test.

APP$^{NL-G-F}$ pyramidal cells were also found to be less stable on the linear track (Mdn$_{WT}$ = 0.8835, Mdn$_{NLGF}$ = 0.7767; $U$(N$_{WT}$ = 59, N$_{NLGF}$ = 59) = 405, p < 0.0001; *Figure 4.41B, top panel*), indicating that the WT pyramidal cell population provided a more stable representation of the linear track than APP$^{NL-G-F}$ pyramidal cells. This analysis was repeated for only the significantly spatial runs in the WT and APP$^{NL-G-F}$ mice. Again, the WT population exhibited significantly more stable neural activity between the two linear track trials (Mdn$_{WT}$ = 0.8912, Mdn$_{NLGF}$ = 0.7556; $U$(N$_{WT}$ = 59, N$_{NLGF}$ = 59) = 429, p < 0.0001; *Figure 4.41B*).

### 4.3.6. Comparing neural activity across recording environments

#### *4.3.6.1. Similar proportions of WT and APP$^{NL-G-F}$ cells were active in each environment.*

There were no differences between WT and APP$^{NL-G-F}$ mice regarding the proportions of cells, both pyramidal cells and interneurons, which fired in different environments (*Figure 4.42A, top row*). A similar proportion of all cells fired in both environments, in the open field only and on the linear track only ($\chi^2_{(2)}$ = 4.646, p = 0.0984; *Figure 4.42B*; *Table 4.8, page 261*) and this was also the case for the pyramidal cells ($\chi^2_{(2)}$ = 4.928, p = 0.0851). Across both groups, the majority of pyramidal cells recorded in the open field also fired on the linear track (77.9% (74/95) of WT pyramidal cells and 64.5% (69/107) of APP$^{NL-G-F}$ pyramidal cells).
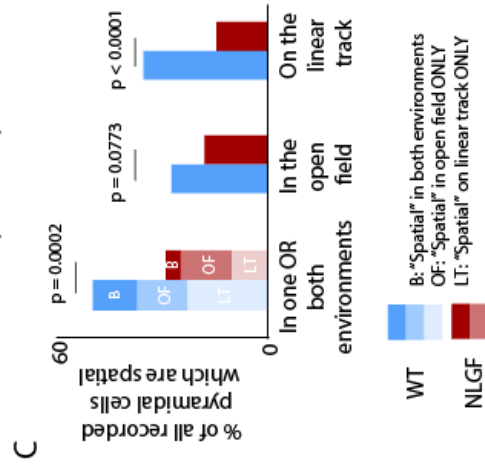
**Figure 4.42 Cells recorded across the open field and linear track.** **A**: Venn diagrams illustrating the firing of all cells (top row), pyramidal cells (middle row) and spatial cells (bottom row) across the two recording environments, shown for WT (blue) and APP^NL-G-F (red) mice. Cells firing in the open field are shown on the left and cells firing on the linear track on the right. The region of overlap indicates cells which fired in both environments. **B**: The proportion of all recorded cells firing on the open field only, the linear track only, and in both environments. **C**: Proportions of all pyramidal cells which were spatial in different environmental conditions. **D&E**: Cross-tabulation for WT (**D**) and APP^NL-G-F (**E**) pyramidal cells. OF = open field, LT = linear track. All p values from χ² testing.

260

**Table 4.8 Distribution of cells firing in the open field and on the linear track.**

| | Cells recorded in: | Wild-Type | APP$^{NL-G-F}$ |
|---|---|---|---|
| **Pyramidal cells AND interneurons** (Cells in specified environment/ total cells recorded) | Open Field | 77.8% (119/153) | 83.9% (151/180) |
| | Linear Track | 83.7% (128/153) | 75.0% (135/180) |
| | Both | 61.4% (94/153) | 58.9% (106/180) |
| | Open Field ONLY | 16.3% (25/153) | 30.0% (45/180) |
| | Linear Track ONLY | 22.2% (34/153) | 16.1% (29/180) |
| **Pyramidal cells ONLY** | Open Field | 76.6% (95/124) | 80.5% (107/133) |
| | Linear Track | 83.1% (103/124) | 71.4% (95/133) |
| | Both | 59.7% (74/124) | 51.9% (69/133) |
| | Open Field ONLY | 16.9% (21/124) | 28.6% (38/133) |
| | Linear Track ONLY | 23.4% (29/124) | 19.5% (26/133) |
| | **Cells classified as spatial in:** | **Wild-Type** | APP$^{NL-G-F}$ |
| **Spatial cells** | **Open Field AND/OR Linear track** | | |
| | % of ALL recorded pyramidal cells | 54.8% (68/124) | 31.6% (42/133) |
| | **Open Field** | | |
| | % of all recorded pyramidal cells | 29.8% (37/124) | 20.3% (27/133) |
| | % of Open Field pyramidal cells | 38.9% (37/95) | 25.2% (27/107) |
| | % of all spatial cells | 54.4% (37/68) | 64.3% (27/42) |
| | **Linear Track** | | |
| | % of all recorded pyramidal cells | 38.7% (48/124) | 15.9% (21/132) |
| | % of Linear Track pyramidal cells | 46.6% (48/103) | 22.1% (21/95) |
| | % of all spatial cells | 70.6% (48/68) | 50.0% (21/42) |
| | **Both** | | |
| | % of all recorded pyramidal cells | 13.7% (17/124) | 4.5% (6/133) |
| | % of pyramidal cells firing in both environments | 23.0% (17/74) | 8.7% (6/69) |
| | % of all spatial cells | 25.0% (17/68) | 14.3% (6/42) |
| | **Open Field ONLY** | | |
| | % of all recorded pyramidal cells | 16.1% (20/124) | 15.8% (21/133) |
| | % of Open Field pyramidal cells | 21.1% (20/95) | 19.6% (21/107) |
| | % of all spatial cells | 29.4% (20/68) | 50.0% (21/42) |
| | **Linear Track ONLY** | | |
| | % of all recorded pyramidal cells | 25.0% (31/124) | 11.3% (15/133) |
| | % of Linear Track pyramidal cells | 30.1% (31/103) | 15.8% (15/95) |
| | % of all spatial cells | 45.6% (31/68) | 35.7% (15/42) |

### 4.3.6.2. Spatial firing on the linear track discriminated more effectively between WT and APP$^{NL-G-F}$ mice than spatial firing in the open field.

All pyramidal cells were categorised according to whether their firing patterns were significantly spatial in the open field, on the linear track, in both environments, or in neither (*Figure 4.42A*). A significantly higher proportion of pyramidal cells were spatial in one or both environments in WT mice compared to APP$^{NL-G-F}$ mice (54.8% (68/124) vs. 26.5% (42/133); $\chi^2_{(1)}$ = 14.182, p = 0.0002; *Figure 4.42C*). The activity of pyramidal cells which fired in both recording environments also effectively discriminated between groups; a significantly higher proportion of these cells were spatial in WT mice (23.0% (17/74) WT vs. 8.7% (6/69) APP$^{NL-G-F}$; $\chi^2_{(1)}$ = 5.393, p = 0.0202).

The proportion of all recorded pyramidal cells which were spatial on the linear track appeared to discriminate more effectively between groups than the proportion which were spatial in the open field (*Table 4.8*; spatial vs. non-spatial pyramidal cells in open field $\chi^2_{(1)}$ = 3.122, p = 0.0773; spatial vs. non-spatial pyramidal cells on linear track $\chi^2_{(1)}$ = 16.88, p < 0.0001; *Figure 4.42C*). This was explored further by comparing the odds ratios between the two environments; in the open field the odds of a WT pyramidal cell being spatial versus an APP$^{NL-G-F}$ pyramidal cell was 1.670 (95% CI 0.9429 to 2.9565) compared to an odds ratio of 3.368 on the linear track (95% CI 1.868 to 6.0751). Although the confidence intervals of the two odds ratios overlap, the odds ratio for the linear track does not include one, indicating that classification of spatial cells on the linear track could be used to reliably

discriminate between WT and APP$^{NL-G-F}$ mice, whereas on the open field it could not.

### 4.3.7. Temporal coding of spatial information was altered in APP$^{NL-G-F}$ mice.

#### *4.3.7.1. There were no differences in theta power when comparing WT and APP$^{NL-G-F}$ mice.*

Power spectra were constructed for all mice in the 0 – 125 Hz range (*Figures 4.43, 4.44 and 4.45, pages 260 – 262*), and the power within each 1Hz bin of the mean power spectra was compared between groups (multiple t-tests, FDR corrected for multiple comparisons). All mice had a prominent peak corresponding to the theta band. APP$^{NL-G-F}$ mice displayed more noise in the 0 – 5 Hz range, and also had significantly greater power in the 6 – 7 Hz band. In contrast, WT mice had greater power in the 8 – 10 Hz range (*Table 4.9; Figure 4.45A*). These differences may reflect a difference in the peak theta frequency between groups rather than a true difference in theta power. There was no significant difference between groups in the theta power index (Mdn$_{WT}$ = 0.2423 vs. Mdn$_{NLGF}$ = 0.2652; $U$(N$_{WT}$ = 4, N$_{NLGF}$ = 4) = 7, p = 0.8857; *Figure 4.45B*) or in the maximum power within the theta band (Mdn$_{WT}$ = 7.829 x 10$^{-5}$ versus Mdn$_{NLGF}$ = 8.798 x 10$^{-5}$; $U$(N$_{WT}$ = 4, N$_{NLGF}$ = 4) = 6, p = 0.6857; *Figure 4.45C*), and, with the exception of one APP$^{NL-G-F}$ mouse, the peak theta frequencies of APP$^{NL-G-F}$ mice were all lower than those in the WT mice (*Figure 4.45D*). However, this result fell short of statistical significance, possibly due to a small sample size (Mdn$_{WT}$ = 7.757 vs. Mdn$_{NLGF}$ = 7.492; $U$(N$_{WT}$ = 4, N$_{NLGF}$ = 4) = 2, p = 0.1143).

| Frequency band (Hz) | Mean power (normalised) | | t ratio | q value |
|---|---|---|---|---|
| | **WT** | APP$^{NL-G-F}$ | | |
| 0 – 1 | 0.08047 | 0.1200 | 6.371 | **< 0.000001** |
| 1 – 2 | 0.06623 | 0.1431 | 12.38 | **< 0.000001** |
| 2 – 3 | 0.04179 | 0.08872 | 7.554 | **< 0.000001** |
| 3 – 4 | 0.03841 | 0.06896 | 4.918 | **0.000032** |
| 4 – 5 | 0.04563 | 0.06505 | 3.125 | **0.028320** |
| 5 – 6 | 0.06319 | 0.07285 | 1.554 | 0.975442 |
| 6 – 7 | 0.09292 | 0.1153 | 3.559 | **0.006966** |
| 7 – 8 | 0.1292 | 0.1354 | 1.001 | 0.975442 |
| 8 – 9 | 0.1116 | 0.08131 | 4.882 | **0.000032** |
| 9 – 10 | 0.06302 | 0.04342 | 3.155 | **0.028320** |
| 10 – 11 | 0.03850 | 0.02923 | 1.492 | 0.975442 |
| 11 – 12 | 0.02725 | 0.02357 | 0.5925 | 0.975442 |

**Table 4.9 A comparison of power between WT and APP$^{NL-G-F}$ power spectra: 0-12Hz.** The differences in power for each 1Hz bin, from multiple t-tests, are outlined above with their respective q values. FDR corrected for multiple comparisons (q = 0.05), df = 750. Frequency range tested was 0 - 125Hz but results are presented for 0 – 12Hz. All significant discoveries were within this range.

Although no significant differences were found between WT and APP$^{NL-G-F}$ mice in the theta power index or the peak theta power, the values obtained from APP$^{NL-G-F}$ mice were more variable. Across both these measures the variance among the APP$^{NL-G-F}$ mice was significantly greater (theta power index: $F_{(3,3)}$ = 64.06, p = 0.0064; peak theta power: $F_{(3,3)}$ = 109.7, p = 0.0029). To assess stability of the theta rhythm the standard deviation of the peak-to-peak distances of the theta analytic signal were compared between groups and no significant difference was found (mean$_{WT}$ +/- s.e.m.$_{WT}$ = 20.24 +/- 0.59 ms vs. mean$_{NLGF}$ +/- s.e.m.$_{NLGF}$ = 21.24 +/- 0.88 ms; $t_{(6)}$ = 0.9428, p = 0.3822).
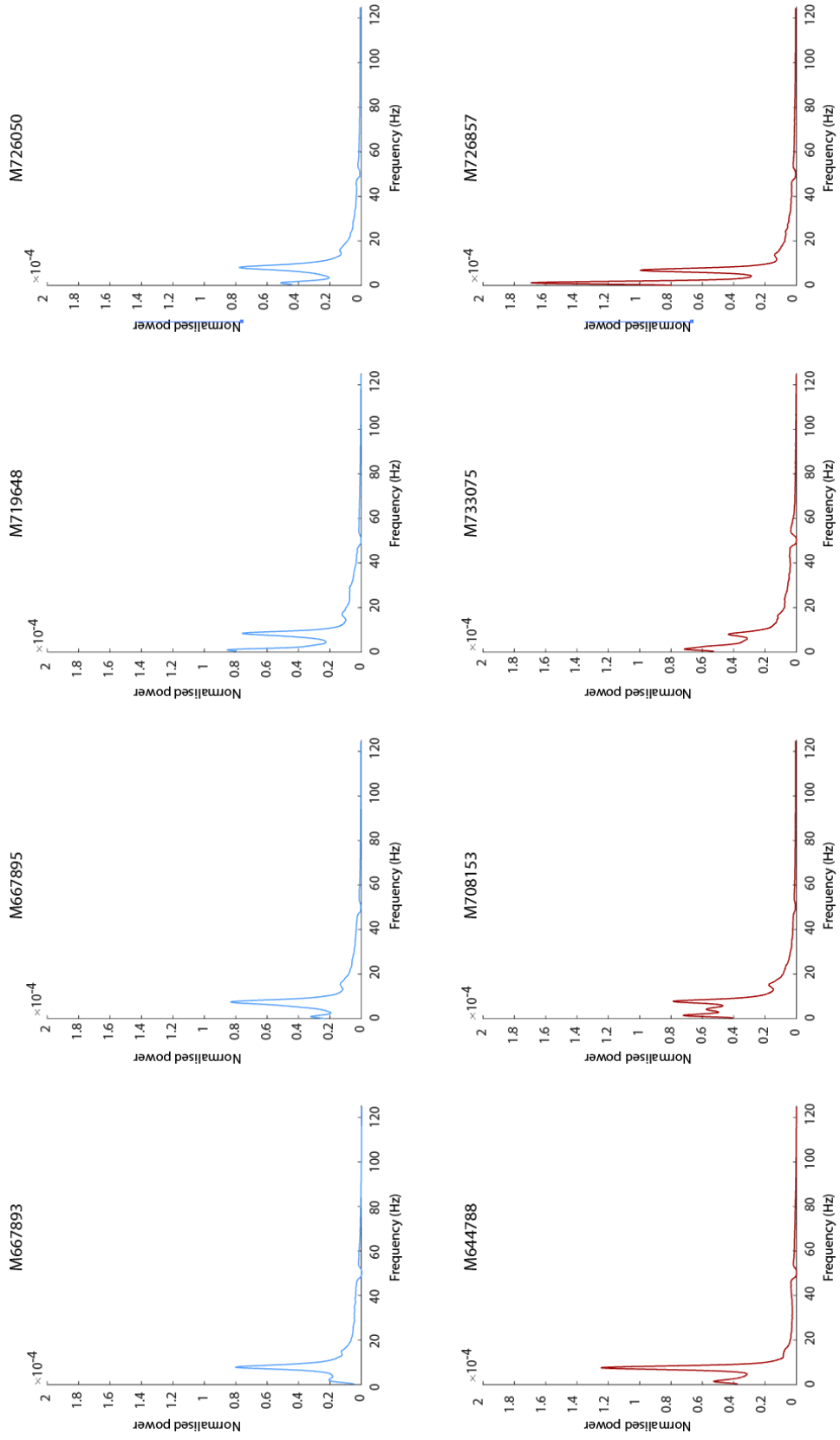
**Figure 4.43 Normalised power spectra for WT and APP$^{\text{NL-G-F}}$ mice: 0 - 125Hz.** Top row indicates power spectra for WT mice (blue) and bottom row for APP$^{\text{NL-G-F}}$ mice (red). Power is normalised to total power within the 4 - 125Hz band. x axis limited to 125Hz.
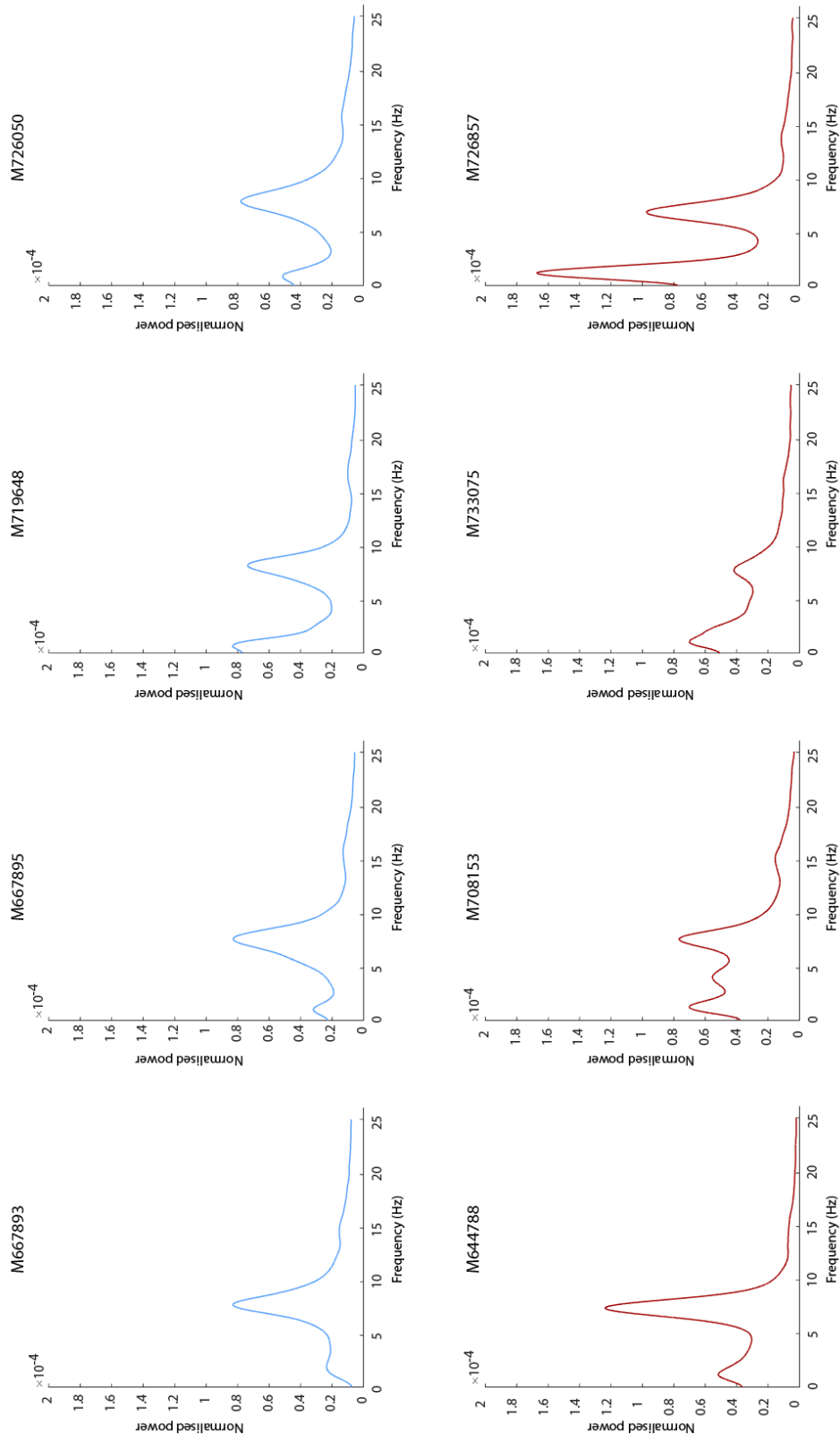
**Figure 4.44 Normalised power spectra for WT and APP^NL-G-F mice: 0 - 25Hz.** Top row indicates power spectra for WT mice (blue) and bottom row for APP^NL-G-F mice (red). Power is normalised to the total power in the 4 - 125Hz band. x axis limited to 25Hz.
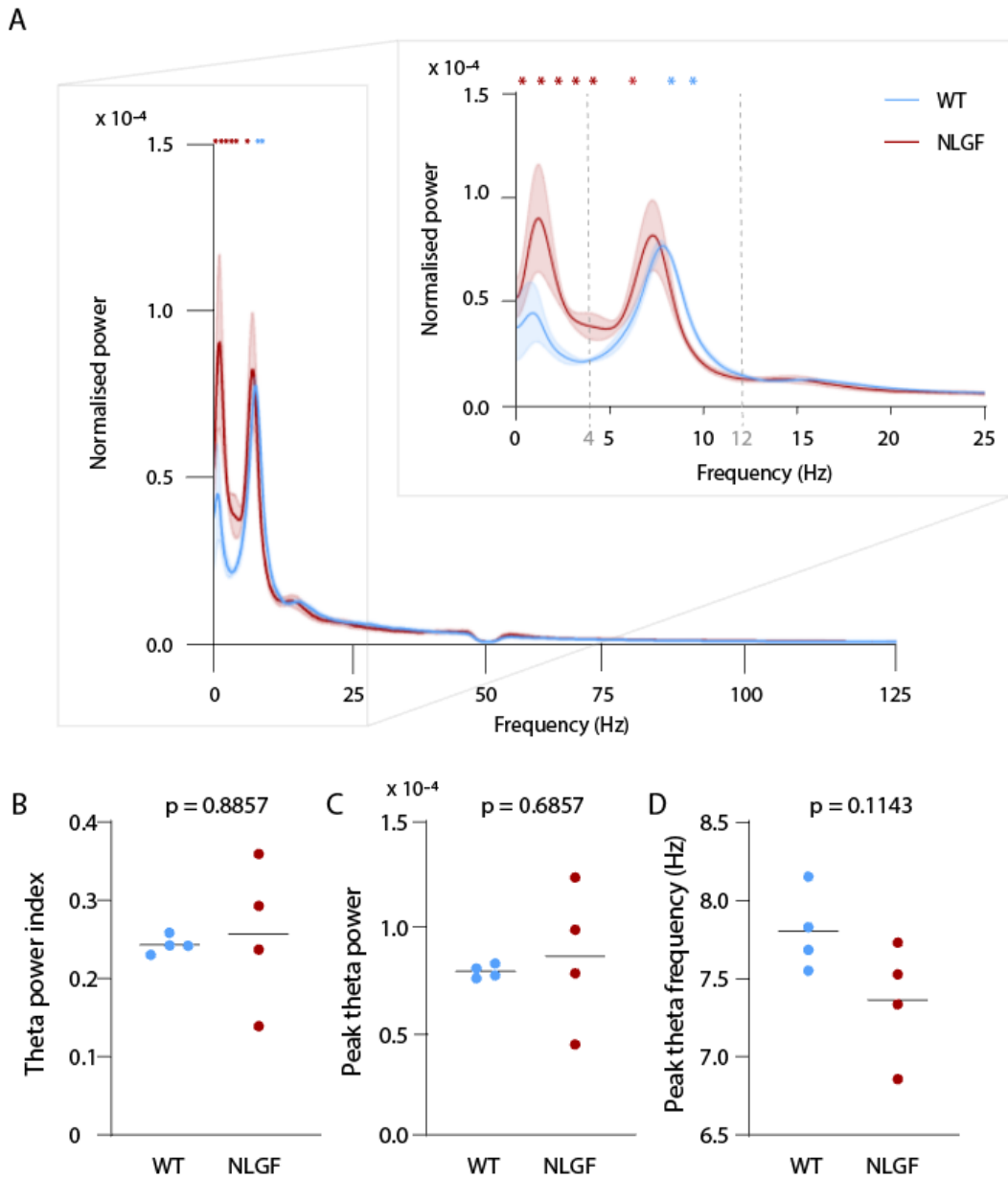
**Figure 4.45 LFP power spectra in WT and APP<sup>NL-G-F</sup> mice. A:** Mean power spectra for WT mice (blue) and APP<sup>NL-G-F</sup> (red) (n = 4 mice in each group) in the 0 - 125 Hz (left) and 0 - 25Hz (inset) ranges. Shaded error envelopes represent standard error of the mean. Grey dotted lines indicate the 4 - 12 Hz theta range. Asterisks indicate 1Hz bins in which there is a statistically significant difference in power between WT and APP<sup>NL-G-F</sup> mice (multiple FDR corrected paired t-tests, q = 0.05). Red asterisks indicate bins in which the power in the APP<sup>NL-G-F</sup> spectra is significantly greater, and blue asterisks the bins in which the power in the WT spectra is greater. **B:** Theta power index in WT vs. APP<sup>NL-G-F</sup> mice. **C:** The maximum power in the theta band (4 – 12 Hz) for WT vs. APP<sup>NL-G-F</sup> mice. Power is normalised to the total power in the 4 – 125 Hz band. **D:** The theta frequency with the maximum power in WT vs. APP<sup>NL-G-F</sup> mice. Solid black bars indicate mean values. p values Obtained from Mann Whitney U testing.

### 4.3.7.2. There was no difference in the theta modulation of WT and APP$^{NL-G-F}$ pyramidal or spatial cell activity.

The autocorrelograms of both WT and APP$^{NL-G-F}$ spatial cells showed that some cells were theta modulated, with characteristic peaks visible in the 100 – 140ms theta range and at the appropriate time delay for the associated theta harmonics (*Figure 4.46A*). On inspection of the raw autocorrelograms, spatial cells from WT mice appeared more strongly theta modulated than those from APP$^{NL-G-F}$ mice, however, there were no significant differences between groups in the parameters used to measure theta modulation (see methods section, *page 218).* There were no significant differences in either the theta modulation index (mean$_{WT}$ +/- s.e.m. = 0.4496 +/- 0.02198, mean$_{NLGF}$ = 0.4031 +/- 0.03442, t$_{51}$ = 1.190, p = 0.2395), or in the theta signal-to-noise ratio (Mdn$_{WT}$ = 15.04, Mdn$_{NLGF}$ = 17.10, *U*(N$_{WT}$ = 44, N$_{NLGF}$ = 21) = 440, p = 0.7648; *Figure 4.46B*). There were also no differences in theta modulation when comparing the two pyramidal cell populations (theta modulation index: mean$_{WT}$ +/- s.e.m. = 0.4442 +/- 0.01556, mean$_{NLGF}$ = 0.4229 +/- 0.02031, t$_{138}$ = 0.8452, p = 0.39945; theta signal-to-noise: Mdn$_{WT}$ = 24.54, Mdn$_{NLGF}$ = 20.63, *U*(N$_{WT}$ = 95, N$_{NLGF}$ = 79) = 3709, p = 0.8969; *Figure 4.46C*).
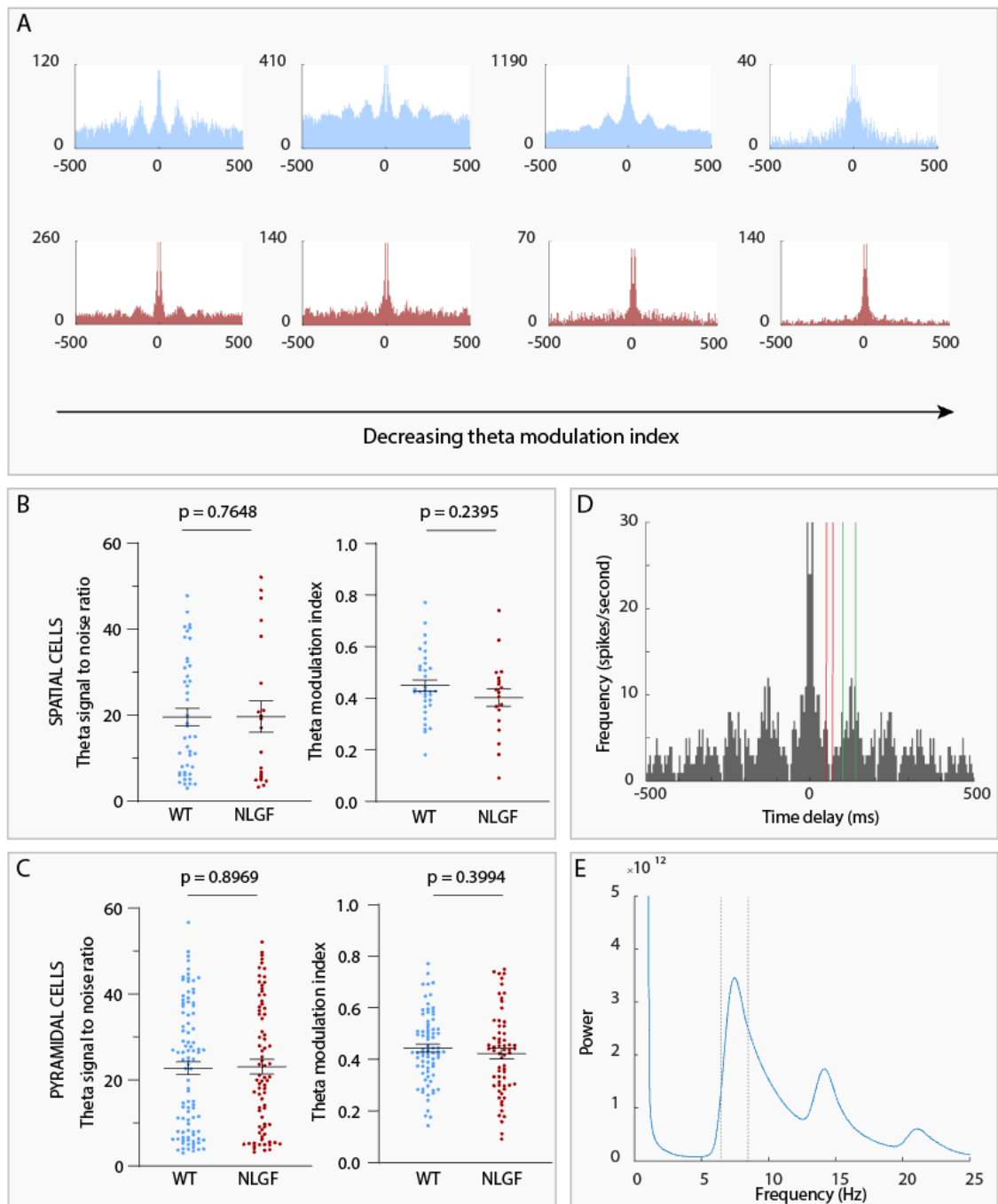
**Figure 4.46 Theta modulation of spatial cells.** Representative autocorrelograms for WT (***A***, blue), and APP[NL-G-F] (***A***, red), spatial cells with time delay (ms) on the x axis versus frequency (spikes/second) on the y axis. Bin size 5ms. Autocorrelograms for all spatial cells were ordered from highest to lowest theta modulation index and examples selected at evenly spaced intervals between these two extremes. ***B&C***: There were no significant differences in theta modulation as measured using the theta signal-to-noise ratio or the theta modulation index between WT and APP[NL-G-F] spatial (***B***), or pyramidal (***C***), cells. p values from Mann Whitney U testing for theta signal-to-noise ratio (non-parametric data), and unpaired t-test for theta modulation index (parametric data). Examples of how the theta modulation index (***D***) and theta signal-to-noise ratio (***E***) are calculated are illustrated for a WT cell (***A***, first autocorrelogram). ***D***: The theta modulation index is the difference between the sum of frequencies in the peak theta range (green lines), and the trough theta range (red lines), divided by their sum. ***E***: The theta signal-to-noise-ratio is the power within the theta peak (the region between the grey lines) divided by the power in the remaining 4 – 125Hz spectrum excluding the peak.

269

### 4.3.7.3. Theta phase-locking was reduced in APP$^{NL-G-F}$ mice compared to WT controls…

*4.3.7.3.1. … on a single cell level.*

The extent to which the firing of each cell was concentrated around a particular theta phase was examined in WT and APP$^{NL-G-F}$ mice. The length of the mean resultant vector for all spike phases was used as a measure of *phase concentration*, i.e., the extent to which a cell was phase-locked, whereas the angle of the resultant vector indicated the cells *preferred theta phase*. Vector lengths of 0 indicated there was no phase-locking and values of 1 implied perfect phase-locking. Spatial cell firing was found to have a significantly higher phase concentration in WT mice than in APP$^{NL-G-F}$ mice: mean$_{WT}$ +/- s.e.m = 0.1593 +/- 0.01044, mean$_{NLGF}$ = 0.08610 +/- 0.01063; $t_{67}$ = 4.228, p < 0.0001 (*Figure 4.47, page 273*). This was also the case for the WT pyramidal cells which had a greater phase concentration than APP$^{NL-G-F}$ pyramidal cells: Mdn$_{WT}$ = 0.1527, Mdn$_{NLGF}$ = 0.08873; $U$(N$_{WT}$ = 104, N$_{NLGF}$ = 96) = 2486, p < 0.0001; *Figure 4.47, page 273*).

A cell was considered *phase-locked* if the distribution of spike phase angles deviated significantly from a uniform circular distribution (*see page 222*). There were significantly more phase-locked cells amongst both the WT spatial and pyramidal cell populations than the equivalent APP$^{NL-G-F}$ cell populations. 70.8% (34/48) of WT spatial cells were phase-locked compared with 42.9% (9/21) of APP$^{NL-G-F}$ spatial cells ($\chi^2_{(1)}$ = 4.869, p = 0.0273), and 66.7% (70/105) of WT pyramidal cells were phase-locked compared with 31.3% (30/96) of APP$^{NL-G-F}$ pyramidal cells ($\chi^2_{(1)}$ = 25.16, p < 0.0001; *Figure 4.47, page 273*). Since cells with a bimodal distribution of

spike phase angles may not be considered significantly phase-locked, the polar plots of all spatial cells were inspected; only one spatial cell was found to have a bimodal distribution and this was in a WT mouse.

*4.3.7.3.2. … across the whole pyramidal cell population.*

Polar plots of the pyramidal cell resultant vectors were constructed for each mouse. Inspection of these plots indicated that in some mice, the phase of the resultant vectors appeared to be concentrated within a 120° range (*Figure 4.48, page 274*). Three out of four WT mice had a distribution of pyramidal cell resultant vectors which significantly differed from a uniform circular distribution, compared to two out of four of the APP$^{NL-G-F}$ mice (Rayleigh testing; *Table 4.10, page 274*).

**Figure 4.47 Phase-locking of spatial and pyramidal cells. *A:*** Representative polar histograms for WT (blue) and APP[NL-G-F] (red) spatial cells showing theta phase (θ axis) vs. spike probability (r axis). Bin size = π/6 radians (30°). Grey arrows represent the mean resultant vectors, with theta phase offset indicated by the angle of the grey arrow in relation to the θ axis. The maximum value on the r axis indicates a spike firing probability of 0.2, or a vector length of 0.3. Plots were arranged from the strongest to the weakest phase-locked spatial cells, and evenly spaced plots selected for presentation. Spatial cells (**B**) and pyramidal cells (**D**) had a significantly greater degree of phase-locking as measured by the resultant vector length. Error bars indicate standard error of the mean, p values from unpaired t-tests (***B***, parametric data) and Mann Whitney U tests (***D***, non-parametric data). ***C&E:*** There were a significantly greater proportion of phase-locked cells in WT mice in both the spatial (***C***), and pyramidal (***E***), cell populations. p values from $\chi^2$ tests.

272
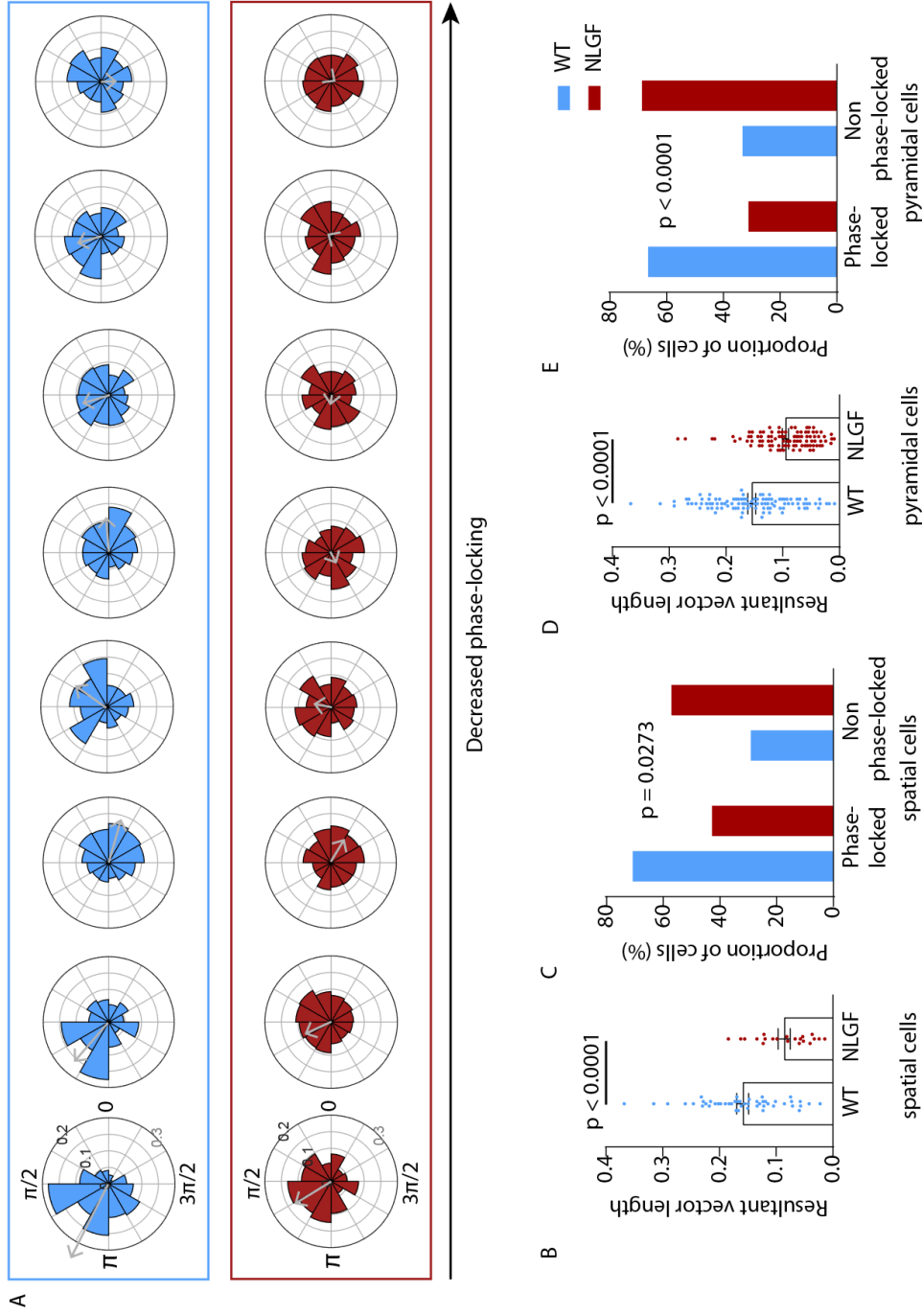
| | Mouse ID | Population resultant vector length | Population resultant vector phase | Rayleigh Z statistic | p value | n |
|---|---|---|---|---|---|---|
| **WT** | **M667893** | 0.8269 | 111° | 25.9809 | **< 0.0001** | 38 |
| | **M667895** | 0.7397 | 65° | 3.2827 | 0.0301 | 6 |
| | **M719648** | 0.4632 | 6° | 8.3674 | **0.0002** | 39 |
| | **M726050** | 0.4650 | 47° | 4.5410 | **0.0092** | 21 |
| **APP^NL-G-F** | **M644788** | 0.4430 | 166° | 1.5700 | 0.2126 | 8 |
| | **M708153** | 0.2362 | 203° | 1.7849 | 0.1683 | 32 |
| | **M733075** | 0.6753 | 288° | 8.2096 | **0.0001** | 18 |
| | **M726857** | 0.5514 | 24° | 11.5527 | **< 0.0001** | 38 |

**Table 4.10 Population resultant vectors by mouse.** The length and phase of the population resultant vectors (equivalent to the black arrows in Figure 4.48) are presented for each mouse. p values are from Rayleigh testing, α = 0.01.
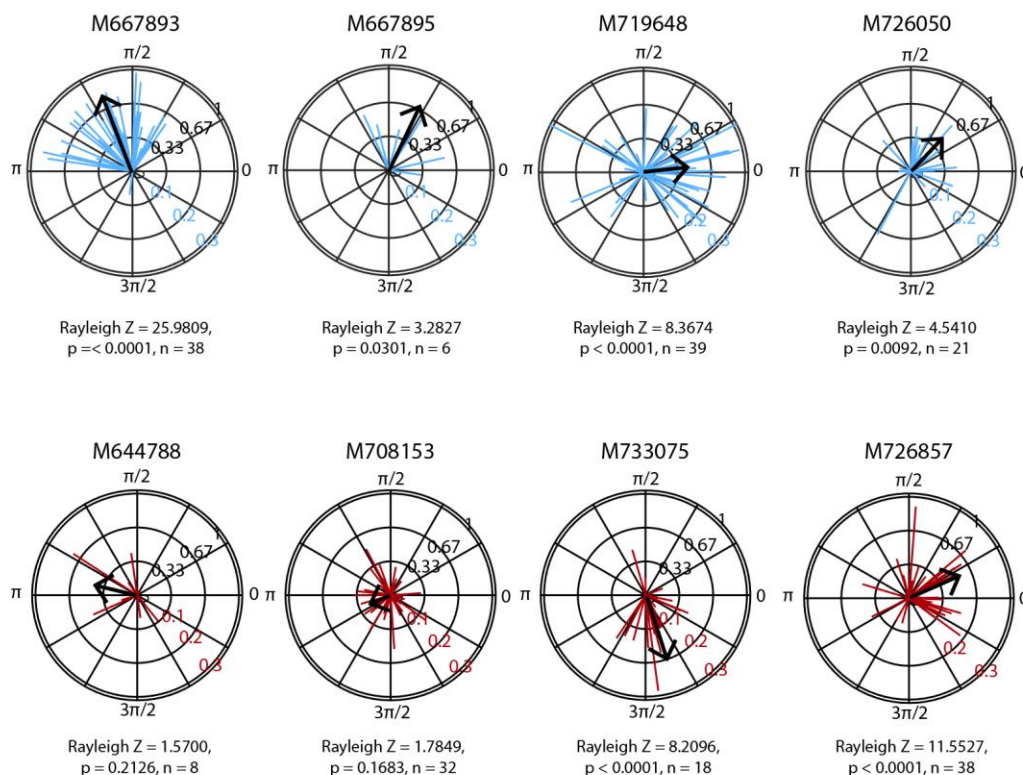


**Figure 4.48 Phase-locking of pyramidal cell populations by mouse.** Polar plots showing the resultant vectors from all pyramidal cells for each mouse (coloured lines). WT plots are in blue and NLGF plots in red. Mouse ID is above each plot. Black arrows represent the resultant vector across all pyramidal cells, i.e., the 'population resultant vector'. The r axis represents both the length of the individual pyramidal cell resultant vectors (coloured), and the length of the population resultant vector (black).

For each mouse, the resultant vector of all the pyramidal cell resultant vectors was calculated. This 'resultant vector of resultant vectors', henceforth referred to as the *population resultant vector,* has a direction (angle) which represents the preferred theta phase across the pyramidal cell population as a whole, weighted by the strength of the contributing individual resultant vectors, and a length which represents the concentration of preferred theta phases across the pyramidal cell population. To investigate the theta phase concentration on a population level between the two groups, the theta phase of pyramidal cell resultant vectors was normalised to zero for each mouse which allowed data to be combined across mice (*Figure 4.49A-B, page 274*). A population resultant vector could then be calculated for each group (WT vs APP$^{NL-G-F}$), where the phase was, by definition, zero, but whose length represented phase concentration on a population level. As can be seen in *Figure 4.49A-B* (black arrows, *page 274*), the population resultant vector was longer in WT mice than in APP$^{NL-G-F}$ mice. To determine whether this difference was significant, the projection of each individual resultant vector onto the population resultant vector was calculated (*Figure 4.49C*). The length of these projection vectors (*Figure 4.49B*, for example, Arv, Brv and Crv) could theoretically range from -1, indicating that a pyramidal cell fired all of its spikes 180° out of phase with the preferred theta phase of the whole population, to 1, indicating that all spikes fired by that pyramidal cell were aligned with the preferred theta phase of the pyramidal cell population. The projection vectors of WT pyramidal cells were significantly longer than those of APP$^{NL-G-F}$ pyramidal cells (Mdn$_{WT}$ = 0.1148, Mdn$_{NLGF}$ = 0.04497; $U$(N$_{WT}$ = 104, N$_{NLGF}$ = 96) =

3064, p < 0.0001; *Figure 4.49D*) indicating a reduced theta phase concentration of pyramidal cells on a population level in the APP$^{NL-G-F}$ mice.

Finally, the extent to which the preferred theta phase of each individual pyramidal cell aligned with the preferred theta phase across the pyramidal cell population was examined. This was achieved by comparing the differences between each pyramidal cell resultant vector and the population resultant vector. This indicated that individual WT pyramidal cells were significantly more likely than APP$^{NL-G-F}$ pyramidal cells to have preferred theta phases which aligned closely with the preferred theta phase of the overall pyramidal cell popuation  (Mdn$_{WT}$ = 33.7°, Mdn$_{NLGF}$ = 49.2°; $U$(N$_{WT}$ = 104, N$_{NLGF}$ = 96) = 4109, p = 0.0307; *Figure 4.50*).
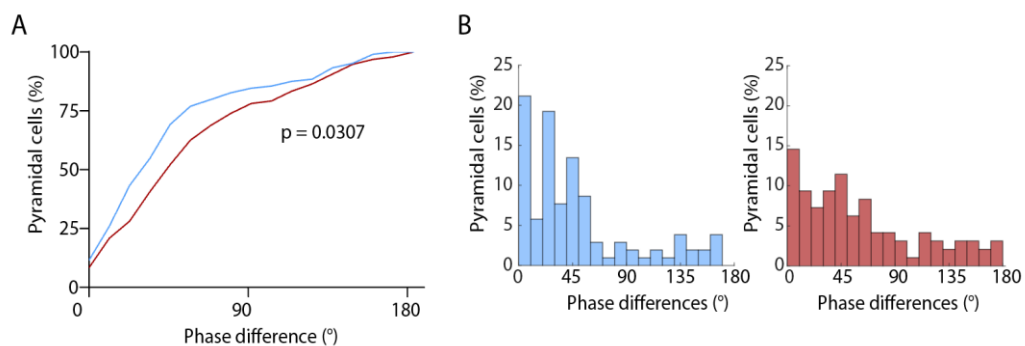


**Figure 4.50 Phase differences between individual pyramidal cells and the population resultant vector. *A*:** Cumulative frequency distribution of phase differences for WT (blue) and NLGF (red) mice. p value from Mann Whitney U test, bin size = 0.2. ***B***: Histograms showing the phase differences between individual pyramidal cell resultant vectors and the population resultant vector for WT (blue) and NLGF (red) mice.
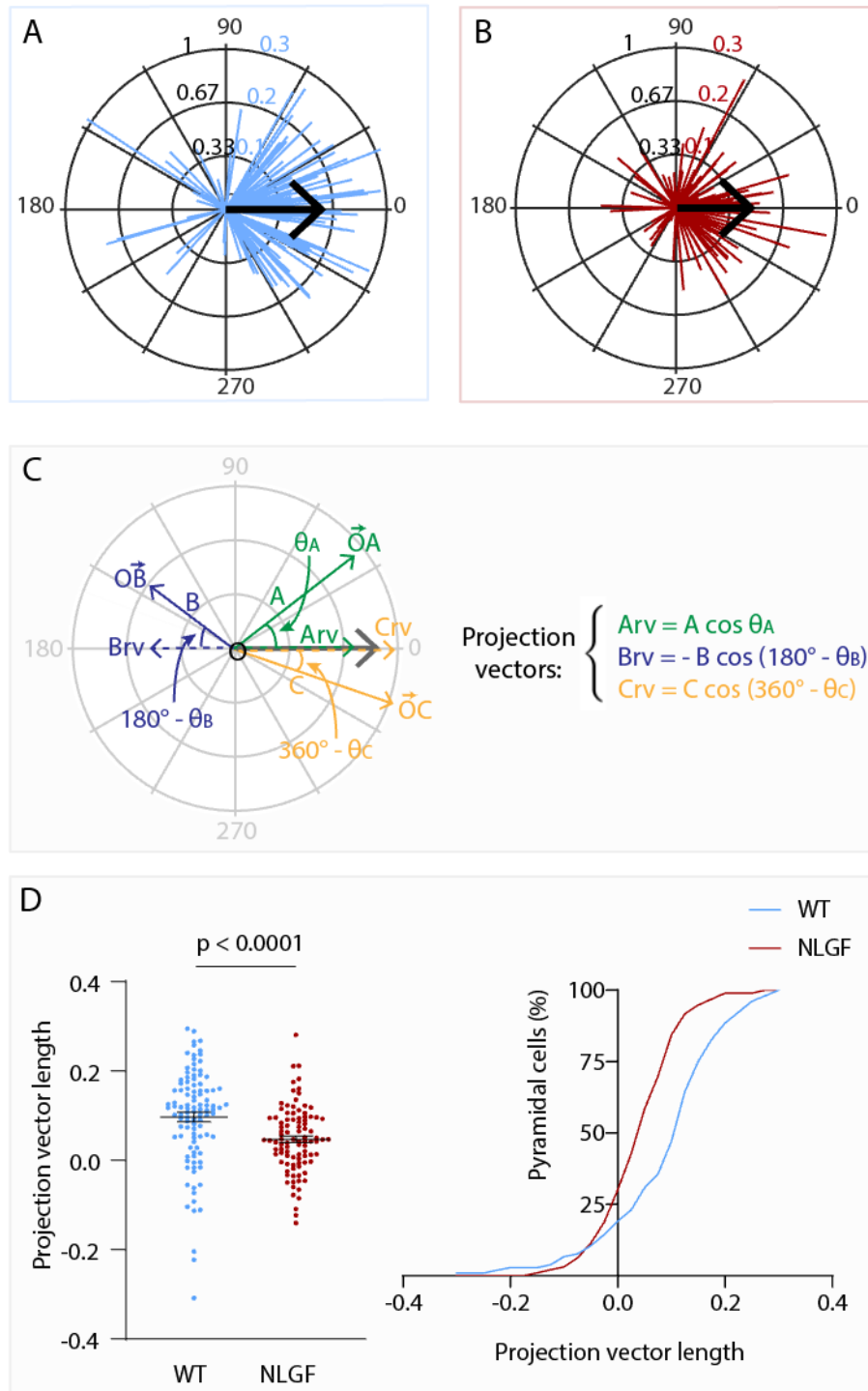
**Figure 4.49 Phase concentration of pyramidal cell populations.** Polar plots show the resultant vectors for all pyramidal cells recorded in WT (**A**) and NLGF (**B**) mice. The theta axis represents the normalised theta phase (the population resultant vector for each mouse was normalised to zero). The r axis indicates the length of individual pyramidal cell resultant vectors (coloured numbers), and the length of the population resultant vector for that group (black arrow and black numbers). To ascertain whether there was a significant group difference in population vector length (black arrows, **A&B**) the projection of each resultant vector onto the population resultant vector was calculated as illustrated in **C**. The lengths of these projection vectors were significantly greater in WT mice compared to NLGF mice (raw values and mean +/- s.e.m shown in **D**, *left*; cumulative frequency distribution of projection vector lengths show in **D**, *right*). p value from Mann Whitney U test. Histogram bin size = 0.025.

### 4.3.7.4. Phase precession in WT and APP$^{NL-G-F}$ mice

To compare phase precession between the two groups of mice, data were analysed from the place field containing the peak firing rate on all significantly spatial runs on the linear track. A normalised in-field position was calculated for each spike, indicating the position of the mouse within the field when that spike fired; a value of 0 indicated that an animal was entering the place field, and a value of 1 signified that an animal was leaving the field. For each place field, a circular linear regression was performed for the normalised in-field position versus the theta phase when the cell fired spikes. A cell was significantly *phase-precessing* if there was a statistically significant negative correlation between these two variables.

### 4.3.7.4.1. Phase precession was not consistently altered in APP$^{NL-G-F}$ mice when using the original place field criteria.

When place fields were defined using the same criteria as for previous analyses, i.e., as regions in which a cells firing rate exceeded 20% of its peak firing rate, a significantly greater proportion of WT spatial runs exhibited phase precession (18.4% (20/109) of WT spatial runs versus 7.9% (6/76) of APP$^{NL-G-F}$ spatial runs; $\chi^2_{(1)}$ = 4.051, p = 0.04413). Although the mean correlation coefficient and gradient of the line-of-best-fit for theta phase versus in-field position were more negative in the WT group, these differences were not statistically significant (correlation coefficient: Mdn$_{WT}$ = - 0.04592, Mdn$_{NLGF}$ = - 0.03653; $U$(N$_{WT}$ = 108, N$_{NLGF}$ = 76) = 3602, p = 0.1590; gradient of best-fit-line: Mdn$_{WT}$ = - 1.218, Mdn$_{NLGF}$ = - 0.6621; $U$(N$_{WT}$ = 108, N$_{NLGF}$ = 76) = 3770, p = 0.3494; *Figure 4.51*). It was noted that phase precession was not always clearly visible on the scatterplots of theta phase

versus in field position, even for cells found to have significant phase precession (*Figure 4.51*). This was particularly the case in the APP$^{NL-G-F}$ mice. In addition, using this definition of a place field resulted in large portions of the linear track being identified as the place field in some spatial cells, making meaningful analysis of phase precession challenging (*Figure 4.52, page 282*). To rule out the possibility that data from cells which were classified as spatial, but had very large place fields, were masking true differences between the groups, an exploratory analysis was undertaken to investigate the effect of applying a maximum threshold for place field width (*Figure 4.53, page 283*).

**Figure 4.51 Phase precession using a place field threshold of 20% of the peak firing rate. *A&B*:** Scatterplots of theta phase versus position in the field, for three examples of phase-precessing cells from WT (*A*) and NLGF (*B*) mice. In both cases the three best examples were selected. Cells are presented in order of decreasing spatial information. Each scatter plot shows theta phase versus 'in field position', where 0 indicates the animal is entering the place field and 1 indicates the animal leaving the place field. A theta phase of 0 corresponds to the positive-to-negative crossing of the x axis in the theta waveform. ***C&D***: no significant differences were seen in the correlation coefficients for theta phase versus in-field position or, ***E&F***: the gradient of the line-of-best-fit, however, ***G***: WT mice had a significantly greater proportion of phase-precessing cells. WT data are shown in blue and NLGF data in red. The horizontal black bar in ***C*** and ***E*** represents the mean, and the error bars show the standard error of the mean. In cumulative frequency distributions bin size is 0.05 in ***D*** and 1 in ***F***. p values from Mann Whitney U testing (***C&E***) and $\chi^2$ testing (***G***).
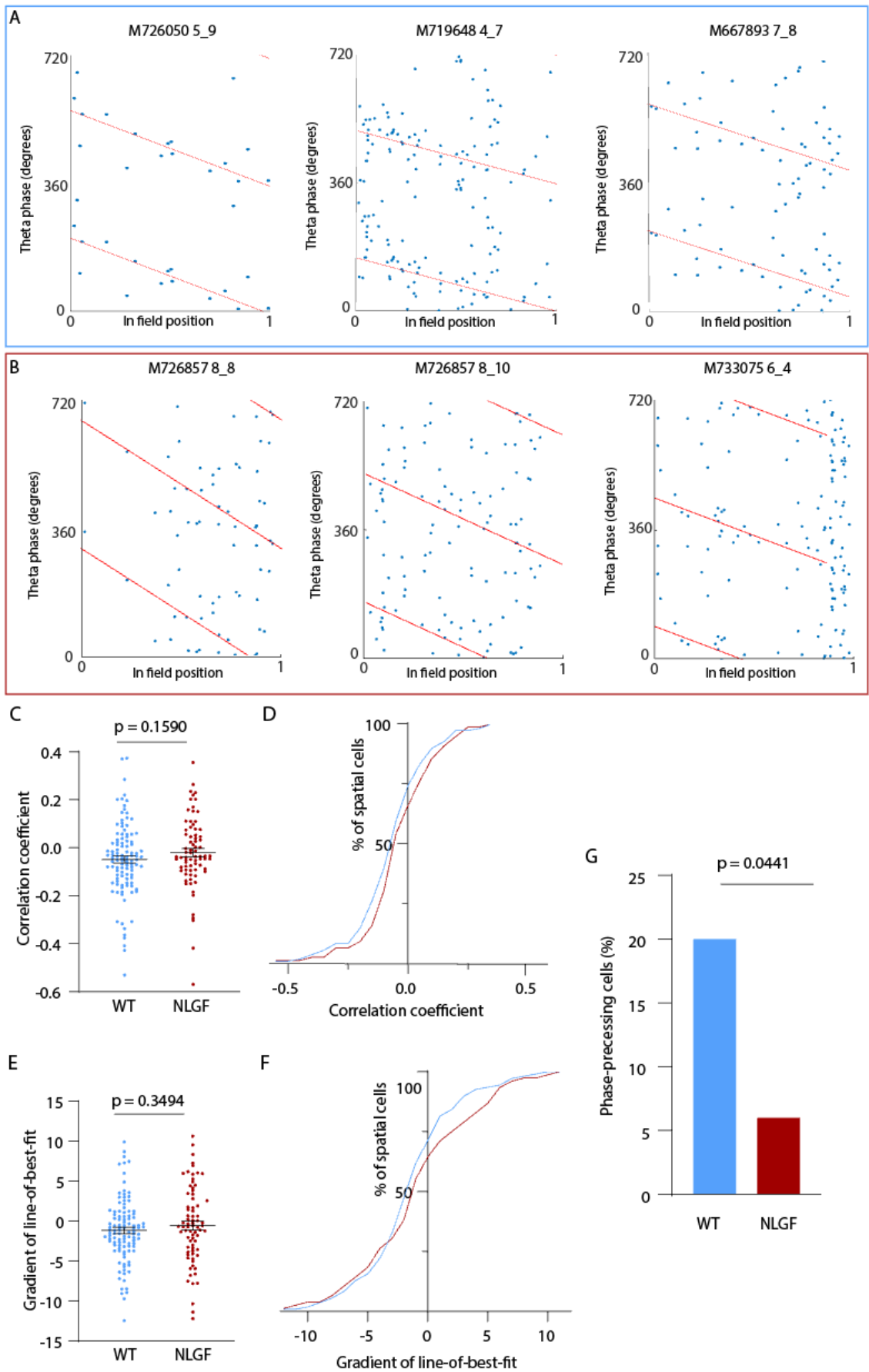
**Figure 4.51 Phase precession using a place field threshold of 20% of the peak firing rate.**
*Full legend on the previous page.*

For both WT and APP$^{NL-G-F}$ mice, the mean correlation coefficient for theta phase versus in-field position was more negative when a maximum field threshold was applied (*Figure 4.53A, page 283*), indicating that stronger phase precession was seen in cells with smaller fields. The application of a field size threshold also had an influence on the proportion of phase-precessing cells; no APP$^{NL-G-F}$ spatial cells were identified as phase-precessing when analysing only data from fields which occupied 75% or less of the track, whereas the proportion of WT spatial cells identified as phase-precessing was greater the more stringent the field size threshold (*Figure 4.53B, page 283*). The use of a field size threshold appeared to improve the quality of the phase-precession identified and enhance the separation between the WT and APP$^{NL-G-F}$ spatial cells. Rather than arbitrarily selecting a value for a maximum field size, it was decided to re-examine phase precession using a more stringent set of criteria to define a place field.
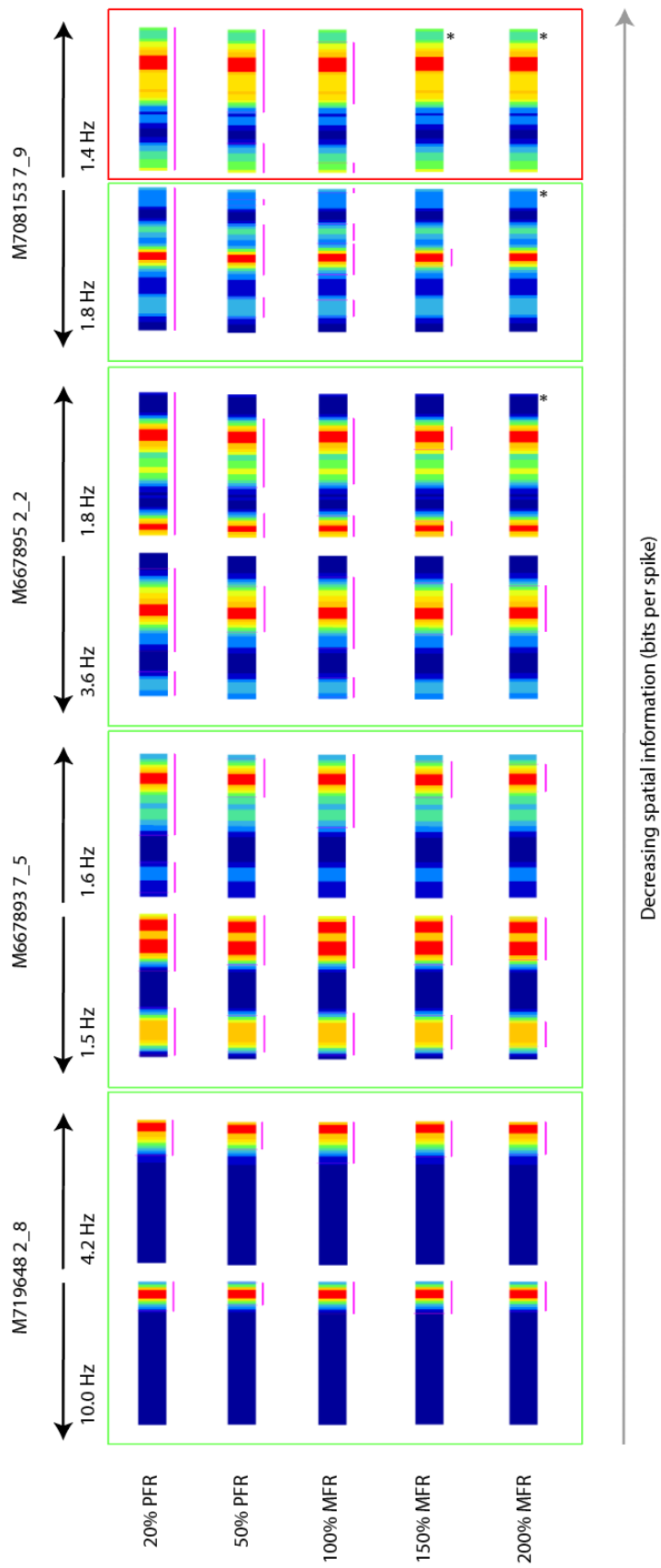
**Figure 4.52 A comparison of place field criteria on the linear track.** Pairs of rate maps are presented for four representative spatial cells, with the mouse's direction of travel indicated by the black arrows and the cell identifiers presented in the top row. Cells are arranged in order of decreasing spatial information to illustrate the effect of applying different place field criteria. These criteria are listed in the left-hand column. PFR = peak firing rate, MFR = mean firing rate. Rate maps are scaled from a firing rate of zero (dark blue) to the maximum rate of that cell (red) with each colour representing a 10% band of the peak firing rate. Unvisited bins are shown in white, and the peak firing rate is shown at the top of each column. The regions of the ratemap corresponding to each identified field are underlined in magenta. Runs in which no place fields were identified are highlighted with an asterisk *. All runs except one (in red box) were significantly spatial.

**Figure 4.53 Phase precession: applying a maximum field width to place fields. *A*:** circular correlation coefficients for in-field position vs. theta phase of WT (blue) and NLGF (red) spatial cells at different field size thresholds. A threshold of 50%, for example, indicates that data from place fields occupying more than 50% of the track were excluded. Phase-precessing cells have a negative correlation coefficient. *B*: the effect of applying field size thresholds on the proportion of phase-precessing cells in WT (blue) and NLGF (red) mice. A cell was significantly phase-precessing cell if it had a negative correlation coefficient and a p value of less than 0.05.

## 4.3.7.4.2. Selecting a new place field definition

The original place field criteria identified fields which were very large, however, the solution of applying a threshold for place field width is problematic; it reduces the number of spatial cells which contribute data to the analysis, and, since when applying the original place field definition, WT mice have significantly narrower place fields than APP$^{NL-G-F}$ mice, the application of such a threshold will exclude more APP$^{NL-G-F}$ data than WT data and could introduce bias. An exploratory analysis was performed to investigate alternative methods to identify place fields. An ideal method would identify place fields:

(i) only in spatial cells with clearly fields visible on their rate maps

(ii) which occupied smaller portions of the linear track, for example less than 50% of the track,

(iii)    of similar sizes between WT and APP$^{NL-G-F}$ mice so that any changes found in phase precession could not be attributed to an underlying difference in place field size.

*Table 4.11* summarises how various firing rate thresholds, based on the mean firing rate of the cell and the peak firing rate, measure up to some of these ideals. Using a more stringent threshold of 200% of the mean firing rate, all place fields occupied approximately half the length of the linear track or less, with a similar proportion of WT and APP$^{NL-G-F}$ spatial cells identified as not having fields (*Table 4.11*). On inspecting the rate maps this criterion also appeared to identify place fields more appropriately than the other criteria considered (*Figure 4.52, page 282*).

| Place field criteria | Spatial cells without field(s) WT/APP$^{NL-G-F}$ | Mean field width (%) WT/APP$^{NL-G-F}$ | Max. field width (%) WT/APP$^{NL-G-F}$ | Place field width (WT vs APP$^{NL-G-F}$) |
|---|---|---|---|---|
| 20% PFR | 0% (0/114) / 0% (0/86) | 64.1 / 79.9 | 100.0 / 100.0 | **p < 0.0001\*** |
| 50% PFR | 0.9% (1/114) / 1.2% (1/86) | 35.2 / 41.3 | 100.0 / 96.1 | p = 0.0126\* |
| 100% MFR | 0.9% (1/114) / 2.3% (2/86) | 44.2 / 48.6 | 100.0 / 96.1 | p = 0.0777\* |
| 150% MFR | 11.4% (13/114) / 14.0% (12/86) | 29.2 / 28.0 | 68.6 / 80.4 | p = 0.5846\* |
| 200% MFR | 32.5% (37/114) / 34.9% (30/86) | 24.0 / 19.9 | 56.7 / 52.9 | p = 0.0429\* |

**Table 4.11 A comparison of place field criteria as applied to spatial cells.** The application of different firing rate thresholds when defining a place field had a large impact on the width of the fields identified. PFR = peak firing rate, MFR = mean firing rate. p values obtained from Mann Whitney U testing of the width of place fields in spatial cells with fields identified in WT versus NLGF mice.

\*The Bonferroni adjusted alpha threshold is α = 0.01 for five comparisons. A bold p value indicates a significant difference in place field width according to this threshold.

### 4.3.7.4.3. When using a more stringent definition of a place field APP$^{NL-G-F}$ mice were found to have reduced phase precession.

When defining a place field as contiguous bins in the rate map of a spatial run which had a firing rate greater than twice the mean firing rate of the cell, significant differences were seen in phase precession when comparing WT and APP$^{NL-G-F}$ mice. A lower proportion of APP$^{NL-G-F}$ spatial runs exhibited significant phase precession (19.7% (13/66) of WT spatial runs versus 4.3% (2/47) of APP$^{NL-G-F}$ spatial runs, and this difference was statistically significant ($\chi^2_{(1)}$ = 5.686, p = 0.0171). APP$^{NL-G-F}$ spatial runs also had a significantly, less negative, correlation coefficient (Mdn$_{WT}$ = - 0.04662, Mdn$_{NLGF}$ = - 0.0088; $U$(N$_{WT}$ = 66, N$_{NLGF}$ = 47) = 1127, p = 0.0132), and gradient of line-of-best-fit, when correlating theta phase and in field position (Mdn$_{WT}$ = - 2.209, Mdn$_{NLGF}$ = - 0.1199; $U$(N$_{WT}$ = 66, N$_{NLGF}$ = 47) = 1172, p = 0.0271; *Figure 4.54*).

**Figure 4.54 Phase precession using a place field threshold of 200% of the mean firing rate. *A&B*:** Scatterplots of theta phase versus position in the field, for three example phase-precessing cells from WT (***A***) and all phase-precessing cells in NLGF (***B***) mice. Each scatter plot shows theta phase versus 'in field position', where 0 indicates the animal is entering the place field and 1 indicates the animal leaving the place field. A theta phase of 0 corresponds to the positive-to-negative crossing of the x axis in the theta waveform. ***C***: WT mice had a significantly greater proportion of phase-precessing cells. ***D&E***: significant differences were seen in the correlation coefficients for theta phase versus in-field position and, ***F&G***: the gradient of the line-of-best-fit. WT data are shown in blue and NLGF data in red. The horizontal black bar in ***D*** and ***F*** represents the mean, and error bars show the standard error of the mean. In cumulative frequency distributions bin size is 0.05 in ***E***, and 1 in ***G***. p values from Mann Whitney U testing (***D&F***) and $\chi^2$ testing (***C***).
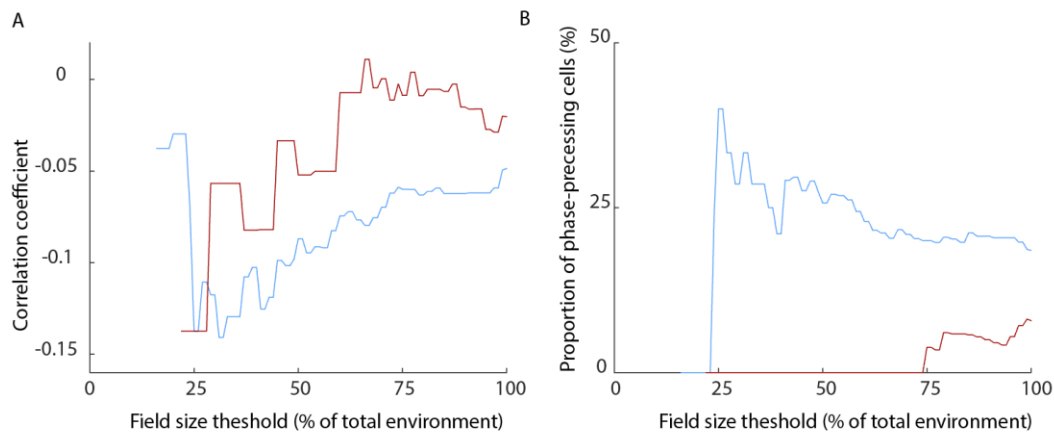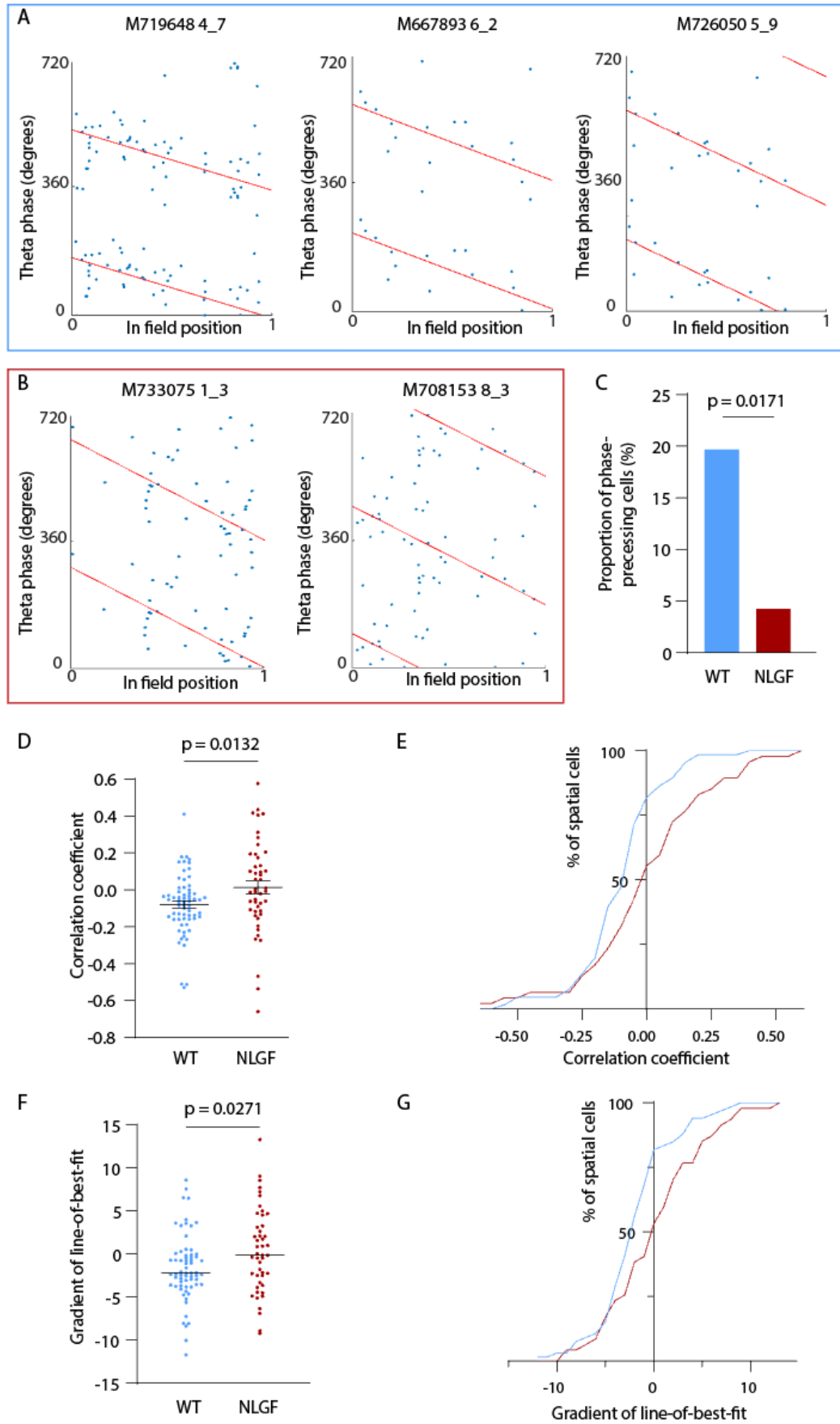
**Figure 4.54 Phase precession using a place field threshold of 200% of the mean firing rate.** *Full legend on previous page.*

## 4.3.8. Relationship between hippocampal function and Aβ pathology

The spatial properties of CA1 pyramidal cells in each APP[NL-G-F] mouse were compared with the extent of Aβ plaque burden. The properties of spatial cells were not compared since relatively small numbers of spatial cells were recorded in each APP[NL-G-F] mouse. For all APP[NL-G-F] mice, the Aβ plaque burden was quantified in both the left and right hippocampal formations across ten evenly spaced coronal sections, and the result expressed as a percentage of the total hippocampal area (*see General Methods, page 130*).

### *4.3.8.1. Impairment in rate coding in CA1 pyramidal cells correlated with Aβ plaque burden in APP[NL-G-F] mice.*

Although the sample size is very small, there was an unexpected strong positive correlation between hippocampal Aβ plaque burden (i.e., the total percentage plaque coverage in the hippocampus of each mouse) and the spatial information content of pyramidal cells in the open field (i.e., the mean spatial information value across all hippocampal pyramidal cells in each mouse). This suggests that pyramidal cells in mice with a greater Aβ plaque burden were less functionally impaired than in mice with a lower plaque burden (Pearson correlation, R = 0.9989, p = 0.0011, n=4; *Figure 4.55*). In accordance with this finding there was a trend towards an increased proportion of spatial cells, a reduced field size and an increased within field firing rate, as Aβ plaque coverage increased, although not all these findings were statistically significant (*Figure 4.55*).
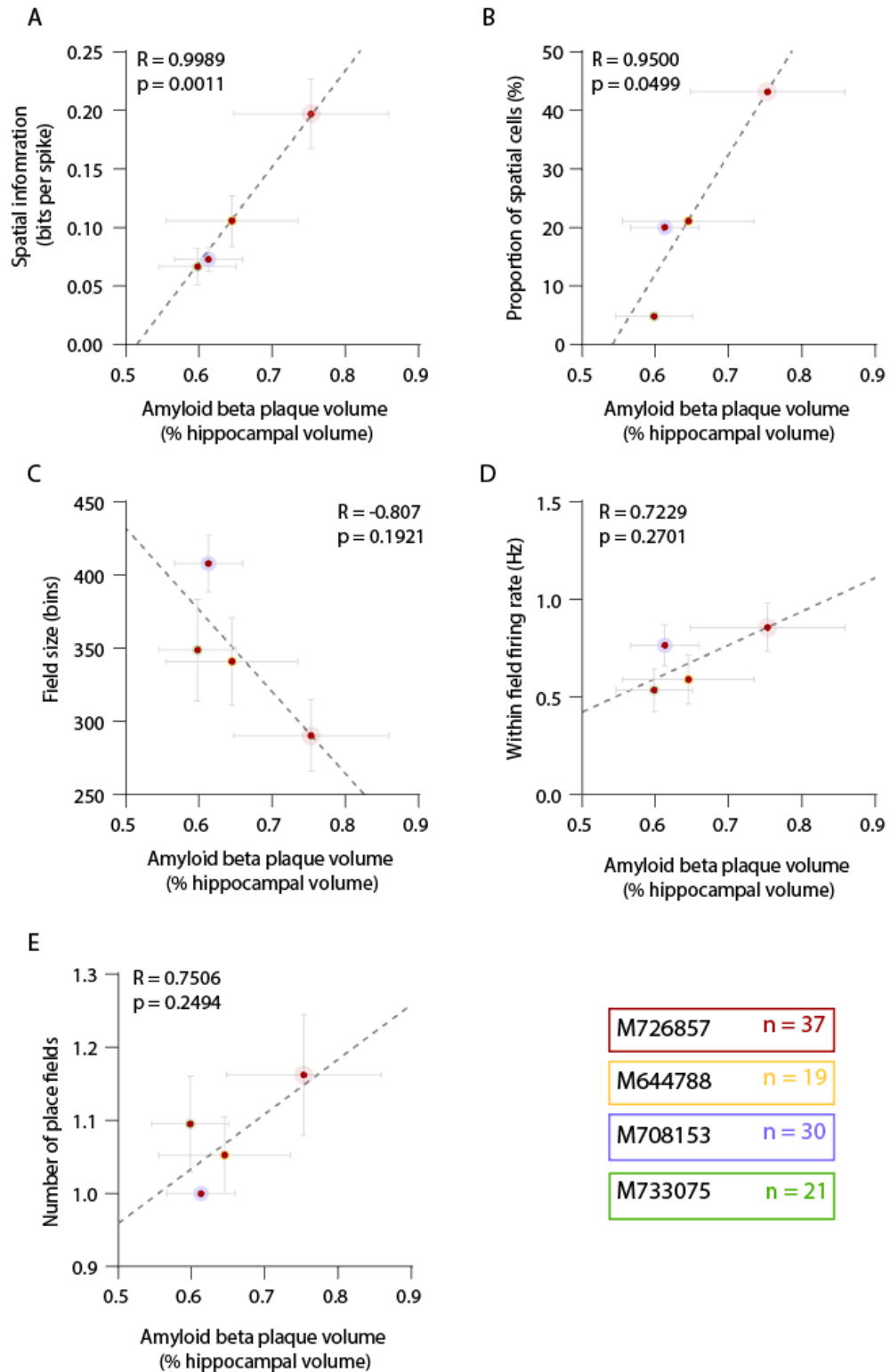
**Figure 4.55 Aβ plaque burden and rate coding of spatial properties in NLGF pyramidal cells.** Spatial information values (*A*), the proportion of pyramidal cells which were spatial (*B*), field size, using a 20% peak firing rate criteria, (*C*), within field firing rate (*D*), and place field number (*E*), were all derived from data recorded in the open field trials and compared with the amyloid β plaque coverage, expressed as the percentage coverage across both hippocampal formations. R and p values are from Pearson correlations, the grey dotted line indicates the line-of-best-fit and error bars the standard error of the mean. The coloured circles surrounding individual data points correspond to the mouse in which data were recorded, and the size of the circle is proportional to the number of pyramidal cells recorded in that animal. This is also stated alongside the mouse ID in the bottom right corner of the figure.

### 4.3.8.2. No relationship was identified between temporal coding in CA1 pyramidal cells and Aβ plaque burden in APP$^{NL-G-F}$ mice.

Scatterplots for measures of theta modulation and phase-locking versus Aβ plaque burden did not show a relationship between these variables (*Figure 4.56*). A correlation was not performed since, from inspection of the scatterplots, it was clear that identification of any underlying relationship, if present, would require a much greater sample size.
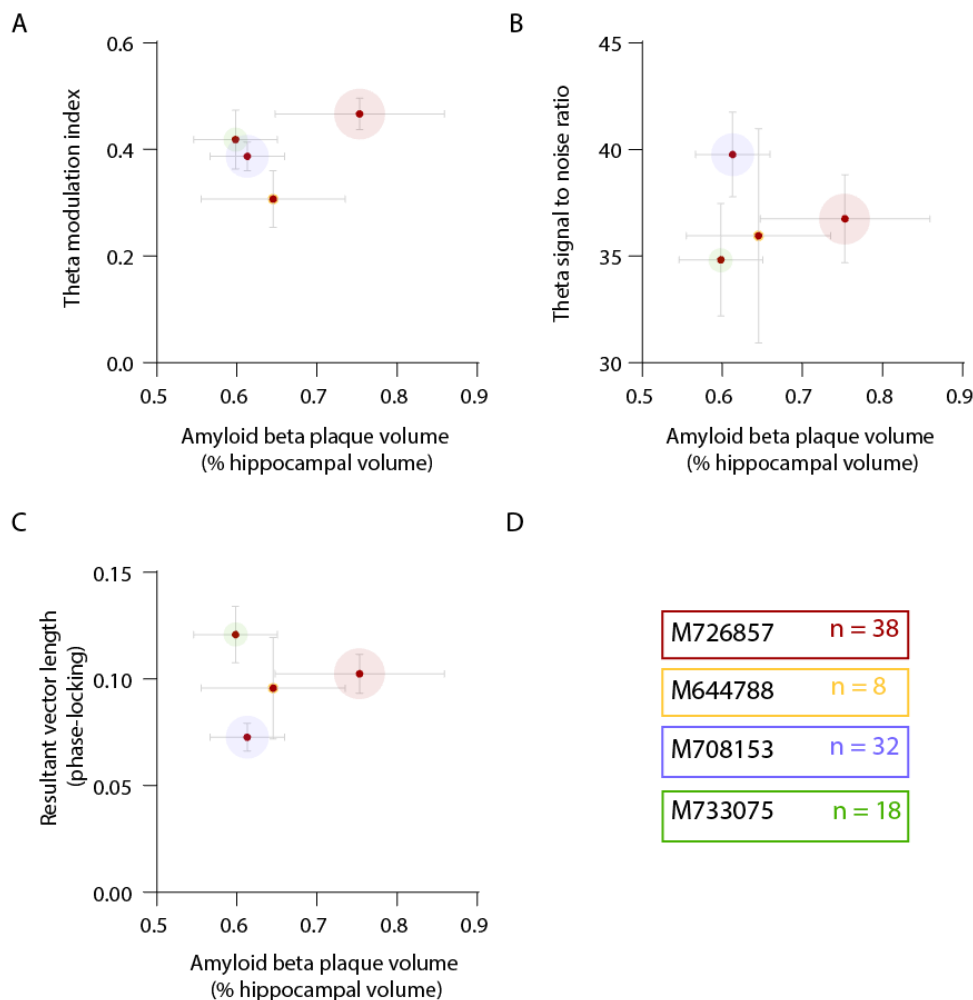


**Figure 4.56 Aβ plaque burden and temporal coding of spatial properties in NLGF pyramidal cells.** Theta modulation index (**A**), theta signal-to-noise ratio (**B**), and the resultant vector length for the preferred theta phase of firing (**C**), were derived from data recorded on the linear track and compared with the amyloid β plaque burden, expressed as the percentage coverage across both hippocampal formations. Error bars represent the standard error of the mean. The coloured circles surrounding individual data points correspond to the mouse in which the data were recorded, and the size of the circle is proportional to the number of pyramidal cells recorded in that animal. This is also stated alongside the mouse ID in **D**.

288

## 4.4. Discussion

### 4.4.1. Overview of main findings

This chapter presents the results of an in-depth characterisation of CA1 pyramidal cell activity in homozygous APP^NL-G-F mice. Electrophysiological recordings were performed in the left hippocampal CA1 subregion of 4 15-month-old, freely moving, APP^NL-G-F mice and 4 WT littermate controls during natural foraging behaviour in an open field environment, and while mice ran up and down a linear track for a food reward. Thioflavin-S staining of 40μm coronal sections through the hippocampal formation enabled quantification of Aβ plaque burden and comparison with measures of place cell function.

APP^NL-G-F CA1 spatial cells (which were presumed to be approximately equivalent to place cells) exhibited deficits in both rate coding and temporal coding of spatial information, indicating that Aβ pathology, in the absence NFTs, was associated with a disruption of hippocampal place cell function. The use of a novel APP knock-in mouse model excludes the possibility that these findings are due to artefacts such as overexpression of non-Aβ APP fragments (153). Although the sample size was small, the results also suggest there may be a correlation between Aβ pathology and an impairment in the rate coding of CA1 pyramidal cells, albeit in an unexpected direction.

**4.4.2. Rate coding of spatial information in CA1 was impaired in APP$^{NL-G-F}$ mice compared to WT controls.**

CA1 pyramidal cells from APP$^{NL-G-F}$ mice were found to be impaired in their ability to encode spatial information through their firing rates when compared to cells from WT controls. In both recording environments a lower proportion of CA1 pyramidal cells were classed as spatial cells in APP$^{NL-G-F}$ mice, and APP$^{NL-G-F}$ pyramidal cells and spatial cells had a significantly lower spatial information content and a reduced spatial coherence. Spatial cells in APP$^{NL-G-F}$ mice also had larger fields, and on the linear track were less likely to display spatial firing patterns in both running directions. These findings cannot be explained by differences in behaviour, or in the positioning of recording tetrodes. The behaviour between groups was broadly similar, although in the open field APP$^{NL-G-F}$ mice did spend a greater proportion of their time at higher running speeds than WT mice, despite there being no difference in the mean speed or distance travelled across the whole trial. An increased running speed is consistent with the observation of an anxiolytic phenotype in other AD mouse models and findings of increased locomotion and reduced thigmotaxis in 6-month-old APP$^{NL-G-F}$ female mice in another study (168). This slight difference in behaviour between the two groups in the open field cannot explain the result, however, since changes in the spatial properties of APP$^{NL-G-F}$ pyramidal cells were also observed on the linear track where there were no measurable behavioural differences. Histological examination confirmed that the locations of the recording tetrodes on the day of recording were

similar between the two groups, and in support of this finding a similar proportion of pyramidal cells and interneurons were recorded in each group.

The finding of impaired rate coding in CA1 place cells in APP$^{NL-G-F}$ mice is consistent with studies of place cell function in APP overexpression models, with and without additional tau mutations (494, 499). The present result suggests these previous findings were not artefacts of APP overexpression models, and in addition, show that mutant human tau is not a prerequisite for Aβ-mediated place cell impairment. In accordance with the present study, another group has recently reported finding 'mildly diminished' spatial tuning of place cells in the CA1 subregion of younger APP$^{NL-G-F}$ mice (503).

The results of the present study suggest that not only is there a breakdown in the spatially-specific firing of individual place cells, but that the firing of these cells is disrupted on a network level. A population vector correlation analysis indicated that the representation of an environment across the CA1 pyramidal cell population was more stable in WT mice compared to APP$^{NL-G-F}$ mice. This appeared to be driven by a reduction in the stability of the APP$^{NL-G-F}$ non-spatial pyramidal cells. This finding is likely a consequence of how spatial cells were classified. The binary approach used here, of classifying CA1 pyramidal cells as spatial, or non-spatial, based on their spatial information value was problematic for two reasons: it does not accurately reflect the existence of a pyramidal cell population with a continuum of spatial information scores and no clear cut-off, and a cell could have a very high spatial information value but with no discernible place field (for example, a cell with a chequerboard patterned rate map would have a high spatial information value but no field). A consequence of the former is

that non-spatial pyramidal cells from the WT mice carried more spatial information than the equivalent APP$^{NL-G-F}$ cell population, explaining why in this cell population the WT cells provided a more stable representation of a spatial environment. The equivalent comparison for spatial cells did not show a significant difference because cells with a similar degree of spatial firing had been from each group had been classified as spatial and so the stability was increased in both populations. The second issue, where spatial cells may not have a discernible place field, created challenges in the phase precession analysis and is discussed further below.

### 4.4.3. Temporal coding of spatial information in CA1 was impaired in APP$^{NL-G-F}$ mice compared to WT controls.

The coordination of place cell firing by the hippocampal theta rhythm was found to be disrupted in APP$^{NL-G-F}$ mice. This could not be attributed to changes in the theta rhythm itself, which had a similar power and frequency in APP$^{NL-G-F}$ and WT mice, with no differences found in theta stability. This finding is in contrast with other studies which report a decline in theta power in APP overexpression models (496, 522, 523), and in rats receiving hippocampal injections of soluble Aβ (524), however in both these experimental paradigms the concentration and distribution of Aβ species was likely to be unphysiological. In the present study no differences were detected in theta modulation using the theta modulation index and the theta signal-to-noise ratio, but the phase-locking of both CA1 pyramidal cells and spatial cells was significantly reduced in APP$^{NL-G-F}$ mice compared to controls. Not only did individual CA1 pyramidal cells in the APP$^{NL-G-F}$ mice show a lesser degree of phase-locking, but across the whole pyramidal cell

population there was less coherence in the preferred theta phase indicating a partial breakdown in theta dynamics on a network level.

A reduction in phase precession was observed in APP$^{NL-G-F}$ mice compared to WT controls and, to the best of my knowledge, this is the first report of an alteration in phase precession in a mouse model of AD. An impairment in phase precession could limit the ability of an animal to deduce its precise location within a place field. A loss of this fine grain temporal code could result in more subtle spatial memory deficits than those occurring secondary to impairments in rate coding and may potentially be detectable at an earlier stage of the disease process before place fields themselves become degraded. It is important to note, however, that the finding of reduced phase precession in APP$^{NL-G-F}$ mice was highly dependent on the criteria used to define a place field. A potential problem when analysing phase precession in APP$^{NL-G-F}$ mice is that, due to the impairment in rate coding that is seen in spatial cells, the quality of the place fields themselves are reduced which could influence the results of a phase precession analysis. Use of a more stringent place field threshold allowed identification of smaller place fields in spatial runs with higher spatial information values. When applying this threshold there was no significant difference in place field width between WT and APP$^{NL-G-F}$ mice, providing a level playing field upon which to analyse phase precession.

Although the differences in phase precession were significant between the two groups, it was noted that the scatterplots of theta phase and in field position appeared noisier than might be expected if the study had been conducted in young rats. It has been demonstrated that phase precession in rats and mice are broadly similar (525), and so this is unlikely to be a

species effect, however, the age of the mice may have resulted in a degradation in the quality of phase precession. It does not appear that the effect of aging on phase precession has been specifically investigated in either rats or mice, although aging has been shown via ensemble recordings of hippocampal neurons in CA1 to have an effect on the stability of the cognitive map in rats (526, 527) and on offline hippocampal sequence reactivation (528). Repeating the present study in a younger cohort of mice would be valuable in determining whether phase precession is affected prior to impairments in rate coding.

### 4.4.4. Possible mechanisms underlying place cell dysfunction

A relationship between Aβ deposition and neuronal hyperexcitability has been demonstrated in several APP overexpression models of AD (529-531) and the risk of unprovoked seizures is increased in AD patients relative to the general population (532). Place cells are known to emit bursts of action potentials as an animal enters the cell's place field, and off-target bursting of neurons could introduce noise into the place cell system, providing an explanation for the impaired place cell function seen in APP$^{NL-G-F}$ mice. However, in the present study, cells recorded from APP$^{NL-G-F}$ mice were not found to be more bursty; APP$^{NL-G-F}$ and WT CA1 pyramidal cells were equally bursty, and had no difference in their mean firing rates. In contrast, APP$^{NL-G-F}$ pyramidal cells had a decreased peak firing rate compared to WT pyramidal cells, reflecting a reduction in spatially-related firing activity. It therefore appears that CA1 pyramidal cells in the APP$^{NL-G-F}$ mice are just as likely to fire as those in WT mice but that their firing has lost spatial specificity.

Although the overall level of neuronal activity appeared similar in WT and APP[NL-G-F] CA1 pyramidal cells, a difference was noted in the shape of the extracellular action potential. Pyramidal waveforms from APP[NL-G-F] mice were found to have a greater peak-to-trough width, potentially indicating a longer repolarisation phase (533) although alternative explanations are possible. This finding supports the idea that Aβ has a local toxic effect on place cells. Repolarisation relies on at least five different $K^+$ currents (533) and the dynamics of any, or several, of these may be disrupted by the presence of Aβ oligomers which are known to have effects on membrane permeability, or could be affected by membrane bound Aβ (534).

The specificity of place cell firing could be affected locally by Aβ, or by a degradation of their inputs. Without directly recording from regions which project to CA1 it is difficult to separate the effects of Aβ pathology within the hippocampus itself, and in the regions projecting to the hippocampus, since the degree of Aβ pathology in these areas is likely to be highly correlated. The superficial layers of the EC are a major source of afferents to the hippocampus and are known to be preferentially affected by AD pathology in humans (281). Recordings from cells in the MEC in 7 – 13 month old APP[NL-G-F] mice have shown a severe reduction in spatial tuning, to the extent that grid cells were noted to be almost absent (503). There is a suggestion from the present study that the inputs to place cells may have been affected in the APP[NL-G-F] mice. We found that fewer field centroids in the APP[NL-G-F] mice aligned with cues at either end of the linear track while the relationship between field centroids and the central cue remained unaffected. This implies that the changes observed in APP[NL-G-F] place cell function are not entirely due to a local Aβ effect as, if this were the case,

cells with centroids at different locations should be affected equally. There were several differences between the central and peripheral cues which could explain why they were perceived differently by the APP$^{NL-G-F}$ mice: the central cue was larger and more visually complex so may have been more salient, the behaviour of mice was different at the extremes of the track with mice having lower running speeds, and the reward zones were also located at the ends of the track.

## 4.4.5. Place cell dysfunction and Alzheimer's disease pathology

In the present study an impairment in hippocampal place cell function was observed in an APP knock-in model which exhibits Aβ deposition but no NFTs. This is interesting given the growing body of evidence that Aβ species and tau may work synergistically to result in neuronal dysfunction, and that the toxic effects of Aβ may be mediated through tau phosphorylation and the accumulation of tau filaments in neurofibrillary tangles (NFTs) (99, 535). The absence of NFTs from the APP$^{NL-G-F}$ model does not, however, preclude a pathogenic role for tau, since phosphorylated tau is elevated in dystrophic neurites around Aβ plaques in the APP$^{NL-G-F}$ mouse. In addition, tau pathology may exert independent deleterious effects on place cell function in AD via distinct pathways which are not modelled in the APP$^{NL-G-F}$ mouse.

The present study found a significant positive correlation between Aβ plaque burden and CA1 pyramidal cell spatial information, albeit in a very small sample of mice. The direction of this relationship was unexpected; as the hippocampal Aβ plaque burden increased so did the spatial information of CA1 pyramidal cells, while place field size decreased. As discussed in

the introductory chapter, soluble Aβ oligomers are widely considered the main pathogenic Aβ species (*page 42*), and have been shown to be more toxic to neurons than Aβ fibrils and protofibrils (109, 110). These observations have led to proposals that Aβ plaque formation could represent a protective mechanism whereby toxic oligomeric Aβ species are rendered inert through their sequestration in more insoluble forms (536). Mice which have a greater proportion of Aβ in an insoluble, aggregated pool, as opposed to a soluble, oligomeric pool, may therefore be partially protected from its toxic effects. In support of this, human studies have shown that Aβ plaques in non-demented individuals are associated with lower concentrations of oligomeric species than in demented individuals, suggesting that plaques may initially sequester oligomers in a less neurotoxic form, but that once this system starts to fail or becomes saturated the clinical features of dementia begin to manifest (124).

The findings in the present study are in direct contrast with findings in the Tg2576 mouse model in which an increasing hippocampal plaque burden was associated with a reduction in spatial information, an increase in field size and a greater degree of impairment on a forced-choice T maze alternation task (494). In this study, performance on the T-maze task, but not measures of place cell function, also correlated with the concentration of soluble $A\beta_{1-40}$, soluble $A\beta_{1-42}$, and total $A\beta_{1-42}$, in the hemibrains of Tg2576 mice, as determined using a standard sandwich ELISA; higher levels of these Aβ species were associated with poorer performance (494). The authors suggest that either Aβ plaques are directly toxic themselves, soluble Aβ species in the vicinity of plaques mediate the observed effects on place cells, or Aβ plaques are a surrogate marker for smaller oligomeric

Aβ. A role for oligomeric Aβ seems highly likely given the results of a separate study in the same mouse model which demonstrated that Aβ plaques were not associated with memory impairment in the absence of Aβ oligomers, and a reduction in the concentration of Aβ oligomers correlated with an improvement in memory (107).

The differences between the study of place cells in the Tg2576 and the present study could be explained by differences in Aβ pathology and dynamics in the Tg2576 and APP$^{NL-G-F}$ models. Not all Aβ plaques are equal; plaques may have distinct morphologies, be formed via different mechanisms, consist of different Aβ isoforms and have different densities (537). It is therefore possible that they have different pathogenicities. In addition, the presence of insoluble Aβ in plaques may not be a good proxy measure for soluble oligomeric Aβ concentrations, and the relationship between different pools of Aβ could vary across mouse models. In one behavioural study, *Locci et al.* noted a similar degree of memory impairment across three different mouse models of AD, however, the models were found to have significantly different Aβ plaque burdens (164). This mirrors observations in humans where Aβ plaque burden does not correlate well with the clinical features of dementia and has prompted researchers to focus on distinct biochemical pools of Aβ (534).

The Tg2576 model displays small, but relatively diffuse plaques, surrounded by haloes of Aβ oligomers (538), in comparison to the APP$^{NL-G-F}$ model which appears to have larger, more dense plaques, which are additionally present in subcortical regions (153) (*Figure 4.57, page 301*). Comparing the results of sandwich ELISAs across studies indicates that the Tg2576 model has concentrations of soluble Aβ$_{1-40}$ and Aβ$_{1-42}$ which are many orders of

magnitude greater than in the APP$^{NL-G-F}$ mouse (539), as would be expected given that the Tg2576 is an overexpression model. Further differences exist; the A$\beta_{1-42}$: A$\beta_{1-40}$ ratio is unaffected in the Tg2576 model but elevated in the APP$^{NL-G-F}$ model due to the presence of the APP Iberian mutation, and the A$\beta$ sequence itself is different in the APP$^{NL-G-F}$ model since the Arctic mutation occurs within this region. Interestingly, Arctic A$\beta_{1-40}$ has been shown to have an increased propensity to aggregate into protofibrils compared to WT A$\beta_{1-40}$, and does so at a faster rate (540). This could potentially seed further aggregation thus representing a mechanism via which A$\beta$ oligomers in APP$^{NL-G-F}$ mice may aggregate more readily into plaques than in other models. Whether or not this is the case, there is certainly strong evidence that the A$\beta$ pathology within the Tg2576 and APP$^{NL-G-F}$ models differs considerably.

Image redacted for copyright reasons
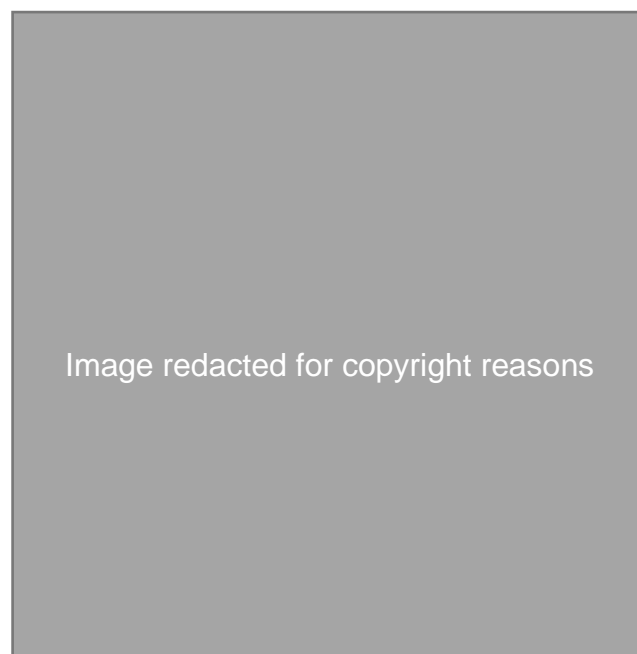
**Figure 4.57 Aβ plaques in NLGF and Tg2576 mice.** Immunostaining of cortical amyloid β in an 11-month NLGF mouse (**A&C**, taken from (542)), a 15-month Tg257 mouse (**B**, taken from (544)), and a 16-month Tg2576 mouse (**D**, taken from (540)). Top row scale bar = 20µm; bottom row scale bar = 200µm.

### 4.4.6. Summary

In conclusion, the APP$^{NL-G-F}$ mouse displays place cell dysfunction on both a single cell and population level, with deficits in both rate coding and temporal coding of spatial information. This dysfunction may be due to a combination of intra- and extra-hippocampal Aβ pathology and provides a potential explanation for the deficits in spatial memory observed in patients with AD. Data from this study suggest that, in the APP$^{NL-G-F}$ mouse model, sequestration of Aβ within plaques could protect the brain from the toxic effect of Aβ oligomers. While these results leave many unanswered questions with scope for many further studies, they clearly demonstrate the potential of studying hippocampal function, and specifically place cell function, to further our understanding of the processes underlying spatial memory impairment in AD.

# 5. General Discussion

The experimental results are discussed in detail in the respective data chapters (*Chapter 3, page 168; Chapter 4, page 289*) and this General Discussion will focus on remaining outstanding questions, and the potential to translate the findings from this thesis into clinical research.

## 5.1. Overview

The aims of this thesis have been twofold; first, to validate a novel behavioural task which can be used to assess, on a behavioural level, EC and hippocampal function in mouse models of AD, and second, to demonstrate that extracellular recording techniques can be used to probe the function of CA1 pyramidal cells in a mouse model of AD. While these two strands of research may appear only loosely connected, the techniques used in both studies can contribute to the unifying hypothesis that <u>Alzheimer's disease pathology causes a disruption of hippocampal function which manifests as alterations of spatially-related single cell activity and behaviour</u>. With respect to the first aim, I have demonstrated that spatial navigation tasks on the Honeycomb Maze are sensitive tests of hippocampal, but not necessarily entorhinal, function. Since the task can be scaled in difficulty, produces a parametric output, and can be learnt by WT rats and mice, the Honeycomb Maze represents a potentially valuable tool for assessing hippocampal function in rodent models of AD. Regarding the second aim, I have demonstrated that in-depth electrophysiology studies of hippocampal function can provide insights into the potential mechanisms underlying the spatial memory impairment seen in AD mouse models. Place cell function is impaired in APP$^{NL-G-F}$ mice on both a single cell and

population level, with impairments in rate coding and temporal coding of spatial information.

## 5.2. Implications and future work

The current findings will be discussed in terms of the contribution they make towards our understanding of the central hypothesis (*page 302*). Establishing causation requires a high standard of scientific evidence and in epidemiological research the *Bradford Hill criteria* can be applied to assess the likelihood that an association between two variables represents a true causal relationship (543). In the following section these criteria will be adapted for application to an experimental context and used as a framework to guide discussion of the present results and the future steps required to address remaining questions.

1. First, what is the ***strength of the association*** between the presence of Aβ pathology, place cell dysfunction, and spatial memory impairment in the APP$^{NL-G-F}$ mouse?

The present results from electrophysiological recordings in aged APP$^{NL-G-F}$ mice clearly indicate that in these mice the representation of spatial information by CA1 pyramidal cells is disrupted compared to WT controls. This was demonstrated across two different recording environments using multiple measures to assess place cell function on both a single cell and population level. Across individual mice, with the exception of one WT mouse with a very low yield of pyramidal cells, all APP$^{NL-G-F}$ mice had lower spatial information scores in CA1 pyramidal cells than WT mice. The data presented come from many recorded cells, although admittedly a small number of mice. Replicating the present finding across a larger sample

would be desirable, however, this needs to be balanced with a requirement to use as few animals as possible to fulfil the principles reduction, refinement, and replacement in animal research.

There did not appear to be any confounding factors which could explain impaired place cell function in APP$^{NL-G-F}$ mice, other than the presence of the mutant humanised APP gene in the APP$^{NL-G-F}$ model. As discussed in *Chapter 4*, findings could not be explained by differences in behaviour during recording or differences in the locations of the recording tetrodes between the two groups. Littermate controls were used and therefore mice had an identical genetic background and were housed in identical conditions. Spike sorting was performed by an experimenter blinded to genotype. Histology confirmed that the APP$^{NL-G-F}$ mice showed widespread deposition of Aβ in plaques throughout the brain unlike their WT counterparts. This strongly suggests that it is the alteration in APP processing and consequent accumulation of pathogenic Aβ species which is associated with place cell dysfunction in the APP$^{NL-G-F}$ mice. Since the physiological role of APP is not fully known it is possible, however, that the mutant APP itself could exert an effect on hippocampal function via an alternative pathway, for example through a developmental effect on hippocampal neurons, and for this reason in future work it will be important to perform electrophysiology in younger groups of mice prior to the onset of pathology. In addition, the present study does not indicate which forms of Aβ may be affecting place cell function (soluble versus insoluble, oligomeric versus multimeric, intraneuronal or extracellular), or even whether place cell dysfunction occurs due to Aβ pathology within the hippocampus itself or is

a downstream effect of Aβ pathology in brain regions which project to the hippocampus such as the EC, or a combination of the two.

While the results of *Chapter 4* speak to a potential relationship between Aβ pathology and place cell dysfunction, no behavioural studies were conducted in APP[NL-G-F] mice and so a link to spatial memory impairment has not been demonstrated. However plausible, the question remains, does impairment of place cell function underlie the spatial memory deficits seen in AD? The Honeycomb Maze presents an opportunity to study spatial behaviour in AD mouse models to a greater depth and with a greater degree of precision than is offered by tasks currently in use. While further work is needed to refine the paradigm used for mice, the validation of spatial navigation tasks on the Honeycomb Maze as paradigms which are sensitive to hippocampal impairment, and the ability to undertake concurrent electrophysiological recordings, provides a unique opportunity to correlate single cell activity with spatial behaviour. Demonstrating a correlation between spatial memory impairment, place cell dysfunction and Aβ pathology in an AD mouse model would strongly support the hypothesis that Aβ-mediated place cell dysfunction contributes to the spatial memory deficits observed in AD. A key future experiment, which would unify the two approaches used in this thesis, would therefore be to test APP[NL-G-F] mice, and WT controls, on the Honeycomb Maze, and on other control tasks such as the forced-choice T-maze alternation task, while recording from CA1 pyramidal cells.

2. Second, is an association between Aβ pathology, place cell dysfunction and behaviour ***consistently*** demonstrated across studies?

All three of these variables have been shown to be associated with one another across different studies. An association between Aβ pathology and impairment of place cell function has been demonstrated, both in the APP$^{NL-G-F}$ model, and in other mouse APP overexpression models (503); in all models there was a reduction in the spatial information of CA1 pyramidal cells, although two studies used models which also contained mutant tau (499). Of note, one of these studies found an association between Aβ pathology, place cell dysfunction, and impairment of spatial working memory on a forced choice T-maze alternation task (494). An association between reduced spatial information of hippocampal place cells and performance deficits on an object-location memory task has been demonstrated in a transgenic rat model of AD which overexpresses mutant APP and PS1, although this model also displays NFTs (552). Links between place cell dysfunction and spatial memory impairment in the absence of Aβ pathology are well established; hippocampal lesions, and therefore place cell destruction, result in deficits on the Morris Water Maze (4), and also on the Honeycomb Maze as demonstrated in *Chapter 3*, and place cell activity has been shown to correlate with spatial memory in rodents (182). Finally, many mouse models which overexpress mutant APP also show age-related deficits in spatial memory which are associated with a corresponding increase in Aβ plaque burden over time. The concentration of oligomeric Aβ species has been shown to correlate with memory impairment in mouse models of AD, and intraventricular injection of Aβ oligomers into healthy rats results in a deficit in learning and memory in the Morris Water Maze (107, 108).

3. Third, is Aβ pathology associated with a ***specific effect*** on entorhinal and hippocampal function or are other brain regions affected?

A major question in the field of AD research is the basis of the apparent selective vulnerability of neurons in the EC and the hippocampus to AD pathology. The vulnerability of these regions has been demonstrated in human post-mortem and neuroimaging studies, with initial cognitive impairments observed in the memory domain followed by the manifestation of additional features as pathology spreads to other brain regions. Although dysfunction in extra-hippocampal brain regions would not disprove the central hypothesis in this study, an evaluation of other brain regions in the APP$^{NL-G-F}$ model, both through electrophysiological recording and behavioural testing, could provide further insights into the mechanisms underlying cognitive dysfunction in AD. For example, are other nodes in the brain's spatial navigation network also particularly vulnerable? Do pyramidal neurons in other brain regions show similar changes to CA1 pyramidal cells, for example, an alteration in the shape of the extracellular action potential? And can APP$^{NL-G-F}$ mice solve the Honeycomb Maze more readily if a paradigm is used which requires a stimulus-response rather than a place-learning strategy?

4. Fourth, what is the ***temporal relationship*** between Aβ pathology and measures of hippocampal dysfunction?

If Aβ pathology causes hippocampal dysfunction it should be detectable prior to the observed changes in place cell firing. The present study looked at only one time point and therefore future studies are warranted which examine spatial behaviour and place cell function in younger APP$^{NL-G-F}$ mice. In such studies it would be important to use additional measures of

Aβ pathology since the development of Aβ plaques is a downstream event which follows the generation of soluble Aβ oligomers, and therefore place cell dysfunction and spatial memory impairment may precede plaque development. There is also an increasing focus on the potentially toxic role of intraneuronal Aβ which appears to precede extracellular Aβ aggregation. Studying younger APP$^{NL-G-F}$ mice will also help address whether the observed changes in phase locking and phase precession are present in younger mice prior to the deterioration of place fields.

A related question is whether entorhinal dysfunction precedes and contributes to hippocampal dysfunction, since in humans with AD, pathology is detected first in the entorhinal cortex before spreading to the hippocampus proper. It has been shown that grid cell function is impaired to a greater extent than place cell function in 7 – 13-month APP$^{NL-G-F}$ mice but a sequential impairment of entorhinal then hippocampal function has not yet been demonstrated (500). Dual hippocampal-entorhinal recordings in a range of younger ages of APP$^{NL-G-F}$ could help to address this question, however it should be noted that although the development of Aβ pathology in the APP$^{NL-G-F}$ mouse approximately recapitulates the Thal stages observed in humans, the APP$^{NL-G-F}$ model exhibits a high degree of subcortical amyloidosis which, while seen in humans carrying the APP Arctic mutation, is not representative of sporadic AD.

5. Fifth, to confirm whether a causative relationship exists between Aβ and measures of hippocampal dysfunction it is important to establish whether there is a ***biological gradient***. Specifically, as Aβ pathology increases, is there an accompanying rise in place cell impairment and spatial memory deficits?

This question is difficult to address since it is not clear what sort of Aβ we should be measuring. In the present study the only measure used was the hippocampal Aβ plaque burden and, as discussed in *Chapter 4*, this may not be a good proxy measure for other species of Aβ. Furthermore, the relationship between the concentrations of Aβ within different biochemical pools may not be consistent across mouse models and could even vary as a function of the age of the animal. Although an interesting correlation was observed in the present study which suggests there may be a biological gradient relating to Aβ pathology, the direction of the correlation was unexpected and contradicted findings in another AD mouse model, and the sample size was very small. Far more research is required, with measurement of different Aβ species across different brain regions and within different pools, to determine whether a biological gradient exists in the APP$^{NL-G-F}$ mouse. Future studies could use ELISAs on post-mortem brain tissue to quantify soluble and insoluble Aβ species in specific brain regions, or on samples collected using *in vivo* techniques such as microdialysis of interstitial fluid, which enables collection of dialysate over a few hours (544), or serial CSF sampling via cisterna magna cannulation which allows CSF sampling over weeks to months (545). An advantage of CSF sampling in rodent models would be its translatability since CSF biomarkers are used to classify individuals at risk of AD in human research studies.

6. Finally, is there a ***plausible biological explanation*** as to how Aβ pathology might cause place cell dysfunction, and how this, in turn could result in impairment in spatial memory? And, in addition, is a causative role

for Aβ pathology consistent with what is already known about the mechanisms underlying AD?

Aβ oligomers have been shown to be toxic to neurons in a wide range of studies and could feasibly cause the death or dysfunction of place cells through a local toxic effect within the hippocampus itself, or through toxic effects on cells in regions such as the entorhinal cortex, which project to the hippocampus. The place cell system represents the neural basis of the hippocampal cognitive map, and a breakdown in this cognitive mapping system would have a profound impact on an animal's ability to navigate to and remember spatial locations.

While there is a plausible biological explanation as to how Aβ pathology might cause spatial memory impairment, an outstanding issue is how to explain the role of tau pathology, specifically NFTs, which are a major histopathological feature of AD and correlate well with the clinical features of dementia but are not seen in APP mouse models. It is unclear why this is the case, with possible explanations including the absence of 3R tau isoforms in mice, and the relatively short lifespan of mice compared with humans. In humans it is possible that NFTs occur as a downstream effect of a pathological, Aβ-initiated cascade but are not themselves pathogenic, or that they represent the endpoint of one of several routes via which altered processing of APP initiates cellular dysfunction. Accumulating evidence suggests that, as with Aβ, it may be tau *oligomers* which are the true pathogenic species (546). Overexpression of tau in rodent models can result in synaptic dysfunction, neuronal death and behavioural deficits in the absence of NFTs (546), and levels of tau oligomers correlate with the onset of clinical symptoms in AD (547, 548) and result in cognitive abnormalities

when injected into the brains of WT mice (549). Tau oligomers from AD brain extracts have also been shown to induce endogenous tau to misfold and propagate in WT mice in a trans-synaptic fashion (139, 550). Methodological challenges have so far precluded a thorough evaluation of tau oligomers in APP mouse models of AD, however, the presence of elevated levels of phosphorylated tau in dystrophic neurites surrounding Aβ plaques in the APP^NL-G-F model indicates that tau dysfunction is present and may still play an important role even in the absence of NFTs.

Future studies could use electrophysiology as a tool to examine the effects of Aβ and tau pathology, and their interaction, within the entorhinal-hippocampal circuit. Use of an APP/PS1 transgenic rat model which displays both Aβ plaques, NFTs and spatial memory deficits (551) could facilitate this, allowing large-scale electrophysiological recordings via next-generation silicon probes (552) to be performed simultaneously in the MEC and hippocampus, alongside concurrent behavioural testing, for example on the Honeycomb Maze, and serial CSF sampling for evaluation of soluble Aβ and tau species. A similar approach could be used to evaluate the effect of Aβ and tau pathology on entorhinal and hippocampal function in combination models; tau spread and NFT formation could potentially be induced in APP knock-in mice via the injection of tau oligomers isolated from AD brains, viral vector tau seeding approaches or the introduction of additional transgenes.

## 5.3. Translation to clinical studies

The results from both data chapters have the potential for translation to clinical studies. The parametric output of the Honeycomb Maze makes it

uniquely suited to tracking the progressive hippocampal impairment seen in both murine and rat models of neurodegenerative disease where it could be used to assess the efficacy of putative therapeutic compounds. The development of an analogous maze task in humans, for example using a virtual reality set-up, would be a powerful means of comparing outcome measures across preclinical and clinical phases of drug trials, assisting successful translation of potential disease modifying therapies and allowing clinicians to assess the efficacy of these treatments in their patients. Currently such comparable outcome measures do not exist, with spatial memory testing on the Morris Water Maze being a key outcome measure in rodents models of AD in preclinical trials, and unrelated measures such as the Mini Mental State Exam, a 30-point questionnaire, being the most common means of assessing human responses in clinical phases of drug trials, despite the fact that spatial memory has already been shown to provide a means of assessing treatment response in those with MCI and AD. A recent study used a computerized version of the Morris Water Maze to demonstrate that donepezil stabilized or improved spatial navigation performance in patients with AD (553).

Since AD pathology is first observed in the EC, and later spreads to the hippocampus, such analogous spatial memory tasks also have the potential to detect disease in the pre-symptomatic and prodromal stages of AD. The value of such a translational approach has, to some extent, already been demonstrated since spatial memory tasks specifically designed to rely upon hippocampal processing have already been shown to be sensitive to AD and predict which patients with MCI will go on to develop dementia (21, 554). Poor performance on spatial memory tests is also associated with a

higher dementia risk score in healthy adults (555). The next challenge is to develop analogous tasks in both rodents and humans which can specifically detect entorhinal impairment, since this is likely to precede hippocampal impairment, enabling even earlier detection of disease. The MEC is known to play an important role in path integration, and a virtual reality path integration task has been shown to differentiate between patients with MCI who are at low and high risk of developing dementia as assessed by their CSF biomarkers (556). Given the flexibility of the Honeycomb Maze apparatus it is feasible that a path integration paradigm could be developed on the Honeycomb Maze to probe entorhinal function. Detection of AD at the earliest possible stages is likely to be crucial for effective therapeutic intervention, and a common criticism of AD treatment trials is that participants have disease which is too advanced for any benefit to be seen; the deposition of Aβ pathology can be detected decades prior to the onset of dementia and targeted spatial memory testing may assist in the identification of at risk cohorts for AD treatment trials in addition to allowing individuals to modify their risk factors and plan for the future.

The electrophysiology results presented in this thesis provide support for the hypothesis that place cell dysfunction may underlie the spatial memory impairment seen in AD and highlight a potential role for electrophysiology in providing an assay of hippocampal neuronal function which could be exploited in translational studies. For example, molecular compounds, such as those targeting specific Aβ oligomers, could be screened to evaluate their effect on place cell function before beginning preclinical treatment trials. In addition, single cell work could provide a platform for mechanistic studies of the effect on neurons of different pathological molecular species, potentially

identifying novel therapeutic targets. Insights from electrophysiology studies of hippocampal and entorhinal neurons could be used to guide future clinical research; for example, if it were confirmed that phase precession was impaired in APP$^{NL-G-F}$ mice prior to the rate coding of spatial information, then a measure of how precisely an animal, or indeed a human participant, can locate themselves within an environment could be included in spatial memory test batteries. Finally, the development of non-invasive methods of recording hippocampal oscillations, such as magnetoencephalography (MEG), provide an opportunity to identify electrophysiological correlates of AD in humans.

## 5.4. Summary

In summary, the electrophysiology results presented in this thesis contribute to an ever-growing body of evidence which supports the notion that Aβ-mediated place cell dysfunction contributes to the spatial memory deficits observed in AD, and also demonstrates that this technique can be incorporated into future studies to address many of the remaining unanswered questions. The development of novel behavioural tasks, such as the Honeycomb Maze, which can be translated across species and force subjects to use a single, identifiable strategy, allow researchers to probe the function of a specific brain region, an approach which is critical for determining the precise behavioural correlates of accumulating pathology and neuronal dysfunction.

# 6. References

1.      ARUK: Dementia Statistics Hub https://www.dementiastatistics.org/statistics2019

2.      Braak H, Braak E, Bohl J. Staging of Alzheimer-related cortical destruction. European neurology. 1993;33(6):403-8.

3.      Thal DR, Rub U, Schultz C, Sassin I, Ghebremedhin E, Del Tredici K, et al. Sequence of Abeta-protein deposition in the human medial temporal lobe. Journal of neuropathology and experimental neurology. 2000;59(8):733-48.

4.      Morris RG, Garrud P, Rawlins JN, O'Keefe J. Place navigation impaired in rats with hippocampal lesions. Nature. 1982;297(5868):681-3.

5.      Moodley K, Minati L, Contarino V, Prioni S, Wood R, Cooper R, et al. Diagnostic differentiation of mild cognitive impairment due to Alzheimer's disease using a hippocampus-dependent test of spatial memory. Hippocampus. 2015;25(8):939-51.

6.      Alzheimer A, Stelzmann RA, Schnitzlein HN, Murtagh FR. An English translation of Alzheimer's 1907 paper, "Uber eine eigenartige Erkankung der Hirnrinde".

7.      Moodley KK, Chan D. The hippocampus in neurodegenerative disease. Frontiers of neurology and neuroscience. 2014;34:95-108.

8.      The Alzheimer's Society. Facts for the media https://www.alzheimers.org.uk/about-us/news-and-media/facts-media2021

9.      McKhann GM, Knopman DS, Chertkow H, Hyman BT, Jack CR, Jr., Kawas CH, et al. The diagnosis of dementia due to Alzheimer's disease: recommendations from the National Institute on Aging-Alzheimer's Association workgroups on diagnostic guidelines for Alzheimer's disease. Alzheimer's & dementia : the journal of the Alzheimer's Association. 2011;7(3):263-9.

10.     Albert MS, DeKosky ST, Dickson D, Dubois B, Feldman HH, Fox NC, et al. The diagnosis of mild cognitive impairment due to Alzheimer's disease: recommendations from the National Institute on Aging-Alzheimer's Association workgroups on diagnostic guidelines for Alzheimer's disease. Alzheimer's & dementia : the journal of the Alzheimer's Association. 2011;7(3):270-9.

11.     Vlassenko AG, Benzinger TLS, Morris JC. PET amyloid-beta imaging in preclinical Alzheimer's disease. Biochimica et Biophysica Acta, 2012. 1822: 370-379.

12.     NICE. Donepezil, galantamine, rivastigmine and memantine for the treatment of Alzheimer's disease. https://www.nice.org.uk/guidance/ta2172011.

13.     Walsh S, Merrick R, Milne R, Brayne C. Aducanumab for Alzheimer's disease? BMJ (Clinical research ed). 2021;374:n1682.

14.     Knopman DS, Jones DT, Greicius MD. Failure to demonstrate efficacy of aducanumab: An analysis of the EMERGE and ENGAGE trials as reported by Biogen, December 2019. Alzheimer's & dementia : the journal of the Alzheimer's Association. 2021;17(4):696-701.

15.     Braak H, Del Tredici K. The pathological process underlying Alzheimer's disease in individuals under thirty. Acta neuropathologica. 2011;121(2):171-81.

16.     Sperling RA, Aisen PS, Beckett LA, Bennett DA, Craft S, Fagan AM, et al. Toward defining the preclinical stages of Alzheimer's disease: recommendations from the

National Institute on Aging-Alzheimer's Association workgroups on diagnostic guidelines for Alzheimer's disease. Alzheimer's & dementia : the journal of the Alzheimer's Association. 2011;7(3):280-92.

17.		Grundman M, Petersen RC, Ferris SH, Thomas RG, Aisen PS, Bennett DA, et al. Mild cognitive impairment can be distinguished from Alzheimer disease and normal aging for clinical trials. Archives of neurology. 2004;61(1):59-66.

18.		Roberts RO, Knopman DS, Mielke MM, Cha RH, Pankratz VS, Christianson TJH, et al. Higher risk of progression to dementia in mild cognitive impairment cases who revert to normal. Neurology, 2014. 82(4): 317-25.

19.		Ganguli M, Dodge HH, Shen C, DeKosky ST. Mild cognitive impairment, amnestic type: an epidemiologic study. Neurology. 2004;63(1):115-21.

20.		Jicha GA, Parisi JE, Dickson DW, Johnson K, Cha R, Ivnik RJ, et al. Neuropathologic outcome of mild cognitive impairment following progression to clinical dementia. Archives of neurology. 2006;63(5):674-81.

21.		Wood RA, Moodley KK, Lever C, Minati L, Chan D. Allocentric Spatial Memory Testing Predicts Conversion from Mild Cognitive Impairment to Dementia: An Initial Proof-of-Concept Study. Frontiers in neurology. 2016;7:215.

22.		Guerreiro R, Hardy J. Genetics of Alzheimer's disease. Neurotherapeutics. 2014;11(4):732-7.

23.		Kim J, Basak JM, Holtzman DM. The role of apolipoprotein E in Alzheimer's disease. Neuron. 2009;63(3):287-303.

24.		Corder EH, Saunders AM, Strittmatter WJ, Schmechel DE, Gaskell PC, Small GW, et al. Gene dose of apolipoprotein E type 4 allele and the risk of Alzheimer's disease in late onset families. Science (New York, NY). 1993;261(5123):921-3.

25.		Strittmatter WJ, Weisgraber KH, Huang DY, Dong LM, Salvesen GS, Pericak-Vance M, et al. Binding of human apolipoprotein E to synthetic amyloid beta peptide: isoform-specific effects and implications for late-onset Alzheimer disease. Proceedings of the National Academy of Sciences of the United States of America. 1993;90(17):8098-102.

26.		Wu L, Rosa-Neto P, Hsiung GY, Sadovnick AD, Masellis M, Black SE, et al. Early-onset familial Alzheimer's disease (EOFAD). Can J Neurol Sci. 2012;39(4):436-45.

27.		Wattendorff AR, Bots GT, Went LN, Endtz LJ. Familial cerebral amyloid angiopathy presenting as recurrent cerebral haemorrhage. Journal of the neurological sciences. 1982;55(2):121-35.

28.		Goate A, Chartier-Harlin MC, Mullan M, Brown J, Crawford F, Fidani L, et al. Segregation of a missense mutation in the amyloid precursor protein gene with familial Alzheimer's disease. Nature. 1991;349(6311):704-6.

29.		Alzforum. Mutations Database: https://www.alzforum.org/mutations2021

30.		Masdeu JC, Zubieta JL, Arbizu J. Neuroimaging as a marker of the onset and progression of Alzheimer's disease. Journal of the neurological sciences. 2005;236(1-2):55-64.

31.		Braak H, Braak E. Neuropathological stageing of Alzheimer-related changes. Acta neuropathologica. 1991;82(4):239-59.

32. Loof A, Schoofs L. Alzheimer's Disease: Is a Dysfunctional Mevalonate Biosynthetic Pathway the Master-Inducer of Deleterious Changes in Cell Physiology? OBM Neurobiology 2019; 3(4).

33. Brion, J., et al., Mise en evidence immunologique de la proteine tau au niveau des lesions de degenerescence neurofibrillaire de la maladie d'Alzheimer. Archives of Biology. 1985;96(2-4):229.

34. Weingarten MD, Lockwood AH, Hwo S-Y, Kirschner MW. A protein factor essential for microtubule assembly. Proceedings of the National Academy of Sciences. 1975;72(5):1858-62.

35. Black MM, Slaughter T, Moshiach S, Obrocka M, Fischer I. Tau is enriched on dynamic microtubules in the distal region of growing axons. Journal of Neuroscience. 1996;16(11):3601-19.

36. Barbier P, Zejneli O, Martinho M, Lasorsa A, Belle V, Smet-Nocca C, et al. Role of Tau as a Microtubule-Associated Protein: Structural and Functional Aspects. Frontiers in Aging Neuroscience. 2019;11(204).

37. Goedert M, Spillantini M, Jakes R, Rutherford D, Crowther R. Multiple isoforms of human microtubule-associated protein tau: sequences and localization in neurofibrillary tangles of Alzheimer's disease. Neuron. 1989;3(4):519-26.

38. Himmler A, Drechsel D, Kirschner MW, Martin DW. Tau consists of a set of proteins with repeated C-terminal microtubule-binding domains and variable N-terminal domains. Molecular and cellular biology. 1989;9(4):1381-8.

39. Love JE, Hayden EJ, Rohn TT. Alternative Splicing in Alzheimer's Disease. J Parkinsons Dis Alzheimers Dis. 2015;2(2).

40. Spillantini MG, Goedert M. Tau protein pathology in neurodegenerative diseases. Trends in neurosciences. 1998;21(10):428-33.

41. Park SA, Ahn S, Gallo J-M. Tau mis-splicing in the pathogenesis of neurodegenerative disorders. BMB Rep. 2016; 49(8): 405-413

42. Grundke-Iqbal I, Iqbal K, Quinlan M, Tung YC, Zaidi MS, Wisniewski HM. Microtubule-associated protein tau. A component of Alzheimer paired helical filaments. The Journal of biological chemistry. 1986;261(13):6084-9.

43. Lee VM, Balin BJ, Otvos L, Jr., Trojanowski JQ. A68: a major subunit of paired helical filaments and derivatized forms of normal Tau. Science (New York, NY). 1991;251(4994):675-8.

44. Savonenko AV, Melnikova T, Li T, Price DL, Wong PC. Alzheimer disease. Neurobiology of brain disorders: Elsevier; 2015. p. 321-38.

45. Rao, A. Untangling Alzheimer's and the spread of misfolded proteins. ASBMB Today. Journal News, 24 Jan 2020. https://www.asbmb.org/asbmb-today/science/012420/from-the-journal-jbc-062420

46. Hyman BT, Van Hoesen GW, Damasio AR, Barnes CL. Alzheimer's disease: cell-specific pathology isolates the hippocampal formation. Science (New York, NY). 1984;225(4667):1168-70.

47. Scoville WB, Milner B. Loss of recent memory after bilateral hippocampal lesions. Journal of neurology, neurosurgery, and psychiatry. 1957;20(1):11-21.

48. O'Keefe J, Dostrovsky J. The hippocampus as a spatial map. Preliminary evidence from unit activity in the freely-moving rat. Brain research. 1971;34(1):171-5.

49.      O'Keefe J, Conway DH. Hippocampal place units in the freely moving rat: why they fire where they fire. Experimental brain research Experimentelle Hirnforschung Experimentation cerebrale. 1978;31(4):573-90.

50.      Hafting T, Fyhn M, Molden S, Moser MB, Moser EI. Microstructure of a spatial map in the entorhinal cortex. Nature. 2005;436(7052):801-6.

51.      Serrano-Pozo A, Frosch MP, Masliah E, Hyman BT. Neuropathological alterations in Alzheimer disease. Cold Spring Harb Perspect Med. 2011;1(1):a006189.

52.      Glenner GG, Wong CW. Alzheimer's disease: initial report of the purification and characterization of a novel cerebrovascular amyloid protein. Biochem Biophys Res Commun. 1984;120(3):885-90.

53.      Masters CL, Simms G, Weinman NA, Multhaup G, McDonald BL, Beyreuther K. Amyloid plaque core protein in Alzheimer disease and Down syndrome. Proceedings of the National Academy of Sciences of the United States of America. 1985;82(12):4245-9.

54.      Fillenbaum GG, van Belle G, Morris JC, Mohs RC, Mirra SS, Davis PC, et al. Consortium to Establish a Registry for Alzheimer's Disease (CERAD) The first 20 years. Alzheimers Dement. 2008. 4(2): 96–109.

55.      Thal DR, Rüb U, Orantes M, Braak H. Phases of Aβ-deposition in the human brain and its relevance for the development of AD. Neurology. 2002;58(12):1791-800.

56.      DeTure MA, Dickson DW. The neuropathological diagnosis of Alzheimer's disease. Mol Neurodegener. 2019 Aug 2;14(1):32.

57.      Müller UC, Deller T, Korte M. Not just amyloid: physiological functions of the amyloid precursor protein family.

58.      Haass C. Take five--BACE and the gamma-secretase quartet conduct Alzheimer's amyloid beta-peptide generation. Embo j. 2004;23(3):483-8.

59.      Haass C, Schlossmacher MG, Hung AY, Vigo-Pelfrey C, Mellon A, Ostaszewski BL, et al. Amyloid beta-peptide is produced by cultured cells during normal metabolism. Nature. 1992;359(6393):322-5.

60.      Haass C, Hung AY, Schlossmacher MG, Teplow DB, Selkoe DJ. beta-Amyloid peptide and a 3-kDa fragment are derived by distinct cellular mechanisms. The Journal of biological chemistry. 1993;268(5):3021-4.

61.      Seubert P, Vigo-Pelfrey C, Esch F, Lee M, Dovey H, Davis D, et al. Isolation and quantification of soluble Alzheimer's beta-peptide from biological fluids. Nature. 1992;359(6393):325-7.

62.      Shoji M, Golde TE, Ghiso J, Cheung TT, Estus S, Shaffer LM, et al. Production of the Alzheimer amyloid beta protein by normal proteolytic processing. Science (New York, NY). 1992;258(5079):126-9.

63.      Haass C, Selkoe DJ. Cellular processing of beta-amyloid precursor protein and the genesis of amyloid beta-peptide. Cell. 1993;75(6):1039-42.

64.      Kang J, Lemaire HG, Unterbeck A, Salbaum JM, Masters CL, Grzeschik KH, et al. The precursor of Alzheimer's disease amyloid A4 protein resembles a cell-surface receptor. Nature. 1987;325(6106):733-6.

65.      Esch FS, Keim PS, Beattie EC, Blacher RW, Culwell AR, Oltersdorf T, et al. Cleavage of amyloid beta peptide during constitutive processing of its precursor. Science (New York, NY). 1990;248(4959):1122-4.

66.     Gu Y, Misonou H, Sato T, Dohmae N, Takio K, Ihara Y. Distinct intramembrane cleavage of the beta-amyloid precursor protein family resembling gamma-secretase-like cleavage of Notch. The Journal of biological chemistry. 2001;276(38):35235-8.

67.     Wippold FJ, Cairns N, Vo K, Holtzman DM, Morris JC. Neuropathology for the Neuroradiologist: Plaques and Tangles. American Journal of Neuroradiology. 2008;29(1):18-22.

68.     Sisodia SS, St George-Hyslop PH. gamma-Secretase, Notch, Abeta and Alzheimer's disease: where do the presenilins fit in? Nat Rev Neurosci. 2002;3(4):281-90.

69.     Willem M, Tahirovic S, Busche MA, Ovsepian SV, Chafai M, Kootar S, et al. η-Secretase processing of APP inhibits neuronal activity in the hippocampus. Nature. 2015;526(7573):443-7.

70.     Jefferson T, Čaušević M, auf dem Keller U, Schilling O, Isbert S, Geyer R, et al. Metalloprotease meprin beta generates nontoxic N-terminal amyloid precursor protein fragments in vivo. The Journal of biological chemistry. 2011;286(31):27741-50.

71.     Qiu T, Liu Q, Chen YX, Zhao YF, Li YM. Aβ42 and Aβ40: similarities and differences. J Pept Sci. 2015;21(7):522-9.

72.     Monro OR, Mackic JB, Yamada S, Segal MB, Ghiso J, Maurer C, et al. Substitution at codon 22 reduces clearance of Alzheimer's amyloid-beta peptide from the cerebrospinal fluid and prevents its transport from the central nervous system into blood. Neurobiology of aging. 2002;23(3):405-12.

73.     Yoon SS, Jo SA. Mechanisms of Amyloid-β Peptide Clearance: Potential Therapeutic Targets for Alzheimer's Disease. Biomol Ther (Seoul). 2012;20(3):245-55.

74.     Chen GF, Xu TH, Yan Y, Zhou YR, Jiang Y, Melcher K, et al. Amyloid beta: structure, biology and structure-based therapeutic development. Acta Pharmacol Sin. 2017;38(9):1205-35.

75.     Gaspar RC, Villarreal SA, Bowles N, Hepler RW, Joyce JG, Shughrue PJ. Oligomers of beta-amyloid are sequestered into and seed new plaques in the brains of an AD mouse model. Experimental neurology. 2010;223(2):394-400.

76.     Yu L, Edalji R, Harlan JE, Holzman TF, Lopez AP, Labkovsky B, et al. Structural characterization of a soluble amyloid beta-peptide oligomer. Biochemistry. 2009;48(9):1870-7.

77.     Kayed R, Lasagna-Reeves CA. Molecular mechanisms of amyloid oligomers toxicity. J Alzheimers Dis. 2013;33 Suppl 1:S67-78.

78.     Sengupta U, Nilson AN, Kayed R. The Role of Amyloid-β Oligomers in Toxicity, Propagation, and Immunotherapy. EBioMedicine. 2016;6:42-9.

79.     Bitan G, Vollers SS, Teplow DB. Elucidation of primary structure elements controlling early amyloid beta-protein oligomerization. The Journal of biological chemistry. 2003;278(37):34882-9.

80.     Bateman RJ, Munsell LY, Morris JC, Swarm R, Yarasheski KE, Holtzman DM. Human amyloid-beta synthesis and clearance rates as measured in cerebrospinal fluid in vivo. Nat Med. 2006;12(7):856-61.

81.     Weller RO, Massey A, Kuo YM, Roher AE. Cerebral amyloid angiopathy: accumulation of A beta in interstitial fluid drainage pathways in Alzheimer's disease. Annals of the New York Academy of Sciences. 2000;903:110-7.

82.     Sikanyika NL, Parkington HC, Smith AI, Kuruppu S. Powering Amyloid Beta Degrading Enzymes: A Possible Therapy for Alzheimer's Disease. Neurochem Res. 2019;44(6):1289-96.

83.     Jansen WJ, Ossenkoppele R, Knol DL, Tijms BM, Scheltens P, Verhey FR, et al. Prevalence of cerebral amyloid pathology in persons without dementia: a meta-analysis. Jama. 2015;313(19):1924-38.

84.     Rogers J, Strohmeyer R, Kovelowski CJ, Li R. Microglia and inflammatory mechanisms in the clearance of amyloid beta peptide. Glia. 2002;40(2):260-9.

85.     Nielsen HM, Veerhuis R, Holmqvist B, Janciauskiene S. Binding and uptake of A beta1-42 by primary human astrocytes in vitro. Glia. 2009;57(9):978-88.

86.     Weller RO, Subash M, Preston SD, Mazanti I, Carare RO. Perivascular drainage of amyloid-beta peptides from the brain and its failure in cerebral amyloid angiopathy and Alzheimer's disease. Brain Pathol. 2008;18(2):253-66.

87.     Mosher KI, Wyss-Coray T. Microglial dysfunction in brain aging and Alzheimer's disease. Biochem Pharmacol. 2014;88(4):594-604.

88.     Peng W, Achariyar TM, Li B, Liao Y, Mestre H, Hitomi E, et al. Suppression of glymphatic fluid transport in a mouse model of Alzheimer's disease. Neurobiology of disease. 2016;93:215-25.

89.     Suzuki N, Cheung TT, Cai XD, Odaka A, Otvos L, Jr., Eckman C, et al. An increased percentage of long amyloid beta protein secreted by familial amyloid beta protein precursor (beta APP717) mutants. Science (New York, NY). 1994;264(5163):1336-40.

90.     De Strooper B, Iwatsubo T, Wolfe MS. Presenilins and γ-secretase: structure, function, and role in Alzheimer Disease. Cold Spring Harb Perspect Med. 2012;2(1):a006304.

91.     Bowen DM, Smith CB, White P, Davison AN. Neurotransmitter-related enzymes and indices of hypoxia in senile dementia and other abiotrophies. Brain: a journal of neurology. 1976;99(3):459-96.

92.     Davies P, Maloney A. Selective loss of central cholinergic neurons in Alzheimer's disease. The Lancet. 1976;308(8000):1403.

93.     Perry EK, Gibson PH, Blessed G, Perry RH, Tomlinson BE. Neurotransmitter enzyme abnormalities in senile dementia: Choline acetyltransferase and glutamic acid decarboxylase activities in necropsy brain tissue. Journal of the neurological sciences. 1977;34(2):247-65.

94.     Rylett R, Ball M, Colhoun E. Evidence for high affinity choline transport in synaptosomes prepared from hippocampus and neocortex of patients with Alzheimer's disease. Brain research. 1983;289(1-2):169-75.

95.     Nilsson L, Nordberg A, Hardy J, Wester P, Winblad B. Physostigmine restores 3 H-acetylcholine efflux from Alzheimer brain slices to normal level. Journal of neural transmission. 1986;67(3-4):275-85.

96.     Hasselmo ME. The role of acetylcholine in learning and memory. Curr Opin Neurobiol. 2006;16(6):710-5.

97.     Huerta PT, Lisman JE. Bidirectional synaptic plasticity induced by a single burst during cholinergic theta oscillation in CA1 in vitro. Neuron. 1995;15(5):1053-63.

98.     Francis PT, Palmer AM, Snape M, Wilcock GK. The cholinergic hypothesis of Alzheimer's disease: a review of progress. Journal of neurology, neurosurgery, and psychiatry. 1999;66(2):137-47.

99.     Selkoe DJ, Hardy J. The amyloid hypothesis of Alzheimer's disease at 25 years. EMBO Mol Med. 2016;8(6):595-608.

100.    Hardy JA, Higgins GA. Alzheimer's disease: the amyloid cascade hypothesis. Science (New York, NY). 1992;256(5054):184-5.

101.    Pimplikar SW. Reassessing the amyloid cascade hypothesis of Alzheimer's disease. Int J Biochem Cell Biol. 2009;41(6):1261-8.

102.    Selkoe D, Mandelkow E, Holtzman D. Deciphering Alzheimer disease. Cold Spring Harb Perspect Med. 2012;2(1):a011460.

103.    Hardy J, Selkoe DJ. The amyloid hypothesis of Alzheimer's disease: progress and problems on the road to therapeutics. Science (New York, NY). 2002;297(5580):353-6.

104.    Lott IT, Head E. Dementia in Down syndrome: unique insights for Alzheimer disease research. Nature reviews Neurology. 2019;15(3):135-47.

105.    Castellano JM, Kim J, Stewart FR, Jiang H, DeMattos RB, Patterson BW, et al. Human apoE isoforms differentially regulate brain amyloid-β peptide clearance. Sci Transl Med. 2011;3(89):89ra57.

106.    Jonsson T, Atwal JK, Steinberg S, Snaedal J, Jonsson PV, Bjornsson S, et al. A mutation in APP protects against Alzheimer's disease and age-related cognitive decline. Nature. 2012;488(7409):96-9.

107.    Lesné S, Kotilinek L, Ashe KH. Plaque-bearing mice with reduced levels of oligomeric amyloid-beta assemblies have intact memory function. Neuroscience. 2008;151(3):745-9.

108.    Shankar GM, Li S, Mehta TH, Garcia-Munoz A, Shepardson NE, Smith I, et al. Amyloid-beta protein dimers isolated directly from Alzheimer's brains impair synaptic plasticity and memory. Nat Med. 2008;14(8):837-42.

109.    Dahlgren KN, Manelli AM, Stine WB, Jr., Baker LK, Krafft GA, LaDu MJ. Oligomeric and fibrillar species of amyloid-beta peptides differentially affect neuronal viability. The Journal of biological chemistry. 2002;277(35):32046-53.

110.    Ahmed M, Davis J, Aucoin D, Sato T, Ahuja S, Aimoto S, et al. Structural conversion of neurotoxic amyloid-beta(1-42) oligomers to fibrils. Nat Struct Mol Biol. 2010;17(5):561-7.

111.    De Felice FG, Wu D, Lambert MP, Fernandez SJ, Velasco PT, Lacor PN, et al. Alzheimer's disease-type neuronal tau hyperphosphorylation induced by A beta oligomers. Neurobiology of aging. 2008;29(9):1334-47.

112.    Jin M, Shepardson N, Yang T, Chen G, Walsh D, Selkoe DJ. Soluble amyloid beta-protein dimers isolated from Alzheimer cortex directly induce Tau hyperphosphorylation and neuritic degeneration. Proceedings of the National Academy of Sciences of the United States of America. 2011;108(14):5819-24.

113.    Kayed R, Sokolov Y, Edmonds B, McIntire TM, Milton SC, Hall JE, et al. Permeabilization of lipid bilayers is a common conformation-dependent activity of soluble amyloid oligomers in protein misfolding diseases. The Journal of biological chemistry. 2004;279(45):46363-6.

114.    Demuro A, Mina E, Kayed R, Milton SC, Parker I, Glabe CG. Calcium dysregulation and membrane disruption as a ubiquitous neurotoxic mechanism of soluble amyloid oligomers. The Journal of biological chemistry. 2005;280(17):17294-300.

115.    Selkoe DJ. Soluble oligomers of the amyloid beta-protein impair synaptic plasticity and behavior. Behavioural brain research. 2008;192(1):106-13.

116.    Shankar GM, Bloodgood BL, Townsend M, Walsh DM, Selkoe DJ, Sabatini BL. Natural oligomers of the Alzheimer amyloid-beta protein induce reversible synapse loss by modulating an NMDA-type glutamate receptor-dependent signaling pathway. The Journal of neuroscience : the official journal of the Society for Neuroscience. 2007;27(11):2866-75.

117.    Li S, Hong S, Shepardson NE, Walsh DM, Shankar GM, Selkoe D. Soluble oligomers of amyloid Beta protein facilitate hippocampal long-term depression by disrupting neuronal glutamate uptake. Neuron. 2009;62(6):788-801.

118.    Cleary JP, Walsh DM, Hofmeister JJ, Shankar GM, Kuskowski MA, Selkoe DJ, et al. Natural oligomers of the amyloid-beta protein specifically disrupt cognitive function. Nature neuroscience. 2005;8(1):79-84.

119.    Morkuniene R, Cizas P, Jankeviciute S, Petrolis R, Arandarcikaite O, Krisciukaitis A, et al. Small Aβ1-42 oligomer-induced membrane depolarization of neuronal and microglial cells: role of N-methyl-D-aspartate receptors. J Neurosci Res. 2015;93(3):475-86.

120.    Freir DB, Nicoll AJ, Klyubin I, Panico S, Mc Donald JM, Risse E, et al. Interaction between prion protein and toxic amyloid β assemblies can be therapeutically targeted at multiple sites. Nat Commun. 2011;2:336.

121.    Sebollela A, Mustata GM, Luo K, Velasco PT, Viola KL, Cline EN, et al. Elucidating molecular mass and shape of a neurotoxic Aβ oligomer. ACS Chem Neurosci. 2014;5(12):1238-45.

122.    Minter MR, Main BS, Brody KM, Zhang M, Taylor JM, Crack PJ. Soluble amyloid triggers a myeloid differentiation factor 88 and interferon regulatory factor 7 dependent neuronal type-1 interferon response in vitro. J Neuroinflammation. 2015;12:71.

123.    Crouse NR, Ajit D, Udan ML, Nichols MR. Oligomeric amyloid-beta(1-42) induces THP-1 human monocyte adhesion and maturation. Brain research. 2009;1254:109-19.

124.    Esparza TJ, Zhao H, Cirrito JR, Cairns NJ, Bateman RJ, Holtzman DM, et al. Amyloid-β oligomerization in Alzheimer dementia versus high-pathology controls. Annals of neurology. 2013;73(1):104-19.

125.    Musiek ES, Holtzman DM. Origins of Alzheimer's disease: reconciling cerebrospinal fluid biomarker and neuropathology data regarding the temporal sequence of amyloid-beta and tau involvement. Current opinion in neurology. 2012;25(6):715-20.

126.    Karran E, Hardy J. A critique of the drug discovery and phase 3 clinical programs targeting the amyloid hypothesis for Alzheimer disease. Annals of neurology. 2014;76(2):185-205.

127.    Knopman DS. Bad news and good news in AD, and how to reconcile them. Nature reviews Neurology. 2019;15(2):61-2.

128.    Miller G. Alzheimer's research. Stopping Alzheimer's before it starts. Science (New York, NY). 2012;337(6096):790-2.

129.     Scheckel C, Aguzzi A. Prions, prionoids and protein misfolding disorders. Nat Rev Genet. 2018;19(7):405-18.

130.     Jarrett JT, Lansbury PT, Jr. Seeding "one-dimensional crystallization" of amyloid: a pathogenic mechanism in Alzheimer's disease and scrapie? Cell. 1993;73(6):1055-8.

131.     Meyer-Luehmann M, Coomaraswamy J, Bolmont T, Kaeser S, Schaefer C, Kilger E, et al. Exogenous induction of cerebral beta-amyloidogenesis is governed by agent and host. Science (New York, NY). 2006;313(5794):1781-4.

132.     Stöhr J, Watts JC, Mensinger ZL, Oehler A, Grillo SK, DeArmond SJ, et al. Purified and synthetic Alzheimer's amyloid beta (Aβ) prions. Proceedings of the National Academy of Sciences of the United States of America. 2012;109(27):11025-30.

133.     Eisele YS, Obermüller U, Heilbronner G, Baumann F, Kaeser SA, Wolburg H, et al. Peripherally applied Abeta-containing inoculates induce cerebral beta-amyloidosis. Science (New York, NY). 2010;330(6006):980-2.

134.     Burwinkel M, Lutzenberger M, Heppner FL, Schulz-Schaeffer W, Baier M. Intravenous injection of beta-amyloid seeds promotes cerebral amyloid angiopathy (CAA). Acta Neuropathol Commun. 2018;6(1):23.

135.     Jaunmuktane Z, Mead S, Ellis M, Wadsworth JD, Nicoll AJ, Kenny J, et al. Evidence for human transmission of amyloid-β pathology and cerebral amyloid angiopathy. Nature. 2015;525(7568):247-50.

136.     Ritchie DL, Adlard P, Peden AH, Lowrie S, Le Grice M, Burns K, et al. Amyloid-β accumulation in the CNS in human growth hormone recipients in the UK. Acta neuropathologica. 2017;134(2):221-40.

137.     Frontzek K, Lutz MI, Aguzzi A, Kovacs GG, Budka H. Amyloid-β pathology and cerebral amyloid angiopathy are frequent in iatrogenic Creutzfeldt-Jakob disease after dural grafting. Swiss Med Wkly. 2016;146:w14287.

138.     Clavaguera F, Hench J, Goedert M, Tolnay M. Invited review: Prion-like transmission and spreading of tau pathology. Neuropathology and applied neurobiology. 2015;41(1):47-58.

139.     Lasagna-Reeves CA, Castillo-Carranza DL, Sengupta U, Guerrero-Munoz MJ, Kiritoshi T, Neugebauer V, et al. Alzheimer brain-derived tau oligomers propagate pathology from endogenous tau. Scientific reports. 2012;2(1):1-7.

140.     Clavaguera F, Akatsu H, Fraser G, Crowther RA, Frank S, Hench J, et al. Brain homogenates from human tauopathies induce tau inclusions in mouse brain. Proceedings of the National Academy of Sciences. 2013;110(23):9535-40.

141.     Frost B, Diamond MI. The expanding realm of prion phenomena in neurodegenerative disease. Prion. 2009;3(2):74-7.

142.     Guo JL, Lee VM. Seeding of normal Tau by pathological Tau conformers drives pathogenesis of Alzheimer-like tangles. The Journal of biological chemistry. 2011;286(17):15317-31.

143.     Guo JL, Lee VM. Neurofibrillary tangle-like tau pathology induced by synthetic tau fibrils in primary neurons over-expressing mutant tau. FEBS letters. 2013;587(6):717-23.

144.     Calafate S, Buist A, Miskiewicz K, Vijayan V, Daneels G, de Strooper B, et al. Synaptic Contacts Enhance Cell-to-Cell Tau Pathology Propagation. Cell Rep. 2015;11(8):1176-83.

145.    Myers A, McGonigle P. Overview of Transgenic Mouse Models for Alzheimer's Disease. Curr Protoc Neurosci. 2019;89(1):e81.

146.    Agrawal S. Alzheimer's Disease: Animal Research Models. Materials and Methods. 2017;7:2686.

147.    Eriksen JL, Janus CG. Plaques, tangles, and memory loss in mouse models of neurodegeneration. Behav Genet. 2007;37(1):79-100.

148.    de Calignon A, Polydoro M, Suarez-Calvet M, William C, Adamowicz DH, Kopeikina KJ, et al. Propagation of tau pathology in a model of early Alzheimer's disease. Neuron. 2012;73(4):685-97.

149.    Hall AM, Roberson ED. Mouse models of Alzheimer's disease. Brain Res Bull. 2012;88(1):3-12.

150.    Hasebe N, Fujita Y, Ueno M, Yoshimura K, Fujino Y, Yamashita T. Soluble β-amyloid Precursor Protein Alpha binds to p75 neurotrophin receptor to promote neurite outgrowth. PloS one. 2013;8(12):e82321.

151.    Tamayev R, D'Adamio L. Inhibition of γ-secretase worsens memory deficits in a genetically congruous mouse model of Danish dementia. Mol Neurodegener. 2012;7:19.

152.    Nilsson P, Saito T, Saido TC. New mouse model of Alzheimer's. ACS Chem Neurosci. 2014;5(7):499-502.

153.    Saito T, Matsuba Y, Mihira N, Takano J, Nilsson P, Itohara S, et al. Single App knock-in mouse models of Alzheimer's disease. Nature neuroscience. 2014;17(5):661-3.

154.    Whyte LS, Hemsley KM, Lau AA, Hassiotis S, Saito T, Saido TC, et al. Reduction in open field activity in the absence of memory deficits in the App(NL-G-F) knock-in mouse model of Alzheimer's disease. Behavioural brain research. 2018;336:177-81.

155.    Latif-Hernandez A, Shah D, Craessaerts K, Saido T, Saito T, De Strooper B, et al. Subtle behavioral changes and increased prefrontal-hippocampal network synchronicity in APP(NL-G-F) mice before prominent plaque deposition. Behavioural brain research. 2019;364:431-41.

156.    Masuda A, Kobayashi Y, Kogo N, Saito T, Saido TC, Itohara S. Cognitive deficits in single App knock-in mouse models. Neurobiology of learning and memory. 2016;135:73-82.

157.    Enzlein T, Cordes J, Munteanu B, Michno W, Serneels L, De Strooper B, et al. Computational Analysis of Alzheimer Amyloid Plaque Composition in 2D- and Elastically Reconstructed 3D-MALDI MS Images. Anal Chem. 2020;92(21):14484-93.

158.    Kobayashi Y, Kohbuchi S, Koganezawa N, Sekino Y, Shirao T, Saido TC, et al. Impairment of ciliary dynamics in an APP knock-in mouse model of Alzheimer's disease. Biochem Biophys Res Commun. 2022;610:85-91.

159.    Zhang H, Wu L, Pchitskaya E, Zakharova O, Saito T, Saido T, et al. Neuronal Store-Operated Calcium Entry and Mushroom Spine Loss in Amyloid Precursor Protein Knock-In Mouse Model of Alzheimer's Disease. The Journal of neuroscience : the official journal of the Society for Neuroscience. 2015;35(39):13275-86.

160.    Bevan RJ, Hughes TR, Williams PA, Good MA, Morgan BP, Morgan JE. Retinal ganglion cell degeneration correlates with hippocampal spine loss in experimental Alzheimer's disease. Acta Neuropathol Commun. 2020;8(1):216.

161.     Benitez DP, Jiang S, Wood J, Wang R, Hall CM, Peerboom C, et al. Knock-in models related to Alzheimer's disease: synaptic transmission, plaques and the role of microglia. Mol Neurodegener. 2021;16(1):47.

162.     Pervolaraki E, Hall SP, Foresteire D, Saito T, Saido TC, Whittington MA, et al. Insoluble Aβ overexpression in an App knock-in mouse model alters microstructure and gamma oscillations in the prefrontal cortex, affecting anxiety-related behaviours. Dis Model Mech. 2019;12(9).

163.     Sakakibara Y, Sekiya M, Saito T, Saido TC, Iijima KM. Cognitive and emotional alterations in App knock-in mouse models of Aβ amyloidosis. BMC neurosicence, 2018. 19(46).

164.     Locci A, Orellana H, Rodriguez G, Gottliebson M, McClarty B, Dominguez S, et al. Comparison of memory, affective behavior, and neuropathology in APP(NLGF) knock-in mice to 5xFAD and APP/PS1 mice. Behavioural brain research. 2021;404:113192.

165.     Nieraad H, de Bruin N, Arne O, Hofmann MCJ, Schmidt M, Saito T, et al. Impact of Hyperhomocysteinemia and Different Dietary Interventions on Cognitive Performance in a Knock-in Mouse Model for Alzheimer's Disease. Nutrients. 2020;12(11).

166.     Mehla J, Lacoursiere SG, Lapointe V, McNaughton BL, Sutherland RJ, McDonald RJ, et al. Age-dependent behavioral and biochemical characterization of single APP knock-in mouse (APP(NL-G-F/NL-G-F)) model of Alzheimer's disease. Neurobiology of aging. 2019;75:25-37.

167.     Saifullah MAB, Komine O, Dong Y, Fukumoto K, Sobue A, Endo F, et al. Touchscreen-based location discrimination and paired associate learning tasks detect cognitive impairment at an early stage in an App knock-in mouse model of Alzheimer's disease. Mol Brain. 2020;13(1):147.

168.     Latif-Hernandez A, Sabanov V, Ahmed T, Craessaerts K, Saito T, Saido T, et al. The two faces of synaptic failure in App(NL-G-F) knock-in mice. Alzheimer's research & therapy. 2020;12(1):100.

169.     Sebastian Monasor L, Müller SA, Colombo AV, Tanrioever G, König J, Roth S, et al. Fibrillar Aβ triggers microglial proteome alterations and dysfunction in Alzheimer mouse models. eLife. 2020;9.

170.     Guariglia CC, Nitrini R. Topographical disorientation in Alzheimer's disease. Arquivos de neuro-psiquiatria. 2009;67(4):967-72.

171.     Daroff RB, Aminoff MJ. Encyclopedia of the neurological sciences: Academic press; 2014.

172.     Aguirre GK, D'Esposito M. Topographical disorientation: a synthesis and taxonomy. Brain : a journal of neurology. 1999;122 ( Pt 9):1613-28.

173.     Jacobs LF. Memory, Spatial. In: Aminoff MJ, Daroff RB, editors. Encyclopedia of the Neurological Sciences. New York: Academic Press; 2003. p. 86-90.

174.     Lester AW, Moffat SD, Wiener JM, Barnes CA, Wolbers T. The Aging Navigational System. Neuron. 2017;95(5):1019-35.

175.     Britton Z, Arshad Q. Vestibular and Multi-Sensory Influences Upon Self-Motion Perception and the Consequences for Human Behavior. Frontiers in neurology. 2019;10(63).

176.     Ungerleider LG, Mishkin M. Two cortical visual systems. . In: D.J. Ingle MAG, & R. Mansfield, editor. Analysis of Visual Behavior. Cambridge: The MIT Press; 1982. p. 549-86.

177. Doeller CF, King JA, Burgess N. Parallel striatal and hippocampal systems for landmarks and boundaries in spatial memory. Proceedings of the National Academy of Sciences of the United States of America. 2008;105(15):5915-20.

178. McDonald RJ, White NM. Parallel information processing in the water maze: evidence for independent memory systems involving dorsal striatum and hippocampus. Behavioral and neural biology. 1994;61(3):260-70.

179. O'Keefe J, Nadel L. Précis of O'Keefe & Nadel's The hippocampus as a cognitive map. Behavioral and Brain Sciences. 1979;2(04):487-94.

180. Packard MG, McGaugh JL. Inactivation of hippocampus or caudate nucleus with lidocaine differentially affects expression of place and response learning. Neurobiology of learning and memory. 1996;65(1):65-72.

181. Iaria G, Petrides M, Dagher A, Pike B, Bohbot VD. Cognitive strategies dependent on the hippocampus and caudate nucleus in human navigation: variability and change with practice. The Journal of neuroscience : the official journal of the Society for Neuroscience. 2003;23(13):5945-52.

182. O'Keefe J, Speakman A. Single unit activity in the rat hippocampus during a spatial memory task. Experimental brain research Experimentelle Hirnforschung Experimentation cerebrale. 1987;68(1):1-27.

183. O'Keefe, J. and Nadel, L., *The Hippocampus as a Cognitive Map*. 1978: Oxford University Press

184. Kant I. The Critique of Pure Reason1781.

185. Tolman EC. Cognitive maps in rats and men. Psychol Rev. 1948;55(4):189-208.

186. Tolman EC, Ritchie B, Kalish D. Studies in spatial learning. I. Orientation and the short-cut. Journal of experimental psychology. 1946;36(1):13.

187. Tolman EC, Ritchie BF, Kalish D. Studies in spatial learning. II. Place learning versus response learning. Journal of experimental psychology. 1946;36(3):221.

188. Muller RU, Kubie JL. The effects of changes in the environment on the spatial firing of hippocampal complex-spike cells. The Journal of neuroscience : the official journal of the Society for Neuroscience. 1987;7(7):1951-68.

189. Ranck JB. Head direction cells in the deep cell layer of dorsolateral pre-subiculum in freely moving rats. Electrical activity of the archicortex. 1985.

190. Lever C, Burton S, Jeewajee A, O'Keefe J, Burgess N. Boundary vector cells in the subiculum of the hippocampal formation. The Journal of neuroscience : the official journal of the Society for Neuroscience. 2009;29(31):9771-7.

191. Eichenbaum H. Hippocampus: cognitive processes and neural representations that underlie declarative memory. Neuron. 2004;44(1):109-20.

192. Eichenbaum, H., A cortical–hippocampal system for declarative memory. Nat Rev Neurosci, 2000. 1: p. 41-50.

193. Bird CM, Burgess N. The hippocampus and memory: insights from spatial processing. Nat Rev Neurosci. 2008;9(3):182-94.

194. Kumaran D, Maguire EA. The human hippocampus: cognitive maps or relational memory? The Journal of neuroscience : the official journal of the Society for Neuroscience. 2005;25(31):7254-9.

195.     Auger SD, Maguire EA. Assessing the mechanism of response in the retrosplenial cortex of good and poor navigators. Cortex; a journal devoted to the study of the nervous system and behavior. 2013;49(10):2904-13.

196.     Burgess N, Maguire EA, Spiers HJ, O'Keefe J. A temporoparietal and prefrontal network for retrieving the spatial context of lifelike events. NeuroImage. 2001;14(2):439-53.

197.     Burgess N. Spatial cognition and the brain. Annals of the New York Academy of Sciences. 2008;1124:77-97.

198.     Reagh ZM, Yassa MA. Object and spatial mnemonic interference differentially engage lateral and medial entorhinal cortex in humans. Proceedings of the National Academy of Sciences of the United States of America. 2014;111(40):E4264-73.

199.     Kessels RP, Postma A, Wijnalda EM, de Haan EH. Frontal-lobe involvement in spatial memory: evidence from PET, fMRI, and lesion studies. Neuropsychol Rev. 2000;10(2):101-13.

200.     Latini-Corazzini L, Nesa MP, Ceccaldi M, Guedj E, Thinus-Blanc C, Cauda F, et al. Route and survey processing of topographical memory during navigation. Psychol Res. 2010;74(6):545-59.

201.     Lithfous S, Dufour A, Despres O. Spatial navigation in normal aging and the prodromal stage of Alzheimer's disease: insights from imaging and behavioral studies. Ageing Res Rev. 2013;12(1):201-13.

202.     Ferbinteanu J, Ray C, McDonald RJ. Both dorsal and ventral hippocampus contribute to spatial learning in Long-Evans rats. Neurosci Lett. 2003;345(2):131-5.

203.     Logue SF, Paylor R, Wehner JM. Hippocampal lesions cause learning deficits in inbred mice in the Morris water maze and conditioned-fear task. Behavioral neuroscience. 1997;111(1):104-13.

204.     Xavier GF, Oliveira-Filho FJ, Santos AM. Dentate gyrus-selective colchicine lesion and disruption of performance in spatial tasks: difficulties in "place strategy" because of a lack of flexibility in the use of environmental cues? Hippocampus. 1999;9(6):668-81.

205.     Kessels RP, de Haan EH, Kappelle LJ, Postma A. Varieties of human spatial memory: a meta-analysis on the effects of hippocampal lesions. Brain Research Reviews. 2001;35(3):295-303.

206.     Ekstrom AD, Kahana MJ, Caplan JB, Fields TA, Isham EA, Newman EL, et al. Cellular networks underlying human spatial navigation. Nature. 2003;425(6954):184-8.

207.     Doeller CF, Barry C, Burgess N. Evidence for grid cells in a human memory network. Nature. 2010;463(7281):657-61.

208.     Andrews-Zwilling Y, Gillespie AK, Kravitz AV, Nelson AB, Devidze N, Lo I, et al. Hilar GABAergic interneuron activity controls spatial learning and memory retrieval. PloS one. 2012;7(7):e40555.

209.     Yamamoto J, Suh J, Takeuchi D, Tonegawa S. Successful execution of working memory linked to synchronized high-frequency gamma oscillations. Cell. 2014;157(4):845-57.

210.     Maguire EA, Gadian DG, Johnsrude IS, Good CD, Ashburner J, Frackowiak RS, et al. Navigation-related structural change in the hippocampi of taxi drivers. Proceedings of the National Academy of Sciences of the United States of America. 2000;97(8):4398-403.

211.     Hartley T, Harlow R. An association between human hippocampal volume and topographical memory in healthy young adults. Frontiers in human neuroscience. 2012;6:338.

212.     Schinazi VR, Nardi D, Newcombe NS, Shipley TF, Epstein RA. Hippocampal size predicts rapid learning of a cognitive map in humans. Hippocampus. 2013;23(6):515-28.

213.     Hartley T, Maguire EA, Spiers HJ, Burgess N. The well-worn route and the path less traveled: distinct neural bases of route following and wayfinding in humans. Neuron. 2003;37(5):877-88.

214.     Marchette SA, Bakker A, Shelton AL. Cognitive mappers to creatures of habit: differential engagement of place and response learning mechanisms predicts human navigational behavior. The Journal of neuroscience : the official journal of the Society for Neuroscience. 2011;31(43):15264-8.

215.     Deacon RM, Bannerman DM, Rawlins NP. Conditional discriminations based on external and internal cues in rats with cytotoxic hippocampal lesions. Behavioral neuroscience. 2001;115(1):43-57.

216.     Dudchenko PA. How do animals actually solve the T maze? Behavioral neuroscience. 2001;115(4):850-60.

217.     Olton DS, Walker JA, Gage FH. Hippocampal connections and spatial discrimination. Brain research. 1978;139(2):295-308.

218.     Barnes CA. Memory deficits associated with senescence: a neurophysiological and behavioral study in the rat. Journal of comparative and physiological psychology. 1979;93(1):74-104.

219.     Morris R. Developments of a water-maze procedure for studying spatial learning in the rat. Journal of neuroscience methods. 1984;11(1):47-60.

220.     Lalonde R. The neurobiological basis of spontaneous alternation. Neuroscience and biobehavioral reviews. 2002;26(1):91-104.

221.     Deacon RM, Rawlins JN. T-maze alternation in the rodent. Nature protocols. 2006;1(1):7-12.

222.     Bromley-Brits K, Deng Y, Song W. Morris water maze test for learning and memory deficits in Alzheimer's disease model mice. Journal of visualized experiments : JoVE. 2011(53).

223.     Stewart S, Cacucci F, Lever C. Which memory task for my mouse? A systematic review of spatial memory performance in the Tg2576 Alzheimer's mouse model. J Alzheimers Dis. 2011;26(1):105-26.

224.     Pengas G, Patterson K, Arnold RJ, Bird CM, Burgess N, Nestor PJ. Lost and found: bespoke memory testing for Alzheimer's disease and semantic dementia. J Alzheimers Dis. 2010;21(4):1347-65.

225.     Chan D, Gallaher LM, Moodley K, Minati L, Burgess N, Hartley T. The 4 Mountains Test: A Short Test of Spatial Memory with High Sensitivity for the Diagnosis of Pre-dementia Alzheimer's Disease. Journal of visualized experiments : JoVE. 2016(116).

226.     Hartley T, Bird CM, Chan D, Cipolotti L, Husain M, Vargha-Khadem F, et al. The hippocampus is required for short-term topographical memory in humans. Hippocampus. 2007;17(1):34-48.

227.    Cushman LA, Stein K, Duffy CJ. Detecting navigational deficits in cognitive aging and Alzheimer disease using virtual reality. Neurology. 2008;71(12):888-95.

228.    Monacelli AM, Cushman LA, Kavcic V, Duffy CJ. Spatial disorientation in Alzheimer's disease: the remembrance of things passed. Neurology. 2003;61(11):1491-7.

229.    deIpolyi AR, Rankin KP, Mucke L, Miller BL, Gorno-Tempini ML. Spatial cognition and the human navigation network in AD and MCI. Neurology. 2007;69(10):986-97.

230.    Lee AC, Levi N, Davies RR, Hodges JR, Graham KS. Differing profiles of face and scene discrimination deficits in semantic dementia and Alzheimer's disease. Neuropsychologia. 2007;45(9):2135-46.

231.    Alescio-Lautier B, Michel BF, Herrera C, Elahmadi A, Chambon C, Touzet C, et al. Visual and visuospatial short-term memory in mild cognitive impairment and Alzheimer disease: role of attention. Neuropsychologia. 2007;45(8):1948-60.

232.    Laczo J, Andel R, Vlcek K, Macoska V, Vyhnalek M, Tolar M, et al. Spatial navigation and APOE in amnestic mild cognitive impairment. Neuro-degenerative diseases. 2011;8(4):169-77.

233.    Cherrier MM, Mendez M, Perryman K. Route learning performance in Alzheimer disease patients. Neuropsychiatry, neuropsychology, and behavioral neurology. 2001;14(3):159-68.

234.    Bird CM, Chan D, Hartley T, Pijnenburg YA, Rossor MN, Burgess N. Topographical short-term memory differentiates Alzheimer's disease from frontotemporal lobar degeneration. Hippocampus. 2010;20(10):1154-69.

235.    Moodley KK, Minati L, Contarino VE, Prioni S, Wood R, Cooper R, et al. Diagnostic differentiation of mild cognitive impairment due to Alzheimer's disease using a hippocampus-dependent test of spatial memory. Hippocampus. 2015.

236.    Nedelska Z, Andel R, Laczo J, Vlcek K, Horinek D, Lisy J, et al. Spatial navigation impairment is proportional to right hippocampal volume. Proceedings of the National Academy of Sciences of the United States of America. 2012;109(7):2590-4.

237.    Laczo J, Vlcek K, Vyhnalek M, Vajnerova O, Ort M, Holmerova I, et al. Spatial navigation testing discriminates two types of amnestic mild cognitive impairment. Behavioural brain research. 2009;202(2):252-9.

238.    Kalova E, Vlcek K, Jarolimova E, Bures J. Allothetic orientation and sequential ordering of places is impaired in early stages of Alzheimer's disease: corresponding results in real space tests and computer tests. Behavioural brain research. 2005;159(2):175-86.

239.    Morganti F, Stefanini S, Riva G. From allo- to egocentric spatial ability in early Alzheimer's disease: a study with virtual reality spatial tasks. Cognitive neuroscience. 2013;4(3-4):171-80.

240.    Pai MC, Yang YC. Impaired translation of spatial representation in young onset Alzheimer's disease patients. Current Alzheimer research. 2013;10(1):95-103.

241.    Hort J, Laczo J, Vyhnalek M, Bojar M, Bures J, Vlcek K. Spatial navigation deficit in amnestic mild cognitive impairment. Proceedings of the National Academy of Sciences of the United States of America. 2007;104(10):4042-7.

242.    Weniger G, Ruhleder M, Lange C, Wolf S, Irle E. Egocentric and allocentric memory as assessed by virtual reality in individuals with amnestic mild cognitive impairment. Neuropsychologia. 2011;49(3):518-27.

243.    Plancher G, Tirard A, Gyselinck V, Nicolas S, Piolino P. Using virtual reality to characterize episodic memory profiles in amnestic mild cognitive impairment and Alzheimer's disease: influence of active and passive encoding. Neuropsychologia. 2012;50(5):592-602.

244.    Bliss TV, Lomo T. Long-lasting potentiation of synaptic transmission in the dentate area of the anaesthetized rabbit following stimulation of the perforant path. The Journal of physiology. 1973;232(2):331-56.

245.    Bliss TV, Collingridge GL. A synaptic model of memory: long-term potentiation in the hippocampus. Nature. 1993;361(6407):31-9.

246.    Bir SC, Ambekar S, Kukreja S, Nanda A. Julius Caesar Arantius (Giulio Cesare Aranzi, 1530-1589) and the hippocampus of the human brain: history behind the discovery. Journal of neurosurgery. 2015;122(4):971-5.

247.    Engelhardt E. Hippocampus discovery First steps. Dementia & neuropsychologia. 2016;10(1):58-62.

248.    de Garengeot RJC. Splanchnologie ou l'anatomie des viscères: Ch. Osmont; 1742.

249.    Winsløw JB. Exposition anatomique de la structure du corps humain: Desprez, Desessartz; 1732.

250.    Iniesta I. On the origin of Ammon's horn. Neurologia (Barcelona, Spain). 2014;29(8):490-6.

251.    Herold C, Coppola VJ, Bingman VP. The maturation of research into the avian hippocampal formation: Recent discoveries from one of the nature's foremost navigators. Hippocampus. 2015;25(11):1193-211.

252.    Insausti R. Comparative anatomy of the entorhinal cortex and hippocampus in mammals. Hippocampus. 1993;3 Spec No:19-26.

253.    Amaral DG, Pierre L. Hippocampal neuroanatomy.  The hippocampus book: Oxford University Press; 2009.

254.    Strange BA, Witter MP, Lein ES, Moser EI. Functional organization of the hippocampal longitudinal axis. Nat Rev Neurosci. 2014;15(10):655-69.

255.    Amaral DG, Insausti R, Cowan WM. The commissural connections of the monkey hippocampal formation. The Journal of comparative neurology. 1984;224(3):307-36.

256.    Raisman G, Cowan W, Powell TJB. The extrinsic afferent, commissural and association fibres of the hippocampus. 1965;88(5):963-96.

257.    Daitz HM, Powell TP. Studies of the connexions of the fornix system. Journal of neurology, neurosurgery, and psychiatry. 1954;17(1):75-82.

258.    Powell TP, Guillery RW, Cowan WM. A quantitative study of the fornixmamillo-thalamic system. Journal of anatomy. 1957;91(4):419-37.

259.    Swanson LW, Cowan WM. Hippocampo-hypothalamic connections: origin in subicular cortex, not ammon's horn. Science (New York, NY). 1975;189(4199):303-4.

260.    Canteras NS, Swanson LW. Projections of the ventral subiculum to the amygdala, septum, and hypothalamus: a PHAL anterograde tract-tracing study in the rat. The Journal of comparative neurology. 1992;324(2):180-94.

261.    Cajal DSRYJAoS. Nueva Concepta De La Histologia De Los Centros Nervosos. 1893;18:122.

262.     Ramon y Cajal SJM, Paris. Histologie du système nerveux de l'homme et des vertébrés. 1911;2:153-73.

263.     Lorente de Nó RJJfPuN. Studies on the structure of the cerebral cortex. II. Continuation of the study of the ammonic system. 1934.

264.     Andersen P, Morris R, Amaral D, O'Keefe J, Bliss T. The hippocampus book: Oxford university press; 2007.

265.     Swanson LW, Kohler C. Anatomical evidence for direct projections from the entorhinal area to the entire cortical mantle in the rat. The Journal of neuroscience : the official journal of the Society for Neuroscience. 1986;6(10):3010-23.

266.     Andersen P, Bliss T, Skrede KKJEBR. Lamellar organization of hippocampal excitatory pathways. 1971;13(2):222-38.

267.     van Strien NM, Cappaert NL, Witter MP. The anatomy of memory: an interactive overview of the parahippocampal-hippocampal network. Nat Rev Neurosci. 2009;10(4):272-82.

268.     Felleman DJ, Van Essen DC. Distributed hierarchical processing in the primate cerebral cortex. Cerebral cortex (New York, NY : 1991). 1991;1(1):1-47.

269.     Deng W, Aimone JB, Gage FH. New neurons and new memories: how does adult hippocampal neurogenesis affect learning and memory? Nat Rev Neurosci. 2010;11(5):339-50.

270.     Witter MP, Doan TP, Jacobsen B, Nilssen ES, Ohara S. Architecture of the Entorhinal Cortex A Review of Entorhinal Anatomy in Rodents with Some Comparative Notes. Frontiers in systems neuroscience. 2017;11:46.

271.     Ramon y Cajal S. Sobre un ganglio especial de la corteza esfeno occipital. 1901.

272.     Fyhn M, Molden S, Witter MP, Moser EI, Moser MB. Spatial representation in the entorhinal cortex. Science (New York, NY). 2004;305(5688):1258-64.

273.     Canto CB, Wouterlood FG, Witter MPJNp. What does the anatomical organization of the entorhinal cortex tell us? 2008;2008.

274.     Witter MJS. Entorhinal cortex. 2011;6(10):4380.

275.     Brodmann K. Vergleichende Lokalisationslehre der Grosshirnrinde in ihren Prinzipien dargestellt auf Grund des Zellenbaues: Barth; 1909.

276.     Krieg WJ. Connections of the cerebral cortex. I. The albino rat. B. Structure of the cortical areas. Journal of Comparative Neurology. 1946;84(3):277-323.

277.     Witter MP, Wouterlood FG, Naber PA, Van Haeften TJAotNYAoS. Anatomical organization of the parahippocampal-hippocampal network. 2000;911(1):1-24.

278.     Burwell RD, Amaral DG. Cortical afferents of the perirhinal, postrhinal, and entorhinal cortices of the rat. The Journal of comparative neurology. 1998;398(2):179-205.

279.     Young BJ, Otto T, Fox GD, Eichenbaum H. Memory representation within the parahippocampal region. The Journal of neuroscience : the official journal of the Society for Neuroscience. 1997;17(13):5183-95.

280.     Dolorfo CL, Amaral DG. Entorhinal cortex of the rat: topographic organization of the cells of origin of the perforant path projection to the dentate gyrus. The Journal of comparative neurology. 1998;398(1):25-48.

281.     Witter MP. The perforant path: projections from the entorhinal cortex to the dentate gyrus. Progress in brain research. 2007;163:43-61.

282.     Amaral DG, Witter MP. The three-dimensional organization of the hippocampal formation: a review of anatomical data. Neuroscience. 1989;31(3):571-91.

283.     Amaral DG, Scharfman HE, Lavenex P. The dentate gyrus: fundamental neuroanatomical organization (dentate gyrus for dummies). Progress in brain research. 2007;163:3-790.

284.     Kaplan MS, Hinds JW. Neurogenesis in the adult rat: electron microscopic analysis of light radioautographs. Science (New York, NY). 1977;197(4308):1092-4.

285.     Blackstad TW, Brink K, Hem J, Jeune B. Distribution of hippocampal mossy fibers in the rat. An experimental study with silver impregnation methods. The Journal of comparative neurology. 1970;138(4):433-49.

286.     Claiborne BJ, Amaral DG, Cowan WM. A light and electron microscopic analysis of the mossy fibers of the rat dentate gyrus. The Journal of comparative neurology. 1986;246(4):435-58.

287.     Amaral DG, Dent JA. Development of the mossy fibers of the dentate gyrus: I. A light and electron microscopic study of the mossy fibers and their expansions. The Journal of comparative neurology. 1981;195(1):51-86.

288.     Freund TF, Buzsaki G. Interneurons of the hippocampus. Hippocampus. 1996;6(4):347-470.

289.     Hjorth-Simonsen A. Projection of the lateral part of the entorhinal area to the hippocampus and fascia dentata. Journal of Comparative Neurology. 1972;146(2):219-31.

290.     Hjorth-Simonsen A, Jeune B. Origin and termination of the hippocampal perforant path in the rat studied by silver impregnation. Journal of Comparative Neurology. 1972;144(2):215-31.

291.     Scharfman HE. Evidence from simultaneous intracellular recordings in rat hippocampal slices that area CA3 pyramidal cells innervate dentate hilar mossy cells. Journal of neurophysiology. 1994;72(5):2167-80.

292.     Soriano E, Frotscher M. Mossy cells of the rat fascia dentata are glutamate-immunoreactive. Hippocampus. 1994;4(1):65-9.

293.     Kohara K, Pignatelli M, Rivest AJ, Jung HY, Kitamura T, Suh J, et al. Cell type-specific genetic and optogenetic tools reveal hippocampal CA2 circuits. Nature neuroscience. 2014;17(2):269-79.

294.     Swanson LW, Wyss JM, Cowan WM. An autoradiographic study of the organization of intrahippocampal association pathways in the rat. The Journal of comparative neurology. 1978;181(4):681-715.

295.     Hjorth-Simonsen A. Some intrinsic connections of the hippocampus in the rat: an experimental analysis. The Journal of comparative neurology. 1973;147(2):145-61.

296.     Chevaleyre V, Siegelbaum SA. Strong CA2 pyramidal neuron synapses define a powerful disynaptic cortico-hippocampal loop. Neuron. 2010;66(4):560-72.

297.     Kitamura T, Pignatelli M, Suh J, Kohara K, Yoshiki A, Abe K, et al. Island cells control temporal association memory. Science (New York, NY). 2014;343(6173):896-901.

298.     Amaral DG, Dolorfo C, Alvarez-Royo P. Organization of CA1 projections to the subiculum: a PHA-L analysis in the rat. Hippocampus. 1991;1(4):415-35.

299.     Surmeli G, Marcu DC, McClure C, Garden DLF, Pastoll H, Nolan MF. Molecularly Defined Circuitry Reveals Input-Output Segregation in Deep Layers of the Medial Entorhinal Cortex. Neuron. 2015;88(5):1040-53.

300.     Amaral D, Witter M. Hippocampal formation: in the rat nervous system. Ed. Paxinos G. Academic Press; 1995.

301.     Witter MP, Groenewegen HJ. The subiculum: cytoarchitectonically a simple structure, but hodologically complex. Progress in brain research. 1990;83:47-58.

302.     O'Mara SM, Commins S, Anderson M, Gigg J. The subiculum: a review of form, physiology and function. Progress in neurobiology. 2001;64(2):129-55.

303.     Baks-Te Bulte L, Wouterlood FG, Vinkenoog M, Witter MP. Entorhinal projections terminate onto principal neurons and interneurons in the subiculum: a quantitative electron microscopical analysis in the rat. Neuroscience. 2005;136(3):729-39.

304.     Verwer RW, Meijer RJ, Van Uum HF, Witter MP. Collateral projections from the rat hippocampal formation to the lateral and medial prefrontal cortex. Hippocampus. 1997;7(4):397-402.

305.     Pitkanen A, Pikkarainen M, Nurminen N, Ylinen A. Reciprocal connections between the amygdala and the hippocampal formation, perirhinal cortex, and postrhinal cortex in rat. A review. Annals of the New York Academy of Sciences. 2000;911:369-91.

306.     Furtak SC, Wei SM, Agster KL, Burwell RD. Functional neuroanatomy of the parahippocampal region in the rat: the perirhinal and postrhinal cortices. Hippocampus. 2007;17(9):709-22.

307.     Kohler C. Intrinsic projections of the retrohippocampal region in the rat brain. I. The subicular complex. The Journal of comparative neurology. 1985;236(4):504-22.

308.     Caballero-Bleda M, Witter MP. Regional and laminar organization of projections from the presubiculum and parasubiculum to the entorhinal cortex: an anterograde tracing study in the rat. The Journal of comparative neurology. 1993;328(1):115-29.

309.     Canto CB, Witter MP. Cellular properties of principal neurons in the rat entorhinal cortex. II. The medial entorhinal cortex. Hippocampus. 2012;22(6):1277-99.

310.     Buzsáki G, Anastassiou CA, Koch C. The origin of extracellular fields and currents — EEG, ECoG, LFP and spikes. Nat Rev Neurosci. 2012 May 18;13(6):407-20.

311.     Green JD, Arduini AA. Hippocampal electrical activity in arousal. Journal of neurophysiology. 1954;17(6):533-57.

312.     Jung R, Kornmüller AE. Eine methodik der ableitung iokalisierter potentialschwankungen aus subcorticalen hirngebieten. Archiv für Psychiatrie und Nervenkrankheiten. 1938;109(1):1-30.

313.     Whishaw IQ, Vanderwolf CH. Hippocampal EEG and behavior: changes in amplitude and frequency of RSA (theta rhythm) associated with spontaneous and learned movement patterns in rats and cats. Behav Biol. 1973;8(4):461-84.

314.     Sławińska U, Kasicki S. The frequency of rat's hippocampal theta rhythm is related to the speed of locomotion. Brain research. 1998;796(1-2):327-31.

315.     Jeewajee A, Lever C, Burton S, O'Keefe J, Burgess N. Environmental novelty is signaled by reduction of the hippocampal theta frequency. Hippocampus. 2008;18(4):340-8.

316.    Mitchell SJ, Ranck JB, Jr. Generation of theta rhythm in medial entorhinal cortex of freely moving rats. Brain research. 1980;189(1):49-66.

317.    Borst JG, Leung LW, MacFabe DF. Electrical activity of the cingulate cortex. II. Cholinergic modulation. Brain research. 1987;407(1):81-93.

318.    Paré D, Collins DR. Neuronal correlates of fear in the lateral amygdala: multiple extracellular recordings in conscious cats. The Journal of neuroscience : the official journal of the Society for Neuroscience. 2000;20(7):2701-10.

319.    Buzsáki G. Theta oscillations in the hippocampus. Neuron. 2002;33(3):325-40.

320.    Petsche H, Stumpf C. [The origin of theta-rhytm in the rabbit hippocampus]. Wien Klin Wochenschr. 1962;74:696-700.

321.    Bland BH, Bird J, Jackson J, Natsume K. Medial septal modulation of the ascending brainstem hippocampal synchronizing pathways in the freely moving rat. Hippocampus. 2006;16(1):11-9.

322.    Vanderwolf CH, Leung LW, Cooley RK. Pathways through cingulate, neo- and entorhinal cortices mediate atropine-resistant hippocampal rhythmical slow activity. Brain research. 1985;347(1):58-73.

323.    Bullock TH, Buzsáki G, McClune MC. Coherence of compound field potentials reveals discontinuities in the CA1-subiculum of the hippocampus in freely-moving rats. Neuroscience. 1990;38(3):609-19.

324.    Lubenov EV, Siapas AG. Hippocampal theta oscillations are travelling waves. Nature. 2009;459(7246):534-9.

325.    Grastyán E, Karmos G, Vereczkey L, Kellényi L. The hippocampal electrical correlates of the homeostatic regulation of motivation. Electroencephalogr Clin Neurophysiol. 1966;21(1):34-53.

326.    Jensen O, Lisman JE. An oscillatory short-term memory buffer model can account for data on the Sternberg task. The Journal of neuroscience : the official journal of the Society for Neuroscience. 1998;18(24):10688-99.

327.    Sainsbury RS. Hippocampal theta: a sensory-inhibition theory of function. Neuroscience and biobehavioral reviews. 1998;22(2):237-41.

328.    Bland BH, Oddie SD. Theta band oscillation and synchrony in the hippocampal formation and associated structures: the case for its role in sensorimotor integration. Behavioural brain research. 2001;127(1-2):119-36.

329.    Buzsáki G, Draguhn A. Neuronal oscillations in cortical networks. Science (New York, NY). 2004;304(5679):1926-9.

330.    O'Keefe J, Recce ML. Phase relationship between hippocampal place units and the EEG theta rhythm. Hippocampus. 1993;3(3):317-30.

331.    Hyman JM, Wyble BP, Goyal V, Rossi CA, Hasselmo ME. Stimulation in hippocampal region CA1 in behaving rats yields long-term potentiation when delivered to the peak of theta and long-term depression when delivered to the trough. The Journal of neuroscience : the official journal of the Society for Neuroscience. 2003;23(37):11725-31.

332.    Bragin A, Jandó G, Nádasdy Z, Hetke J, Wise K, Buzsáki G. Gamma (40-100 Hz) oscillation in the hippocampus of the behaving rat. The Journal of neuroscience : the official journal of the Society for Neuroscience. 1995;15(1 Pt 1):47-60.

333.    Buzsáki G. Hippocampal sharp waves: their origin and significance. Brain research. 1986;398(2):242-52.

334.    Vanderwolf CH. Hippocampal electrical activity and voluntary movement in the rat. Electroencephalography and Clinical Neurophysiology. 1969;26(4):407-18.

335.    O'Keefe J. Place units in the hippocampus of the freely moving rat. Experimental neurology. 1976;51(1):78-109.

336.    Buzsáki G, Leung LW, Vanderwolf CH. Cellular bases of hippocampal EEG in the behaving rat. Brain research. 1983;287(2):139-71.

337.    Freemon FR, Walter RD. Electrical activity of human limbic system during sleep. Compr Psychiatry. 1970;11(6):544-51.

338.    Suzuki SS, Smith GK. Single-cell activity and synchronous bursting in the rat hippocampus during waking behavior and sleep. Experimental neurology. 1985;89(1):71-89.

339.    Wilson MA, McNaughton BL. Dynamics of the hippocampal ensemble code for space. Science (New York, NY). 1993;261(5124):1055-8.

340.    Ranck JB, Jr. Studies on single neurons in dorsal hippocampal formation and septum in unrestrained rats. I. Behavioral correlates and firing repertoires. Experimental neurology. 1973;41(2):461-531.

341.    Muller R. A quarter of a century of place cells. Neuron. 1996;17(5):813-22.

342.    Olton DS, Branch M, Best PJ. Spatial correlates of hippocampal unit activity. Experimental neurology. 1978;58(3):387-409.

343.    McHugh TJ, Blum KI, Tsien JZ, Tonegawa S, Wilson MA. Impaired hippocampal representation of space in CA1-specific NMDAR1 knockout mice. Cell. 1996;87(7):1339-49.

344.    Ulanovsky N, Moss CF. Hippocampal cellular and network activity in freely moving echolocating bats. Nature neuroscience. 2007;10(2):224-33.

345.    Ludvig N, Tang HM, Gohil BC, Botero JM. Detecting location-specific neuronal firing rate increases in the hippocampus of freely-moving monkeys. Brain research. 2004;1014(1-2):97-109.

346.    Hartley T, Lever C, Burgess N, O'Keefe J. Space in the brain: how the hippocampal formation supports spatial cognition. Philosophical transactions of the Royal Society of London Series B, Biological sciences. 2014;369(1635):20120510.

347.    Fenton AA, Kao HY, Neymotin SA, Olypher A, Vayntrub Y, Lytton WW, et al. Unmasking the CA1 ensemble place code by exposures to small and large environments: more place cells and multiple, irregularly arranged, and expanded place fields in the larger space. The Journal of neuroscience : the official journal of the Society for Neuroscience. 2008;28(44):11250-62.

348.    Zhang K, Ginzburg I, McNaughton BL, Sejnowski TJ. Interpreting neuronal population activity by reconstruction: unified framework with application to hippocampal place cells. Journal of neurophysiology. 1998;79(2):1017-44.

349.    Redish AD, Battaglia FP, Chawla MK, Ekstrom AD, Gerrard JL, Lipa P, et al. Independence of firing correlates of anatomically proximate hippocampal pyramidal cells. The Journal of neuroscience : the official journal of the Society for Neuroscience. 2001;21(5):Rc134.

350.    Jung MW, Wiener SI, McNaughton BL. Comparison of spatial firing characteristics of units in dorsal and ventral hippocampus of the rat. The Journal of neuroscience : the official journal of the Society for Neuroscience. 1994;14(12):7347-56.

351.    Kjelstrup KB, Solstad T, Brun VH, Hafting T, Leutgeb S, Witter MP, et al. Finite scale of spatial representation in the hippocampus. Science (New York, NY). 2008;321(5885):140-3.

352.    Hill AJ. First occurrence of hippocampal spatial firing in a new environment. Experimental neurology. 1978;62(2):282-97.

353.    Thompson LT, Best PJ. Long-term stability of the place-field activity of single units recorded from the dorsal hippocampus of freely behaving rats. Brain research. 1990;509(2):299-308.

354.    Ziv Y, Burns LD, Cocker ED, Hamel EO, Ghosh KK, Kitch LJ, et al. Long-term dynamics of CA1 hippocampal place codes. Nature neuroscience. 2013;16(3):264-6.

355.    Thompson LT, Best PJ. Place cells and silent cells in the hippocampus of freely-behaving rats. The Journal of neuroscience : the official journal of the Society for Neuroscience. 1989;9(7):2382-90.

356.    Huxter J, Burgess N, O'Keefe J. Independent rate and temporal coding in hippocampal pyramidal cells. Nature. 2003;425(6960):828-32.

357.    Harris KD, Hirase H, Leinekugel X, Henze DA, Buzsáki G. Temporal interaction between single spikes and complex spike bursts in hippocampal pyramidal cells. Neuron. 2001;32(1):141-9.

358.    Huxter JR, Senior TJ, Allen K, Csicsvari J. Theta phase-specific codes for two-dimensional position, trajectory and heading in the hippocampus. Nature neuroscience. 2008;11(5):587-94.

359.    Skaggs WE, McNaughton BL, Wilson MA, Barnes CA. Theta phase precession in hippocampal neuronal populations and the compression of temporal sequences. Hippocampus. 1996;6(2):149-72.

360.    Quirk GJ, Muller RU, Kubie JL. The firing of hippocampal place cells in the dark depends on the rat's recent experience. The Journal of neuroscience : the official journal of the Society for Neuroscience. 1990;10(6):2008-17.

361.    Lever C, Wills T, Cacucci F, Burgess N, O'Keefe J. Long-term plasticity in hippocampal place-cell representation of environmental geometry. Nature. 2002;416(6876):90-4.

362.    Anderson MI, Jeffery KJ. Heterogeneous modulation of place cell firing by changes in context. The Journal of neuroscience : the official journal of the Society for Neuroscience. 2003;23(26):8827-35.

363.    Leutgeb S, Leutgeb JK, Barnes CA, Moser EI, McNaughton BL, Moser MB. Independent codes for spatial and episodic memory in hippocampal neuronal ensembles. Science (New York, NY). 2005;309(5734):619-23.

364.    Knierim JJ, Kudrimoti HS, McNaughton BL. Place cells, head direction cells, and the learning of landmark stability. The Journal of neuroscience : the official journal of the Society for Neuroscience. 1995;15(3 Pt 1):1648-59.

365.    Hetherington PA, Shapiro ML. Hippocampal place fields are altered by the removal of single visual cues in a distance-dependent manner. Behavioral neuroscience. 1997;111(1):20-34.

366.     Fenton AA, Csizmadia G, Muller RU. Conjoint control of hippocampal place cell firing by two visual stimuli. I. The effects of moving the stimuli on firing field positions. J Gen Physiol. 2000;116(2):191-209.

367.     Jeffery KJ, Donnett JG, Burgess N, O'Keefe JM. Directional control of hippocampal place fields. Experimental brain research Experimentelle Hirnforschung Experimentation cerebrale. 1997;117(1):131-42.

368.     Jeffery KJ, O'Keefe JM. Learned interaction of visual and idiothetic cues in the control of place field orientation. Experimental brain research Experimentelle Hirnforschung Experimentation cerebrale. 1999;127(2):151-61.

369.     Barry C, Lever C, Hayman R, Hartley T, Burton S, O'Keefe J, et al. The boundary vector cell model of place cell firing and spatial memory. Reviews in the neurosciences. 2006;17(1-2):71-97.

370.     Markus EJ, Qin YL, Leonard B, Skaggs WE, McNaughton BL, Barnes CA. Interactions between location and task affect the spatial and directional firing of hippocampal neurons. The Journal of neuroscience : the official journal of the Society for Neuroscience. 1995;15(11):7079-94.

371.     Zinyuk L, Kubik S, Kaminsky Y, Fenton AA, Bures J. Understanding hippocampal activity by using purposeful behavior: place navigation induces place cell discharge in both task-relevant and task-irrelevant spatial reference frames. Proceedings of the National Academy of Sciences of the United States of America. 2000;97(7):3771-6.

372.     Lenck-Santini PP, Muller RU, Save E, Poucet B. Relationships between place cell firing fields and navigational decisions by rats. The Journal of neuroscience : the official journal of the Society for Neuroscience. 2002;22(20):9035-47.

373.     Cressant A, Muller RU, Poucet B. Failure of centrally placed objects to control the firing fields of hippocampal place cells. The Journal of neuroscience : the official journal of the Society for Neuroscience. 1997;17(7):2531-42.

374.     Cressant A, Muller RU, Poucet B. Further study of the control of place cell firing by intra-apparatus objects. Hippocampus. 1999;9(4):423-31.

375.     Shapiro ML, Tanila H, Eichenbaum H. Cues that hippocampal place cells encode: dynamic and hierarchical representation of local and distal stimuli. Hippocampus. 1997;7(6):624-42.

376.     Tanila H, Shapiro ML, Eichenbaum H. Discordance of spatial representation in ensembles of hippocampal place cells. Hippocampus. 1997;7(6):613-23.

377.     Knierim JJ. Dynamic interactions between local surface cues, distal landmarks, and intrinsic circuitry in hippocampal place cells. The Journal of neuroscience : the official journal of the Society for Neuroscience. 2002;22(14):6254-64.

378.     Renaudineau S, Poucet B, Save E. Flexible use of proximal objects and distal cues by hippocampal place cells. Hippocampus. 2007;17(5):381-95.

379.     Knierim JJ, Rao G. Distal landmarks and hippocampal place cells: effects of relative translation versus rotation. Hippocampus. 2003;13(5):604-17.

380.     Siegel JJ, Neunuebel JP, Knierim JJ. Dominance of the proximal coordinate frame in determining the locations of hippocampal place cell activity during navigation. Journal of neurophysiology. 2008;99(1):60-76.

381.     Save E, Cressant A, Thinus-Blanc C, Poucet B. Spatial firing of hippocampal place cells in blind rats. The Journal of neuroscience : the official journal of the Society for Neuroscience. 1998;18(5):1818-26.

382.    Save E, Nerad L, Poucet B. Contribution of multiple sensory information to place field stability in hippocampal place cells. Hippocampus. 2000;10(1):64-76.

383.    Zhang S, Manahan-Vaughan D. Spatial olfactory learning contributes to place field formation in the hippocampus. Cerebral cortex (New York, NY : 1991). 2015;25(2):423-32.

384.    Roy V, Menant O, Hacquemand R, Vallier C, Ensch E, Rovira K, et al. A case of visuo-auditory sensory substitution in rats. Behav Processes. 2019;164:157-66.

385.    Gener T, Perez-Mendez L, Sanchez-Vives MV. Tactile modulation of hippocampal place fields. Hippocampus. 2013;23(12):1453-62.

386.    Rossier J, Haeberli C, Schenk F. Auditory cues support place navigation in rats when associated with a visual cue. Behavioural brain research. 2000;117(1-2):209-14.

387.    Mittelstaedt H. A new solution to the problem of the subjective vertical. Naturwissenschaften. 1983;70(6):272-81.

388.    Cohen HS. Vestibular disorders and impaired path integration along a linear trajectory. J Vestib Res. 2000;10(1):7-15.

389.    Stackman RW, Clark AS, Taube JS. Hippocampal spatial representations require vestibular input. Hippocampus. 2002;12(3):291-303.

390.    Wallace DG, Hines DJ, Pellis SM, Whishaw IQ. Vestibular information is required for dead reckoning in the rat. The Journal of neuroscience : the official journal of the Society for Neuroscience. 2002;22(22):10009-17.

391.    McNaughton BL, Barnes CA, O'Keefe J. The contributions of position, direction, and velocity to single unit activity in the hippocampus of freely-moving rats. Experimental brain research Experimentelle Hirnforschung Experimentation cerebrale. 1983;52(1):41-9.

392.    Gothard KM, Skaggs WE, McNaughton BL. Dynamics of mismatch correction in the hippocampal ensemble code for space: interaction between path integration and environmental cues. The Journal of neuroscience : the official journal of the Society for Neuroscience. 1996;16(24):8027-40.

393.    Sharp PE, Blair HT, Etkin D, Tzanetos DB. Influences of vestibular and visual motion information on the spatial firing patterns of hippocampal place cells. The Journal of neuroscience : the official journal of the Society for Neuroscience. 1995;15(1 Pt 1):173-89.

394.    Wiener SI, Korshunov VA, Garcia R, Berthoz A. Inertial, substratal and landmark cue control of hippocampal CA1 place cell activity. The European journal of neuroscience. 1995;7(11):2206-19.

395.    Russell NA, Horii A, Smith PF, Darlington CL, Bilkey DK. Long-term effects of permanent vestibular lesions on hippocampal spatial firing. The Journal of neuroscience : the official journal of the Society for Neuroscience. 2003;23(16):6490-8.

396.    Russell NA, Horii A, Smith PF, Darlington CL, Bilkey DK. Lesions of the vestibular system disrupt hippocampal theta rhythm in the rat. Journal of neurophysiology. 2006;96(1):4-14.

397.    Pastalkova E, Itskov V, Amarasingham A, Buzsaki G. Internally generated cell assembly sequences in the rat hippocampus. Science (New York, NY). 2008;321(5894):1322-7.

398.	Chen G, Lu Y, King JA, Cacucci F, Burgess N. Differential influences of environment and self-motion on place and grid cell firing. Nat Commun. 2019;10(1):630.

399.	Chen G, King JA, Burgess N, O'Keefe J. How vision and movement combine in the hippocampal place code. Proceedings of the National Academy of Sciences of the United States of America. 2013;110(1):378-83.

400.	Rich PD, Liaw HP, Lee AK. Place cells. Large environments reveal the statistical structure governing hippocampal representations. Science (New York, NY). 2014;345(6198):814-7.

401.	O'Keefe J, Burgess N. Geometric determinants of the place fields of hippocampal neurons. Nature. 1996;381(6581):425-8.

402.	Muller RU, Bostock E, Taube JS, Kubie JL. On the directional firing properties of hippocampal place cells. The Journal of neuroscience : the official journal of the Society for Neuroscience. 1994;14(12):7235-51.

403.	Battaglia FP, Sutherland GR, McNaughton BL. Local sensory cues and place cell directionality: additional evidence of prospective coding in the hippocampus. The Journal of neuroscience : the official journal of the Society for Neuroscience. 2004;24(19):4541-50.

404.	Wood ER, Dudchenko PA, Robitsek RJ, Eichenbaum H. Hippocampal neurons encode information about different types of memory episodes occurring in the same location. Neuron. 2000;27(3):623-33.

405.	Frank LM, Brown EN, Wilson M. Trajectory encoding in the hippocampus and entorhinal cortex. Neuron. 2000;27(1):169-78.

406.	Cheng S, Frank LM. New experiences enhance coordinated neural activity in the hippocampus. Neuron. 2008;57(2):303-13.

407.	Mehta MR, Barnes CA, McNaughton BL. Experience-dependent, asymmetric expansion of hippocampal place fields. Proceedings of the National Academy of Sciences of the United States of America. 1997;94(16):8918-21.

408.	Mehta MR, Quirk MC, Wilson MA. Experience-dependent asymmetric shape of hippocampal receptive fields. Neuron. 2000;25(3):707-15.

409.	Lee I, Knierim JJ. The relationship between the field-shifting phenomenon and representational coherence of place cells in CA1 and CA3 in a cue-altered environment. Learn Mem. 2007;14(11):807-15.

410.	Schmidt R, Diba K, Leibold C, Schmitz D, Buzsáki G, Kempter R. Single-trial phase precession in the hippocampus. The Journal of neuroscience : the official journal of the Society for Neuroscience. 2009;29(42):13232-41.

411.	Hok V, Lenck-Santini PP, Roux S, Save E, Muller RU, Poucet B. Goal-related activity in hippocampal place cells. The Journal of neuroscience : the official journal of the Society for Neuroscience. 2007;27(3):472-82.

412.	Gauthier JL, Tank DW. A Dedicated Population for Reward Coding in the Hippocampus. Neuron. 2018;99(1):179-93.e7.

413.	Omer DB, Maimon SR, Las L, Ulanovsky N. Social place-cells in the bat hippocampus. Science (New York, NY). 2018;359(6372):218-24.

414.	MacDonald CJ, Lepage KQ, Eden UT, Eichenbaum H. Hippocampal "time cells" bridge the gap in memory for discontiguous events. Neuron. 2011;71(4):737-49.

415.    O'Keefe J, Krupic J. Do hippocampal pyramidal cells respond to non-spatial stimuli? Physiol Rev. 2021.

416.    Buzsáki G, Horváth Z, Urioste R, Hetke J, Wise K. High-frequency network oscillation in the hippocampus. Science (New York, NY). 1992;256(5059):1025-7.

417.    Wilson MA, McNaughton BL. Reactivation of hippocampal ensemble memories during sleep. Science (New York, NY). 1994;265(5172):676-9.

418.    Morris RG. D.O. Hebb: The Organization of Behavior, Wiley: New York; 1949. Brain Res Bull. 1999;50(5-6):437.

419.    Foster DJ, Wilson MA. Reverse replay of behavioural sequences in hippocampal place cells during the awake state. Nature. 2006;440(7084):680-3.

420.    Ólafsdóttir HF, Bush D, Barry C. The Role of Hippocampal Replay in Memory and Planning. Current biology : CB. 2018;28(1):R37-r50.

421.    Dragoi G, Tonegawa S. Preplay of future place cell sequences by hippocampal cellular assemblies. Nature. 2011;469(7330):397-401.

422.    Johnson A, Redish AD. Neural ensembles in CA3 transiently encode paths forward of the animal at a decision point. The Journal of neuroscience : the official journal of the Society for Neuroscience. 2007;27(45):12176-89.

423.    Foster DJ, Wilson MA. Hippocampal theta sequences. Hippocampus. 2007;17(11):1093-9.

424.    Klausberger T, Somogyi P. Neuronal diversity and temporal dynamics: the unity of hippocampal circuit operations. Science (New York, NY). 2008;321(5885):53-7.

425.    Huh CY, Amilhon B, Ferguson KA, Manseau F, Torres-Platas SG, Peach JP, et al. Excitatory Inputs Determine Phase-Locking Strength and Spike-Timing of CA1 Stratum Oriens/Alveus Parvalbumin and Somatostatin Interneurons during Intrinsically Generated Hippocampal Theta Rhythm. The Journal of neuroscience : the official journal of the Society for Neuroscience. 2016;36(25):6605-22.

426.    Csicsvari J, Hirase H, Czurkó A, Mamiya A, Buzsáki G. Fast network oscillations in the hippocampal CA1 region of the behaving rat. The Journal of neuroscience : the official journal of the Society for Neuroscience. 1999;19(16):Rc20.

427.    Montgomery SM, Sirota A, Buzsáki G. Theta and gamma coordination of hippocampal networks during waking and rapid eye movement sleep. The Journal of neuroscience : the official journal of the Society for Neuroscience. 2008;28(26):6731-41.

428.    Navas-Olive A, Valero M, Jurado-Parras T, de Salas-Quiroga A, Averkin RG, Gambino G, et al. Multimodal determinants of phase-locked dynamics across deep-superficial hippocampal sublayers during theta oscillations. Nat Commun. 2020;11(1):2217.

429.    Hafting T, Fyhn M, Bonnevie T, Moser MB, Moser EI. Hippocampus-independent phase precession in entorhinal grid cells. Nature. 2008;453(7199):1248-52.

430.    Burgess N, O'Keefe J. Models of place and grid cell firing and theta rhythmicity. Curr Opin Neurobiol. 2011;21(5):734-44.

431.    Maurer AP, Cowen SL, Burke SN, Barnes CA, McNaughton BL. Phase precession in hippocampal interneurons showing strong functional coupling to individual pyramidal cells. The Journal of neuroscience : the official journal of the Society for Neuroscience. 2006;26(52):13485-92.

432.     Zugaro MB, Monconduit L, Buzsáki G. Spike phase precession persists after transient intrahippocampal perturbation. Nature neuroscience. 2005;8(1):67-71.

433.     Zipser D. A computational model of hippocampal place fields. Behavioral neuroscience. 1985;99(5):1006-18.

434.     Sharp PE. Computer simulation of hippocampal place cells. Psychobiology. 1991;19(2):103-15.

435.     Hartley T, Burgess N, Lever C, Cacucci F, O'Keefe J. Modeling place fields in terms of the cortical inputs to the hippocampus. Hippocampus. 2000;10(4):369-79.

436.     Burgess N, Jackson A, Hartley T, O'Keefe J. Predictions derived from modelling the hippocampal role in navigation. Biol Cybern. 2000;83(3):301-12.

437.     Bird CM, Bisby JA, Burgess N. The hippocampus and spatial constraints on mental imagery. Frontiers in human neuroscience. 2012;6:142.

438.     Samsonovich, A. and B.L. McNaughton. Path integration and cognitive mapping in a continuous attractor neural network model. J Neurosci. 1997. 17(15): p. 5900-20.

439.     McNaughton BL, Barnes CA, Gerrard JL, Gothard K, Jung MW, Knierim JJ, et al. Deciphering the hippocampal polyglot: the hippocampus as a path integration system. J Exp Biol. 1996;199(Pt 1):173-85.

440.     McNaughton BL, Battaglia FP, Jensen O, Moser EI, Moser MB. Path integration and the neural basis of the 'cognitive map'. Nat Rev Neurosci. 2006;7(8):663-78.

441.     Drieu C, Zugaro M. Hippocampal Sequences During Exploration: Mechanisms and Functions. Front Cell Neurosci. 2019;13:232.

442.     Cacucci F, Lever C, Wills TJ, Burgess N, O'Keefe J. Theta-modulated place-by-direction cells in the hippocampal formation in the rat. The Journal of neuroscience : the official journal of the Society for Neuroscience. 2004;24(38):8265-77.

443.     Lengyel M, Szatmary Z, Erdi P. Dynamically detuned oscillations account for the coupled rate and temporal code of place cell firing. Hippocampus. 2003;13(6):700-14.

444.     Boccara CN, Kjonigsen LJ, Hammer IM, Bjaalie JG, Leergaard TB, Witter MP. A three-plane architectonic atlas of the rat hippocampal region. Hippocampus. 2015;25(7):838-57.

445.     Fyhn M, Hafting T, Witter MP, Moser EI, Moser MB. Grid cells in mice. Hippocampus. 2008;18(12):1230-8.

446.     Barry C, Hayman R, Burgess N, Jeffery KJ. Experience-dependent rescaling of entorhinal grids. Nature neuroscience. 2007;10(6):682-4.

447.     Stensola H, Stensola T, Solstad T, Frøland K, Moser MB, Moser EI. The entorhinal grid map is discretized. Nature. 2012;492(7427):72-8.

448.     Moser EI, Roudi Y, Witter MP, Kentros C, Bonhoeffer T, Moser MB. Grid cells and cortical representation. Nat Rev Neurosci. 2014;15(7):466-81.

449.     Moser EI, Moser MB. A metric for space. Hippocampus. 2008;18(12):1142-56.

450.     Barry C, Ginzberg LL, O'Keefe J, Burgess N. Grid cell firing patterns signal environmental novelty by expansion. Proceedings of the National Academy of Sciences of the United States of America. 2012;109(43):17687-92.

451.     Krupic J, Bauza M, Burton S, Barry C, O'Keefe J. Grid cell symmetry is shaped by environmental geometry. Nature. 2015;518(7538):232-5.

452.    Solstad T, Boccara CN, Kropff E, Moser MB, Moser EI. Representation of geometric borders in the entorhinal cortex. Science (New York, NY). 2008;322(5909):1865-8.

453.    Stewart S, Jeewajee A, Wills TJ, Burgess N, Lever C. Boundary coding in the rat subiculum. Philosophical transactions of the Royal Society of London Series B, Biological sciences. 2014;369(1635):20120514.

454.    Kadir SN, Goodman DF, Harris KD. High-dimensional cluster analysis with the masked EM algorithm. Neural Comput. 2014;26(11):2379-94.

455.    Schneider CA, Rasband WS, Eliceiri KW. NIH Image to ImageJ: 25 years of image analysis. Nat Methods. 2012;9(7):671-5.

456.    Science AIfB. Allen Mouse Brain Atlas https://mouse.brain-map.org/experiment/thumbnails/100048576?image_type=atlas2004

457.    Morris RG. Spatial localization does not require the presence of local cues. Learning and motivation. 1981;12(2):239-60.

458.    Hollup SA, Molden S, Donnett JG, Moser MB, Moser EI. Place fields of rat hippocampal pyramidal cells and spatial learning in the watermaze. The European journal of neuroscience. 2001;13(6):1197-208.

459.    Pinnell RC, Almajidy RK, Kirch RD, Cassel JC, Hofmann UG. A Wireless EEG Recording Method for Rat Use inside the Water Maze. PloS one. 2016;11(2):e0147730.

460.    Hull CL. The goal-gradient hypothesis and maze learning. Psychological Review. 1932;39(1):25.

461.    Dashiell JF. Direction orientation in maze running by the white rat. Comparative Psychology Monographs. 1930.

462.    Sutherland RJ, Whishaw IQ, Kolb B. A behavioural analysis of spatial localization following electrolytic, kainate- or colchicine-induced damage to the hippocampal formation in the rat. Behavioural brain research. 1983;7(2):133-53.

463.    Hales JB, Schlesiger MI, Leutgeb JK, Squire LR, Leutgeb S, Clark RE. Medial entorhinal cortex lesions only partially disrupt hippocampal place cells and hippocampus-dependent place memory. Cell Rep. 2014;9(3):893-901.

464.    Parron C, Save E. Evidence for entorhinal and parietal cortices involvement in path integration in the rat. Experimental Brain Research. 2004;159(3):349-59.

465.    Steffenach HA, Witter M, Moser MB, Moser EI. Spatial memory in the rat requires the dorsolateral band of the entorhinal cortex. Neuron. 2005;45(2):301-13.

466.    Ormond J, O'Keefe J. Hippocampal place cells use vector computations to navigate. bioRxiv. 2021:2021.06.23.449621.

468.    Paul C-M, Magda G, Abel S. Spatial memory: Theoretical basis and comparative review on experimental methods in rodents. Behavioural brain research. 2009;203(2):151-64.

469.    Spence KW. The order of eliminating blinds in maze learning by the rat. Journal of Comparative Psychology. 1932;14(1):9.

470.    Lashley K. The criterion of learning in experiments with the maze. Jour Animal Behav. 1917;7:66-70.

471.    Hubbert HB, Lashley K. Retroactive association and the elimination of errors in the maze. Journal of Animal Behavior. 1917;7(2):130-8.

472.     Yoshioka JG. Direction as a factor in maze solution in rats. The Pedagogical Seminary and Journal of Genetic Psychology. 1930;38(1-4):307-20.

473.     Gengerelli JA. The principle of maxima and minima in animal learning. Journal of Comparative Psychology. 1930;11(2):193.

474.     Tolman EC, Honzik CH. Degrees of hunger, reward and non-reward, and maze learning in rats. University of California Publications in Psychology. 1930.

475.     Carr H. The distribution and elimination of errors in the maze. Journal of Animal Behavior. 1917.

476.     Peterson J. The effect of length of blind alleys on maze learning: an experiment on twenty-four white rats: H. Holt; 1917.

477.     O'Keefe J. In: Bloom P, editor. Language and Space Oxford University Press; 1991. p. 273-95.

478.     Schenk F, Morris RG. Dissociation between components of spatial memory in rats after recovery from the effects of retrohippocampal lesions. Experimental brain research Experimentelle Hirnforschung Experimentation cerebrale. 1985;58(1):11-28.

479.     Nagahara AH, Otto T, Gallagher M. Entorhinal-perirhinal lesions impair performance of rats on two versions of place learning in the Morris water maze. Behavioral neuroscience. 1995;109(1):3-9.

480.     Liu P, Bilkey DK. Perirhinal cortex contributions to performance in the Morris water maze. Behavioral neuroscience. 1998;112(2):304-15.

481.     Van Cauter T, Camon J, Alvernhe A, Elduayen C, Sargolini F, Save E. Distinct Roles of Medial and Lateral Entorhinal Cortex in Spatial Cognition. Cerebral Cortex. 2012;23(2):451-9.

482.     Burwell RD, Saddoris MP, Bucci DJ, Wiig KA. Corticohippocampal contributions to spatial and contextual learning. The Journal of neuroscience : the official journal of the Society for Neuroscience. 2004;24(15):3826-36.

483.     Bouffard JP, Jarrard LE. Acquisition of a complex place task in rats with selective ibotenate lesions of hippocampal formation: combined lesions of subiculum and entorhinal cortex versus hippocampus. Behavioral neuroscience. 1988;102(6):828-34.

484.     Bannerman DM, Yee BK, Lemaire M, Wilbrecht L, Jarrard L, Iversen SD, et al. The role of the entorhinal cortex in two forms of spatial learning and memory. Experimental brain research Experimentelle Hirnforschung Experimentation cerebrale. 2001;141(3):281-303.

485.     Bannerman DM, Yee BK, Lemaire M, Jarrard L, Iversen SD, Rawlins JN, et al. Contextual fear conditioning is disrupted by lesions of the subcortical, but not entorhinal, connections to the hippocampus. Experimental brain research Experimentelle Hirnforschung Experimentation cerebrale. 2001;141(3):304-11.

486.     Jarrard LE, Davidson TL, Bowring B. Functional differentiation within the medial temporal lobe in the rat. Hippocampus. 2004;14(4):434-49.

487.     Aggleton JP, Vann SD, Oswald CJ, Good M. Identifying cortical inputs to the rat hippocampus that subserve allocentric spatial processes: a simple problem with a complex answer. Hippocampus. 2000;10(4):466-74.

488.     Naber PA, Caballero-Bleda M, Jorritsma-Byham B, Witter MP. Parallel input to the hippocampal memory system through peri- and postrhinal cortices. Neuroreport. 1997;8(11):2617-21.

489.     Dolleman-Van der Weel MJ, Witter MP. Nucleus reuniens thalami innervates gamma aminobutyric acid positive cells in hippocampal field CA1 of the rat. Neurosci Lett. 2000;278(3):145-8.

490.     Knierim JJ, Neunuebel JP, Deshmukh SS. Functional correlates of the lateral and medial entorhinal cortex: objects, path integration and local-global reference frames. Philosophical transactions of the Royal Society of London Series B, Biological sciences. 2014;369(1635):20130369.

491.     Neunuebel JP, Yoganarasimha D, Rao G, Knierim JJ. Conflicts between local and global spatial frameworks dissociate neural representations of the lateral and medial entorhinal cortex. The Journal of neuroscience : the official journal of the Society for Neuroscience. 2013;33(22):9246-58.

492.     Burwell RD. The parahippocampal region: corticocortical connectivity. Annals of the New York Academy of Sciences. 2000;911:25-42.

493.     Suthana NA, Ekstrom AD, Moshirvaziri S, Knowlton B, Bookheimer SY. Human hippocampal CA1 involvement during allocentric encoding of spatial information. The Journal of neuroscience : the official journal of the Society for Neuroscience. 2009;29(34):10512-9.

494.     Cacucci F, Yi M, Wills TJ, Chapman P, O'Keefe J. Place cell firing correlates with memory deficits and amyloid plaque burden in Tg2576 Alzheimer mouse model. Proceedings of the National Academy of Sciences of the United States of America. 2008;105(22):7863-8.

495.     Zhao R, Fowler SW, Chiang AC, Ji D, Jankowsky JL. Impairments in experience-dependent scaling and stability of hippocampal place fields limit spatial learning in a mouse model of Alzheimer's disease. Hippocampus. 2014;24(8):963-78.

496.     Cayzac S, Mons N, Ginguay A, Allinquant B, Jeantet Y, Cho YH. Altered hippocampal information coding and network synchrony in APP-PS1 mice. Neurobiology of aging. 2015;36(12):3200-13.

497.     Cheng J, Ji D. Rigid firing sequences undermine spatial memory codes in a neurodegenerative mouse model. eLife. 2013;2:e00647.

498.     Booth CA, Witton J, Nowacki J, Tsaneva-Atanasova K, Jones MW, Randall AD, et al. Altered Intrinsic Pyramidal Neuron Properties and Pathway-Specific Synaptic Dysfunction Underlie Aberrant Hippocampal Network Function in a Mouse Model of Tauopathy. The Journal of neuroscience : the official journal of the Society for Neuroscience. 2016;36(2):350-63.

499.     Mably AJ, Gereke BJ, Jones DT, Colgin LL. Impairments in spatial representations and rhythmic coordination of place cells in the 3xTg mouse model of Alzheimer's disease. Hippocampus. 2017;27(4):378-92.

500.     Fu H, Rodriguez GA, Herman M, Emrani S, Nahmani E, Barrett G, et al. Tau Pathology Induces Excitatory Neuron Loss, Grid Cell Dysfunction, and Spatial Memory Deficits Reminiscent of Early Alzheimer's Disease. Neuron. 2017;93(3):533-41.e5.

501.     Andorfer C, Kress Y, Espinoza M, de Silva R, Tucker KL, Barde YA, et al. Hyperphosphorylation and aggregation of tau in mice expressing normal human tau isoforms. Journal of neurochemistry. 2003;86(3):582-90.

502.     Guo JL, Narasimhan S, Changolkar L, He Z, Stieber A, Zhang B, et al. Unique pathological tau conformers from Alzheimer's brains transmit tau pathology in nontransgenic mice. The Journal of experimental medicine. 2016;213(12):2635-54.

503.    Jun H, Bramian A, Soma S, Saito T, Saido TC, Igarashi KM. Disrupted Place Cell Remapping and Impaired Grid Cells in a Knockin Model of Alzheimer's Disease. Neuron. 2020;107(6):1095-112.e6.

504.    Deshmukh SS, Yoganarasimha D, Voicu H, Knierim JJ. Theta modulation in the medial and the lateral entorhinal cortices. Journal of neurophysiology. 2010;104(2):994-1006.

505.    Liu P, Reed MN, Kotilinek LA, Grant MK, Forster CL, Qiang W, et al. Quaternary structure defines a large class of amyloid-β oligomers neutralized by sequestration. Cell reports. 2015;11(11):1760-71.

506.    D'Amore J, Kajdasz S, McLellan M, Bacskai B, Stern E, Hyman B. In vivo multiphoton imaging of a transgenic mouse model of Alzheimer disease reveals marked thioflavine-S-associated alterations in neurite trajectories. Journal of Neuropathology & Experimental Neurology. 2003;62(2):137-45.

507.    Knowles RB, Wyart C, Buldyrev SV, Cruz L, Urbanc B, Hasselmo ME, et al. Plaque-induced neurite abnormalities: implications for disruption of neural networks in Alzheimer's disease. Proceedings of the National Academy of Sciences. 1999;96(9):5274-9.

508.    Stern EA, Bacskai BJ, Hickey GA, Attenello FJ, Lombardo JA, Hyman BT. Cortical synaptic integration in vivo is disrupted by amyloid-β plaques. Journal of Neuroscience. 2004;24(19):4535-40.

509.    Skaggs WE, McNaughton BL, Gothard KM, editors. An information-theoretic approach to deciphering the hippocampal code. Advances in neural information processing systems; 1993.

510.    Langston RF, Ainge JA, Couey JJ, Canto CB, Bjerknes TL, Witter MP, et al. Development of the spatial representation system in the rat. Science (New York, NY). 2010;328(5985):1576-80.

511.    Ebbesen CL, Reifenstein ET, Tang Q, Burgalossi A, Ray S, Schreiber S, et al. Cell Type-Specific Differences in Spike Timing and Spike Shape in the Rat Parasubiculum and Superficial Medial Entorhinal Cortex. Cell Rep. 2016;16(4):1005-15.

512.    Akaike H. A new look at the statistical model identification. IEEE Transactions on Automatic Control. 1974;19(6):716 - 23.

513.    Latuske P, Toader O, Allen K. Interspike Intervals Reveal Functionally Distinct Cell Populations in the Medial Entorhinal Cortex. The Journal of neuroscience : the official journal of the Society for Neuroscience. 2015;35(31):10963-76.

514.    Muller RU, Kubie JL. The firing of hippocampal place cells predicts the future position of freely moving rats. The Journal of neuroscience : the official journal of the Society for Neuroscience. 1989;9(12):4101-10.

515.    Carpenter F, Burgess N, Barry C. Modulating medial septal cholinergic activity reduces medial entorhinal theta frequency without affecting speed or grid coding. Scientific reports. 2017;7(1):14573.

516.    Cacucci F, Lever C, Wills TJ, Burgess N, O'Keefe J. Theta-Modulated Place-by-Direction Cells in the Hippocampal Formation in the Rat. The Journal of Neuroscience. 2004;24(38):8265-77.

517.    Hilbert D. Grundzüge einer allgemeinen Theorie der linearen Integralgleichungen.  Integralgleichungen und Gleichungen mit unendlich vielen Unbekannten: Springer; 1989. p. 8-171.

518.    Berens P. CircStat: A MATLAB Toolbox for Circular Statistics. Journal of Statistical Software. 2009;31(10).

519.    Boccara CN, Sargolini F, Thoresen VH, Solstad T, Witter MP, Moser EI, et al. Grid cells in pre- and parasubiculum. Nature neuroscience. 2010;13(8):987-94.

520.    Mardia KV, Jupp PE. Directional statistics: John Wiley & Sons; 2009.

521.    Kempter R, Leibold C, Buzsáki G, Diba K, Schmidt R. Quantifying circular-linear associations: hippocampal phase precession. Journal of neuroscience methods. 2012;207(1):113-24.

522.    Scott L, Feng J, Kiss T, Needle E, Atchison K, Kawabe TT, et al. Age-dependent disruption in hippocampal θ oscillation in amyloid-β overproducing transgenic mice. Neurobiology of aging. 2012;33(7):1481.e13-23.

523.    Schneider F, Baldauf K, Wetzel W, Reymann KG. Behavioral and EEG changes in male 5xFAD mice. Physiol Behav. 2014;135:25-33.

524.    Villette V, Poindessous-Jazat F, Simon A, Léna C, Roullot E, Bellessort B, et al. Decreased rhythmic GABAergic septal activity and memory-associated theta oscillations after hippocampal amyloid-beta pathology in the rat. The Journal of neuroscience : the official journal of the Society for Neuroscience. 2010;30(33):10991-1003.

525.    Mou X, Cheng J, Yu YSW, Kee SE, Ji D. Comparing Mouse and Rat Hippocampal Place Cell Activities and Firing Sequences in the Same Environments. Frontiers in cellular neuroscience. 2018;12:332-.

526.    Schimanski LA, Lipa P, Barnes CA. Tracking the course of hippocampal representations during learning: when is the map required? Journal of Neuroscience. 2013;33(7):3094-106.

527.    Barnes CA, Suster MS, Shen J, McNaughton BL. Multistability of cognitive maps in the hippocampus of old rats. Nature. 1997;388(6639):272-5.

528.    Gerrard JL, Burke SN, McNaughton BL, Barnes CA. Sequence reactivation in the hippocampus is impaired in aged rats. Journal of Neuroscience. 2008;28(31):7883-90.

529.    Palop JJ, Chin J, Roberson ED, Wang J, Thwin MT, Bien-Ly N, et al. Aberrant excitatory neuronal activity and compensatory remodeling of inhibitory hippocampal circuits in mouse models of Alzheimer's disease. Neuron. 2007;55(5):697-711.

530.    Kam K, Duffy Á M, Moretto J, LaFrancois JJ, Scharfman HE. Interictal spikes during sleep are an early defect in the Tg2576 mouse model of β-amyloid neuropathology. Scientific reports. 2016;6:20119.

531.    Del Vecchio RA, Gold LH, Novick SJ, Wong G, Hyde LA. Increased seizure threshold and severity in young transgenic CRND8 mice. Neuroscience letters. 2004;367(2):164-7.

532.    Scarmeas N, Honig LS, Choi H, Cantero J, Brandt J, Blacker D, et al. Seizures in Alzheimer disease: who, when, and how common? Archives of neurology. 2009;66(8):992-7.

533.    Gold C, Henze DA, Koch C, Buzsáki G. On the origin of the extracellular action potential waveform: A modeling study. Journal of neurophysiology. 2006;95(5):3113-28.

534.    Steinerman JR, Irizarry M, Scarmeas N, Raju S, Brandt J, Albert M, et al. Distinct pools of beta-amyloid in Alzheimer disease-affected brain: a clinicopathologic study. Archives of neurology. 2008;65(7):906-12.

535. Bloom GS. Amyloid-β and tau: the trigger and bullet in Alzheimer disease pathogenesis. JAMA neurology. 2014;71(4):505-8.

536. Haass C, Selkoe DJ. Soluble protein oligomers in neurodegeneration: lessons from the Alzheimer's amyloid beta-peptide. Nat Rev Mol Cell Biol. 2007;8(2):101-12.

537. D'Andrea MR, Nagele RG. Morphologically distinct types of amyloid plaques point the way to a better understanding of Alzheimer's disease pathogenesis. Biotech Histochem. 2010;85(2):133-47.

538. Kim T-K, Lee J-E, Park S-K, Lee K-W, Seo J-S, Im J-Y, et al. Analysis of differential plaque depositions in the brains of Tg2576 and Tg-APPswe/PS1dE9 transgenic mouse models of Alzheimer disease. Experimental & Molecular Medicine. 2012;44(8):492-502.

539. Bielarczyk H, Jankowska-Kulawy A, Hoefling C, Ronowska A, Gul-Hinc S, Rossner S, et al. AβPP-transgenic 2576 mice mimic cell type-specific aspects of acetyl-CoA-linked metabolic deficits in Alzheimer's disease. Journal of Alzheimer's Disease. 2015;48(4):1083-94.

540. Nilsberth C, Westlind-Danielsson A Fau - Eckman CB, Eckman Cb Fau - Condron MM, Condron Mm Fau - Axelman K, Axelman K Fau - Forsell C, Forsell C Fau - Stenh C, et al. The 'Arctic' APP mutation (E693G) causes Alzheimer's disease by enhanced Abeta protofibril formation. (1097-6256 (Print)).

541. Uruno A, Matsumaru D, Ryoke R, Saito R, Kadoguchi S, Saigusa D, et al. Nrf2 Suppresses Oxidative Stress and Inflammation in &lt;em&gt;App&lt;/em&gt; Knock-In Alzheimer's Disease Model Mice. Molecular and Cellular Biology. 2020;40(6):e00467-19.

542. Goncalves MB, Clarke E, Hobbs C, Malmqvist T, Deacon R, Jack J, et al. Amyloid β inhibits retinoic acid synthesis exacerbating A lzheimer disease pathology which can be attenuated by an retinoic acid receptor α agonist. European Journal of Neuroscience. 2013;37(7):1182-92.

543. Hill A. The environment and disease: association or causation? Proc R Soc Med. 1965;58:295 - 300.

544. Cirrito JR, May PC, O'Dell MA, Taylor JW, Parsadanian M, Cramer JW, et al. In vivo assessment of brain interstitial fluid with microdialysis reveals plaque-associated changes in amyloid-beta metabolism and half-life. The Journal of neuroscience : the official journal of the Society for Neuroscience. 2003;23(26):8844-53.

545. Liu L, Duff K. A Technique for Serial Collection of Cerebrospinal Fluid from the Cisterna Magna in Mouse. Journal of visualized experiments : JoVE. 2008;21.

546. Shafiei SS, Guerrero-Muñoz MJ, Castillo-Carranza DL. Tau Oligomers: Cytotoxicity, Propagation, and Mitochondrial Damage. Front Aging Neurosci. 2017;9:83.

547. Maeda S, Sahara N, Saito Y, Murayama S, Ikai A, Takashima A. Increased levels of granular tau oligomers: an early sign of brain aging and Alzheimer's disease. Neuroscience research. 2006;54(3):197-201.

548. Patterson KR, Remmers C, Fu Y, Brooker S, Kanaan NM, Vana L, et al. Characterization of prefibrillar Tau oligomers in vitro and in Alzheimer disease. The Journal of biological chemistry. 2011;286(26):23063-76.

549. Lasagna-Reeves CA, Castillo-Carranza DL, Sengupta U, Clos AL, Jackson GR, Kayed R. Tau oligomers impair memory and induce synaptic and mitochondrial dysfunction in wild-type mice. Mol Neurodegener. 2011;6:39.

550.     Wu JW, Herman M, Liu L, Simoes S, Acker CM, Figueroa H, et al. Small misfolded Tau species are internalized via bulk endocytosis and anterogradely and retrogradely transported in neurons. The Journal of biological chemistry. 2013;288(3):1856-70.

551.     Cohen RM, Rezai-Zadeh K, Weitz TM, Rentsendorj A, Gate D, Spivak I, et al. A transgenic Alzheimer rat with plaques, tau pathology, behavioral impairment, oligomeric aβ, and frank neuronal loss. Journal of Neuroscience. 2013;33(15):6245-56.

552.     Steinmetz NA, Koch C, Harris KD, Carandini M. Challenges and opportunities for large-scale electrophysiology with Neuropixels probes. Current opinion in neurobiology. 2018;50:92-100.

553.     Hort J, Andel R, Mokrisova I, Gazova I, Amlerova J, Valis M, et al. Effect of donepezil in Alzheimer disease can be measured by a computerized human analog of the Morris water maze. Neuro-degenerative diseases. 2014;13(2-3):192-6.

554.     Moodley K, Minati L, Contarino V, Prioni S, Wood R, Cooper R, et al. Diagnostic differentiation of mild cognitive impairment due to Alzheimer's disease using a hippocampus-dependent test of spatial memory 2014.

555.     Ritchie K, Carriere I, Howett D, Su L, Hornberger M, O'Brien JT, et al. Allocentric and Egocentric Spatial Processing in Middle-Aged Adults at High Risk of Late-Onset Alzheimer's Disease: The PREVENT Dementia Study. J Alzheimers Dis. 2018;65(3):885-96.

556.     Howett D, Castegnaro A, Krzywicka K, Hagman J, Marchment D, Henson R, et al. Differentiation of mild cognitive impairment using an entorhinal cortex-based test of virtual reality navigation. Brain : a journal of neurology. 2019;142(6):1751-66.

557.     Ludkiewicz B, Wójcik S, Spodnik E, Domaradzka-Pytel B, Klejbor I, Morys J. Cholinergic innervation of parvalbumin- and calbindin-containing neurons in the hippocampus during postnatal development of the rat brain. Folia morphologica. 2002;61:89-96.